DEVELOPMENT OF NOVEL STRATEGIES FOR DETECTION AND TREATMENT OF CANCER

by

THILANI NISHANTHIKA SAMARAKOON

B. Sc. (Hons), University of Colombo, Sri Lanka, 2004

AN ABSTRACT OF A DISSERTATION

submitted in partial fulfillment of the requirements for the degree

DOCTOR OF PHILOSOPHY

Department of Chemistry
College of Arts and Sciences

KANSAS STATE UNIVERSITY
Manhattan, Kansas

2010

Abstract

Cancer is one of the leading causes of death in the world. Billions of dollars are spent to treat cancer every year. This clearly shows the need for developing improved treatment techniques that are affordable to every person. Early diagnosis and imaging of tumors is equally important for the battle against this disease. This dissertation will discuss new approaches for discovering and developing novel detection and treatment techniques for cancer using organic ligands, and Fe/Fe_3O_4 core/shell magnetic nanoparticles.

A series of *o*-phenylenediamine derivatives with nitro-, methyl- and chloro- substituents were synthesized and studied their ability to act as anticancer agents by using steady-state, UV/Vis-, and fluorescence spectroscopy. In the absence of zinc(II), intercalation with DNA is the most probable mode of interaction. Upon addition of zinc(II), DNA-surface binding of the supramolecular aggregates was observed. The interaction of the supramolecular $(-ligand-Zn^{2+}-)_n$ aggregates with MDA 231 breast cancer cells led to significant cell death in the presence of UVA at $\lambda=313$ nm displaying their potential as anticancer agents.

Bimagnetic Fe/Fe_3O_4 core/shell nanoparticles (MNPs) were designed for cancer targeting after intratumoral or intravenous administration. Their inorganic center was protected by dopamine-oligoethylene glycol ligands. TCPP (4-tetracarboxyphenyl porphyrin), a fluorescent dye, was attached to the dopamine-oligoethylene glycol ligands. These modified nanoparticles have the ability to selectively accumulate within the cancerous cells. They are suitable candidates for local hyperthermia treatment. We have observed a temperature increase of 11 ºC in live mice when subcutaneously injecting the MNPs at the cancer site and applying an alternating magnetic field. The system is also suitable for Magnetic Resonance Imaging (MRI), which is a diagnostic

tool to obtain images of the tumors. Our superparamagnetic iron oxide nanoparticles have the ability to function as T_1 weighted imaging agents or positive contrasting agents. We were able to image tumors in mice using MRI.

Various proteases are over-expressed by numerous cancer cell lines and, therefore, of diagnostic value. Our diagnostic nanoplatforms, designed for the measurement of protease activities in various body fluids (blood, saliva, and urine), comprise Fe/Fe_3O_4 core/shell nanoparticles featuring consensus sequences, which are specific for the target protease. Linked to the consensus sequence is a fluorescent organic dye (e.g. TCPP). Cleavage of the sequence by the target protease can be detected as a significant increase in fluorescence occurring from TCPP. We were able to correlate our diagnostic results with cancer prognosis.

DEVELOPMENT OF NOVEL STRATEGIES FOR DETECTION AND TREATMENT OF CANCER

by

THILANI NISHANTHIKA SAMARAKOON

B.Sc. (Hons), University of Colombo, Sri Lanka, 2004

A DISSERTATION

submitted in partial fulfillment of the requirements for the degree

DOCTOR OF PHILOSOPHY

Department of Chemistry
College of Arts and Sciences

KANSAS STATE UNIVERSITY
Manhattan, Kansas

2010

Approved by:

Major Professor
Dr. Stefan H. Bossmann

Copyright

THILANI NISHANTHIKA SAMARAKOON

2010

Abstract

Cancer is one of the leading causes of death in the world. Billions of dollars are spent to treat cancer every year. This clearly shows the need for developing improved treatment techniques that are affordable to every person. Early diagnosis and imaging of tumors is equally important for the battle against this disease. This dissertation will discuss new approaches for discovering and developing novel detection and treatment techniques for cancer using organic ligands, and Fe/Fe_3O_4 core/shell magnetic nanoparticles.

A series of *o*-phenylenediamine derivatives with nitro-, methyl- and chloro- substituents were synthesized and studied their ability to act as anticancer agents by using steady-state, UV/Vis-, and fluorescence spectroscopy. In the absence of zinc(II), intercalation with DNA is the most probable mode of interaction. Upon addition of zinc(II), DNA-surface binding of the supramolecular aggregates was observed. The interaction of the supramolecular $(\text{-ligand-}Zn^{2+}\text{-})_n$ aggregates with MDA 231 breast cancer cells led to significant cell death in the presence of UVA at $\lambda=313$ nm displaying their potential as anticancer agents.

Bimagnetic Fe/Fe_3O_4 core/shell nanoparticles (MNPs) were designed for cancer targeting after intratumoral or intravenous administration. Their inorganic center was protected by dopamine-oligoethylene glycol ligands. TCPP (4-tetracarboxyphenyl porphyrin), a fluorescent dye, was attached to the dopamine-oligoethylene glycol ligands. These modified nanoparticles have the ability to selectively accumulate within the cancerous cells. They are suitable candidates for local hyperthermia treatment. We have observed a temperature increase of 11 ºC in live mice when subcutaneously injecting the MNPs at the cancer site and applying an alternating magnetic field The system is also suitable for Magnetic Resonance Imaging (MRI), which is a diagnostic

tool to obtain images of the tumors. Our superparamagnetic iron oxide nanoparticles have the ability to function as T_1 weighted imaging agents or positive contrasting agents. We were able to image tumors in mice using MRI.

Various proteases are over-expressed by numerous cancer cell lines and, therefore, of diagnostic value. Our diagnostic nanoplatforms, designed for the measurement of protease activities in various body fluids (blood, saliva, and urine), comprise Fe/Fe_3O_4 core/shell nanoparticles featuring consensus sequences, which are specific for the target protease. Linked to the consensus sequence is a fluorescent organic dye (e.g. TCPP). Cleavage of the sequence by the target protease can be detected as a significant increase in fluorescence occurring from TCPP. We were able to correlate our diagnostic results with cancer prognosis.

Table of Contents

List of Figures

List of Tables

Acknowledgements

I would like to take this opportunity to immortally recognize everyone who helped and supported me for the success of my project.

I would first and foremost like to thank my major professor Dr. Stefan H. Bossmann for continuously advising and encouraging me during the project. Without his support, this project would not have been possible. His interest in my views has added greatly to my confidence in myself and my work. His guidance has been crucial throughout my stay at the Department of Chemistry at Kansas State University. He is an exceptional advisor and an extraordinary teacher.

I also would like to extend gratitude to the members of my committee, Dr. Duy Hua, Dr. Eric Maatta, Dr. Christopher T. Culbertson, Dr. John Tomich, Dr. Om Prakash and outside chair person Dr. Ruth Welti for their time and scheduling flexibility.

Next I would like to thank Katharine Bossmann for her friendship and small talks during my difficult times and for cheering me up. Thank you for taking such good care of our research group and helping us in every possible way.

A big thank you to former members of Bossmann's group, Dr. Pubudu Gamage and Dr. Cherry Leaym for the wonderful times and laughs we had together.

I would also like to thank my current group members Ayomi Perera, Dr. Hongwang Wang and David Villanueva for their friendship.

This project became a success through contributions from several collaborators. Sivasai Balivada, Dr. Raja Shekar Rachakatla, Marla Pyle, Dr. Masa Tamura, Dr. Deryl L. Troyer from Department of Veterinary Medicine at Kansas State University, Raj Kumar Dani, Dr. Leila Maurmann, Dr. Viktor Chikan from Department of Chemistry, Dr. Franklin O. Kroh, Brandon Walker, Dr. Xiaoxuan Leaym, Dr. Olga B. Koper from NanoScale Corporation, Manhattan, KS. I would specially like to thank Dr. Hongwang Wang for the contributions he made for the success of this project.

Additionally, I would like to thank Linda Gibbs and Mary Dooley for their warm hugs and cheerful smiles.

I also must thank all the Sri Lankans in Manhattan for making me feel home. Specially Manindu and Dulan for being such wonderful friends.

I would like to thank my family, my parents for everything they have done for me. I would not be the person I am today without their support, guidance and love, and my brother Roshan, for his love and support.

Last but not least I would like to thank my husband, Dhanushka for his love and support in every step of my life. I am blessed to have you in my life.

Dedication

I would like to dedicate my dissertation to my parents and my husband.

Chapter 1 - Study of Derivatives of *o*-Phenylenediamine as Anti-cancer Agents

1.1 Introduction

Cancer is characterized by the uncontrolled rapid cell division that leads to cells with abnormal characteristics. One characteristic feature of the cancer cells is the ability to spread to all parts of the body, which makes cancer diagnosis and treatment more difficult. Cancer is one of the leading causes of death in the world. In the USA, cancer is the second most common cause of death. According to the American Cancer Society, in 2008 more than 0.5 million people have died, from cancer, in USA alone. The numbers in the whole planet are not promising either. In 2004 more than 7.4 million people died from cancer, and the future numbers estimate that by year 2030, it will be 12 million.[1] This data, combined with the billions of dollars spent to treat cancer every year, is a clear indication for the desperate need of improved anti-cancer drugs.

Chemotherapy, surgery and radiation therapy are the most commonly used methods for the treatment of cancer. Sometimes combinations of several treatment methods are used. Chemotherapy is the use of drugs to kill cancer cells. This can be a single drug or a combination of several. Even though chemotherapy is a popular method used, it has several drawbacks. The major drawback of most of the chemotherapeutic drugs is their severe side effects. Side effects include hair loss, bleeding, nausea, vomiting and fatigue. The drugs are designed to kill fast growing cancer cells. But once the drugs enter normal cells they affect and harm these healthy cells as well leading to severe side effects.[2]

There are more than 100 drugs approved by Food and Drug Administration (FDA) and these drugs are used in chemotherapy.[3] Most of these drugs interact with the DNA of the cancer cells and impair vital cell function leading to cell death (necrosis or apoptosis).[4] To achieve a

higher selectivity of treating cancer cells vs. healthy cells, it is very important to understand the mode of interaction of each drug. A part of my thesis is concerned with DNA-binding drugs. In order to enhance their effectiveness, and to select the right drug or combination of drugs in the first place, I have performed DNA-binding studies to elucidate the mechanism and the strength of DNA-binding. This research was based on the hypothesis that DNA-binders that take up sufficient space outside the DNA-double helix can effectively impair the function enzymes that have to dock to DNA to facilitate DNA-replication (e.g. topoisomerase I and II or helicase).

1.2 Structure of DNA

DNA or deoxyribonucleic acid stores the genetic information required for the development and functioning of a cell. The main building block of DNA is called a nucleotide. A nucleotide consists of 3 parts: a pentose sugar, heterocyclic base and a phosphate group. The backbone of the DNA is made out of pentose sugar phosphate groups, which are linked by phosphodiester bonds. The four bases found in DNA are adenine (abbreviated A), cytosine (C), guanine (G) and thymine (T). Adenine and guanine bases are known as purines, while cytosine and thymine are known as pyrimidines. Adenine will couple with thymine and guanine with cytosine via hydrogen bonds, resulting in the double helical structure. The two strands of the double helix are anti-parallel to each other. The helix is a right-handed and it gives rise to two grooves namely the major groove and the minor groove. The width of the major groove is 22 Å and the minor groove is 12 Å only. Figure 1.1 further explains the structure of the helix.[5]
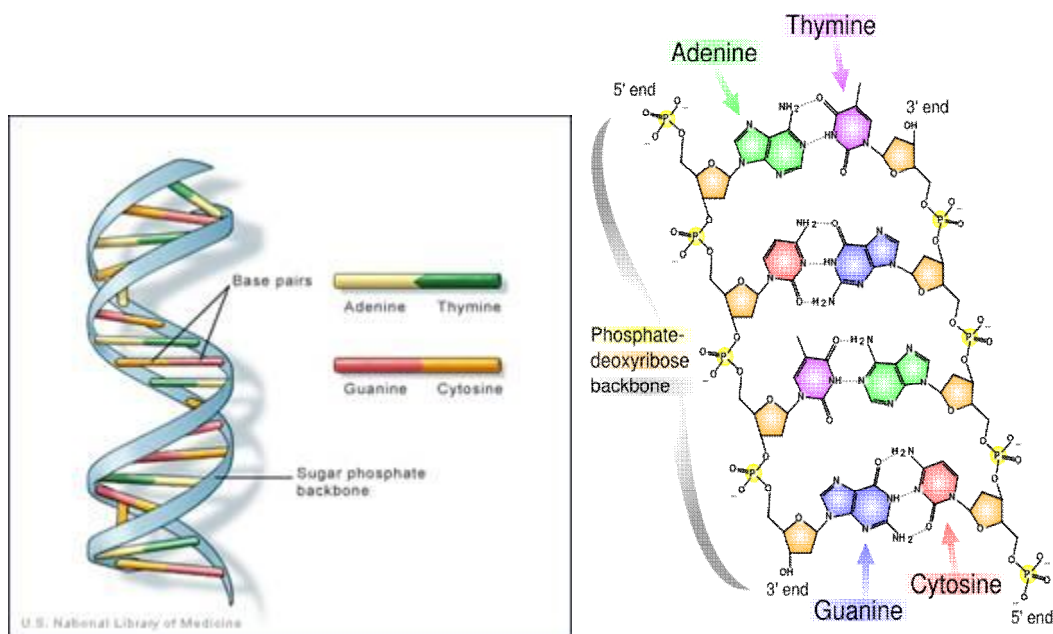
Figure 1.1: (a) DNA double helical structure and (b) pyrimidines and purines base pairing[6,7]

In biological systems we can observe mainly 3 types of DNA, A-DNA. B-DNA and Z-DNA. These structures differ from each other in their geometry and dimensions. The most common type of DNA found in human cells is the B-DNA.[5]

1.3 Binding Modes of Drug Molecules to DNA

DNA binding agents interact noncovalently with DNA. These modes of interactions can be predicted by studying the structure of the binding molecules. When a drug molecule binds to the DNA, the mode of binding will vary from molecule to molecule. The drug could bind to the surface of the DNA, either to the major groove or the minor groove or it could stack in between base pairs (intercalate).[8]

Groove binding of molecules especially metal complexes with DNA is well known, and ruthenium(II) polypridine complexes are one of the best studied transition metal complexes. There have been extensive studies on synthesis of small molecules showing minor groove

binding in B-DNA.[9] The DNA backbone is negatively charged due to the presence of PO_4^- groups. If the binding molecule is positively charged there will be electrostatic interactions between the ligand and the helix, which will further be stabilized by intermolecular forces such as Van der Waals, hydrophobic interactions and hydrogen bonding.[8,9]

Another discussed method of DNA interaction with small molecules is intercalation with the helix. DNA intercalation is the insertion of a small ligand or a fragment between two adjacent base pairs in the DNA strand, forming stable sandwich-like structures. Usually polyaromatic, planar molecules act as intercalators.[10] The intercalation between the heterocyclic base pairs and aromatic ligands is stabilized by π-π stacking and dipole-dipole interactions. As a result of intercalation the opening of a space between base pairs will lead to unwinding of the helical structure, lengthening it and disturbing its biological functions such as DNA replication or transcription.[11] During intercalation the angle of the PO_4^- groups change leading to lengthening of the structure by 3.4 Å.[12] The intercalating ligand will be rigidly held perpendicular to the helical axis stiffening the helix.[8] The intercalation behaves according to the "neighbor exclusion principle" where binding of one intercalator prevents the access of another intercalator to the neighboring intercalation site. There are numerous studies in such intercalators displayed anti-tumor activity.[11] Doxorubicin is one of the primary chemotherapeutic agents utilized for the treatment of cancer. Its mechanism of action occurs via intercalation into DNA and inhibiting the biosynthesis via blocking the enzyme helicase which unwinds DNA prior to replication.[13]
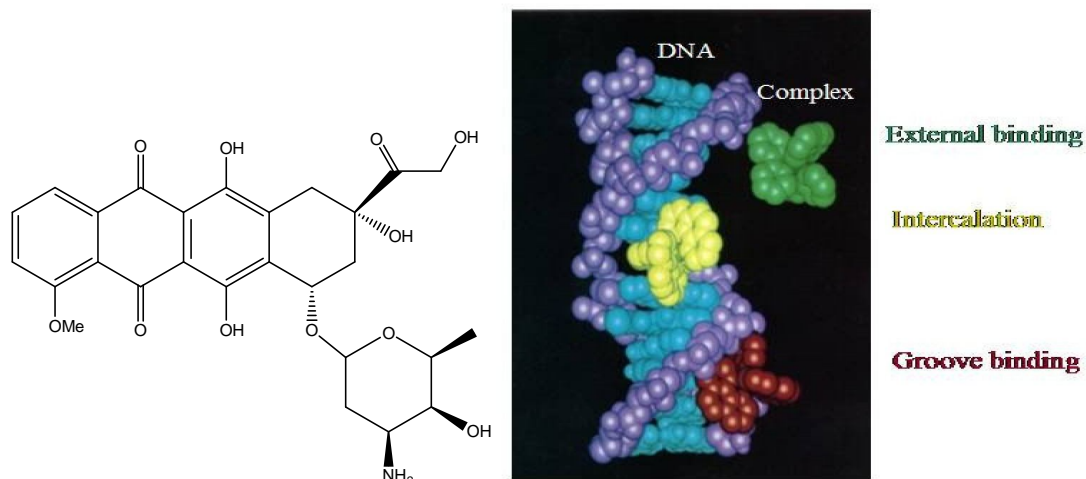
Figure 1.2: (a) Structure of Doxorubicin (b) Binding modes of a ligand to DNA double helical structure[14]

Once the DNA is bound to the molecule it loses its double helical form and its physical properties such as viscosity and melting temperature change. The photochemical properties of the ligands and DNA also show significant variations upon binding. The DNA drug interactions and binding can be studied using several methods. The most commonly used techniques are NMR, UV/Visible spectroscopy and fluorescence spectroscopy.[15] Establishing the actual binding mode of a ligand to DNA is a difficult task to achieve because one experimental technique sometimes may not generate enough evidences. But combinations of different techniques will give better insight into the host guest binding modes.[11] I have synthesized different derivatives of *o*-phenylenediamine which have the ability to intercalate with DNA double helical structure.

1.4 Synthesis of *o*-phenylenediamine Derivatives for DNA Binding

2,3-diaminophenazine and a series of *o*-phenylenediamine derivatives were synthesized with nitro-, methyl- and chloro- substituents in 5-position, and their binding ability to DNA was

studied using fluorescence and UV/Vis spectroscopy. The binding constants were calculated and the binding mode was predicted using the obtained data.
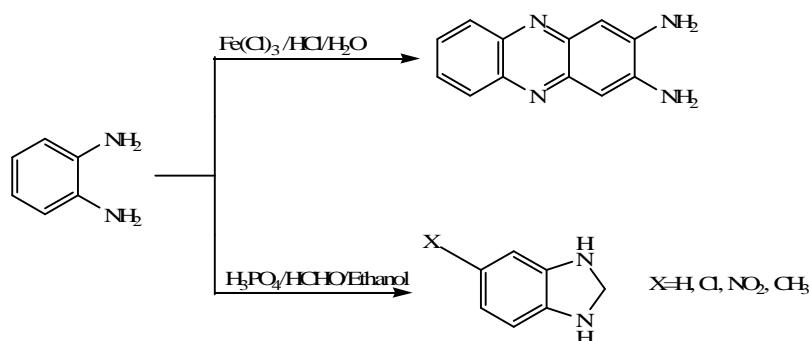
Figure 1.3: Synthetic scheme of *o*-phenylenediamine derivatives

    o-phenylenediamine has attracted great interest among heterocyclic synthetic chemists due to the presence of 1,2 diamino function, which can be further cyclized to obtain many nitrogen containing heterocycles, which possess significant biological properties (e.g.: antitumor activity, antibacterial activity, and antifungal activity).[16] According to its *Material Safety Data Sheet*, *o*-phenylenediamine and its substituents are known to cause mutagenic effects on human cells, bacteria and laboratory animals, which can be regarded as further evidence for their direct interactions with DNA.

    There are reports of platinum(II) complexes having ligands derived from 1,2-phenylenediamine displaying antitumor activity. The authors discuss that this effect is demonstrated due to the chelating ability of the aromatic diamine with DNA.[17] Jennerwein and coworkers[18] studied the influence of the phenylenediamine ring substituents on the antitumor activity of these complexes. They were able to demonstrate that the electron withdrawing groups such as nitro- and fluorine- caused significantly higher toxicities on cancerous cells than that of electron donating substituents.[18]
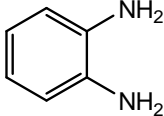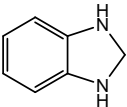
With this information in mind I have synthesized a series of 2,3-dihydro-1H-benzo[*d*]imidazole derivatives, 2,3-diaminophenazine, the Zn^{2+} complex of 2,3-dihydro-1H-benzo[*d*]imidazole, and conducted their binding studies with calf thymus DNA using fluorescence, UV/Vis spectroscopy and time resolved spectroscopy. The antitumor activity of the Zn^{2+} complex of 2,3-dihydro-1H-benzo[*d*]imidazole was studied using the MDA 231 cancer cell line. Furthermore the ability of this complex to cleave oligonucleotide chains in the presence of irradiation was evaluated and a mechanism was proposed.
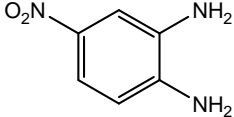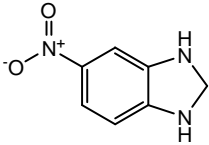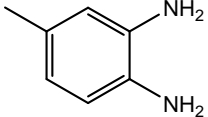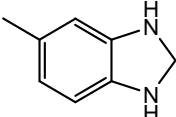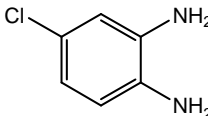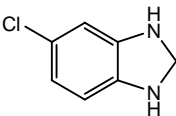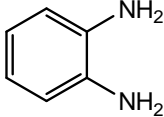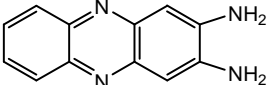
1.4.1 Study of 2,3-dihydro-1H-benzo[*d*]imidazole Derivatives

2,3-dihydro-1H-benzo[*d*]imidazole derivatives were synthesized as a one-pot reaction by reacting *o*-phenylenediamine and its substituents with formaldehyde in a mixture of ethanol and 85% H_3PO_4.[19] After the reaction was completed, the isolation and purification yielded the derivatives in 20-40% yields. The reactions resulted in several possible competing intermediates which decreases the yield of the reaction.[19] The compounds were characterized by ^{1}H NMR, ^{13}C NMR, UV visible, and mass spectroscopy.

1.4.2 UV/Vis- and Fluorescence Characterization of the Reaction Products

Table 1.1: UV Characterization of *o*-phenylenediamine derivatives

Starting material	Maxima of the UV/Vis-absorption bands of the products	Excitation and emission maxima of the products
o-phenylenediamine 211, 238, 293 nm	2,3-dihydro-1H-benzo[*d*]imidazole 205, 267, 272, 460 nm	552 nm (excitation at 472 nm)
4-nitrobenzene-1,2-diamine	5-nitro-2,3-dihydro-1H-benzo[*d*]imidazole	488 nm, 540 nm (excitation at 420 nm)

O₂N–⬡(NH₂)(NH₂) 202, 224, 269, 401 nm	⬡ nitro-benzimidazole structure 201, 236, 298, 410 nm	
4-methylbenzene-1,2-diamine methyl-benzene diamine structure 211, 239, 290 nm	5-methyl-2,3-dihydro-1H-benzo[d]imidazole methyl-benzimidazole structure 211, 260, 273, 420 nm	465 nm, 515 nm (excitation at 420 nm)
4-chlorobenzene-1,2-diamine chloro-benzene diamine structure 212, 248, 312 nm	5-chloro-2,3-dihydro-1H-benzo[d]imidazole chloro-benzimidazole structure 211, 277, 284, 445 nm	474 nm (excitation at 450 nm)
o-phenylenediamine phenylenediamine structure 211, 238, 293 nm	2,3-diaminophenazine diaminophenazine structure 256, 420 nm	557 nm (excitation at 420 nm)

The peaks in the UV region are due to π-π* transitions of the benzene ring. When there are n-π* transitions from electron donating atoms such as nitrogen, the peaks are normally observed in the range of 400-450 nm. These peaks were clearly visible for 2,3-diaminophenazine. In the case of other compounds a much weaker band was observed when the compounds were subjected UV studies. For all the compounds, significant fluorescence emission were observed after excitation.

1.5 UV/Vis- Binding Studies

The absorption spectra of the ligands were recorded in the absence and presence of different concentrations of pre-dialyzed calf thymus DNA (0-50 µM). Calf thymus DNA (CT-DNA) is considered ideal for intercalation experiments, because it contains almost equal

amounts of all four nucleotides. The concentration of the ligand was kept a constant and the concentration of DNA was increased. The binding of the ligand to DNA is associated with a red shift of the absorption band of the ligand in the peak corresponding to π-π transitions. If the ligand is a metal complex, the presence of the metal to ligand charge transfer band (MLCT) provides positive evidence for the interactions of the ligand with the DNA.

The DNA-binding properties of compounds were further established by monitoring the changes in absorbance at 260 nm which is the maximum absorption for CT-DNA. Different sets of measurements were carried out at fixed concentration of complex with varying concentrations of calf thymus DNA. The interaction of the ligand with CT-DNA was confirmed from the changes observed in the absorption band. Calf thymus DNA exhibits hyperchromism or an increase in the absorption band. Hyperchromism upon interaction with DNA implies DNA binding or unwinding. It is generally is an indicative of a surface binding of the ligand or complex on DNA.[20,21]

1.5.1 2,3-Diaminophenazine

The binding studies of 2,3-diaminophenazine were conducted using UV/Vis and fluorescence spectroscopy. The UV/Vis absorption and fluorescence emission spectra were obtained as a function of pH. Both emission and absorption are dependent on pH. So it is important to maintain a constant pH value during the course of the study.[22]
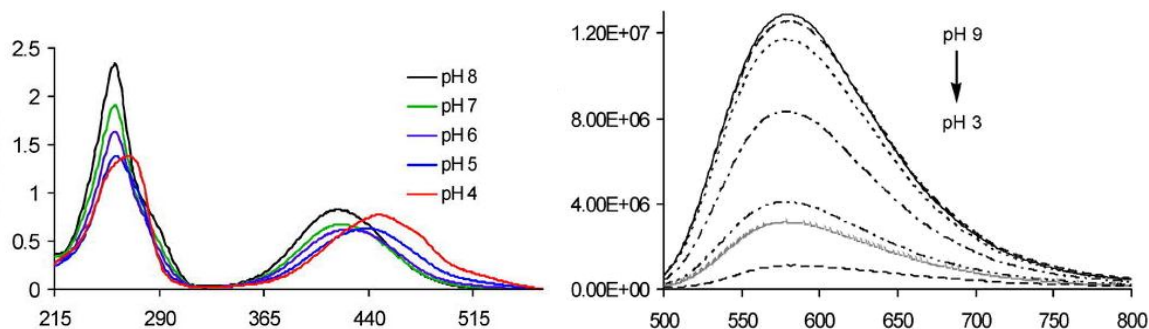
Figure 1.4: UV/Vis absorption and fluorescence emission (Excitation at 420 nm) spectra of 2,3-diaminophenazine at different pH values[22]
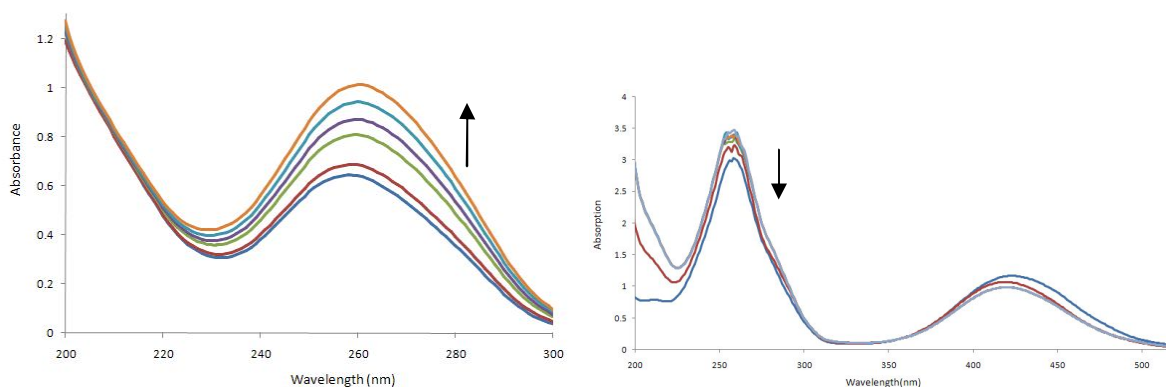
Figure 1.5: UV/Vis absorption spectra of (a) calf thymus DNA upon addition of 2,3-diaminophenazine. Arrows show the increase in absorbance. (b) 2,3-diaminophenazine upon addition of CT-DNA. Arrows show the change in absorbance upon increasing the DNA concentration

As observed from the UV/Vis absorption spectrum of CT-DNA, there is clear hyperchromism upon interaction with 2,3-diaminophenazine indicating that the binding of the ligand to DNA. The band at 419 nm showed hyperchromism by 18.1% and a red shift of 3nm as the DNA concentration was increased to 50 µM.

.

1.5.2 UV/Vis Binding studies of 2,3-dihydro-1H-benzo[d]imidazole Derivatives

The DNA binding studies of -CH₃, -NO₂, and -Cl derivatives were studied using UV/Vis and fluorescence spectroscopy titrations. The measurements were conducted at pH=7.4 phosphate buffer with dialyzed calf thymus DNA. The spectra were recorded in the presence of different concentrations of CT-DNA (0-50 µM).
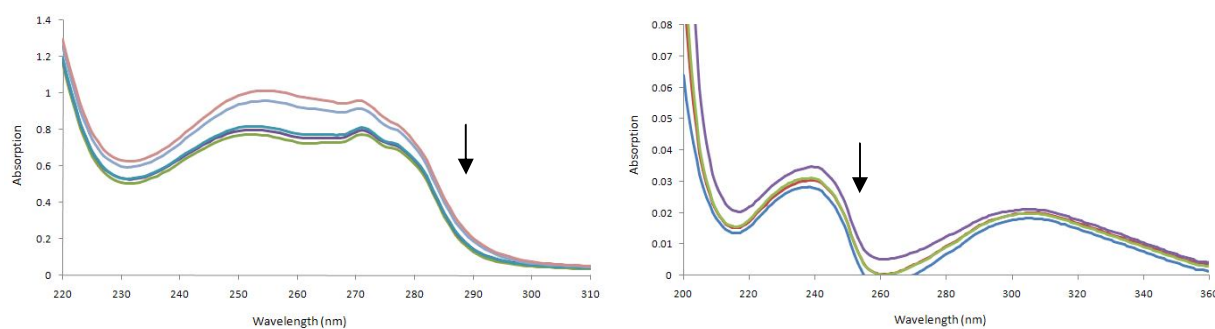
Figure 1.6: UV/Vis absorption spectra of (a) 2,3-dihydro-1H-benzo[d]imidazole and (b) 5-nitro-2,3-dihydro-1H-benzo[d]imidazole upon addition of CT-DNA. Arrows show the change in absorbance upon increasing the DNA concentration
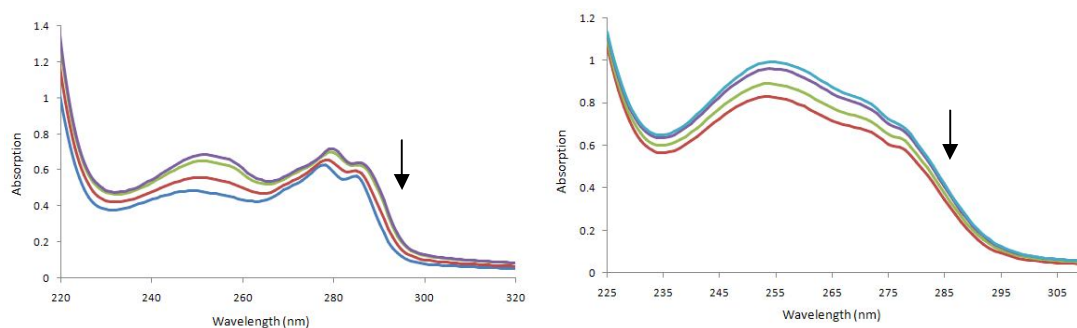
Figure 1.7: UV/Vis absorption spectra of (a) 5-chloro-2,3-dihydro-1H-benzo[d]imidazole and (b) 5-methyl-2,3-dihydro-1H-benzo[d]imidazole upon addition of CT-DNA. Arrows show the change in absorbance upon increasing the DNA concentration

11

The effects of the various ligand concentrations on UV/Vis absorption spectra of calf thymus DNA were studied using different concentrations of ligand. The spectra were recorded with increasing concentration of the ligand. The UV band of the DNA, which is at 260 nm increased providing further evidence for the binding of the ligand to DNA.
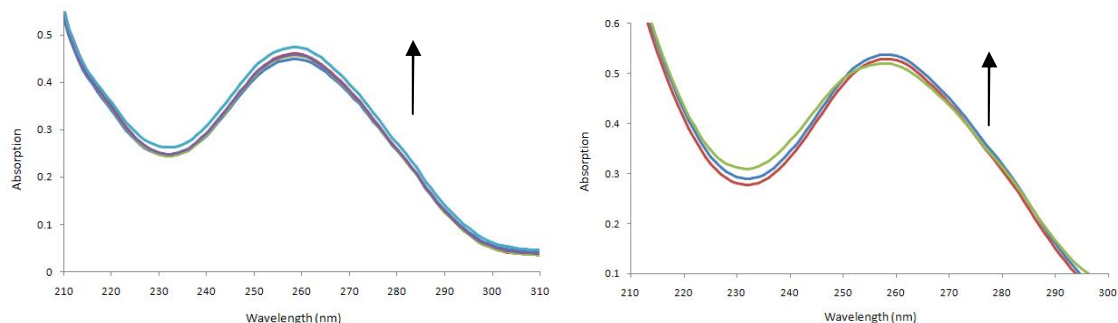
Figure 1.8: UV/Vis absorption spectra of calf thymus DNA upon addition of (a) 2,3-dihydro-1H benzo[d]imidazole and (b) 5-nitro-2,3-dihydro-1H-benzo[d]imidazole Arrows show the increase in absorbance
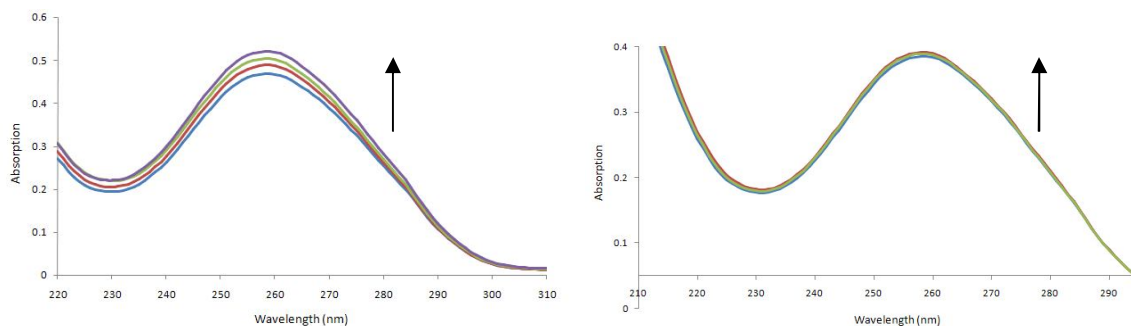
Figure 1.9: UV/Vis absorption spectra of calf thymus DNA upon addition of (a) 5-chloro-2,3-dihydro-1H-benzo[d]imidazole and (b) 5-methyl-2,3-dihydro-1H-benzo[d]imidazole. Arrows show the increase in absorbance

1.6 Fluorescence Binding Studies of 2,3-dihydro-1H-benzo[*d*]imidazole Derivates to DNA

Upon excitation at selected wavelengths all the 2,3-dihydro-1H-benzo[*d*]imidazole derivatives showed luminescence in the phosphate buffer. Upon introduction of CT-DNA, the luminescence intensities of the ligands were enhanced. This enhancement was different for each ligand. The relative enhancement in fluorescence induced by CT-DNA was recorded as a measure of I/I^0 where I and I^0 are the emission intensities of the ligands or complexes in the presence and absence of CT-DNA. Our mechanistic hypothesis is that binding of the ligand to DNA releases water molecules from the DNA helical structure. When the ligand or complex is intercalated in- between the base pairs of the DNA, its mobility is limited. The accessibility of H_2O molecules to the ligand or complex is restricted due to the hydrophobic nature of the inside environment of the DNA helix. Due to this reason there is a decrease in the vibrational energy transfer from the ligand or complex to H_2O, leading to a higher emission intensity.[23]
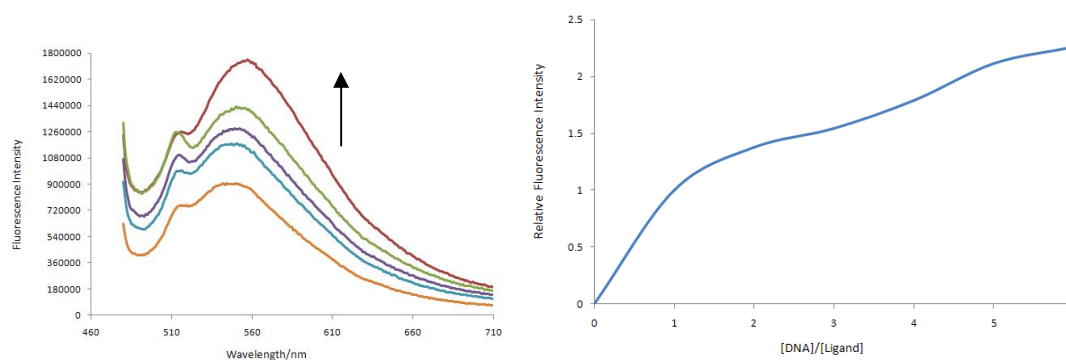
Figure 1.10: Emission spectra of ligand (a) 2,3-dihydro-1H-benzo[*d*]imidazole in the presence and absence (bottom line) of CT-DNA. The arrow shows the intensity change upon increasing DNA concentrations. (b) Plot of relative integrated emission intensity vs. [DNA]/[ligand]
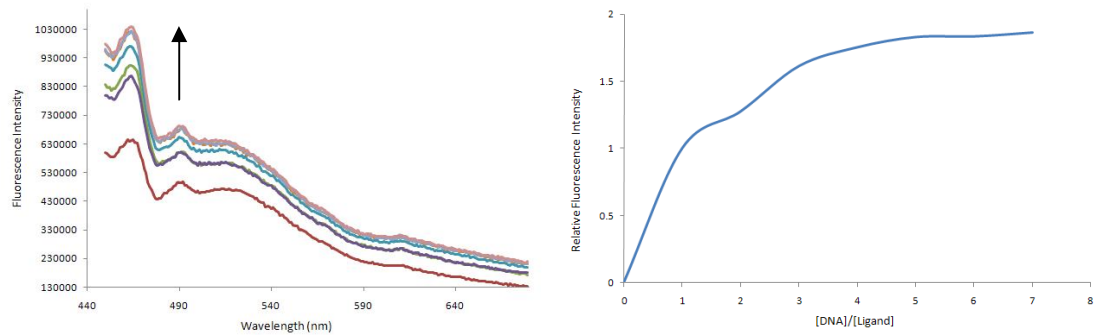
Figure 1.11: Emission spectra of ligand (a) 5-chloro-2,3-dihydro-1H-benzo[*d*]imidazole in the presence and absence (bottom line) of CT-DNA. The arrow shows the intensity change upon increasing DNA concentrations. (b) Plot of relative integrated emission intensity vs. [DNA]/[ligand]
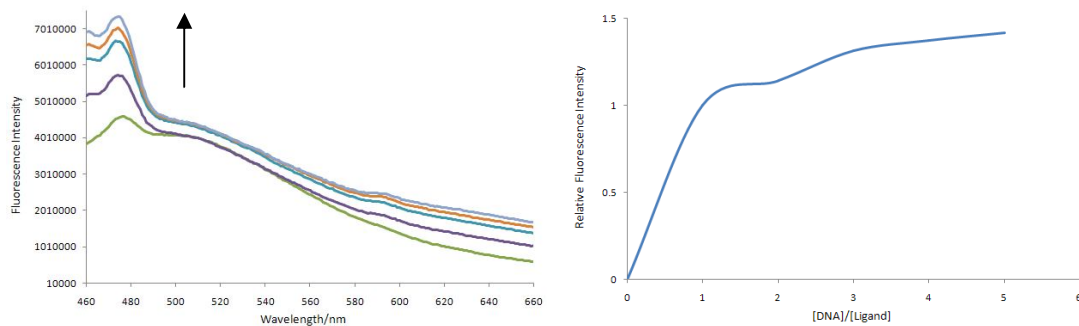
Figure 1.12: Emission spectra of ligand (a) 5-methyl-2,3-dihydro-1H-benzo[*d*]imidazole in the presence and absence (bottom line) of CT-DNA. The arrow shows the intensity change upon increasing DNA concentrations. (b) Plot of relative integrated emission intensity vs. [DNA]/[ligand]

14
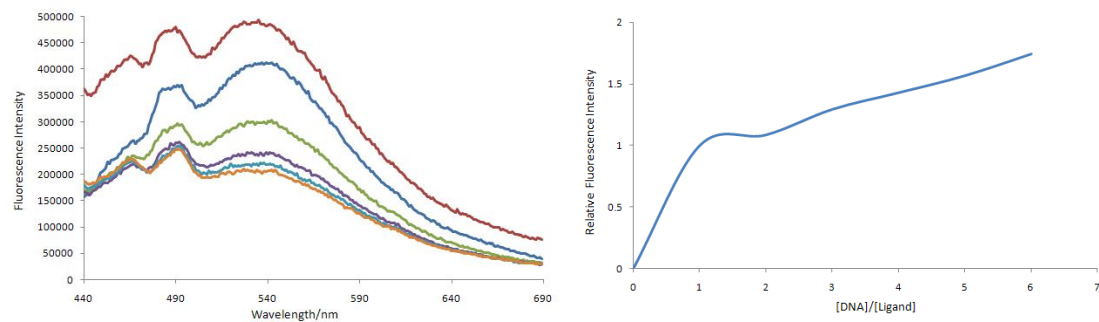
Figure 1.13: Emission spectra of ligand (a) 5-nitro-2,3-dihydro-1H-benzo[*d*]imidazole in the presence and absence (bottom line) of CT-DNA. The arrow shows the intensity change upon increasing DNA concentrations. (b) Plot of relative integrated emission intensity vs. [DNA]/[ligand]

It can be predicted that the plot of the relative intensities vs. [DNA]/[ligand] will show saturation with increasing concentration of CT-DNA due to the limitations in the substrate since the same substrate concentration will be maintained throughout the titration. As the titration was conducted with successive addition of DNA aliquots, the saturating value was reached when the [DNA]/[ligand] ratio was 5 for all the compounds, except for the nitro derivative. 2,3-dihydro-1H-benzo[*d*]imidazole, 5-chloro-2,3-dihydro-1H-benzo[*d*]imidazole, 5-methyl-2,3-dihydro-1H-benzo[*d*]imidazole and 5-nitro-2,3-dihydro-1H-benzo[*d*]imidazole emission intensities were found to be enhanced by 2.26, 1.86, 1.42, 2.19 folds, respectively, compared to their emission intensities in the absence of DNA. This indicates that the ligands interact with the double helical structure of the DNA and are efficiently protected by the hydrophobic environment inside the helix.

1.6.1 Scatchard Plots

The DNA-ligand binding constant and the number of nucleotides per bound ligand were calculated using a modified Scatchard equation and the fluorescence spectroscopic data discussed above.

As discussed above, the data for the analysis was obtained as a one-cuvette experiment where the titration was conducted in a fixed quantity of the ligand, with increasing concentrations of the CT-DNA aliquots. The experiment was carried out as explained in the previous section. The plot of $[M]_{total}/f$ versus 1/1-f is a straight line (for a detailed explanation,

see below), therefore the binding constant and the number of binding sites can be calculated from the slope and the intercept, respectively. The other advantage of the method is that the calculation of the binding constant does not require the knowledge of the exact initial concentration of the ligand.[24] This is of great advantage in all the cases where the solubility of the ligand in aqueous buffers is limited.

$$\frac{[M]_{total}}{f} = \frac{1}{Nk_f(1-f)} + \frac{[L_{total}]}{N}$$

$[M]_{total}$ = DNA concentration over the course of titration
$[L]_{total}$ = Initial concentration of the ligand
N = Total number of binding sites
K_f = Binding constant

$$f = \frac{F_{observed} - F_l}{F_{max} - F_l}$$

f = Fraction of the ligand bound to DNA during titration
F_l = Fluorescence of free ligand
$F_{observed}$ = Fluorescence observed after the addition of DNA
F_{max} = Maximum fluorescence when all possible ligands are bound
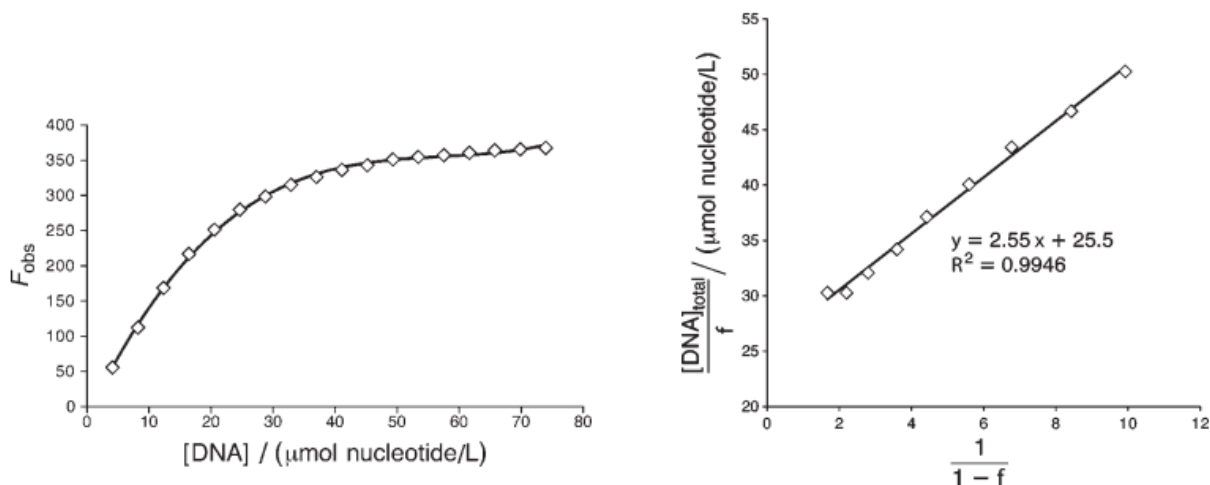
Figure 1.14: A typical fluorescence titration curve(a), and a plot of 1/1-f versus [DNA]/f[24]

The typical curve between the observed fluorescence with the increase concentration of CT-DNA will reach the saturation as shown in the first graph of Figure 1.14, and the Scatchard plot is a straight line where the binding constant and the number of binding sites can be calculated.[24]

The Scatchard-type calculations were carried out for all the four derivatives of 2,3-dihydro-1H-benzo[d]imidazole.
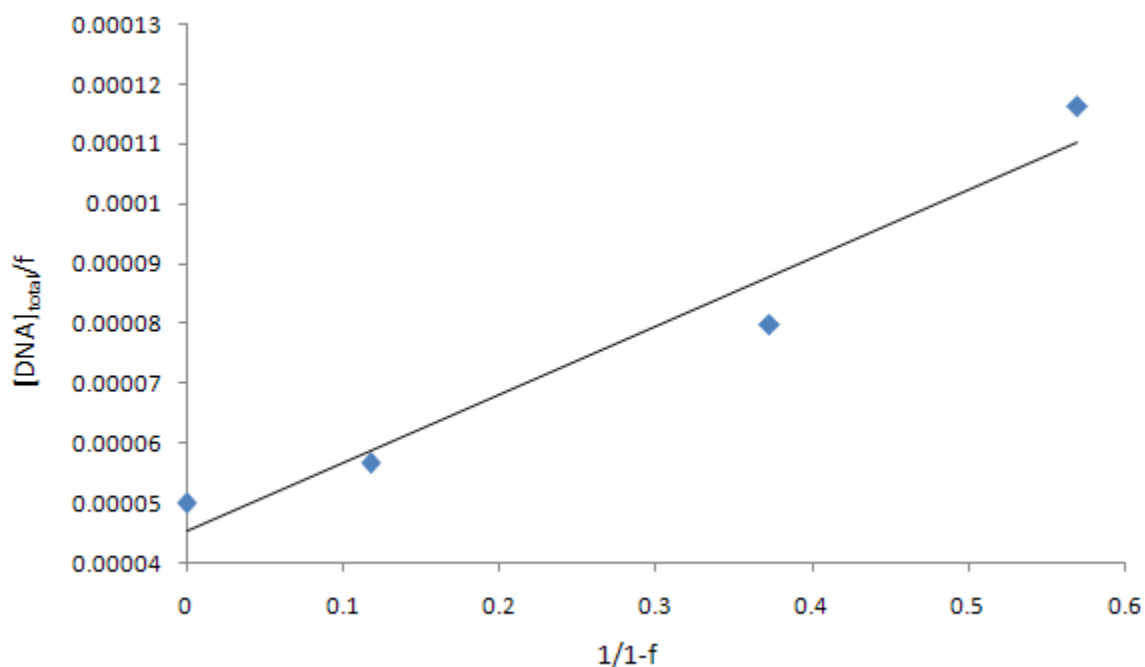
Figure 1.15: The Scatchard plot of 1/1-f versus [DNA]/f for 2,3-dihydro-1H-benzo[d]imidazole

The calculated binding constant was 4.02×10^3 L mol^{-1}. The n value or the number of binding sites for the ligand was calculated to be 2.023. The calculations were repeated for the chloro- and methyl-substituted 2,3-dihydro-1H-benzo[d]imidazole derivatives and the calculated binding constants were 4.751×10^3 and 3.31×10^3 L mol^{-1}, respectively. The binding constants

were greater for the substituents indicating strong intercalation with the double helical structure of CT-DNA.

1.7 Fluorescence Binding Studies of 2,3-diaminophenazine to DNA
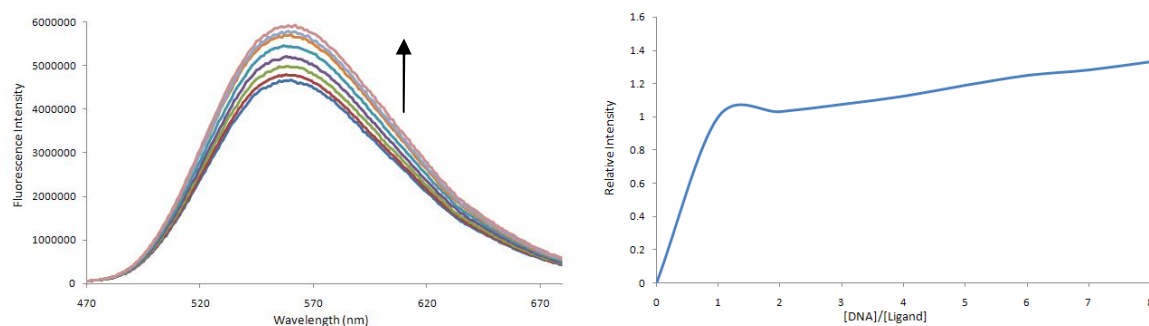
Figure 1.16: Emission spectra of ligand (a) 2,3-diaminophenazine in the presence and absence (bottom line) of CT-DNA. The arrow shows the intensity change upon increasing DNA concentrations. (b) Plot of relative integrated emission intensity vs. [DNA]/[ligand]

The binding constant of 2,3- diaminophenazine was calculated fitting the fluorescence data into a Scatchard plot. The binding constant was 5.35×10^3 L mol^{-1} and the number of binding sites were estimated to be 2.22. This is in good agreement with the previous data obtained by Niu and cowokers[25] in 2004 on the same system using cyclic voltammetry, where binding constant was calculated to be 5.03×10^3 L mol^{-1} and the number of binding sites 2. However the binding constants were low for these molecules compared to commercially available ligands such as ethidium bromide ($K_b = 10^5$ L mol^{-1}). The experiments carried out at our lab indicate that the use of fluorescence enhancement with DNA can be used for the successful calculation of binding constants.[22]

1.8 Supra Molecular Structures Formed with Zn^{2+} and 2,3-dihydro-1H-benzo[*d*]imidazole and Their Binding to B-DNA

Equimolar amounts of $ZnCl_2$ and 2,3-dihydro-1H-benzo[d]imidazole were heated to 60 °C in methanol to obtain the complex as a white powder, which was further purified with repeated washing with a water-/methanol mixture (80:20). The UV/Vis- spectrum obtained from the complex shows a peak around 438 nm corresponding to a metal to ligand charge transfer band (MLCT) (Figure 1.17). The UV/Vis- and the fluorescence spectra of the free and the bound 2,3-dihydro-1H-benzo[d]imidazole were not significantly different from each other.

1.8.1 The UV/Vis and Fluorescence Binding Studies

The binding studies of the Zn^{2+} complex were carried out using UV/Vis- and fluorescence spectroscopy, as described for the previous *o*-phenylenediamine derivatives. The observed decrease in the maxima of the UV/Vis-spectra following the addition of CT-DNA supports the assumption that this supramolecular complex has the ability to interact with DNA. Furthermore, the fluorescence titrations show a clear increase in the spectra with increasing amount of CT-DNA. But the I/I^0 value (maximal increase in luminescence) for the complex was 1.48 where as for the free ligand, it was 2.26. It is our mechanistic hypothesis that the I/I^0 value is greater for the ligand alone, because it can be better "protected" from the surrounding water when intercalating in the hydrophobic environment of double stranded B-DNA. Since the I/I^0 value is less for the supramolecular Zn^{2+}-complex, we propose that once the Zn^{2+} and 2,3-dihydro-1H-benzo[*d*]imidazole complex is formed it restricts the ability of the ligand to efficiently intercalate with DNA probably due to the reduced flexibility of the complex. Furthermore, the Zn^{2+}-metal centers could have the ability to bind to the phosphate-bridges of DNA, which would cause, at least partially, the surface-binding and not intercalation of the

supramolecular assemblies. The binding vs. intercalation vs. surface binding is discussed below in more detail.
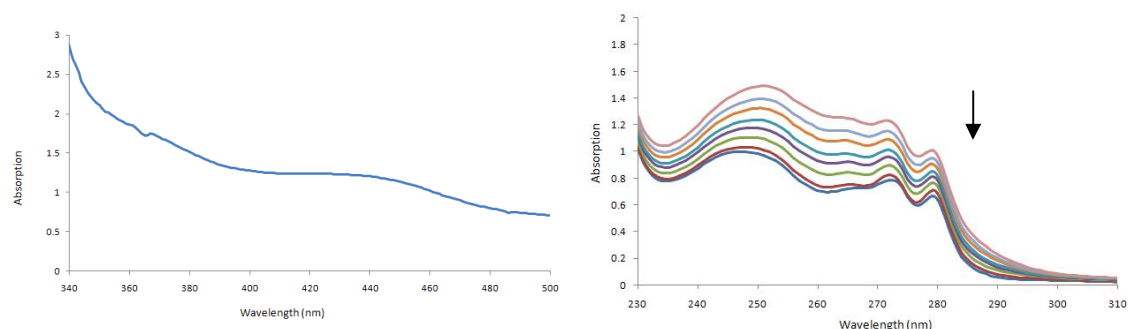
Figure 1.17: UV/Vis absorption spectra of (a) 2,3-dihydro-1H-benzo[d]imidazole Zn^{2+} complex showing the MLCT band (b) 2,3-dihydro-1H-benzo[d]imidazole, Zn^{2+} upon addition of CT-DNA. Arrows show absorbance changes upon increasing the DNA concentration
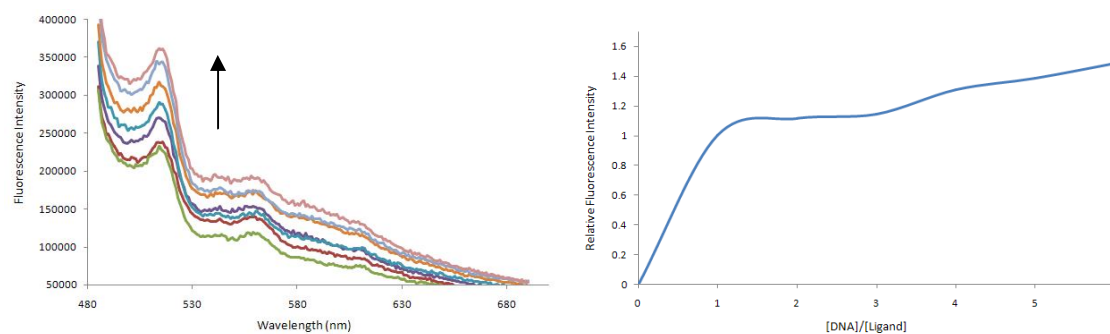
Figure 1.18: Emission spectra of complex (a) 2,3-dihydro-1H-benzo[d]imidazole, Zn^{2+} in the presence and absence (bottom line) of CT-DNA. The arrow shows the intensity change upon increasing DNA concentrations. (b) Plot of relative integrated emission intensity vs. [DNA]/[ligand]

The binding constant of the supramolecular 2,3-dihydro-1H-benzo[d]imidazole-Zn^{2+} complex to B-DNA was calculated using Scatchard plots to be $K_b=6.35\times10^4$ L mol^{-1}. When compared to $K_b=4.02\times10^3$ L mol^{-1} for the free 2,3-dihydro-1H-benzo[d]imidazole ligand alone, the higher binding constant measured in the presence of Zn^{2+} indicates a stronger interaction between organic ligand and B-DNA with the introduction of the Zn^{2+}. I have interpreted this

finding as support for the general assumption of an electrostatic attraction between Zn^{2+} and PO_4^- in 2,3-dihydro-1H-benzo[d]imidazole-Zn^{2+}-DNA complexes.

1.8.2 Effect of 2,3-dihydro-1H-benzo[d]imidazole-Zn^{2+}-DNA Complexes on MDA 231 Cancer Cell Line in the Dark and Under Irradiation

After the binding experiments described above, the supramolecular 2,3-dihydro-1H-benzo[d]imidazole-Zn^{2+} complex was tested on the MDA 231 cancer cell line to study its potential as an agent in photodynamic therapy.

1.8.2.1 Photodynamic Therapy (PDT)

Photodynamic therapy is excitation of a photosensitizing agent in a specific wavelength to induce photochemical processes in a cell which will lead to irreversible cell death.[26] History of modern photodynamic therapy dates back almost a hundred years, but the discovery of potent photo sensitizers during the last 25 years has led to great advancement in PDT specially as a treatment methods for cancers.[27]
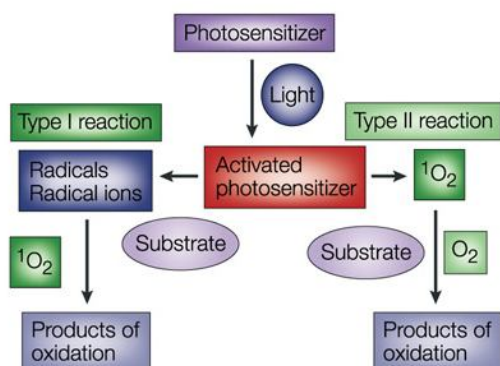
Figure 1.19: Type I and type II reaction in photodynamic therapy[27]

There are two types of reaction during PDT. The absorption of a specific wavelength will result in transforming the photosensitizer from its ground state to single excited state, which then

generates longer lived triplet states via efficient intersystem crossing.[27] The activated sensitizer is able to undergo two different photosensitized processes, namely type I and type II photoreaction, depending on its chemical structure and the excitation wavelength. In type I processes, the photosensitizer transfers or accepts an electron to/from nearby molecules, such as the cell membrane or a protein or DNA-segment in a cell. In type II reactions, the interaction of the excited triplet state of the photosensitizer with ground state (triplet) oxygen ($^3O_2$) will lead to the formation of singlet oxygen ($^1O_2$) and the singlet ground state of the sensitizer. Singlet oxygen is a very reactive species, which can damage biomolecules including proteins, nucleic acids, carbohydrates and (membrane-) lipids.[26,27] The effectiveness of the photochemical activity of the photosensitizer is dependent on the concentration of oxygen present in tissues. The exact mechanism of action by each photosensitizer is difficult to predict and may vary depending on the experimental conditions (oxygen content, viscosity of the medium, concentration of the sensitizer in biological tissues or cells, strengths and spectra distribution of the light source).[27]

The results from a preliminary cell experiment, which has been performed in the group of Dr. Claudia Turro at Ohio State University, Columbus/OH by Dr. Patty Fu, show that a 1:1 mixture (molar) of 2,3-dihydro-1H-benzo[d]imidazole and zinc(II)dichloride can efficiently kill cancer cells when irradiated with 313 nm for 30 min. The determination of the 2,3-dihydro-1H-benzo[d]imidazole zinc(II) induced inhibition of cell growth has been performed using subconfluent (70-75% confluent) monolayer of MDA 231 cells (breast carcinoma) in 60 mm culture dishes. The monolayers were washed twice using phosphate-buffered saline (PBS). Then the 2,3-dihydro-1H-benzo[d]imidazole zinc(II) concentrations were added in concentrations between 1.0×10^{-10} mol L^{-1} and 1.0×10^{-3} mol L^{-1} in pH adjusted (7.4) PBS buffer. After 1 h, the cells were removed by trypsinization and seeded into well culture dishes. Then, incubation in

MDA 231 medium took place, until the treated group had reached confluence (usually after 3 h). The cells were then lifted with trypsin and counted on a hemacytometer in the presence of trypan blue to distinguish live and dead cells.
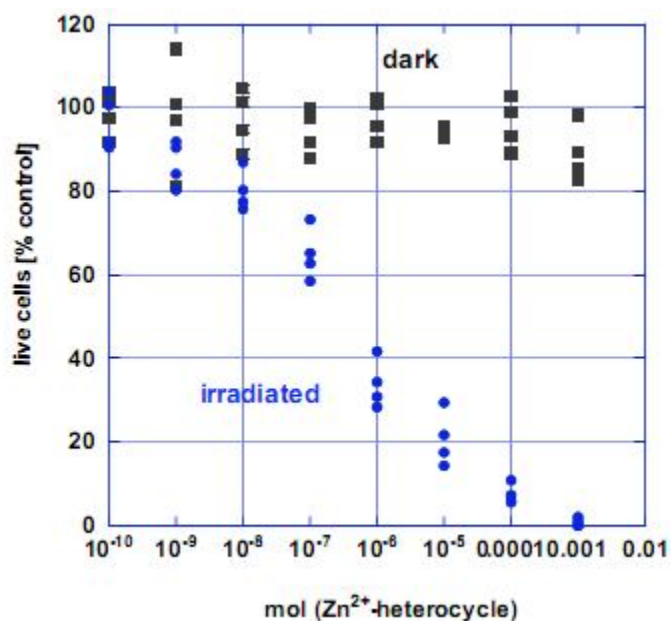
Figure 1.20: The effect of different concentration of the complex on the cell viability when irradiated at 313 nm (Hg-medium pressure lamp, HPK 125 using optical filters and a water-filter for 30 min, and in the dark)

In sharp contrast, the investigated cancer cells stayed alive when grown in the dark. Apparently, the components 2,3-dihydro-1H-benzo[d]imidazole and zinc(II) were not toxic in concentrations up to the millimolar region. However, a significant phototoxicity was observed, when the cells were irradiated, making this supramolecular adduct a great prospective photodynamic drug. Human cancer cells-(MDA 231) were able to take up the components 2,3-dihydro-1H-benzo[d]imidazole and zinc(II) quickly and they also showed significant phototoxic effects. As it can be estimated from Figure 1.20, the IC$_{50}$ can be estimated to 5×10^{-6} mol L^{-1} for

both components. If either component was added to the PBS-buffer in the absence of the other component when incubating the cells, no phototoxic effect could be found.

1.8.3 The Study of the Fragmentation of DNA-Oligomers

The next set of experiments was performed with DNA-oligomers. The 17-mer oligonucleotide 5'-ACGGCACTACGGCTCGT-5' and its complement were synthesized on an ABI synthesizer and purified by C18 reverse phase HPLC both before and after the removal of the trityl-protecting group. The complementary DNA-strands were annealed by heating at 90 ^{o}C for 5 min in phosphate buffer (0.50 mmol containing 150 mmol of NaCl) and then cooling down to 25 ^{o}C during 2 h. 1.0 mL of buffer solution containing 20 μmol of 17-mer was mixed with 1 μmol of 2,3-dihydro-1H-benzo[d]imidazole-zinc(II), incubated for 1h, and was irradiated at 313 nm for 5 min. HPLC-analysis of the resulting mixture indicated the presence of all four nucleotides, dAMP, dCMP, dGMP and dTMP. The comparison with commercially available nucleotides clearly indicated that indeed all four nucleotides were formed. Besides the four nucleotides, many other fragments, but only traces of the original 17-mer, were present in the photolysis mixture. It is noteworthy that cleavage of the DNA occurs in the presence and absence of dissolved oxygen.

Based on the data available, we proposed a mechanistic hypothesis to explain the behavior of Zn^{2+} complex. As already pointed out, it is the specific aim of this proposed mechanism to explain the ability of the complex to actively kill cancer cells. Since the cleavage of the oligo nucleotide occurs in the absence of dissolved oxygen there is a decreased chance for the type I and type II photosensitized processes to be active.

1.8.4 The Proposed Mechanism for the Zn^{2+}, 2,3-dihydro-1H-benzo[d]imidazole Complex

In a previous study, a complex of quercetin and zinc(II) was tested against human cancer cell lines HepG2, SMMc 7721 and A 549. The complex showed significantly higher cytotoxicity compared to the free ligand. The cells underwent apoptosis and cell death was observed. Based on these results Tan and coworkers proposed a mechanism to explain the DNA cleavage ability the quercetin zinc(II) complex. This was published in 2009 and there are similarities in the mechanism for what we had already proposed.[28]
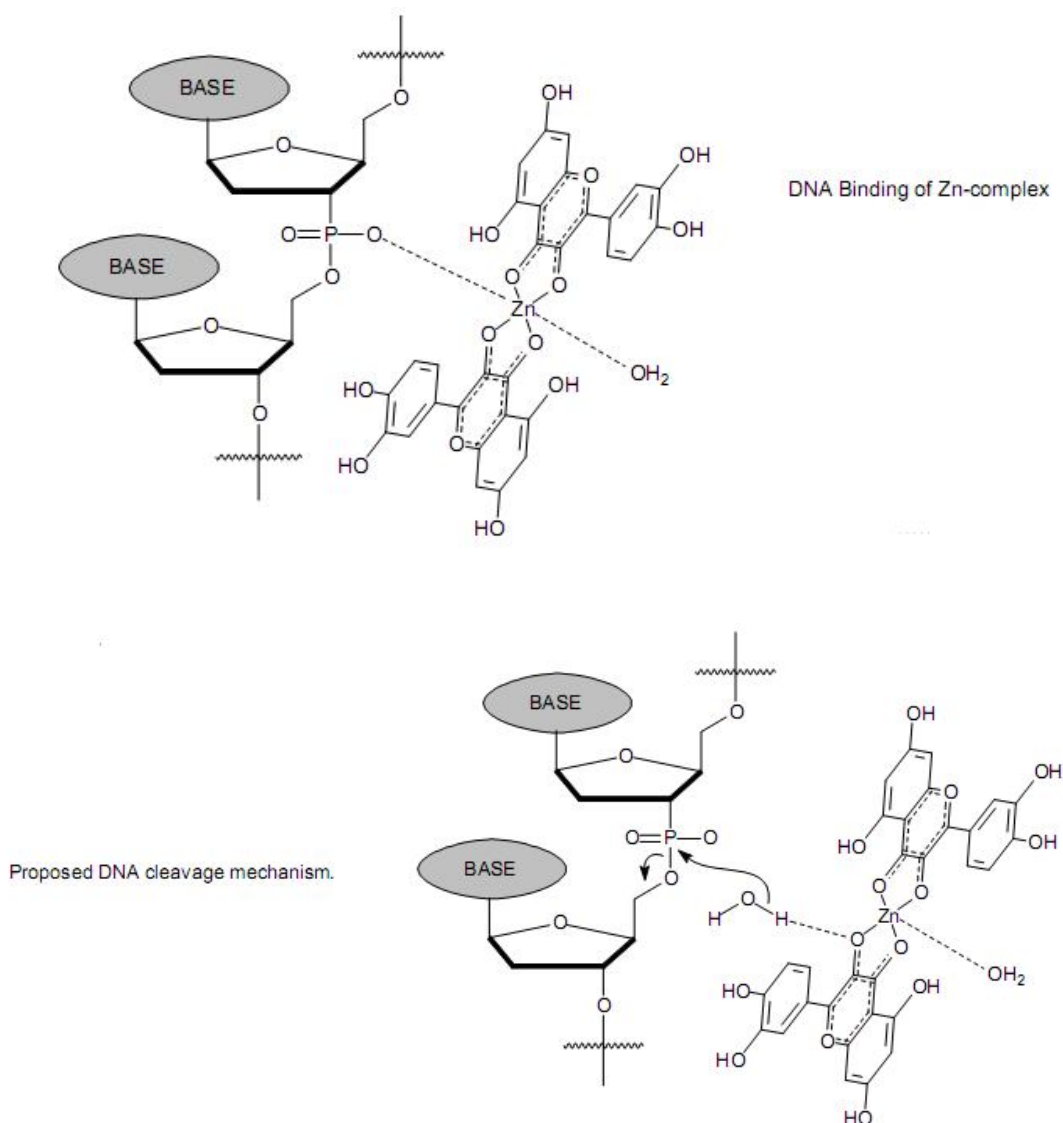
Figure 1.21: Proposed hypothesized mechanism for quercetin and zinc(II)[28]

Molecular modeling studies employing simple MM2-Force-Fields have revealed that Zn^{2+}-bridged supramolecular structures are possible. However, they appear not to be linear, but form flexible helices.
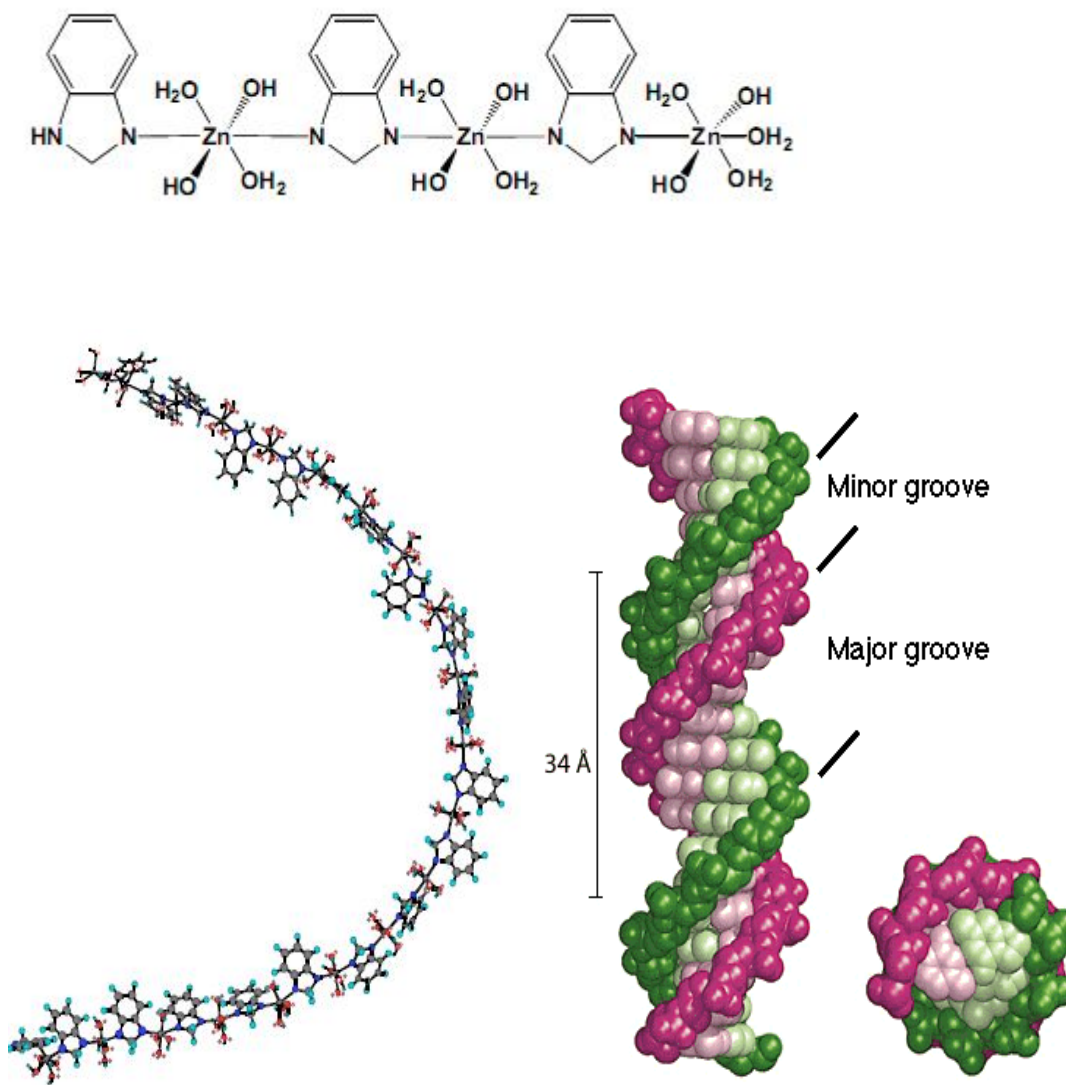
Figure 1.22: The flexible helical structure of Zn^{2+} and 2,3-dihydro-1H-benzo[*d*]imidazole complex and the DNA double helical structure

The distance between two zinc(II)-cations in this supramolecular structure is approximately 0.38 nm. This is slightly larger than the distance between two nucleotides in a

DNA strand, which is 0.33 nm. This difference has two very important consequences that are important for the proposed mechanism: 1) The supramolecular helix is able to form or wrap around the DNA double-helix (preferentially B-DNA). 2) The zinc(II) cation coordinates to the phosphate bridges between the deoxyribose units.
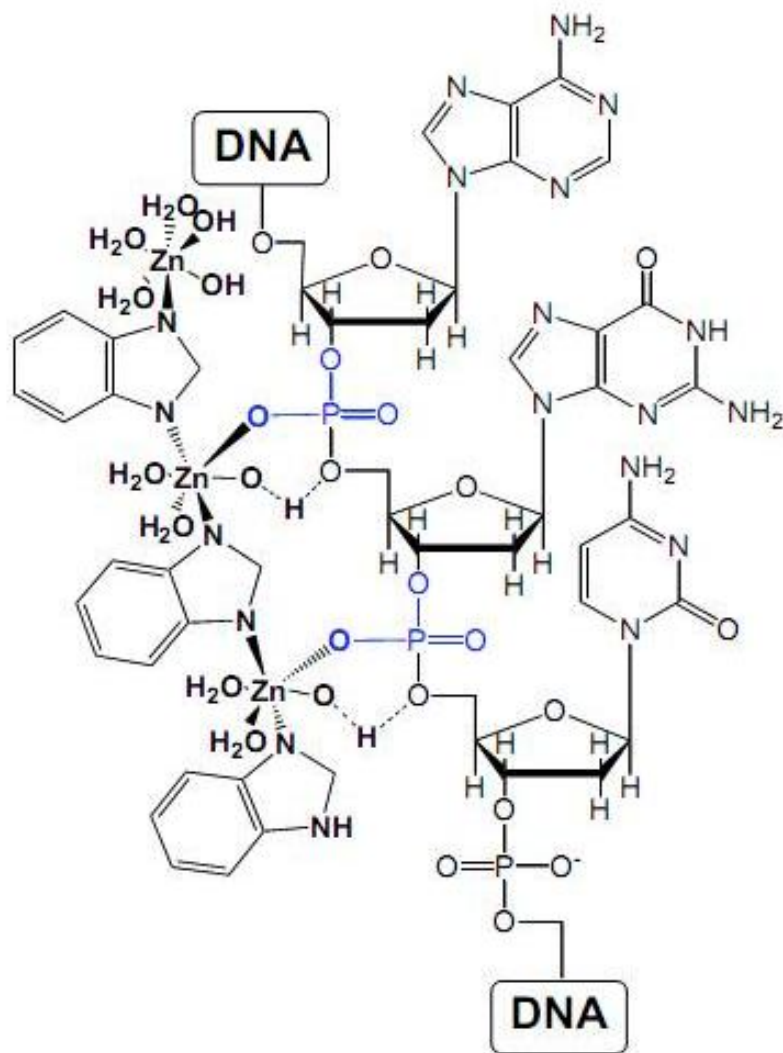
Figure 1.23: "Docking" of the supramolecular adduct along a DNA-strand. The thermodynamic driving force at pH=6-8 is the formation zinc(II)-oxygen-phosphorous bridges

In this docking process, the phosphate-group will be anchored to the octahedral zinc(II)-center via a zinc(II)-oxygen-phosphorous bridge. A second, but weaker, hydrogen-bond can form between a zinc(II)-hydroxyl group and the 5'-oxygen of deoxyribose, which forms an ester-bridge to the phosphate unit. It can be safely assumed that this fit is not absolutely perfect and that the presence of the supramolecular adduct is most likely causing some slight deformation of the structure of B-DNA. Note that neither the charges of the zinc(II) nor of the hydroxyl groups (-1) or secondary amines (-1) are shown for reasons of simplicity.
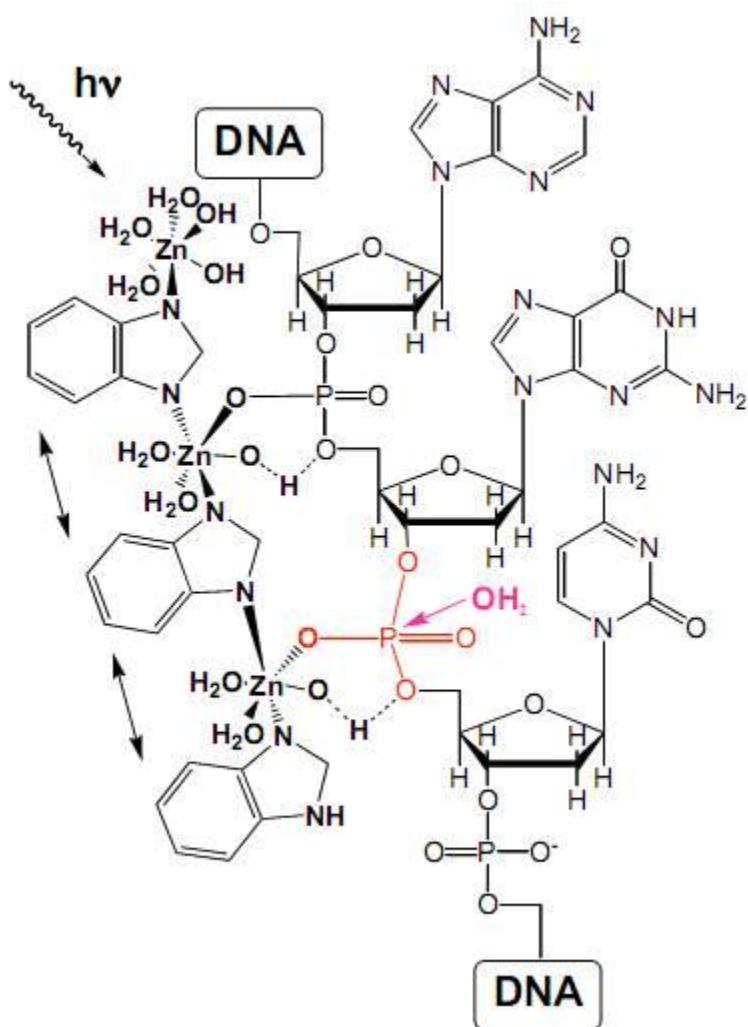
Figure 1.24: The weak interactions of Zn^{2+} and 2,3-dihydro-1H-benzo[d]imidazole complex with the double helical structure of the DNA

Light-absorption leads to the population of the first electronically excited singlet state (S_1^*). This state is very short-lived. However, deactivation of the absorbed energy will lead to the population of higher vibrational levels of the ground state (S_0) due to internal conversion.

In the next step, the photo-triggered vibration of the supramolecular adduct will be partially transferred to the sugar-phosphate backbone of DNA. Apparently, the P-O-bond (dissociation energy: 92 kJ mol^{-1}) is the weakest link in the chain (C-O: 334 kJ mol^{-1}). Although the energy of the exciting photon (λ=313 nm corresponds to 382 kJ mol^{-1}) is in the energetic range of the C-O-bond, it is nevertheless reasonable that the weakest link will preferentially break.
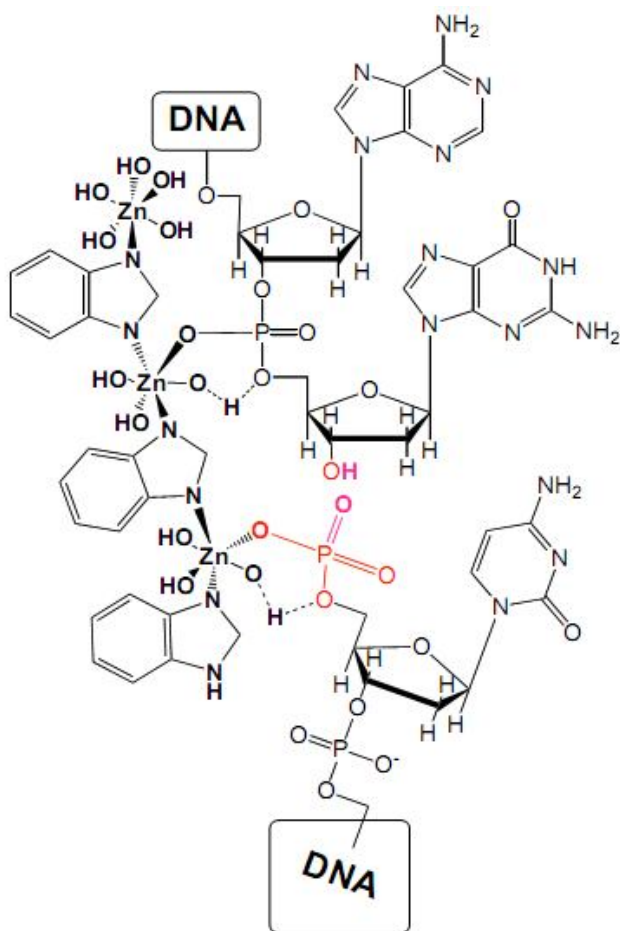
Figure 1.25: The cleavage of the DNA nucleotide after excitation at 313 nm

After the hydrolytic cleavage of the sugar-phosphate-backbone is achieved, the DNA strand is broken. In order to break the DNA double-strand, this process has to take place at both backbones of the DNA double helix. HPLC-experiments indicate that this is indeed the case in the model experiment involving the 17-mer DNA and the supramolecular adduct. This mechanism predicts the formation of nucleotides as DNA-cleavage products.

After this sequence of events, the nucleotide is successfully "freed" from the sugar-phosphate backbone of DNA. The "docking" of the supramolecular adduct occurs most likely during the beginning of the S-phase, when most of the DNA-protein complexes, which compete for DNA-binding, are dissolved in order to allow for the duplication of the genetic material.

1.8.5 Time Resolved Spectroscopic Studies

The proposed mechanism was further studied with time resolved spectroscopy. Time resolved spectroscopy is an important technique for studying electronic excitation and relaxation processes of a molecule in solution, as well as energy and electron transfer processes between two or several molecules or components of a bigger molecule or supramolecular assemblies.[29] In general, time resolved spectroscopy offers the opportunity to study these processes in a window between 10^3 to 10^{13} s^{-1}. We speak about nanosecond laser spectroscopy, if the observation window is between 0 and 10 ns (1 ns=10^{-9} s). Since the excited state lifetime of a fluorophore (=molecule that emits light upon photoexcitation) is very sensitive to the environment, time-resolved emission spectroscopy will provide information about the changes in the molecular environment[29]. The time-resolved experiments reported here have been performed by Dr. Viktor Chikan using his laser-setup consisting of a Ti:sapphire-laser (λ_0=1064 nm), which was operating at its tripled frequency (λ_3=1064 nm/3=354.67 nm) and pumping a dye laser using a coumarine dye. Fluorescence life times were measured after exciting the molecule at 470 nm and

recording the emission at 550 nm. Our supramolecular assemblies between B-DNA, 2,3-dihydro-1H-benzo[d]imidazole and Zn^{2+} have been excited using short pulses (pulse width: 45 ps) (1 ps=10^{-12} s), which have permitted studying the fluorescence decay kinetics in the detection window of 0-12 ns, which has allowed us to observe differences in the fluorescence behavior in the presence and absence of zinc(II). Furthermore, the analysis of the emission spectra has provided information on the polarization of 2,3-dihydro-1H-benzo[d]imidazole with or without zinc(II) complexes, which is consistent with information on the mobility of the intercalated or DNA-surface bound ligands, as well as the decay kinetics.

In general, fluorescence decay kinetics can be described by applying exponential kinetics. The general differential equation for exponential decay processes can be written as follows:

$$\frac{dN(t)}{dt} = -\lambda N$$

where N(t) is the number of excited states at the time t, and N_0 is the initial number of excited states (t=0). Λ is called the decay constant.

The solution to this differential equation is

$$N(t) = N_0 e^{-\lambda t}$$

The mean lifetime (also called lifetime or exponential time constant) of an exponential decay process is the reciprocal value of the decay constant. It is consistent with the time required to reduce the number of excited states N(0) by a factor of e.

$$\tau = \frac{1}{\lambda}$$

The solution to the general differential equation becomes then

$$N(t) = N_0 e^{-t/\tau}$$

The mean lifetime is not to be mistaken as the half-life time, which is the time required for the decay of 50 percent of the initially formed excited states.

$$t_{1/2} = \frac{\ln 2}{\lambda} = \tau \ln 2$$

In cases in which a decay process cannot successfully described by assuming a single exponential decay, a second decay process can be postulated. Principally, even more decay processes can be assumed, however, this does not reflect the presence of two or more chemically different excited states. In these cases, one rather must assume that a statistical distribution of many decay processes exist that can be fitted by assuming two or three exponential decay processes.[30] When assuming two exponential decays that occur independent of each other, the differential equation becomes:

$$\frac{dN(t)}{dt} = -(\lambda_1 + \lambda_2)N$$

The solution is then:

$$N(t) = N_0 e^{-(\lambda_1 + \lambda_2)t}$$

1.8.5.1 Time-Resolved Fluorescence Occurring from 2,3-dihydro-1H-benzo[d]imidazole and 2,3-dihydro-1H-benzo[d]imidazole-Zn^{2+} in the Absence and Presence of DNA

As already explained, 2,3-dihydro-1H-benzo[d]imidazole, 2,3-dihydro-1H-benzo[d]imidazole in the presence of B-DNA and the supramolecular complex of 2,3-dihydro-1H-benzo[d]imidazole and zinc(II) in the presence of B-DNA were studied by using time-resolved laser emission spectroscopy. The ligands, complexes and DNA-adducts were excited at λ_{EX}=470 nm. The emission was monitored at λ_{EM}=550 nm.
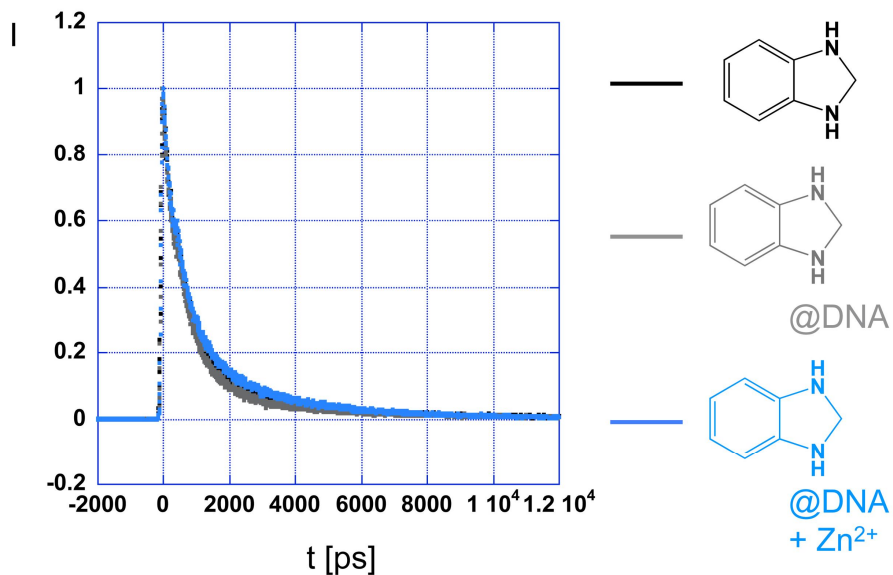
Figure 1.26: Time resolved fluorescence of 2,3-dihydro-1H-benzo[*d*]imidazole, 2,3-dihydro-1H-benzo[*d*]imidazole in the presence of CT-DNA and 2,3-dihydro-1H-benzo[*d*]imidazole-Zn^{2+} in the presence of CT-DNA. A mixture of 1:10 dimethylsulfoxide to water was used as the solvent, λ_{EX}= 470 nm, λ_{EM}=550 nm

The first step of our analysis consisted in plotting the natural logarithm (ln) of the observed fluorescence intensity vs. a linear time scale. If the fluorescence decay is monoexponential, a linear decay of ln (I) vs. t would be observed. Apparently, this is not the case here. Therefore, the spectra were further studied at different time intervals. Each spectrum was separated into "early" and "later" stages and the life times were calculated for each time period.
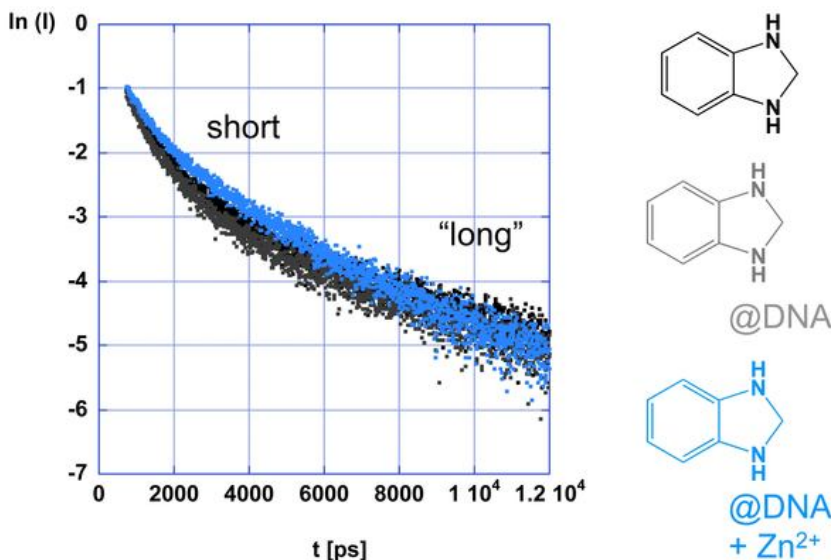
Figure 1.27: Time resolved fluorescence of 2,3-dihydro-1H-benzo[d]imidazole, 2,3-dihydro-1H-benzo[d]imidazole in the presence of CT-DNA and 2,3-dihydro-1H-benzo[d]imidazole-Zn^{2+} in the presence of CT-DNA. λ_{EX}=470 nm, λ_{EM}=550 nm

The fluorescence decays (ln (I) Vs. t) occurring in the short window (0.6 to 2.5 ns) are shown in Figure 28. The short fluorescence component occurring from 2,3-dihydro-1H-benzo[d]imidazole in the absence of B-DNA and zinc(II) was determined to $\tau = \lambda^{-1}$=812±10 ps. Interestingly, the fluorescence lifetime of 2,3-dihydro-1H-benzo[d]imidazole in the presence of B-DNA decreased slightly to 794±12 ps, which is within the error margins when compared with the lifetime obtained in the absence of B-DNA. It is noteworthy that the observed stationary luminescence intensity increases significantly, as this is shown in Figure 28. In the presence of zinc(II) and B-DNA, τ increases to 979±20 ps, which is clearly different from the luminescence lifetimes obtained before. From these data, we have concluded that the presence of zinc(II) leads to a different chemical environment of 2,3-dihydro-1H-benzo[d]imidazole when bound to DNA. This is in agreement with our paradigm that DNA-intercalation of 2,3-dihydro-1H-

benzo[d]imidazole is favored in the absence of zinc(II), whereas surface binding occurs in the presence.
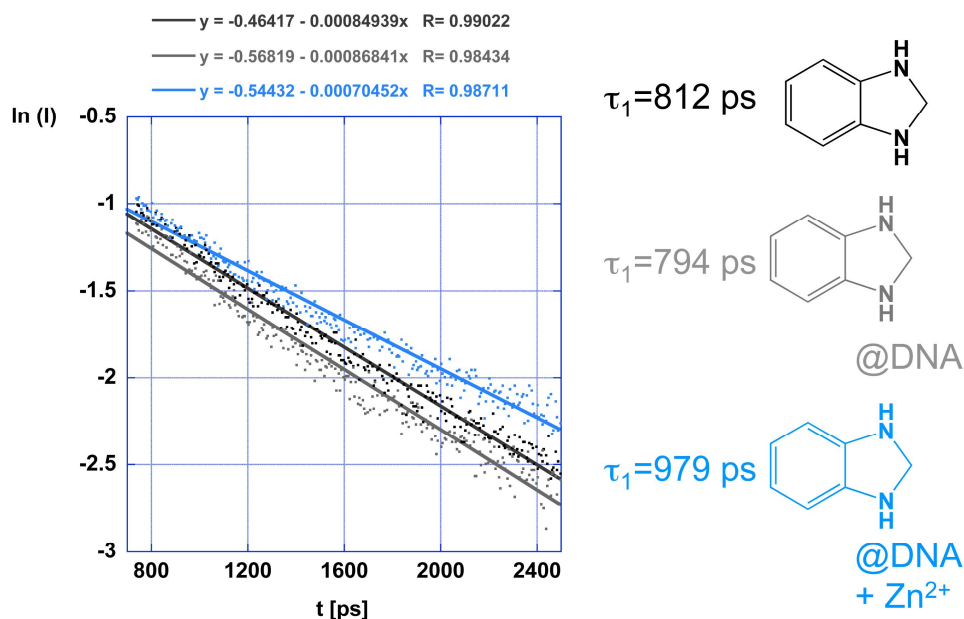
Figure 1.28: Time resolved fluorescence of 2,3-dihydro-1H-benzo[d]imidazole, 2,3-dihydro-1H-benzo[d]imidazole in the presence of CT-DNA and 2,3-dihydro-1H-benzo[d]imidazole-Zn^{2+} in the presence of CT-DNA. λ_{EX}=470 nm, λ_{EM}=550 nm

The decay of fluorescence intensity (ln(I) vs. t) occurring in the longer window is shown in Figure 29. Again, the longer components of the fluorescence lifetimes of 2,3-dihydro-1H-benzo[d]imidazole τ=2880±120 ps and 2,3-dihydro-1H-benzo[d]imidazole in the presence of B-DNA τ=2850±170 ps are within the margins of error, whereas for 2,3-dihydro-1H-benzo[d]imidazole in the presence of B-DNA and zinc(II) a distinctly shorter lifetime τ=2295±170 ps is found. Which conclusions can be drawn from this finding? Apparently, also the longer fluorescent components are indicative of less differences between 2,3-dihydro-1H-benzo[d]imidazole and 2,3-dihydro-1H-benzo[d]imidazole in the presence of DNA than of 2,3-

35

dihydro-1H-benzo[*d*]imidazole in the presence of both, zinc(II) and DNA. It is noteworthy that the longer fluorescence lifetime of 2,3-dihydro-1H-benzo[*d*]imidazole + Zn^{2+} at DNA is shorter than for 2,3-dihydro-1H-benzo[*d*]imidazole and 2,3-dihydro-1H-benzo[*d*]imidazole at DNA, whereas it was the longest of the three fluorescence lifetimes in the shorter observation window.
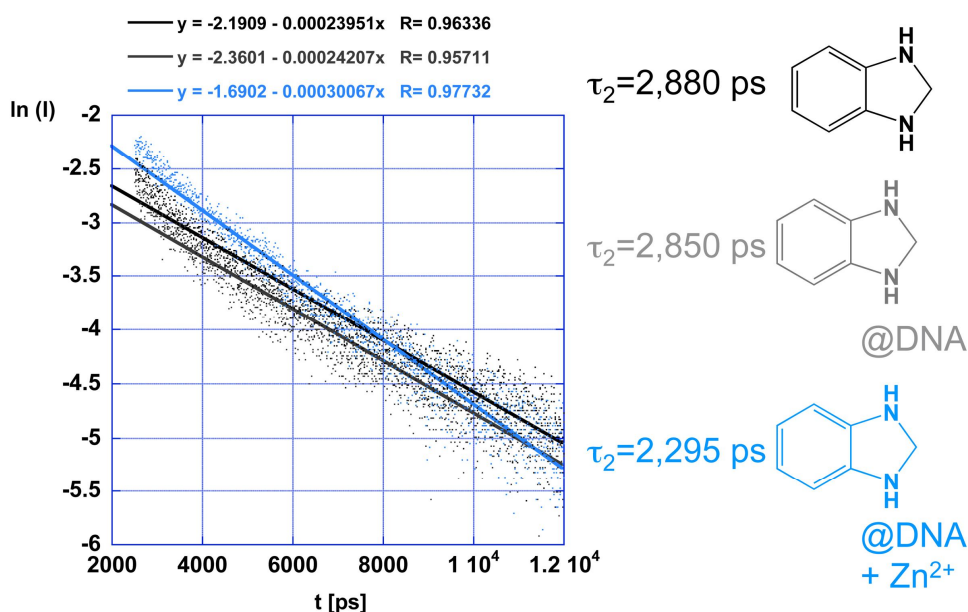
Figure 1.29: Time resolved fluorescence of 2,3-dihydro-1H-benzo[*d*]imidazole, 2,3-dihydro-1H-benzo[*d*]imidazole in the presence of CT-DNA and 2,3-dihydro-1H-benzo[*d*]imidazole-Zn^{2+} in the presence of CT-DNA. λ_{EX}=470 nm, λ_{EM}=550 nm

Fluorescence anisotropy (A) is a measure of a molecule's mobility during the time window after fluorescence excitation. When excited with linearly polarized light, as this is typical for a laser light source, the molecule will emit its photon in exactly the same plane that has been defined by the polarization of the absorbed photon. In fact, only molecules that were oriented correctly with respect to the linear polarization of the incoming light were able to absorb a photon.[31] However, any molecular motion that occurs after photoexcitation leads to the emission of photons that are not aligned with the plane of linear polarization. The maximum

value of A is 1, that is when $I_{parallel}$ is maximal and $I_{perpendicular}$ is zero. In this case, no molecular motion occurs. The minimum value of A is -0.5 indicating very fast molecular motion.

$$A = \frac{I_{parallel} - I_{perpendicular}}{I_{parallel} + 2I_{perpendicular}}$$

$I_{parallel}$ –emission light that is parallel to the plane of previously absorbed linearly polarized light

$I_{perpendicular}$ – emission light that is perpendicular to the plane of previously absorbed linearly polarized light

A – Fluorescence anisotropy

As Figure 30 shows, the fluorescence anisotropy recorded immediately after excitation is again very similar for 2,3-dihydro-1H-benzo[d]imidazole (A=0.17) and 2,3-dihydro-1H-benzo[d]imidazole in the presence of B-DNA (A=0.175), whereas a distinctly different value for 2,3-dihydro-1H-benzo[d]imidazole and zinc(II) in the presence of B-DNA (A=0.20) was measured. It must be noted that fluorescence anisotropies of less than 0.50 indicate that there is a high degree of motion. This result is not in agreement with assuming a completely DNA-intercalated ligand, because intercalation would increase the fluorescence anisotropy. Interestingly, the presence of zinc(II) is increasing the measured fluorescence anisotropy, indicating that there is indeed a supramolecular effect.
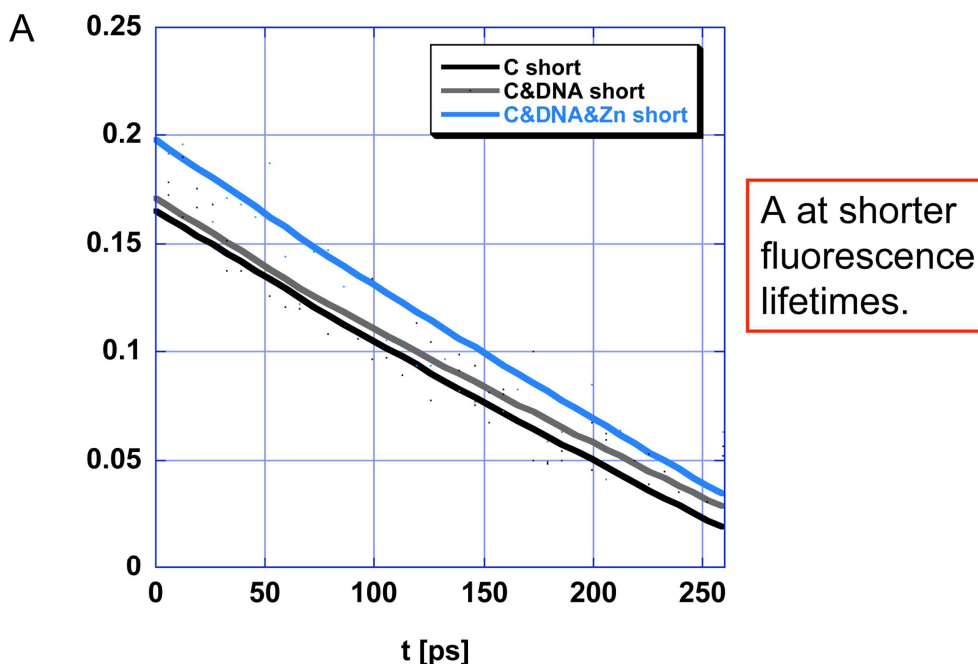
Figure 1.30: Time resolved fluorescence anisotropy of 2,3-dihydro-1H-benzo[*d*]imidazole, 2,3-dihydro-1H-benzo[*d*]imidazole in the presence of CT-DNA and 2,3-dihydro-1H-benzo[*d*]imidazole-Zn^{2+} in the presence of CT-DNA. λ_{EX}=470 nm, λ_{EM}=550 nm

1.9 Conclusions

Several derivatives of 2,3-dihydro-1H-benzo[*d*]imidazole were synthesized by derivatizing *o*-phenylenediamine. The binding mode of these derivatives to double helical calf thymus DNA was studied using UV-visible, fluorescence and time resolved fluorescence spectroscopy. The data obtained were analyzed to gather information on the binding nature of the compounds to DNA. Our studies have shown that the interaction mode between the organic ligands and DNA changes upon the addition of zinc(II). In the absence of zinc(II), ligand - intercalation into the DNA-double helix is the most probable mode of interaction. Upon addition of zinc(II), DNA-surface binding of the supramolecular (-ligand-Zn^{2+}-)$_n$ aggregates was observed. These findings have been corroborated by time-resolved laser fluorescence studies.

1.10 Experimental

All chemicals were obtained from Acros Organics and Sigma Aldrich, unless noted otherwise. The instrumentation used were 400 MHz and 200 MHz Varian NMR-spectrometer, UV/Vis spectra: FT-UV Diodearray HP 6543, Fluorescence spectrometer; F-3000, Hitachi LTD/SLM-Aminco 8000 C at the Department of Chemistry at Kansas State University, The mass spectra were obtained from Applied Biosystems API-4000 triple quadrupole mass spectrometer with electrospray and APCI sources at Department of Biology at Kansas State University.

1.10.1 Synthesis of 2,3-dihydro-1H-benzo[*d*]imidazole Derivatives

Equilmolar amounts of *o*-phenylenediamine (2.00 g, 0.0185 mol) and formaldehyde (0.55 g, 0.0185 mol) were thoroughly mixed in 60.0 mL of ethanol. To this mixture 5.0 mL of phosphoric acid was added and was heated under reflux for 6 h until the reaction is completed according to TLC. The mixture was cooled to room temperature and neutralized with 1M NaOH. After the neautralization additional 20.0 mL of water was added to the mixture and an oily material was separated out. This was extracted out with ethyl acetate and washed with water and sodium chloride. The organic layer was dried over sodium sulphate and further purified by column chromatography using hexane-ethyl acetate (3:1) on silica column. The yield was calculated to be 15%. ^{1}H NMR (400 MHz, DMSO), δ (ppm) 3.3 (s, 2H), 4.3 (s, 2H), 6.3 (d, 2H), 6.4 (m, 2H); ^{13}C NMR (400 MHz, DMSO), δ (ppm) 58.41, 114.75, 117.52, 135.12, Mass, ESI $C_7H_8N_2$ calculated 120.15, found MS-ESI$^+$: *m/z* 118.0

1.10.2 Synthesis of 5-nitro-2,3-dihydro-1H-benzo[*d*]imidazole Derivatives

Equilmolar amounts of 4-nitrobenzene-1,2-diamine (2.00 g, 0.013 mol) and formaldehyde (0.392 g, 0.013 mmol) were thoroughly mixed in 60.0 mL of ethanol. To this

mixture 5.0 mL of phosphoric acid was added and was heated under reflux for 12 h until the reaction is completed according to TLC. The mixture was cooled to room temperature and neutralized with 1 M NaOH. After the neutralization additional 20.0 mL of water was added to the mixture and a white solid was separated out. This was recrystalized using water to yield the desired product in 25%. ^{1}H NMR (400 MHz, DMSO), δ (ppm) 3.0 (s, 2H), 5.0 (s, 2H), 6.0 (s, 1H), 6.3 (d, 1H), 7.4 (m, 1H); ^{13}C NMR (400 MHz, DMSO), δ (ppm) 66.12, 107.85, 111.24, 115.48, 133.72, 136.51, 141.18; Mass, ESI $C_7H_7N_3O_2$ calculated 165.05, found MS-ESI$^+$: *m/z* 167.1

1.10.3 Synthesis of 5-chloro-2,3-dihydro-1H-benzo[*d*]imidazole Derivatives

Equilmolar amounts of 4-chlorobenzene-1,2-diamine (2.00 g, 0.014 mol) and formaldehyde (0.422 g, 0.014 mol) were thoroughly mixed in 60.0 mL of ethanol. To this mixture 5.0 mL of phosphoric acid was added and was heated under reflux for 6 h until the reaction is completed according to TLC. The mixture was cooled to room temperature and neutralized with 1 M NaOH. After the neautralization additional 20.0 mL of water was added to the mixture and an oily material was separated out. This was washed with acetone to remove the unreacted starting material. The resulting oil was further purified by column chromatography using hexane-ethyl acetate (3:1) on silica column. The calculated yield of the reaction was 18%. ^{1}H NMR (400 MHz, DMSO), δ (ppm) 3.05 (s, 2H), 4.65 (s, 2H), 6.3 (d, 1H), 6.4 (d, 1H), 6.5 (s, 1H); ^{13}C NMR (400 MHz, DMSO), δ (ppm) 66.36, 112.45, 113.44, 114.75, 120.08, 133.68, 136.44; Mass, ESI $C_7H_7ClN_2$ calculated 154.02, found MS-ESI$^+$: *m/z* 153.0

1.10.4 Synthesis of 5-methyl-2,3-dihydro-1H-benzo[*d*]imidazole Derivatives

Equilmolar amounts of 4-methylbenzene-1,2-diamine (2.00 g, 0.0163 mol) and formaldehyde (0.490 g, 0.0163 mol) were thoroughly mixed in 60.0 mL of ethanol. To this

mixture 5.0 mL of phosphoric acid was added and was heated under reflux for 5 h until the reaction is completed according to TLC. The mixture was cooled to room temperature and neutralized with 1M NaOH. After the neutralization the product mixture was extracted with ethyl acetate and the resulting oil was further purified by column chromatography using hexane-ethyl acetate (3:1) on silica column to yield the desired product was 22.5%. ^{1}H NMR (400 MHz, DMSO), δ (ppm) 2.0 (s, 3H), 3.6 (s, 2H), 4.4 (s, 1H), 6.3 (m, 2H), 6.4 (m, 1H); ^{13}C NMR (400 MHz, DMSO), δ (ppm) 18.47, 51.45, 113.60, 117.31, 119.69, 122.08, 133.21, 135.06; Mass, ESI $C_8H_{10}N_2$ calculated 134.08, found MS-ESI$^+$: *m/z* 132.0

1.10.5 Synthesis of 2,3-phenazinediamine[32]

3.73 g (0.011 mol) of Fe(Cl)$_3$ was dissolved in 100.0 mL of water and the resulting solution was poured into a stirred solution containing 1.00 g (0.009 mol) of *o*-phenylenediamine and 1.4 mL of HCl in 100.0 mL of water at room temperature. A red precipitate was formed immediately. The precipitate was filtered dissolved in hot water and allowed to be cooled. The crystals were collected and recrystalization in water was repeated. The resulting crystals were washed with diethylether 3-4 times. Then the product was further recrystalized by dissolving in methanol. The NMR was obtained but the peaks corresponding to NH$_2$ was not observed. So the product was then dissolved in hot water and 20.0 mL of 0.5 M EDTA solution was added to remove any remaining Fe^{2+}. The yield was 0.20 g (12%). ^{1}H NMR (400 MHz, DMSO), δ (ppm) 5.8 (s, 4H), 6.9 (s, 2H), 7.7 (m, 2H), 8.0 (m, 2H); ^{13}C NMR (400 MHz, DMSO), δ (ppm) 96.12, 129.13, 129.45, 139.52, 143.25, 146.02; Mass, ESI $C_{12}H_{10}N_4$ calculated 210.03, found MS-ESI$^+$: *m/z* 213.0

1.10.6 Synthesis of the 2,3-dihydro-1H-benzo[*d*]imidazole Zn^{2+} Complex

2,3-dihydro-1H-benzo[*d*]imidazole (0.10 g, 0.00095 mol) was dissolved in 5.0 mL of methanol and heated to 60 °C. To the heated solution $ZnCl_2$ was added in 1:2 ratio and the mixture was stirred for 0.5 h to obtain a white solid. The solid was filtered under vacuum filtration and washed with a 20:80 mixture of methanol and water. The solid was analyzed using UV/Vis spectroscopy.

1.10.7 DNA Dialysis

Calf thymus DNA was purchased from Aldrich as the sodium salt. The DNA was further purified to remove the protein bound to it by dialysis. A solution of calf thymus DNA in a dialysis tube was equilibrated in pH=7.4 PBS with 50 mM NaCl. The buffer solution was changed three times in 4 h intervals. The UV absorption at 260 nm and 280 nm gave a ratio of 1.8:1, indicating that the DNA solution was free of proteins. The DNA concentration was determined at 260 nm by UV/Vis absorption spectroscopy using the molar absorption co-efficient ($6600 \text{ M}^{-1} \text{cm}^{-1}$).

1.10.8 UV/Vis Titrations

All UV/Vis titrations experiments were carried out in buffer (pH=7.4, phosphate buffer, 50 mM NaCl) at room temperature. A stock solution of calf thymus DNA was prepared in the above buffer and the UV absorbance at 260 nm and 280 nm were recorded indicating that the DNA is free of proteins. The concentration of the CT-DNA stock solution was determined spectrophotometrically using the molar absorption co-efficient ($6600 \text{ M}^{-1} \text{ cm}^{-1}$). The titrations were carried out using a fixed concentration of the ligand (10 µM), to which the CT-DNA was added in increasing concentration of DNA (0-50 µM). The solution was allowed to equilibrate 3 min before recording the spectra. The stock solutions were stored at 4 °C for further use.

1.10.9 Fluorescence Titrations

All fluorescence titration experiments were carried out in buffer (pH=7.4, phosphate buffer, 50 mM NaCl) at room temperature. A stock solution of calf thymus DNA was prepared in the above buffer and the UV absorbance at 260 nm and 280 nm were recorded indicating that the DNA is free of proteins. The concentration of the CT-DNA stock solution was determined spectrophotometrically using the molar absorption co-efficient (6600 M^{-1} cm^{-1}). The titrations were carried out using fixed concentration of the ligand (10 µM), to which the CT-DNA was added in increasing concentration of DNA (0-50 µM). The ligands were excited at selected wavelengths and the excitation fluorescence was recorded. The solution was allowed to equilibrate 3 min before recording the spectra.

1.10.10 Time Resolved Spectroscopy

Time resolved emission results are obtained by time-correlated single photon counting using fluorescence spectrophotometer in Dr. Viktor Chikan's laboratory at the Department of Chemistry at Kansas State University. In the apparatus used in these studies, the sample is excited with approximately 15 nJ, 15 fs pulses from the second harmonic of a Ti:sapphire laser at a repetition rate of 80 MHz. The laser pulse is characterized using a home-built autocorrelator with a GaAsp photodiode as the non linear medium. The excitation wavelength is fixed at 470 nm with excitation spot sizes of about 1 mm. Detection is accomplished with a Hamamatsu 6 µ MCP PMT and a time correlated single photon counting electronics. Wavelength selection is accomplished using interference filters. The instrument response function is determined by observing the laser scatter, and is about 60 ps FWHM. Polarized emission detection is accomplished using an emission polarizer in a perpendicular detection scheme relative to the excitation laser. The vertical and horizontal components of the intensity of the emitted light were

measured and the data was used to calculate the anisotropy of the complex. During the experiment the samples were placed in a covered box to avoid the entering light.

References

1. http://www.cancer.gov/cancertopics/what-is-cancer
2. http://www.cancer.gov/cancertopics/chemotherapy-and-you
3. http://www.maacenter.org/mesothelioma/treatment/chemotherapy/index.php
4. Lowe, S. W.; Lin, A. W., Apoptosis in Cancer, *Carcinogenesis*, **2000**, *21(3)*, 485-495
5. Stryer, L., Biochemistry, New York, W.H.Freeman, *4th edition*, **1995**
6. http://en.wikipedia.org/wiki/Image:DNA_chemical_structure.svg
7. http://www.ocw.cn/NR/rdonlyres/Biology/
8. Long, E. C.; Barton, J. K., On Demonstrating DNA Intercalation, *Acc. Chem. Res.*, **1990**, *23(9)*, 271–273
9. Spillane, C. B.; Smith , J. A.; Morgan, J. L.; Keene, F. R., DNA Affinity Binding Studies Using a Fluorescent Dye Displacement Technique: The Dichotomy of the bBinding Site, *Journal of Biological Inorganic Chemistry*, **2007**, *12(6)*, 819-824
10. Li, S.; Cooper, V. R.; Thonhauser, T.; Lundqvist, B. I.; Langreth, D. C., Stacking Interactions and DNA Intercalation, *J. Phys. Chem. B*, **2009**, *113 (32)*, 11166–1117
11. Berge, T.; Jenkins, N. S.; Hopkirk, R. B.; Waring, M. J.; Edwardson , J. M.; Henderson , R.M., Structural Perturbations in DNA Caused by bis-intercalation of Ditercalinium Visualised by Atomic Force Microscopy, *Nucleic Acids Research*, **2002**, *30(13)*, 2980-2986
12. Neto, B. A. D.; Lapis, A. A. M.; Recent Developments in the Chemistry of Deoxyribonucleic Acid (DNA) Intercalators: Principles, Design, Synthesis, *Applications and Trends, Molecules*, **2009**, *14*, 1725-1746
13. Fornari, F. A.; Randolph , J. K.; Yalowich , J. C.; Ritke, M. K.; Gewirtz, D. A., Interference by Doxorubicin with DNA Unwinding in MCF-7 Breast Tumor Cells, *Molecular Pharmacology*, **1994**, *45*, 4649-656
14. http://www.photobiology.com/photoiupac2000/pierard/Interactionmain.html

15. Deng, H.; Cai , J.; Xu H.; Zhanga, H.; Ji , L., Ruthenium(II) complexes Containing Asymmetric Ligands: Synthesis, Characterization, Crystal Structure and DNA-Binding, *Dalton trans.*, **2003**, 325-330

16. Amer, A. M.; El-Bahnasawi, A. A.; Mahran , M. R. H.; Lapib , M.; On the Synthesis of Pyrazino[2,3-b]phenazine and 1H-Imidazo[4,5-b]phenazine Derivatives, *Monatshefte für Chemie*, **1999**, *130(10)*, 1217-1225

17. De Almeida, M. V.; Chaves, J. D. S.; Fontes, A. P. S.; Césarb, E. T.; Gielen, M.; Synthesis and Characterization of Platinum(II) Complexes from Trifluoromethyl Phenylenediamine, Picoline and N-Benzyl Ethylenediamine Derivatives, *J. Braz. Chem. Soc.*, **2006**, *17(7)*, 1266-1273

18. Jennerwein, M.; Wappes, B.; Gust, R.; Sch6nenberger, H.; Engel, J.; Seeber, S.; Osieka, R.; Influence of Ring Substituents on the Antitumor Effect of Dichloro(1,2-diphenylethylenediamine)platinum(II) Complexes, *J Cancer Res Clin Oncol.*, **1988**, *114*, 347-358

19. Kumar, A.; Maurya, R. A.; Ahmad , P.; Diversity Oriented Synthesis of Benzimidazole and Benzoxa/(thia)zole Libraries Through Polymer-Supported Hypervalent Iodine Reagent, *J. Comb. Chem.*, **2009**, *11 (2)*, 198–201

20. Chauhan, M.; Banerjee, K.; Arjmand, F.; DNA Binding Studies of Novel Copper(II) Complexes Containing L-Tryptophan as Chiral Auxiliary: In Vitro Antitumor Activity of Cu−Sn2Complex in Human Neuroblastoma Cells*, Inorg. Chem.*, **2007**, *46 (8)*, 3072–3082

21. Wu, M.; Teng, H.; Ke, X.; Xu, W.; Su, J.; Liang, S.; Hu, X.; Copper(II) Complexes of Salicylaldehyde Hydrazones: Synthesis, Structure, and DNA Interaction, *Chemistry & Biodiversity*, **2007**, *4(9)*, 2198 – 2209

22. Fu, P. K.L.; Abuzakhm, S.; Turro, C.; Photoinduced DNA Cleavage and Cellular Damage in Human Dermal Fibroblasts by 2,3-Diaminophenazine, *Photochemistry and Photobiology*, **2005**, *81(1)*, 89-95

23. Nagababua, P.; Lathab, J. N. L.; Satyanarayana, S., DNA-Binding Studies of Mixed-Ligand (Ethylenediamine)ruthenium(II) Complexes, *Chemistry & Biodiversity*, **2006**, *3(11)*, 1219-1229

24. Healy, E. F., Quantitative Determination of DNA–Ligand Binding Using Fluorescence Spectroscopy, *J. Chem. Educ.*, **2007**, *84(8)*, 1304-1307.

25. Niu, S. Y. ; Zhang, S. S. ; Ma, L. B., Electrochemical and Spectroscopic Studies on the Interaction Between DNA and the Product of Enzyme-catalyzed Reaction of OPD-H_2O_2-HRP, *Bulletin of the Korean Chemical Society*, **2004**, *25(6)*, 829-832

26. Dougherty, T. J.; Gomer, C. J.; Henderson, B. W.; Jori, G.; Kessel, D.; Korbelik, M.; Moan, , J.; Peng, Q., Photodynamic Therapy, *Journal of the National Cancer Institute*, **1998**, *90(12)*, 889-905

27. Dolmans, D.E.; Fukumura D.; Jain R.K., Photodynamic Therapy for Cancer, *Nat Rev Cancer*, **2003**, *3(5)*, 380-387

28. Tan, J.; Wang, B.; Zhu, L., DNA Binding, Cytotoxicity, Apoptotic Inducing Activity, and Molecular Modeling Study of quercetin zinc(II) Complex, *Bioorganic & Medicinal Chemistry*, **2009**, *17(2)*, 614-620

29. Bright, F. V.; Munson, C. A., Time-resolved Fluorescence Spectroscopy for Illuminating Complex Systems, *Analytica Chimica Acta*, **2003**, 71–104

30. Turro, N. J., Modern Molecular Photochemistry, University Science Books, Mill Valley, California, USA, **1978**

31. Soutar,I.; Swanson, L.; Christensen, R. L.; Drake, R. C.; Phillips, D., Time-Resolved Luminescence Anisotropy Studies of the Relaxation Behavior of Polymers, Intramolecular Segmental Relaxation of Poly(methyl methacrylate) and Poly(methyl acrylate) in Dilute Solutions in Dichloromethane, *Macromolecules*, **1996**, *29 (14)*, 4931–4936

32. Jang, D.; Yoo, Y.; Oh, S. M., Electropolymerization Mechanism for Poly(*o*-phenylenediamine) (PPD) and Its Electrostatic Behavior for O_2 Reduction, *Bulletin of the Korean Chemical Society*, **1995**, *16(5)*, 392-396

Chapter 2 - Modification of Iron(0)/iron Oxide Core/shell Magnetic Nanoparticles for Local Hyperthermia Treatment

2.1 Introduction

The first reported medical applications of magnetic materials date back to 10th century AD in ancient Egypt.[1] Since then magnetic nanoparticles have extended their applications into medical diagnosis and treatment of various diseases in dentistry, cardiology, neurosurgery, oncology, radiology, etc. The use of magnetic nanoparticles for hyperthermia is very appealing in modern treatment of cancers due to fewer side effects compared to chemotherapy and radiotherapy. This method has the ability to selectively treat cancers deep down in tissues by selectively accumulating the nanoparticles into the cancerous cells and heating them by applying an external magnetic field. The use of iron oxide nanoparticles as contrasting agents in Magnetic Resonance Imaging (MRI) has further expanded the window of medical applications of nanoparticles. MRI is a non invasive method of diagnosing cancerous tissues making use of the nuclear spins of the hydrogen atoms present in all tissues. The ability to correctly diagnose cancer can be greatly improved using contrast-enhancing agents such as highly paramagnetic iron nanoparticles[1]. Iron nanoparticles are suitable for developing sensors for the detection of the presence of cancer specific proteases such as matrix metalloproteinases (MMP's). The nanoparticles will act as a nanoplatform that can be modified with organic ligands separating a chromophore by a protease specific peptide sequence. The fluorophore will be inactive at the beginning and will only be activated in the presence of the specific protease. The activation of the fluorophore can be measured as an enhanced fluorescence signal. This system can be used to develop sensors for a wide range of proteases for the detection of the different stages of a cancer cycle.[2]

The following chapters will discuss the chemical modifications of iron(0)/iron oxide core/shell magnetic nanoparticles that have been developed and synthesized by our industrial partners from NanoScale Corporation, Manhattan, KS , with the aim to meet the biophysical requirements of the applications discussed above .

2.1.1 Iron(0)/iron Oxide Core/shell Magnetic Nanoparticles

The unique features of magnetic nanoparticles such as magnetic and catalytic properties have been attracting interest of many researchers in fields of biotechnology and biomedical applications covering a wide range of applications including magnetic resonance imaging, hyperthermia, drug delivery, and gene targeting.[3,4] Magnetic nanoparticles mainly composed of ferrous or ferric oxide and relatively non-toxic compared to cobalt or nickel particles.[4] These particles can be easily accumulated in high levels in tissues due to their nanosize that can be varied from 2 nm to 100 nm during their synthesis.[5] The ability to obtain a narrow size distribution range gives uniform chemical and physical properties, which are important in obtaining reproducible results during experimental procedures.[6] Biocompatibility and injectability are other important properties of iron nanoparticles in biomedical applications.[4] Surface coating of nanoparticles with biocompatible polymers like polyoxamines, polyethylene glycol, and attachment of targeting molecules on to these polymers should allow the nanoparticles to reach the target tissues in high concentrations.[6]

There are several methods well established for the synthesis of iron nanoparticles. Thermal decomposition of iron pentacarbonyl, sonochemical decomposition of iron carbonyl and reduction of iron salts and oxides are commonly used synthetic methods.[7] NanoScale Corporation, Manhattan, Kansas has provided the highly uniform Fe/Fe_3O_4-nanoparticles. The synthetic procedure is proprietary information of NanoScale Corporation.
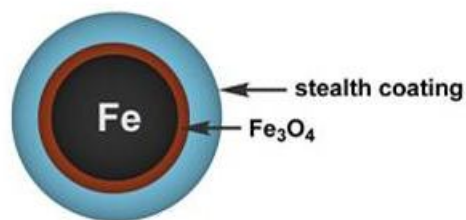
Figure 2.1: The Structure of the nanoparticle. The diameter of the Fe(0) core was 5.4±1.1 nm, and the diameter of the inorganic Fe/Fe_3O_4 was 7.2±2.8 nm. The stealth coating is the protective ligands surrounding the particle

The main disadvantage of iron nanoparticles is the high sensitivity to oxygen and air, where iron can be easily oxidized. Maintaining the iron in it's zero-valent state and modifying the outer core of the particle with organic ligands or gold shells do limit the corrosive nature in environments where water and oxygen are abundant.[7]

Bioavailability and high blood circulation times are significant factors when considering magnetic nanoparticles for biological applications. The size of the nanoparticle is an important parameter in determination of the blood circulation time. If the nanoparticles have sizes greater than 200 nm, the blood circulation time will be lower due to the aggregation and mechanical filtration of the particles by the spleen followed by removal through phagocyte cells. Rapid removal of particles via renal excretion and extravasation was reported when the size is less than 10 nm. The optimal size of a nanoparticle should be in the range of 10-100 nm for subcutaneous injection and higher blood circulation times.[6]

2.2.2 Uptake Mechanisms of Nanoparticles by Cancerous Tissues

Once entered the blood stream the nanoparticles can reach the target cancerous cells via passive or active targeting. Passive targeting is due to the enhanced permeation retention effect (EPR) of the cancerous tissues.[8] During the angiogenesis or generation of new blood vessels by

50

tumor tissues, the release of cytokines leads to generation of loosely packed disorganized blood vessels with enlarged gaps with adjacent endothelial cells. Since these gaps have sizes ranging from 600 nm to 800 nm nanoparticles can easily penetrate and accumulate in the tumor interstitial space.[9,10]
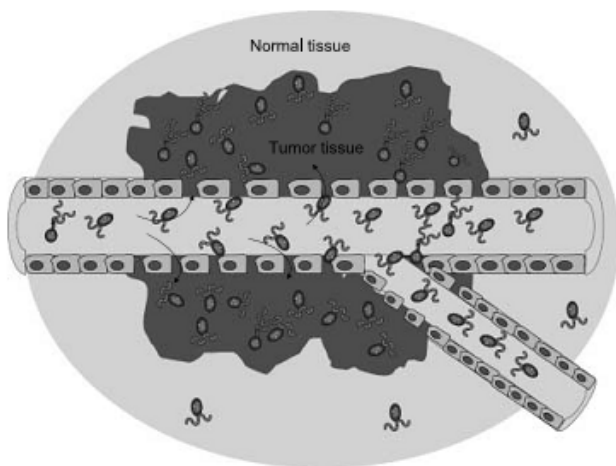
Figure 2.2: Passive Targeting of nanoparticles to tumor tissues via enhanced permeation retention effect[10]

Passive specific targeting of nanoparticles to tumor tissues is achieved by modifying the particle surface with an anti body or a targeting ligand.[10] Tumor tissues are known to over express folate receptors.[11] Zhang and coworkers[12] have reported that surface modified superparamagnetic nanoparticles with folic acid facilitated the uptake of the particles in human breast cancer cells (BT 20). Coupling of monoclonal antibodies to nanoparticles is another strategy to achieve site specific delivery to tumor tissues. According to the research conducted by Steinhauser and coworkers[13] nanoparticles coupled with antibody trastuzumab, was taken up by HER2-positive cells via receptor mediated endocytosis.[13]
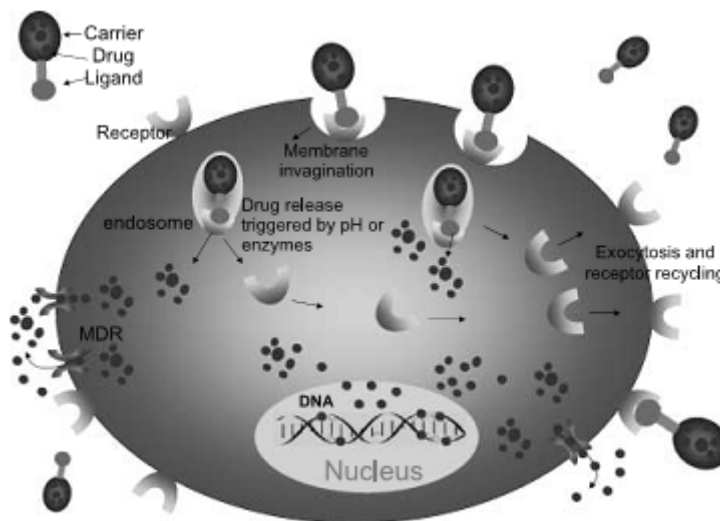
Figure 2.3: Active transportation of nanoparticles into tumor cells triggered by tumor specific ligand or antibodies[10]

2.2.3 Coating of the Nanoparticles with Organic Ligands

Since the modified ligand is playing a key role in targeting and protection of the nanoparticles, it is crucial that the functional molecule and the nanoparticles have stable bonding. The inorganic core is preferably coated with an organic layer and the ligand has to be stable and immobilized on the surface. The ligand should be comprised of functional groups that are attracted to the metal surface of the nanoparticles. Thiols- are commonly used on gold nanoparticles to form monolayers to achieve surface functionalization.[14] There is no demonstrated evidence that these molecules could functionalize magnetic iron oxide nanoparticles. Au, polymers and silica have been used as surface modifiers for iron nanoparticles. Xu and coworkers[15] reported the synthesis of dopamine based functionalized nanoparticles which has attracted great interest due to its ability to be further derivatized by reacting the free NH_2 group of the dopamine with different groups like carboxylic acids to form amide bonds.[15] Dopamine has the potential to coordinate to the surface of the iron oxide nanoparticle with an octahedral geometry forming a ring via M-O bonds.[16] According to

52

Langmuir isotherms the desorption of the dopamine is less favorable from the surface than adsorption. This explains why dopamine is used as a versatile linker.[15] Iron oxide nanoparticles can further be decorated with aminosilane which is non toxic and biocompatible and will prevent the core from bio corrosion under physiological conditions for much longer time (up to 2 weeks) than a dopamine-coating (up to several days).[17]

To avoid aggregation and bio-corrosion of the nanoparticles and to stabilize them under physiological conditions, the nanoparticles are stealth coated and stabilized with a layer of ligand. The stealth coating can be attached directly to the nanoparticles or may be added as a second monolayer surrounding the dopamine protecting layer. Dextran, and polyvinyl coated nanoparticles are reported in early literature.[18] Polyethylene glycol (PEG) is a superior candidate to serve this purpose and it has been observed that nanoparticles coated with PEG has enhanced life time in the blood stream.[19] The free OH end of ethylene glycol allows the molecule to react with a ligand initially coated with a COOH, forming ester bonds.[18] There are several other advantages of using PEG as a coating agent apart from biocompatibility. The free OH end of the PEG can be used for further functionalization of the particles, the oxygen atom has the ability to form hydrogen bonds thus increasing the water solubility of the system, PEG is environmentally friendly, non toxic and less expensive compared to other coating materials.[19,20] Depending on the requirements of the final product, tetraethyleneglycol, dodecaethyleneglycol, and polyethylene glycol can be used to enhance the stability, solubility and reactivity of the nanoparticles.

It is important that the nanoparticles be modified with functional groups for selective uptake by target tissues. Cancer cells for example are known to over express many receptors and antigens including folate receptors, antigens such as hyaluronan, a linear polysaccharide and GLUT, a family of trans-membrane proteins.[21,22] These targeting moieties can be used in

selective targeting of tumor cells over normal cells, and may result in larger accumulation of the injected material within the tumor regions minimizing side effects to healthy tissues.

Porphyrin have been found to trigger selective uptake by cancer cells which over express low density lipoprotein (LDL) receptors in their cell membranes. Porphyrins are precursors for the biosynthesis of heme and other prosthetic groups and coenzymes, which are needed to satisfy the higher metabolic rate of cancer cells.[23] Once these hydrophobic porphyrins are administrated intravenously they have the ability to strongly bind to lipoproteins and be transported in the blood stream. Then the low density lipoprotein receptors, which are over-expressed in cancer cells, have the ability to take up the bound porphyrin through simultaneous lipid uptake mechanism or through the apolipoprotein (apo) B/E specific LDL receptor pathway.[24,25] The selectivity could be further enhanced by increasing the hydrophobicity of the porphyrin.

2.2.4 Hyperthermia

The search for cancer-treatment methodologies, which can overcome multidrug resistance, is of the utmost importance in the battle against this powerful disease. The occurrence of multidrug resistance in many cancer types means the success rate of chemotherapy is, in general, limited. Furthermore, future anti-cancer drugs should not only be highly effective, but also readily available at modest costs to be able to treat millions of patients. The emerging technology of using nanoparticles as a platform for the diagnosis and treatment of cancer can provide a solution for these problems. There exists a critical need for multi dimentional functionalized nanoparticles that can achieve the following aims simultaneously: a) to have higher blood circulation time by evading the reticuloendothelial system, b) to accumulate within the tumor tissue with high selectivity, c) to permit the Magnetic resonance imaging (MRI) detection of the cancer tissue, d) to verify that the tissue identified by using MRI is indeed

cancerous by means of an *in-vivo* luminescence assay and e) finally selective hyperthermia treatment of the formerly identified cancer tissue by applying an external A/C-magnetic field.[2, 6]

The introduction of novel anti cancer drugs with high efficiency and low toxicity has decreased greatly over the last decade. The question emerging from these data is whether the anticancer drug development is focusing on the proper strategies and addressing the issues associated with the existing drugs. The early attention focused on extracting active substances from natural products, which then have been synthesized in the laboratories following the studies of their activity using *in vitro* cyctotoxicity assays. With the expansion of information available on cellular and molecular changes associated specially with cancerous tissues, anti cancer drug development has moved into the "molecular target" area. This strategy has been successful up to some extent (e.g. imatinib mesylate for the treatment of chronic myelogenous leukemia and gastrointestinal stromal tumors); however, the genetic complexity and diversity of tumor cells, has limited the applications of molecular targeting. The progression of a normal cell to a cancer cell involves several gene mutations so the attention on a certain gene was not effective enough for the proper treatment of the cancer. There are certain biological pathways that are associated with cancers and are either up regulate or down regulate some molecules or enzymes (e.g. Matrix metalloproteinases are up regulated in tumor tissues). But availability of alternative pathways is an obstacle to overcome in this strategy, and a successful cancer therapy has to combine several approaches. Hyperthermia, radiotherapy, selective delivery of drugs using stem cell delivery, use of photodynamically active organic compounds in photodynamic therapy, and the design of molecules that combine cancer diagnostics and treatment (theranostics) e.g. modified iron nanoparticles, are "hot" areas of interest that may be offering new opportunities when working towards the development of new anticancer drugs.[27]

Hyperthermia is the heat treatment of cancers with artificially increased temperatures of 40 to 48 ºC, 3-11 ºC above body temperature, or a region using an external energy source to destroy or prevent further development of the cancerous cells.[28,29] The history of use of hyperthermia to treat various diseases is dating back to 3000 BC but the interest in modern hyperthermia treatment in cancer therapy was raised by the first international Congress on Hyperthermic Oncology in Washington in 1975.[29] Hyperthermia treatment is especially effective in environments with low oxygen and pH making cancer cells slightly more susceptible to hyperthermia than healthy cells, and can enhance the sensitivity of cells for radiation and chemotherapeutics.[29] The radio sensitivity of the tissues will be increased by improvement of oxygen supply to the tissues with increasing blood flow by high temperatures. The *in vivo* experiments have showed that hyperthermia can act as potent radiosensitizer that could enhance the effect of radiation therapy by factor of 5. The elevated blood flow will increase the intracellular delivery and uptake of the drugs contributing to better clinical results obtained with combined therapy of hyperthermia and chemotherapy.[28,29] Based on the impact of heat on tissues, the use of high temperature can be categorized as coagulation (temperatures less than 50 ºC), thermal ablation (60-90 ºC), and charring (temperatures less than 200 ºC). The exposure time and the temperature are the most significant factors to be considered during hyperthermia treatment.[29] There is a break point in the cell survival rate and after that the cell death increase exponentially with temperature.[30]
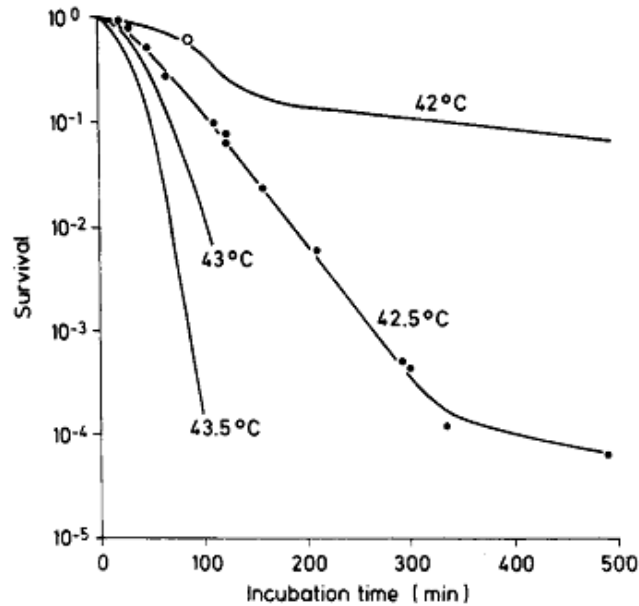
Figure 2.4: The survival rates of cells exposed to different temperature[30]

One of the main advantages of this method is that the normal cells are unharmed when exposed to temperatures of 44 °C for 1 h.[29] The typical difference in tumor physiology and environment such as high vascular nature, low interstitial pH make cancer cells more sensitive to heat. As of now the exposure of the 90% of the tumor volume to temperatures of 43 °C for less than 30 minutes is regarded as the ideal condition in hyperthermia. The higher exposure times and temperatures may seem to be more effective, the major drawback is that they can damage the cells in the central nervous system.[28,29]

There are three main distinguished categories of hyperthermia, depending on the location, and depth of tumor, namely local, regional and whole body hyperthermia.[28] Out of these methods local hyperthermia is the mostly practiced method, where the heat is localized mainly to the tumor area.[28,29] Therefore, the development of methods to selectively target hyperthermia treatment in cancer cells remains one of the challenges in this field. This is equally important when attempting to treat solid tumors within the human body. The energy sources used in local

increase in temperature are microwaves, electromagnetic radiation, and ultrasound energy.[28,29] Hyperthermia is very efficient against cancers located in or just below the skin. The use of magnetic fields for the generation of heat have given the opportunity to treat tumors located in deeper tissues.[28] During local hyperthermia the distribution of heating is not only dependent on the energy source, but the tissue characteristics and the blood flow of cancers. Since the cancers naturally have a low flow of blood to its tissues, the waste of heat to adjacent normal tissues is limited.[29]

There is a new inventive approach in hyperthermia treatment using ironic magnetic nanoparticles. These therapeutic nanoplatform or particles are administered to tumor tissues, preferably using a pharmaceutically acceptable carrier. Liposomal delivery of the nanoparticles to the cancerous tissues may also be used, including thermolabile liposomes.[31] Experimental studies have shown that hyperthermia has led to an increase in the liposome permeability of blood vessels thus accumulating more particles in the tumor site.[31] The nanoparticles can be administered by injection to a localized region, via direct injection into or near the tumor site, or can be administered intravenously by injection into the bloodstream.[4] When injecting nanoparticles intravenously the surface can be easily modified with organic molecules to achieve cancer cell specific accumulation.[3]
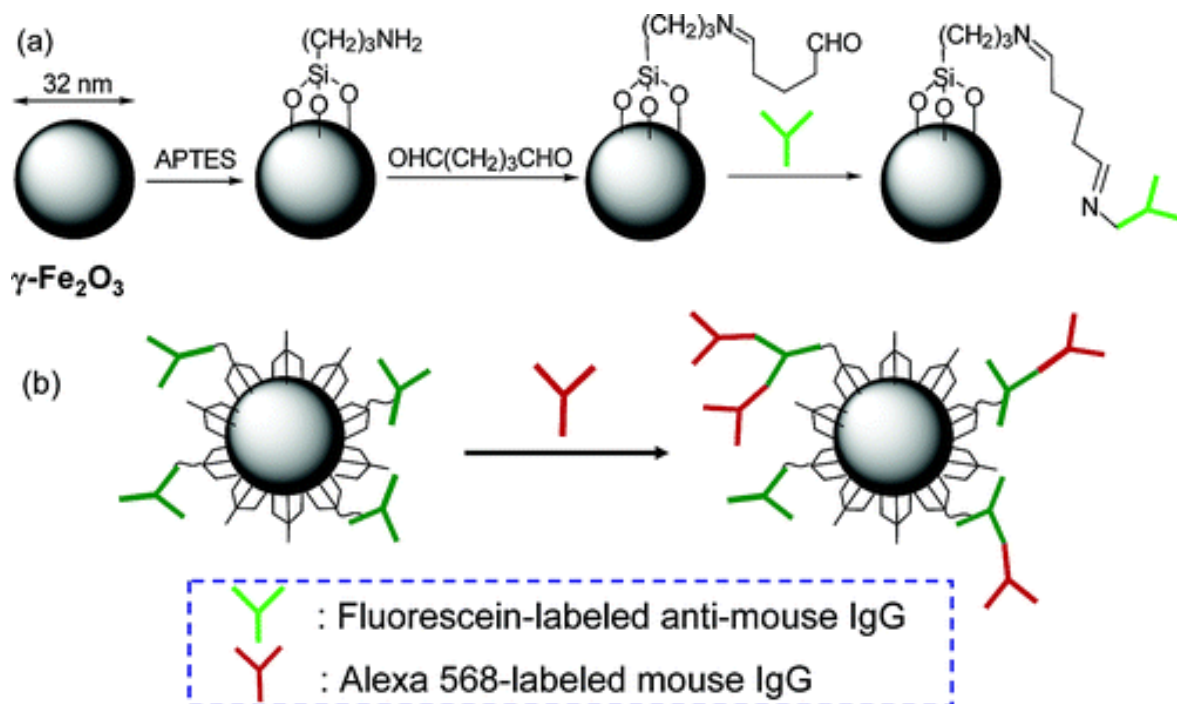
Figure 2.5: Surface modified nanoparticles. Surface modification of γ-Fe$_2$O$_3$ nanoparticles with APTES for the immobilization of fluorescein-labeled anti-mouse IgG (FL anti-mouse IgG)[32]

Once the nanoparticles have been taken up by the cancer cells and located in the cancer tissue, the target region of interest is heated using an alternating magnetic field (AMF). The majority of the intracellular hyperthermia studies have been carried out using solutions of superparamagnetic magnetite (Fe$_3$O$_4$) or maghemite (γ-Fe$_2$O$_3$).[4,33] Excitation is preferably performed at frequencies ranging from about 0.05 to 1.2 MHz and amplitudes of 0-15 k Am^{-1}.[5] There is a clinical trial reported in literature for treatment of brain cancer using magnetic hyperthermia. There, a water suspension of superparamagnetic iron oxide nanoparticles with a core size of 15 nm in a field amplitude of 13.5 k Am^{-1} at 100 kHz was used as the treatment conditions.[33] It was demonstrated that the surrounding healthy tissues were able to tolerate the temperature when they were exposed to a frequency of 90 kHz for more than an hour.[33] The time interval between the administration of the nanoparticles and the A/C magnetic heating greatly

depends on the method of administration. It is generally estimated that accumulation of 5-10 mg of magnetic material in each 1 cm^3 of tumor tissue, and direct tumor injection is the most efficient administration method which can fulfill this requirement.[5] The A/C-excitation raises the temperature of the nanoparticles, this heat is then dissipated into and raises the temperature of the cancerous tissue, resulting in growth inhibition, and cell death. Because the nanomaterials are selectively taken up by the target cancerous tissue, the heat remains relatively confined to the target tissue minimizing damage to surrounding healthy tissue.

At high temperatures resulting from plasmonic and intense A/C-magnetic hyperthermia, partial carbonization, massive protein denaturation and a partial dissolution of cell and mitochondrial membranes in the surrounding buffer solution are observed. The fluidity and the stability of the cell membranes are disturbed during hyperthermia treatment. This will directly have an effect on the membrane transport channels, resulting in an imbalance of sodium, calcium and potassium in the cytosol and leading to pH changes in the cell.[30] Most of the stimuli involved in apoptosis or programmed cell death are activated by the cell itself during the hyperthermia treatment and will lead to self destruction of the cell.[30,34] These processes result in necrosis (uncontrolled, premature cell death), which is characterized by cell swelling, chromatin digestion, and disruption of the plasma membrane and organelle membranes, followed by extensive DNA degration, vacuolation of the endoplasmic reticulum, organelle breakdown (especially mitochondria and lysosomes) and, eventually, nuclear disintegration leading to cell death.[30,34] Damage to the lysosomes usually triggers the release of lysosomal cysteine proteinases (caspases and other proteases), which first lyse many vital cell structures and then are released from the dead cell.[35] They can trigger a chain reaction of further cell death of neighboring cells. When heated to medium temperatures of about 43 ºC to 45 ºC, vital proteins

60

of the cancer cell become damaged (e.g. misfolded) and/or unfolded and aggregates in the cell matrix. . Polymerization of RNA and DNA during the protein synthesis is noticeably terminated at elevated temperatures, due to the inhibition of DNA polymerases.[30] After hyperthermia, significant increases in TRAIL (tumor necrosis factor (TNF)-related apoptosis-inducing ligand) is observed. In short, hyperthermia induces apoptosis in cells that is mediated by caspase-3 and other caspases as a result of activation of cell-death membrane receptors of the tumor-necrosis-factor family. For hyperthermia treatment of cancerous tissue, apoptosis is preferred to necrosis because it is less damaging to surrounding healthy tissue.[36] It has been found that if temperatures of between about 43 to 45 ºC are retained for an extended period of time the anti-tumor immune response can be markedly enhanced, since most of the cellular processes that lead to cell death are activated are in a heat dose dependent manner.[30] The heat shock proteins (HSP) which are produced in abundant quantities in cells exposed to heat, are potent immune modulators and have the ability to interact with denatured hydrophobic proteins thus preventing irreversible interactions with other proteins. The result would be the lost of the function of the proteins.[30] When HSP interacts with tumor specific proteins they have the ability to activate T-cells against the cancer cells. Hyperthermia treatments can further lead to changes in the cellular immune responses. It is observed that the total NK-lymphocyte count of patients treated with temperature exceeding 42 ºC increased as a response to heat shock. There was a direct relationship observed between the presence of higher amounts of lymphocytes in the cell cytosol and the activation of cell apoptosis in animal models.
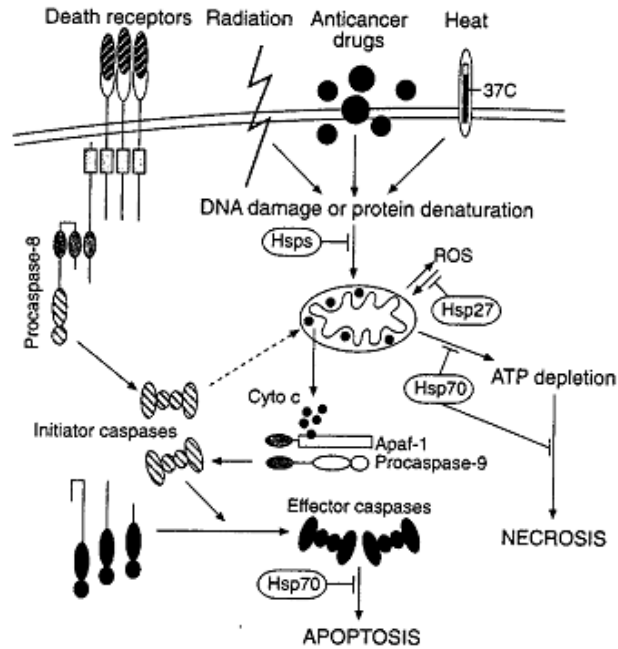
Figure 2.6: The function of heat shock proteins during cell death[30]

There are advantages of using hyperthermia treatment compared to chemotherapy and radiotherapy. The method is cost effective compared to other treatments, and results in fewer side effects. Even though the laboratory trials have proven to be highly efficient, the use of hyperthermia is not widely recognized as a preferred treatment method.

The most pronounced side effect of hyperthermia usually the skin burns. The damages to tissues and subcutaneous fat layers are reported in patients treated with regional and whole body hyperthermia. These methods normally require intensive labor since the treatment times do exceed more than an hour. There is a lack of equipment suitable for the treatment and heating techniques are sometimes not up to the standards.[29] Most of these disadvantages can easily be addressed using local hyperthermia treatments with modified iron nanoparticles in the presence of an alternative magnetic field.

The nanoparticles utilized in the nanoplatforms, should have a very narrow size/mass distribution of from about 10-100 nm. The heat generated from nanoparticles should be as high as possible for them to generate enough heat to raise body temperature. There are several factors contributing to the generation of heat e.g. size, mass shape, crystallinity of the particles, content of impurity and defects on the surface of the particle. So it is important that the nanoparticles selected for hyperthermia treatment are uniform in size distribution with optimum radius of less than 15nm. Polydispersity in a sample can rapidly decrease the heating capability.[37] In addition, the nanoparticles should feature a strongly paramagnetic iron-core. Compared to existing superparamagnetic iron-oxides for hyperthermia applications, superparamagnetic iron possesses a higher magnetic moment and a higher saturation magnetization. Preferably nanoparticles featuring a Fe_3O_4 shell around the iron core is used in biomedical applications. These nanoparticles comprising a Fe/Fe_3O_4 core/shell can then be surrounded by a siloxane protecting layer or a ligand monolayer resulting in more stable particles in water and physiological conditions. The core shell nanoparticles smaller than 15 nm are superparamagnetic at room temperature. Iron alone is more susceptible to corrosion and oxidation. The presence of the iron oxide shell will help to retain the magnetic moment of pure iron and protect it against corrosion. The high magnetic moment permits both lower concentrations and shorter A/C- heating times during the treatment of patients.[38]

An important factor for A/C magnetic hyperthermia is the Specific Absorption Rate or SAR of the nanoparticle, which is determined by $SAR=C*\Delta T/\Delta t$, where C is the specific heat capacity of the sample and T and t are the temperature and time, respectively. Large SAR values are required for hyperthermia treatments and will preferably have a specific absorption rate (SAR) of 1 kW/g. Even though this is the optimum value beneficial for hyperthermia, it is not

feasible to reach it since the SAR is very sensitive to the material properties[39].   Hysteresis, Néel and Brownian relaxation and frictional losses mainly contributes to converting magnetic energy in to heat energy. Heat can be induced magnetically when exposed to alternative magnetic fields due to the hysteretic properties of ferromagnetic particles. Generation of Eddy current is not reported with nanoparticles used in hyperthermia treatments due to their smaller size. Strongly anisotropic magnets like Nd-Fe-B can be used to increase the amount of heat generated by hysteresis heating.   In multi-domain particles the dominant heating is hysteresis loss due to the movement of domain walls at impurities or particle boundary defects, it is not so in case of small particles. The two main contributing mechanisms of SAR in single domain magnetic nanoparticles are the Brownian and Néel relaxations.[33] When the magnetic field is removed the magnetization of the particles relaxes back to zero in response to thermal energy of the environment. It is referred to as Brownian motion when the relaxation is a physical rotation of the particles, and the Néel relaxations are explained as a rotation of the magnetic moment within the particle. According to the Rosensweig equation both Brownian and Néel relaxations depend on the nanoparticles particles size and the magnetic core radius.[33]

Rosensweig equation,

$$\frac{1}{\tau} = \frac{1}{\tau_B} + \frac{1}{\tau_N}$$

τ = Nanoparticle time constant (time required to realign the particle magnetic moment with the applied magnetic field.

τ_B = Nanoparticle radius

τ_N = Magnetic core radius

Even though the entire rotation of the nanoparticles is hindered especially closer to a tumor or after binding to a cell, Néel relaxations will still be observed. In case of typical nanoparticles used in hyperthermia treatment with diameters ranging from 5-20 nm the dominant mechanism is the Néel relaxations.[33]

2.2 Experiments and Results

We have synthesized "intelligent nanomaterials" capable of spatially dissolved in-situ diagnosis and adaptable treatment of various cancers. The nanomaterials consist of a central bimagnetic iron/iron oxide nanoparticle (Fe/Fe_3O_4 NP), which was further modified for cancer treatment with organic ligands.

2.2.1 Synthesis of the Organic Stealth Ligands

We have synthesized ligands for the complexation and stabilization of the Fe/Fe_3O_4 nanoparticles. The Fe/Fe_3O_4 core shell nanoparticles were synthesized by NanoScale Corporation, Manhattan, Kansas. The core and the particle diameter were estimated using transmission electron microscopy (TEM) images. It was important that the particles are in the size range of 8-20 nm for our applications. The diameter of the Fe(0) core as calculated using TEM images was 5.4 ± 1.1 nm, and the diameter of the inorganic Fe/Fe_3O_4 was 7.2 ± 2.8 nm. Polydispersity index was calculated using IMAGE (NIH) program to be 1.31. As discussed previously this is an important parameter to be considered when using magnetic nanoparticles for hyperthermia treatments.

Nanoparticles were further purified prior to ligand modification to remove the larger particles that were not completely water soluble. 20.0 mg of Fe/Fe_3O_4 were suspended in 10.0 mL of tetrahydrofuran (THF) and the suspension was sonicated for 0.5 h, followed by low speed centrifugation at 1500 rpm. The supernatant was transferred to a separate tube and the

nanoparticles were collected using a strong magnet and the solution was carefully removed. The particles were washed three times with 5.0 mL of THF and dried under vacuum to obtain the nanoparticles.

The purified nanoparticles were then coated with a dopamine based ligand followed by attachment of porphyrin (4-tetracarboxyphenyl porphyrin, TCPP) labels to achieve target specific delivery. The ligand was synthesized separately and will be discussed in detail later in the chapter.
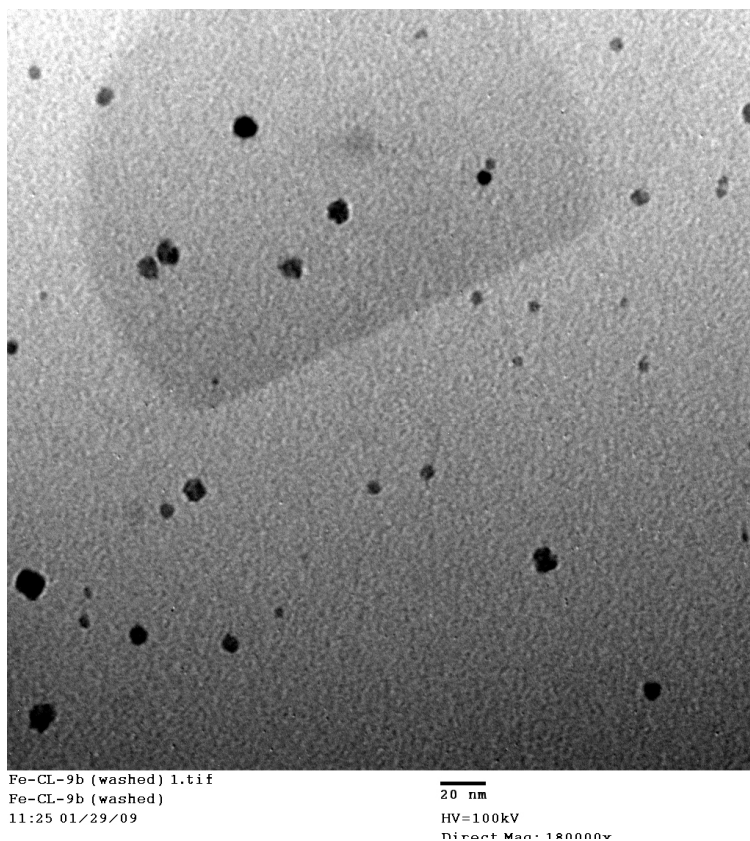
Figure 2.7: TEM image of Fe/Fe$_3$O$_4$ core shell nanoparticles with the organic protective dopamine anchored stealth layer

According to the calculations (from AM1-Chemdraw Ultra 3D package, Cambridge Soft Corporation, Cambridge), the stealth layer (TCPP linked, dopamine anchored

tetraethyleneglycol) has a total length of 2.5 nm. So the ligand modified Fe/Fe$_3$O$_4$ core shell nanoparticles were in the size range of 12±3 nm.
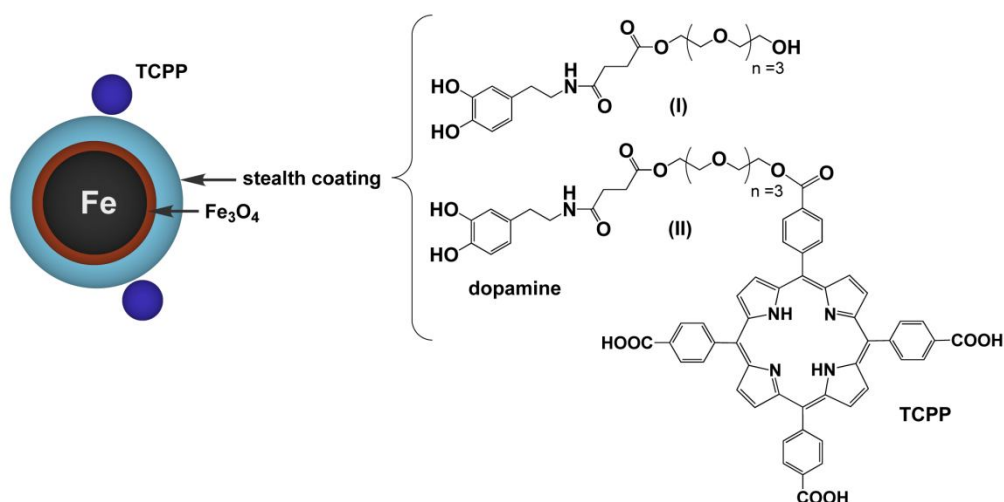
Figure 2.8: The composition of the Fe/Fe$_3$O$_4$ core shell nanoparticles coated with 4-tetracarboxyphenyl porphyrin labeled, organic ligand

The binding of the TCPP free ligand to nanoparticles was achieved in anhydrous THF by sonicating for 2 h followed by repeated washings (3x1.0 mL). Next 17.0 mg of TCPP porphyrin, 2.0 mg of 4-dimethylaminopyridine (DMAP), and 4.0 mg of 1-Ethyl-3-(3-dimethylaminopropyl)carbodiimide (EDC) were added to the suspension and sonicated for 1 h to form the ester linkage between the free OH end of tetraethyleneglycol and COOH of porphyrin. The solid was collected using a strong magnet and washed repeatedly with THF (8x1.0 mL) until the washing is colorless. The organic liquid from the washing procedures were subjected to UV/Vis-absorption spectroscopy, and the UV/Vis spectra were recorded until the peaks from porphyrin had disappeared. The absence of characteristic peaks from TCPP at 417, 511, 546, 589, and 645 nm, indicated that all the non-bonded TCPP had been removed. Typically, three consecutive washing procedures were sufficient.

67

We have calculated the number of ligands required to form a complete monolayer on the nanoparticle surface using Poisson distribution. There were mainly two assumptions taken into consideration during this calculation. We assumed that the nanoparticles are perfect spheres and and according to PM3 calculations (using Chemdraw software) the space demand of the dopamine which anchors to the surface of the particle is 1.094 nm^2. We further assumed that each ligand has the same affinity towards surface binding. It is important that the water solubility of the ligand is retained after attachment of the porphyrin which is hydrophobic in nature.

Poisson distribution is used to predict the number of events occurring in a specified interval such as area and volume, with a known average rate and independently of the time since the last event.

$$f(k, \lambda) = \left(\frac{e^{-\lambda} \lambda^{k}}{k!} \right)$$

λ: expected number of occurrences, a real positive number
k: integer number of occurrences(0,1,2,3…)
f: probability for exactly k occurrences
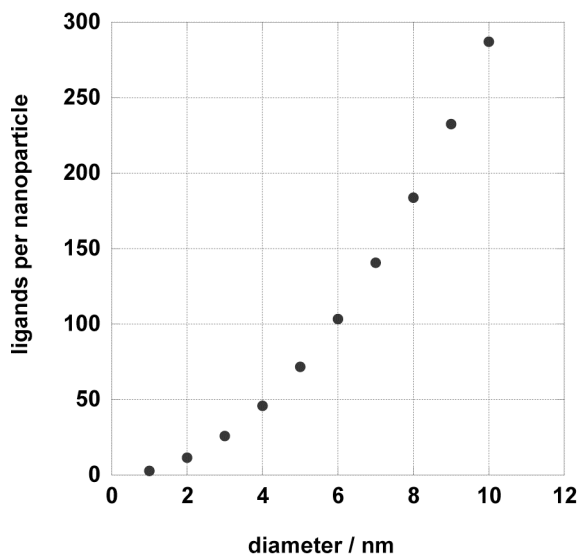
Figure 2.9: Number of dopamine-anchored ligands per nanoparticles as a function of the nanoparticle-diameter

By applying this simple model, the effect of variations in the nanoparticle-diameters on the number of ligands that form a monolayer on the nanoparticle-surface can be estimated. The number of required to completely cover the surface of a nanoparticles with a diameter of 7.2 nm is estimated to be approximately 120.

According to Poisson distribution the probability of a nanoparticle having at least one chemically linked TCPP unit is 96.4 percent. Since porphyrin is a bulky group the highest practical number of ligand on one nanoparticle should be roughly 10. This is sufficient to facilitate the LDL receptor mediated uptake of the nanoparticles, and the water solubility of the nanoparticles will not be decreased.

The number of TCPP units actually bound to nanoparticles was estimated using UV/Vis absorption spectroscopy. 17.0 mg of TCPP was dissolved in 5.0 mL THF and the initial UV spectrum was recorded. Then TCPP was reacted with the free end of tetraethyleneglycol in the presence of DMAP and EDC by sonicating the suspension for 1 h. The particles were collected

using a strong magnet and the supernatant was subjected to UV absorption spectroscopy. The difference corresponds to the amount of porphyrin bound with the nanoparticles. Using these data, it is estimated that each nanoparticles will have 5 TCPP units bound to it. The solubility of the organically coated Fe/Fe_3O_4 nanoparticles was 0.35 mg mL^{-1}.

2.2.2 Determination of the Iron Content in Magnetic Nanoparticles

Inductively coupled plasma atomic emission spectroscopy (ICP-AES) and ferrozine based UV/Vis-spectrophotometric iron estimation methods were used to measure the iron content of the nanoparticles.

2.2.2.1 Inductively Coupled Plasma Atomic Emission Spectroscopy (ICP-AES)

This is an emission spectroscopic technique very specific for a given element, and the intensity of the energy emitted at the chosen wavelength is proportional to the amount (concentration) of that element in the analyzed sample.

A standard series of Fe(II) ranging from 10-50 ppm was prepared from the 1000 ppm ICP standard stock solution. Iron/ iron core shell nanoparticles, and the ligand modified nanoparticle samples were subjected to ICP studies. The samples were prepared by dissolving the nanoparticle samples in conc. HCl overnight. Then the samples were filtered and diluted with 4M HCl. The measurements were conducted using inductively coupled plasma atomic emission spectrophotometer in Dr. Ganga Hettiarachchi's laboratory at the Department of Agronomy. The excitation wavelength was 260.94 nm. The test concentrations were determined using the standard curve.

2.2.2.2 Ferrozine Based UV/Vis-Spectrophotometric Assay[40]

Iron concentration in MNPs was measured using the ferrozine-based spectrophotometric iron estimation method. For this method, 50.0 µL of MNPs were diluted to 1.0 mL with distilled

water. MNPs were then lysed by incubating for 2 h at 65-70 ºC after the addition of 0.5 mL of 1.2 M HCl and 0.2 mL of 2M ascorbic acid. After incubation, 0.2 mL of reagent containing 6.5 mM ferrozine, 13.1 mM neocuproine, 2 M ascorbic acid, and 5 M ammonium acetate was added and incubated for 0.5 h at room temperature. After 0.5 h, the optical density of the samples was measured using a UV-Vis spectrophotometer at 562 nm. A standard curve was prepared using 0, 0.1, 0.2, 0.5, 1, 2, 5 μg/mL ferrous ammonium sulfate samples. Water with all other reagents was used as the blank. The iron content of the sample was estimated to be 0.35 mg mL^{-1}.

2.2.3 The UV/Vis- and Fluorescence Studies of Fe/Fe$_3$O$_4$ Core/Shell Nanoparticles Featuring Chemically Attached Porphyrin Units (TCPP)

Both experiments were carried out in 4.0 mL quartz-cuvettes (Helma) using a spectrofluorometer (Fluoromax2) with dual monochromators and a diode array UV-Vis absorption spectrometer (HP 8453) in a medium of phosphate buffer (pH=7.2)

The absorption and scattering peak of the nanoscopic Fe/Fe$_3$O$_4$ core/shell nanoparticles can be observed at approx. 320 nm. At higher wavelengths no UV/Vis absorption and scattering is observed. However, when meso-tetrakis (4-carboxyphenyl) porphyrin is chemically linked to the Fe/Fe$_3$O$_4$ core/shell nanoparticles, it dominates the UV/Vis-absorption in the visible range. The electronic absorption spectrum of a typical porphyrin consists of a strong transition to the second excited state (S$_0$ to S$_2$) at about 400 nm (the Soret or B band) and a weak transition to the first excited state (S$_0$ to S$_1$) at about 550 nm (the Q band). The B and the Q bands both arise from π–π* transitions[41]. For meso-tetrakis (4-carboxyphenyl) porphyrin the Soret band was observed at 417 nm and Q bands were appearing at 511, 546, 589, 645 nm.

The light emission behavior is shown in Figure 2.10. TCPP tethered to the Fe/Fe$_3$O$_4$-NPs has two emission bands at λ=654 nm, and λ=718 nm. The excitation wavelength was 417 nm.
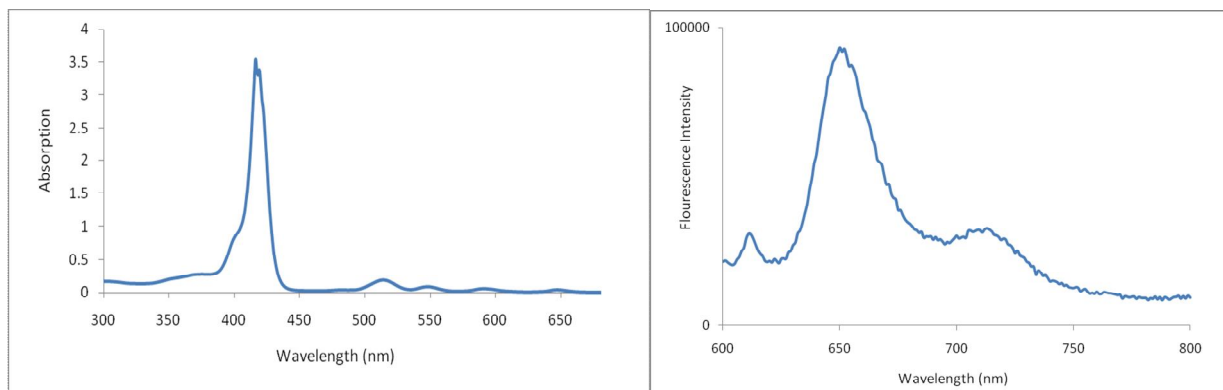
Figure 2.10: The UV/Vis and fluorescence spectra of Fe/Fe$_3$O$_4$ core/shell nanoparticles featuring chemically attached porphyrin units (TCPP)

The peak position of the Soret band (extremely intense near-ultraviolet band) is λ=417 nm for TCPP. The absorption coefficients are 4.8 x 10^5 M^{-1} cm^{-1} for TCPP in principal agreement with the literature. The chemical attachment to the bimagnetic Fe/Fe$_3$O$_4$ nanoparticles via a dopamine-tetraethylene glycol bridge decreases the absorption coefficient of TCPP but the position of the peaks were not changed significantly. Figure 2.11 shows the UV/Vis-spectra for two TCPP-doped nanoparticles, with the ratios of Fe/Fe$_3$O$_4$ to porphyrin to 1:5 and 1:1.2.
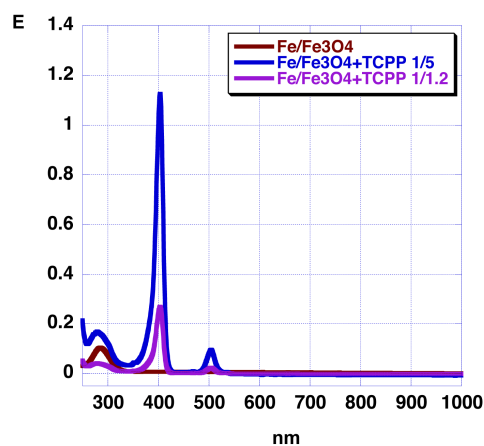
Figure 2.11: UV/Vis-spectra of Fe/Fe$_3$O$_4$ core/shell nanoparticles containing 0, 1.2 and 5 TCPP units per nanoparticle (statistical average) in aqueous phosphate buffer (pH=7.2)
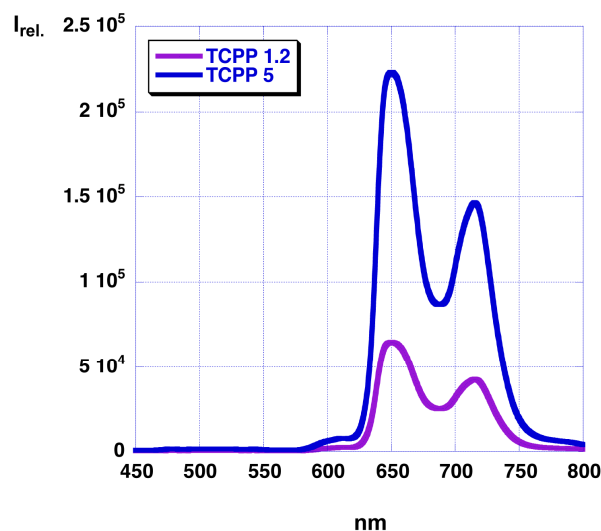
Figure 2.12: Fluorescence emission of Fe/Fe$_3$O$_4$ core/shell nanoparticles 1.2 and 5 TCPP units per nanoparticle (statistical average) in aqueous phosphate buffer (pH=7.2); excitation wavelength: 417 nm

2.2.4 Synthesis of Porphyrin-tethered Stealth Coated Magnetic Fe/Fe$_3$O$_4$ Nanoparticles

The modification of the nanoparticles was conducted in Dr. Stefan Bossmann's Laboratory at the Department of Chemistry at Kansas State University. The synthesis starts with the protection and deprotection of the primary aliphatic amino group of dopamine. The amino group is selectively protected with tert-butyl dicarbonate in the presence of triethylamine. The phenolic OH of the dopamine is then protected with benzyl bromide. The deprotection of the amino group with trifluoroacetic acid resulted in the free amine. The synthesis was continued with the benzyl-protected dopamine, which reacts first with succinic anhydride and then with commercially available tetraethylene glycol or dodecaethylene glycol in the presence of 1-ethyl-3-[3-dimethylaminopropyl]carbodiimide (EDC), 4-dimethyl-aminopyridine (DMAP), in dimethylformamide (DMF). To further enhance the solubility of the stealth-protected Fe/Fe$_3$O$_4$-nanoparticles, a fluorenylmethyloxycarbonyl (Fmoc) protected glycine-unit was connected to the

73

dopamine-anchored tetraethylene glycol ligand via an ester bond by using EDC/DMAP. Both protection groups, Bn and Fmoc, were removed together by hydrogenation.

The Fe/Fe$_3$O$_4$-nanoparticles were dispersed in THF by sonication and a mixture of dopamine-anchored tetraethylene glycol ligand and glycine-tipped tetraethylene glycol ligand (95/5; mol/mol) was added. The mixture was allowed to sonicate for 0.5 h. The nanoparticles were then collected by using a strong magnet (0.5 T). Up to 10 redispersion and washing procedure were followed. TCPP was co-dissolved in THF and tethered by an amide-bond to the amine-function of the "glycine-tipped" tetraethylene glycol ligands in the presence of EDC/NHS to yield a dopamine-anchored tethered porphyrin, which can trigger the porphyrin-receptor for cell uptake.[15,16]
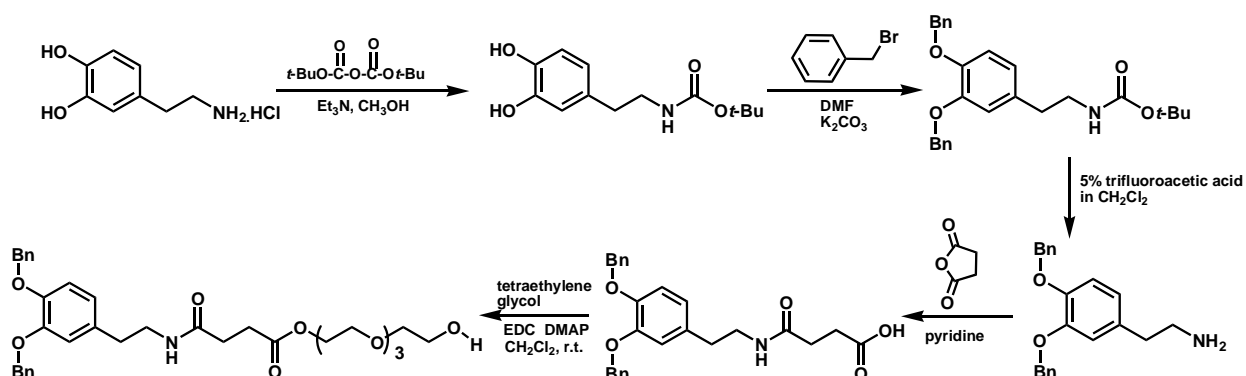
Figure 2.13: Synthesis of tetraethylene glycol linked dopamine ligand

74
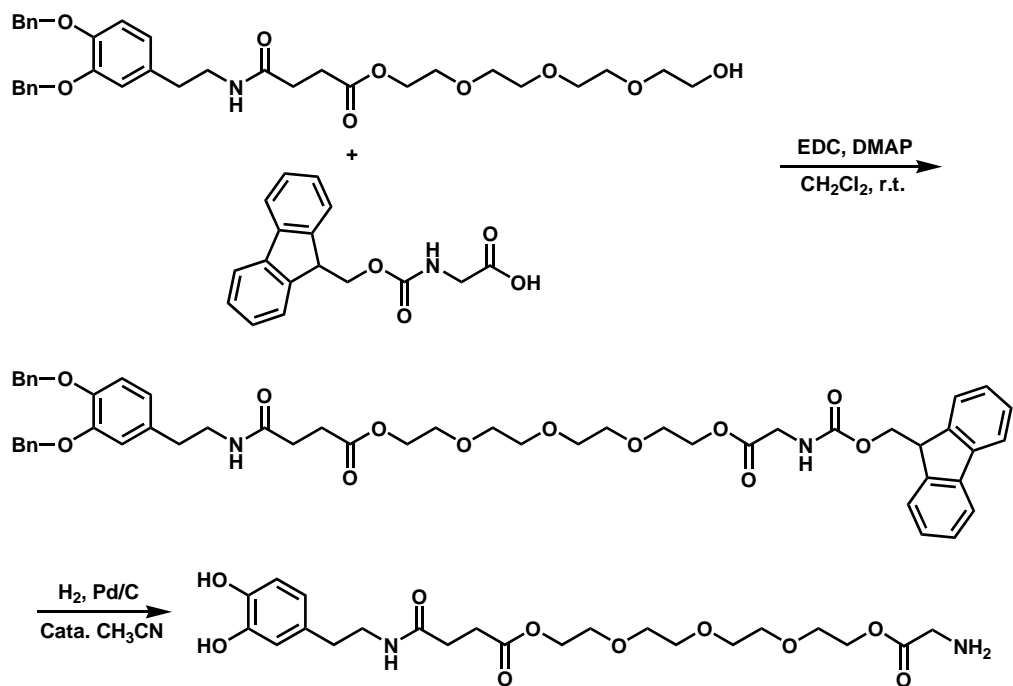
Figure 2.14: Synthesis of glycine tipped dopamine-tetraethylene glycol ligand
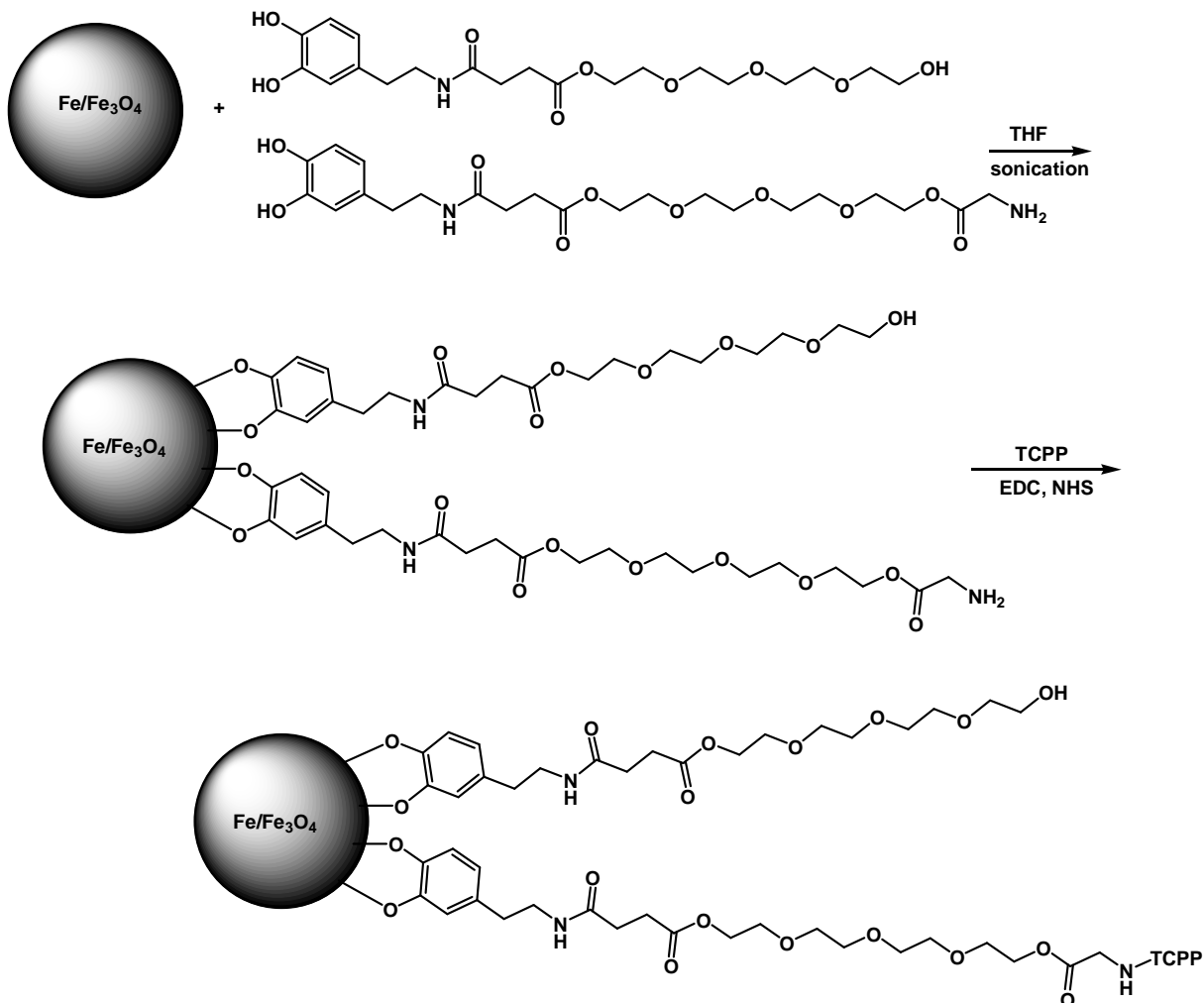
Figure 2.15: Binding of the final ligand to Fe/Fe$_3$O$_4$ nanoparticles

2.2.5 Specific Absorption Rate of Fe/Fe$_3$O$_4$ Nanoparticles

The SAR value is an important factor to be considered when using Fe/Fe$_3$O$_4$ nanoparticles for hyperthermia treatment. SAR is determined by SAR=C*ΔT/Δ t, where C is the specific heat capacity of the sample and T and t are the temperature and time, respectively. The temperature change of the samples were measured using the apparatus designed in Dr. Viktor Chikan's laboratory at the Department of Chemistry at Kansas State University.

The hyperthermia apparatus used here has a "heavy duty" induction heater converted to allow measurement of the temperature change of a sample. In the setup, a remote fiber optic probe (Neoptix) is used to monitor the temperature change. The frequency is fixed (366 kHz, sine wave pattern); field amplitude is 5 kA/m. The coil diameter is 1 inch, and was continuously water cooled. The change in the temperature was detected using the remote IR probe. The solubility of the nanoparticles was determined using ICP measurements. The diameters of the particles were obtained using TEM images.

Table 2.1: Calculation of SAR values for different Fe/Fe_3O_4 nanoparticles

Fe/Fe_3O_4 product	$\Delta T_{max}(^oC)$	Fe(0) core size (nm)	Diameter of the inorganic NP (nm)	Solubility in H_2O (mg/mL)	SAR (W/g (Fe))
#1 Fe/Fe_3O_4	18	2.1 ± 0.4	5.5 ± 0.8	0.015	24.5
#2 Fe/Fe_3O_4	25	4.1 ± 1.3	6.2 ± 1.4	0.16	47.6
#3 Fe/Fe_3O_4	23	5.3 ± 1.2	7.0 ± 2.2	0.11	46.4
#4 Fe/Fe_3O_4	34	5.4 ± 1.1	7.2 ± 2.8	0.35	63.9
#5 Fe_2O_3	5	/	7.5 ± 2.9	0.38	5.2

Smaller particles are suited for treating various region of the body part for the hyperthermia treatment because the SAR curves for the smaller particles are adjustable and easily increased linearly by manipulating the power of AMF.

2.2.6 Study of the Cellular uptake of Magnetic Nanoparticles by B16-F10 Melanoma Cells and it's Cytotoxicity

All the cell experiments were carried out in Dr. Deryl L Troyer's laboratory at the Department of Anatomy and Physiology at Kansas State University. B16-F10 melanoma cells were purchased from ATCC (Manassas, VA) and maintained in DMEM (Dulbecco's Modified Eagle Medium) supplemented with 10% fetal bovine serum (FBS) and 1% penicillin-streptomycin in a humidified 37 ºC incubator at 5% CO_2.

The toxicity of magnetic nanoparticles was tested based on iron concentration in MNPs. Media containing various iron concentrations of MNPs (5,10, 15, 20, and 25 µg/mL iron) were added to B16-F10 cells and incubated overnight. After incubation, the medium was removed, and the cells were washed twice with DMEM. After collection by trypsinization, cells were counted via hemocytometer with Trypan blue staining. This method also allows counting of non-viable cells, since only they allow the blue stain into the cell. All experiments were run in triplicate. The toxic effect of these MNPs increased with increasing iron concentration.

The loading efficiency of MNPs into B16-F10 cells was assessed using Perl's Prussian Blue stain kit (Polysciences, Inc., Warrington, PA). After overnight incubation in B16-F10 cells medium containing 25.0 µg/mL iron in MNPs, Prussian blue staining was used for demonstrating the presence of ferric ions in tissue sections, we have used same protocol for magnetic nanoparticles testing. After 6 h the cells, which were replated (6 h is the time required for the cells to attach to the plate surface) were fixed with 4% glutaraldehyde and incubated for 0.5 h. Then 4% potassium ferrocyanide in 4% HCl was added. The assay was then incubated for 0.5 h. Potassium ferrocyanide reacts with ferric ions in the presence of HCl and forms a blue colored complex (Prussian Blue). From the images obtained the blue stained spots corresponding to loaded nanoparticles were clearly visible. The loading of the nanoparticles into the B16-F10

cells was improved, when they are modified with porphyrins. After studying the effect of the nanoparticles on B16-F10 cells the experiments were further extended to study the suitability of the modified Fe/Fe_3O_4 nanoparticles for hyperthermia treatments.
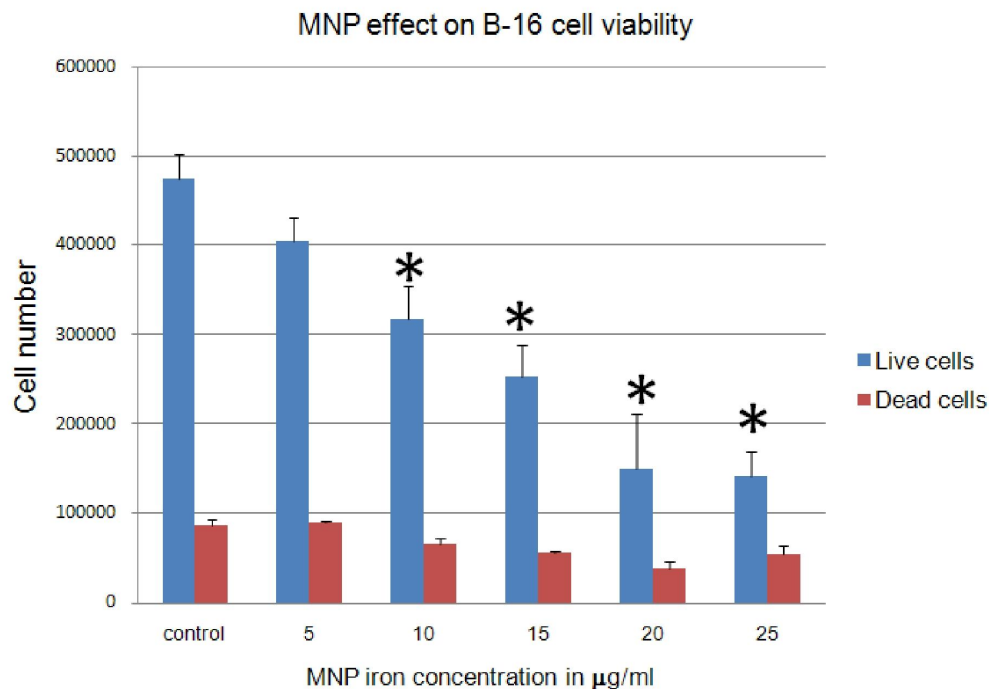
Figure 2.16: In vitro cell viability of B16-F10's cultured in medium containing increasing concentrations of MNPs, as measured by iron concentration. *Statistically significant (p-value less than 0.05;two tail ANOVA)
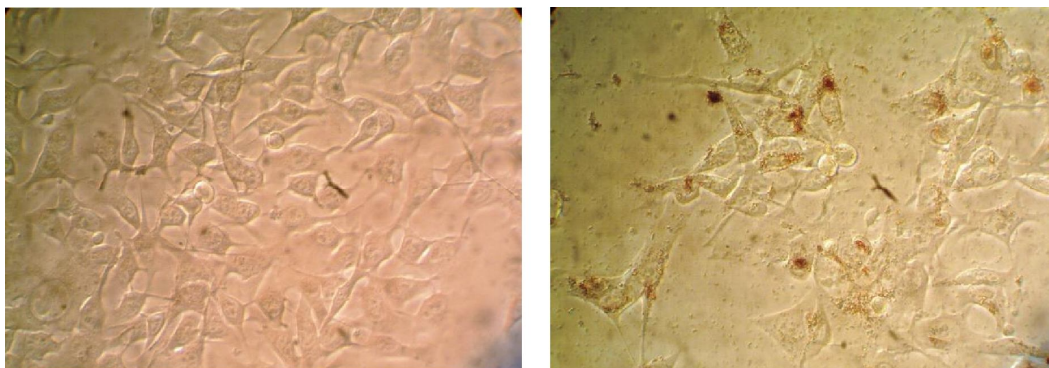
Figure 2.17: B16-F10 cells after overnight incubation with TCPP labeled MNP; A: control B16-F10 cells (without MNP); B: B16-F10 cells incubated with MNP; C:MNP-incubated B16-F10 cells after Prussian blue staining (MNP are blue in color)

2.2.7 The Effect of Hyperthermia on Subcutaneously Melanoma

All the mice experiments were carried out in Dr. Deryl L Troyer's laboratory at the Department of Anatomy and Physiology at Kansas State University. 6-8 week old mice female C57/BL6 mice were purchased from Charles River Laboratories (Wilmington, MA). Mice were maintained according to approved institutional IACUC guidelines in the Comparative Medicine Group Facility of Kansas State University. All animal experiments were conducted according to these IACUC guidelines. Ten mice were transplanted subcutaneously into each rear limb above the stifle with 1×10^6 B16-F10 melanoma cells suspended in 50.0 μL PBS. 120.0 μL of saline were injected into melanomas on the left leg of all mice and 120.0 μl MNPs containing 1.0 mg Fe/mL were injected into right leg tumors of all mice in three injections on days 4, 5, 6 (total of 360.0 μg iron). Both left (saline) and right (MNPs) leg tumors of five of the mice were exposed to AMF for 10 min soon after the MNP injections. Tumors on the remaining five mice were not exposed to AMF. Based on this, there were 4 groups which tested the effects of MNPs with and without AMF and of AMF alone: Group 1, Intratumoral saline injection, not exposed to AMF (left legs of first five mice); Group 2, Intratumoral injection of saline, exposed to AMF (left legs of remaining five mice); Group 3, Intratumoral injection of MNPs, not exposed to AMF (right

legs of first five mice); Group 4, Intratumoral injection of MNP, exposed to AMF (right legs of remaining five mice). After three AMF exposures, tumor sizes were measured every day with a caliper on days 8 to 14, and tumor volume was calculated using the formula $0.5axb^2$ (a=longest diameter; b=smaller diameter). After 14 days mice were euthanized, tumors were excised, and tumor weights were measured. The tumor weights are summarized in table 2.2.

Table 2.2: The change of tumor volume (mm^3) with number of days of treatment

		day-8	day-9	day-10	day-11	day12	day13	day14
control	Left leg	31.85	66.04	93.52	151.79	208.71	254.57	355.19
	right leg	16.54	26.99	31.2	74.34	109.69	172.7	172.2
experimental	left leg	42.9	58.04	58.14	128.78	181.35	206.5	360.4
	right leg	1.97	9.29	12.24	25.81	59.76	45.5	84.51
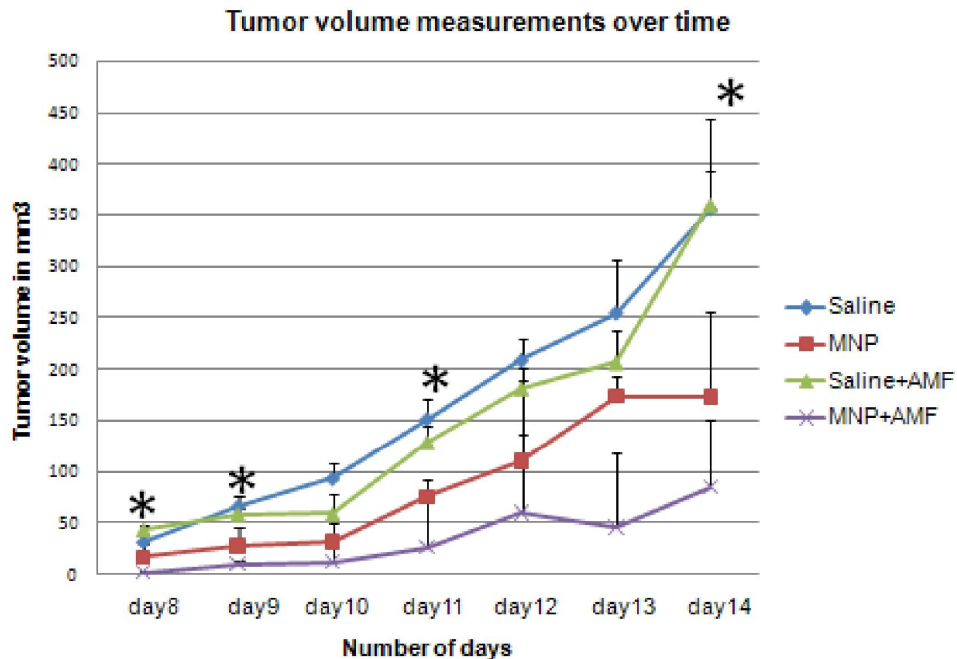
Figure 2.18: The effect of AMF treatments on tumor volumes over time. *Statistically significant (p-value less than 0.1)

The tumor volume was measured after exposure to AMF starting from day 8 to day 14. There was a decrease in the tumor volume in both mice groups that were exposed to AMF. This effect could be due to the reason that the magnetic nanoparticles are modified with porphyrin ligand which is a well known photosensitizer. Porphyrin upon absorption of light can act as phototherapeutic agents forming reactive oxygen species, which can be harmful to cells. Since the mice were exposed to light during the experimental time period this cytotoxicity observed in the mice treated with only the nanoparticles can be explained as a result of porphyrin activity.[42] During the experiment the direct temperature raise of the tumor was not measured. The insertion of the fiber optic probe into the tumor will damage the tumor tissues thus leading to infection and leakage of the gelatinous tissues in the tumor. The result would be a significant change in the tumor volume.

The increase in the temperature at the site of injection was measured while exposing the nanoparticle injected site to AMF. For all *in vivo* experiments, the mice were placed into the induction coil using a specially designed teflon supporter so that tumors were located exactly in the region of the AMF possessing the highest field density. There was a temperature increase of 11 °C, with an exposure time of 10 min. One end of the probe was inserted in to the tumor site and the other end was inserted to the leg which was not injected with nanoparticles. The temperature difference between the two sites were recorded over time.
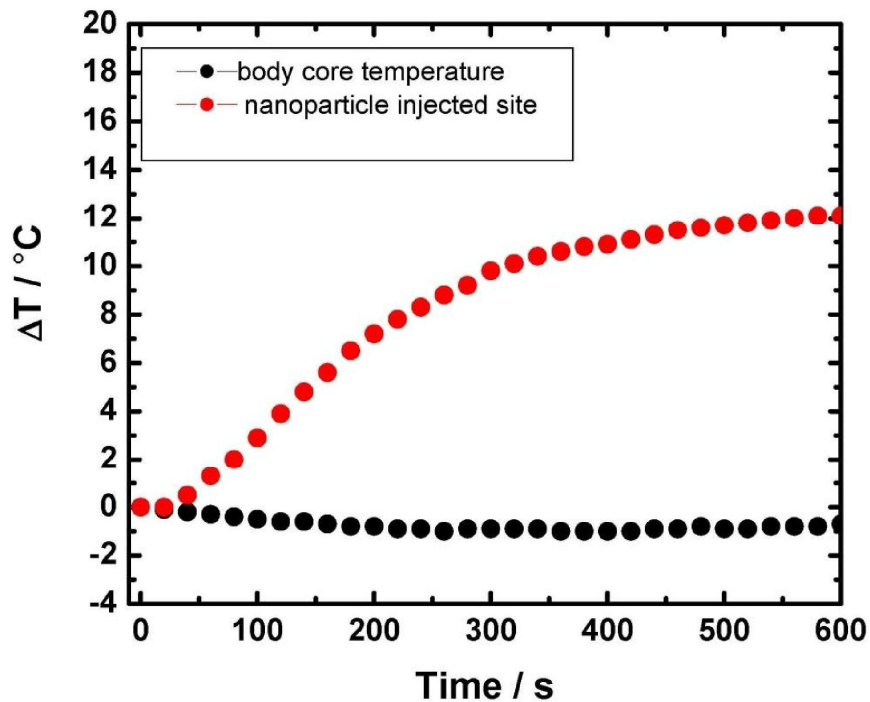
Figure 2.19: The study of the temperature change at MNP injection site and in body core during AMF exposure, measured with a fiber optic temperature probe

2.2.8 Intravenous Administration(IV) of MNPs with AMF Exposure

On day 0, 3.5×10^5 B16-F10 melanoma cells were injected subcutaneously into the right legs of 27 mice. Mice were randomly divided into three groups: Group 1, IV MNPs, no AMF; Group II, IV MNPs, AMF; Group III, DMEM control, no AMF. On days 6, 9, and 11 after tumor cell transplant, MNPs corresponding to 226 μg of iron were injected intravenously into each mouse in groups I and II. On the same day, DMEM was injected intravenously into group III. For group II, tumors were exposed to AMF for 10 min one day after each injection (total of three AMF treatments). Tumor sizes were measured using a caliper on days 14 and 18, and tumor volume was calculated as described above. On day 18 all mice were euthanized, tumors were excised, and tumor weights were measured.
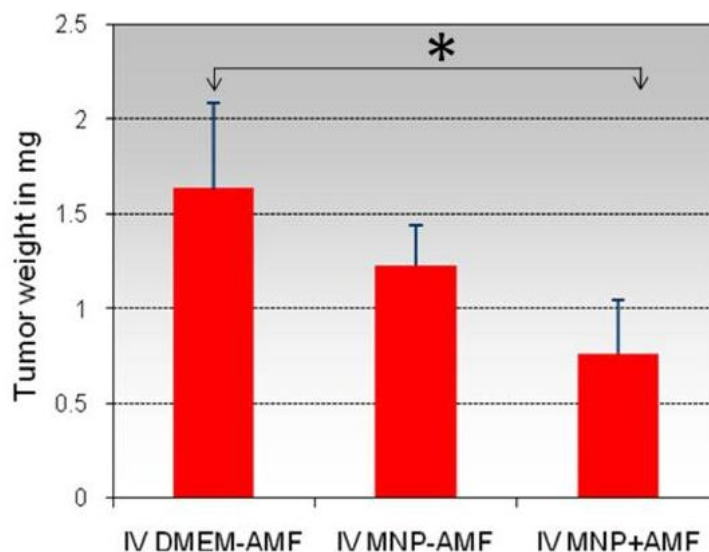
Figure 2.20: Effect of intravenous injection of MNP and AMF on tumor weight. *Statistically significant (p-value less than 0.1) between control and IV MNP+AMF groups

There is a significant reduction in the tumor of the mice exposed to AMF treatments weight compared to the control group. This effect should be due to the hyperthermia effect of the magnetic nanoparticle in the tumors. The other important conclusion we could proposed based on this observation is that the porphyrin modified nanoparticles have been taken up by the cancerous tissues. The preferential affinity of the porphyrin group to cancerous cells can further be supported by this observation. Prussian blue staining of the tumor sections were carried out after the tumors were harvested and sectioned. MNPs in tumor sections and other tissues, such as lungs and brains were identified as Prussian blue positive cells in tumor bearing mice intravenously injected with MNPs.
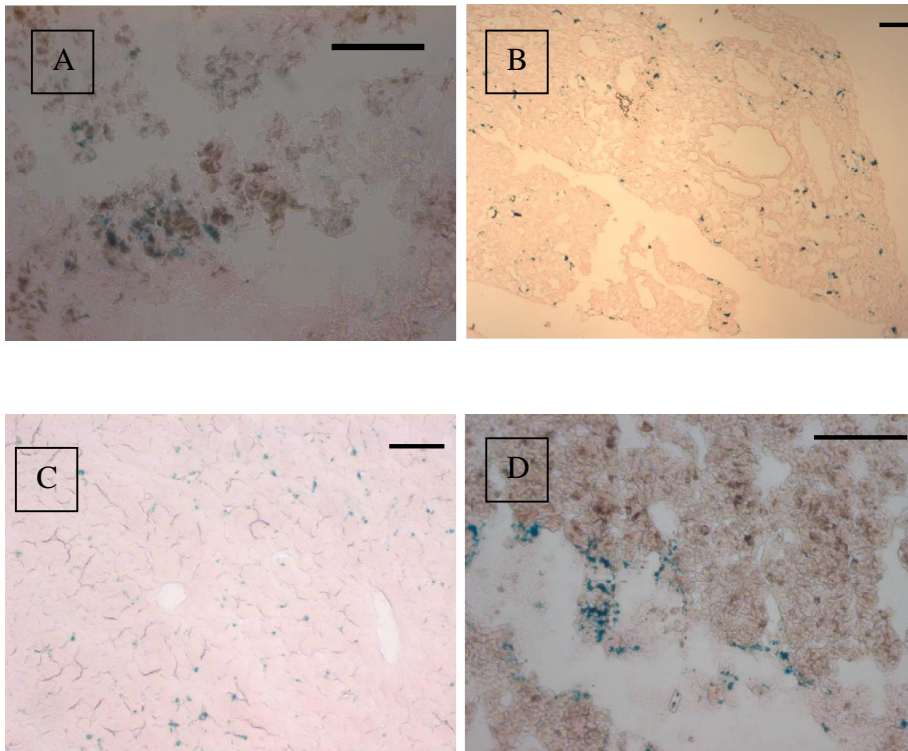
Figure 2.21: Prussian blue staining on tissue sections after the in vivo experiment. A-C: IV MNP + AMF in tumor, lung, and liver, respectively D: IT MNP+AMF tumor (Scale bar=100 µm)

The tumor sections were then subjected to apoptosis assay with the modified TUNEL assay. This method is used to detect DNA degradation in a cell during apoptosis. The apoptotic positive cells will show green fluorescence while other cells will be blue in color.

The TUNEL assay showed the most apoptotic positive cells were resulted in during the AMF treatment of mice injected with MNP intratumoraly, intermediate apoptosis levels in mice that received magnetic nanoparticles intravenously was observed. The fewest apoptotic cells were present in the control group that was injected with saline followed by AMF exposure.
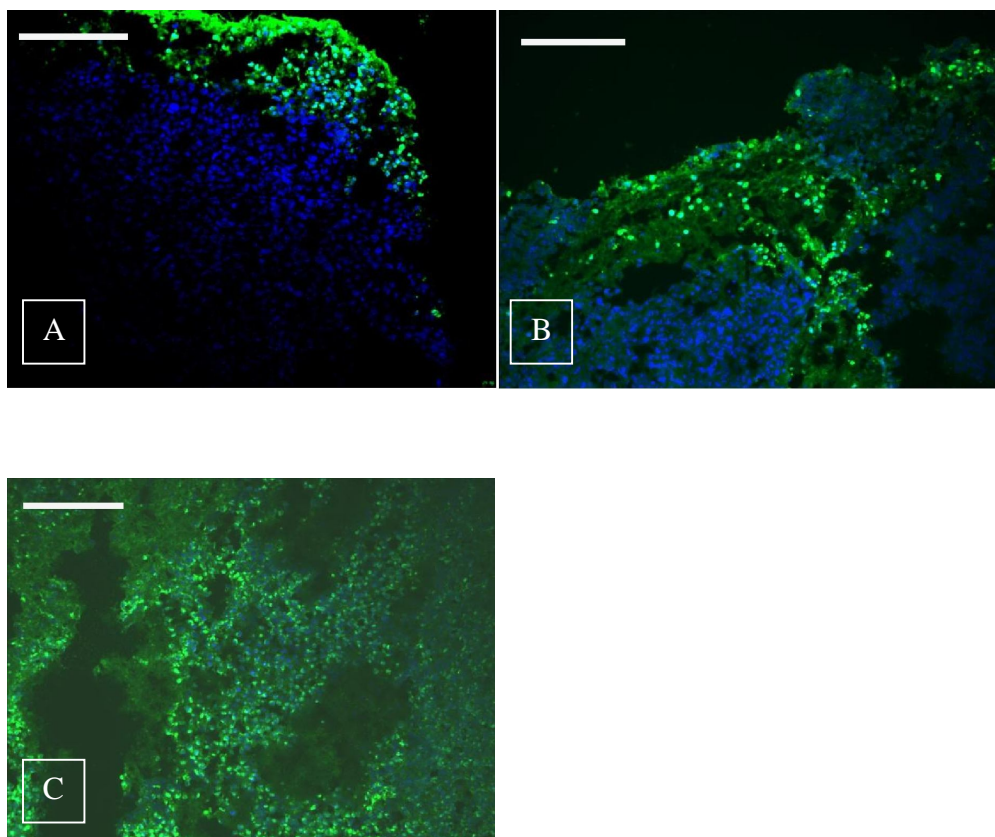
Figure 2.22: Green fluorescence indicates apoptosis positive and blue is DAPI counterstaining. A-C: Apoptosis assay pictures. A: Control tumor section. B: Tumor section with intravenous MNP administration followed by AMF. C: Tumor section with intratumoral MNP administration followed by AMF (Scale bar=100 µm)

2.3 Discussion

We have successfully synthesized Fe/Fe_3O_4 core shell nanoparticles with an organic stealth coating and tethered porphyrin (TCPP) units, which permit the multitargeting of the LDL-receptor (low density lipoprotein receptor) that is overexpressed in numerous cancer cell lines. The modification of the particles with a stealth layer of tetraethylenegylcol has given the biocompatibility and the solubility to the particles in physiological conditions. Dopamine in this case act as the anchoring ligand and allows further modification of the ligand. These nanoparticles are small enough (>10 nm) to be taken up by tumors from the bloodstream because

of the EPR effect (enhanced permeation and retention). The presence of magnetic nanoparticles in tumor tissues was observed with Prussian Blue staining of the tumor sections after the administration of the magnetic nanoparticles intravenously. This is evidence that they have reached the interstitium of the tumor, and the targeting ligands trigger their rapid uptake. Our cell experiments employing B16-F10 melanoma cells have indicated that the uptake is complete in less than 12 h. One of the advantages of this approach is that it permits receptor-mediated intake into cytoplasm avoiding partial enzymatic degradation during endocytosis. Another advantage of direct uptake is that it is a much faster process than endocytosis.

The direct injection of the nanoparticles was more effective than the intravenous injection. Nanoparticles were present in numerous tissues of the mice such as brain and lungs, followed by the intravenous injections. But after 6 days of injection all the mice were still alive. There were no fatalities of mice reported during the treatment period which indicates that significant accumulation of nanoparticles in tissues haven't had any prominent side effects on mice. Since the nanoparticles were less than 10 nm in diameter they will eventually be excreted from the body and no blocking of arteries was observed. During the hyperthermia experiments it was a challenge to maintain the body temperature of the mice. However the probe did allow us to measure the temperature difference between the area treated with AMF and the control body regions that was exposed to AMF. There was a significant increase in the temperature of the tumor tissues that were injected with magnetic nanoparticles intratumorally. Even though we found significant amount of iron in lungs and liver, there was no heat generated in these tissues during the treatment, since the AMF exposure was only limited to the tumor area. We collected tumors 24 h after the last AMF treatment on some of the mice to investigate potential mechanisms. We found that the apoptotic index was increased in the mice group where the

method of injection was intratumoral, indicating that the targeted magnetic hyperthermia had a measurable effect on cell viability 24 h after the last treatment. Hence, apoptosis appears to be a mechanism involved in reduced tumor volumes.

Once in the tumor, the Fe/Fe_3O_4 core shell nanoparticles heat up in the presence of an A/C-magnetic field (mostly likely according to Néel relaxation) and permit spatially resolved magnetic hyperthermia treatment of cancer. We have obtained experimental evidence from our mouse experiments that this approach is highly successful: we have achieved 87% tumor growth inhibition in Charles River mice that have been impregnated with B16-F10 melanomas. Interestingly there was a reduction in the tumor volume of the mice administrated with magnetic nanoparticles without AMF exposure. This could be due to two reasons. The elevated iron-levels in the tumor due to the biocorrosion of the Fe/Fe_3O_4 core shell nanoparticles could inhibit the tumor growth due to enhanced oxidative stress. It has been reported in literature that the metabolic activity and proliferation of cells can be inhibited after internalizing magnetic nanoparticles.[43] The other factor that contributed for this cytotoxicity could be the presence of porphyrin units on the nanoparticles which can act as photosensitizers producing toxic oxygen species with exposure to light.[42] Since we are achieving target specific delivery of the nanoparticles using porphyrin the side effects to normal cells due to these two factors can be minimized.

2.4 Conclusions

In conclusion, we have shown that we were able to design a working nanoparticle system for the targeting and A/C-magnetic hyperthermia treatment of cancer. The presence of porphyrin permits cancer diagnostics and the biocorrosion leads to additional therapeutic effects. The system is suitable for local hyperthermia treatments since the site specific delivery of the

particles can be achieved using porphyrin and the AMF exposure can be limited to the tumor region preventing unwanted hyperthermia. The cellular uptake experiments carried out using B16-F10 melanoma cells were successful and the mechanism of cell death at the tumor site was apoptosis as indicated by the TUNEL assay. Overall the system we developed using bimagnetic iron/iron oxide nanoparticle was indeed gave us promising results to be used in local hyperthermia treatments. The nanoparticle ligand system is still under investigation for modification that could further enhance the selectivity and heating ability with fewer side effects.

2.5 Experimental

All chemicals were obtained from Acros Organics and Sigma Aldrich, unless noted otherwise. The instrumentation used were 400 MHz and 200 MHz Varian NMR-spectrometer, UV/Vis spectra: FT-UV Diodearray HP 6543, at the Department of Chemistry at Kansas State University, The mass spectra were obtained from Applied Biosystems API-4000 triple quadrupole mass spectrometer with electrospray and APCI sources at Department of Biology at Kansas State University.

2.5.1 Synthesis of Porphyrin (TCPP)
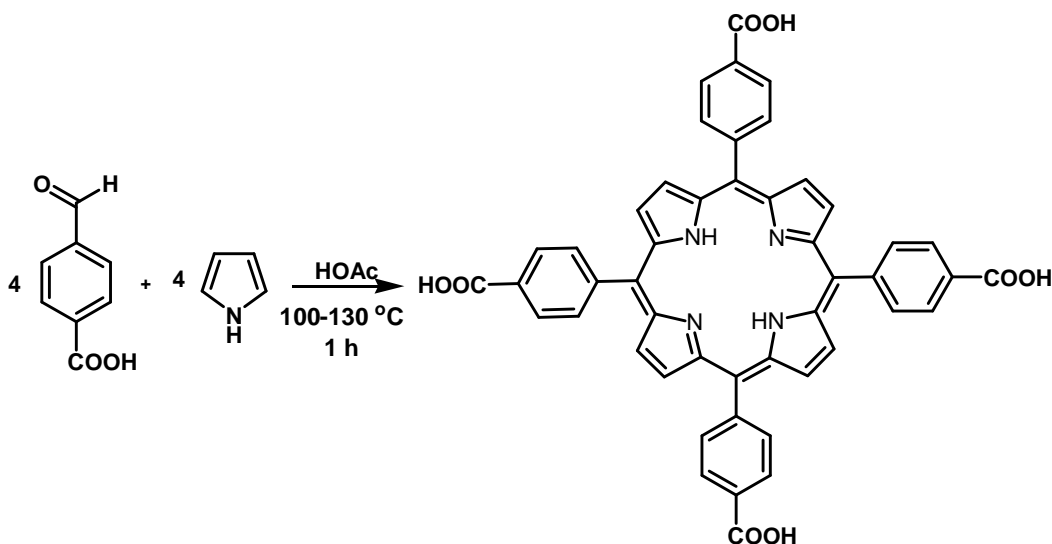
       1.50 g 4-carboxybenzaldehyde was dissolved in 80.0 mL acetic acid. The solution was warmed to 100 ^{o}C and a solution of 0.67 g pyrrole in 10.0 mL acetic acid was added dropwise in 20 min. Upon completion of addition, the solution was warmed up to 130 ^{o}C slowly and kept at 130 ^{o}C for 1 h. The mixture was cooled to 80 ^{o}C and 100.0 mL 95% ethanol was added and the temperature was lowered to room temperature while stirring in 3 h. Then the mixture was kept in at -15 ^{o}C for 24 h. Purple solid was collected by vacuum filtration. The filter cake was washed with cold 50/50 ethanol/acetic acid (3×5mL) and dried under high vacuum (oil pump) overnight. 0.51 g pure product was obtained (25.5% yield). ^{1}H NMR (DMSO-d_6) δ: -2.94 (s, 2H); 8.35 (d, 8H); 8.39 (d, 8H); 8.86 (s, 8H); 13.31 (s, 4H). ^{13}C NMR (DMSO-$d6$) δ: 119.31; 127.90; 130.51; 134.44; 145.42; 167.46. MS-ESI^{+}: m/z 791.2. Molecular weight calculated for 790.2.

2.5.2 Boc-protection of Dopamine
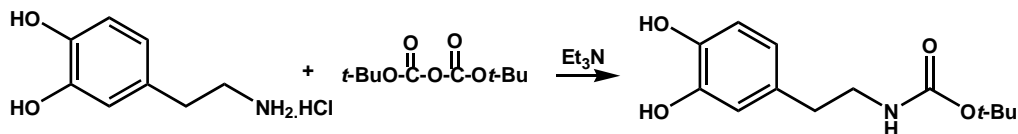
A solution of dopamine (310 mg, 1.63 mmol) in methanol (8.0 mL) was stirred under N_2 for 5 min. Triethanolamine (TEA) (1.8 mmol) was added followed by Boc-anhydride (393 mg, 1.8 mmol). The mixture was stirred under N_2 for 12 h and the solvent was removed under reduced pressure. The remaining residue was dissolved in 40.0 mL methylenechloride (CH_2Cl_2) and washed with 1 N HCl (3×5.0 mL) and brine (5.0 mL). The organic layer was dried over anhydrous Na_2SO_4. After filtration, the organic phase was kept at -5 °C for 3 h. The product was collected as a white precipitate by filtration. Overall yield is 85%. ^{1}H NMR (DMSO-d_6) δ: 1.73 (s, 9H); 2.48 (t, 2H); 3.02 (q, 2H); 6.40 (d, 1H); 6.54 (s, 1H); 6.61 (d, 1H); 6.83 (t, 1H); 6.85 (s, 1H); 6.76 (s, 1H).

2.5.3 Benzyl-protection of Boc-dopamine
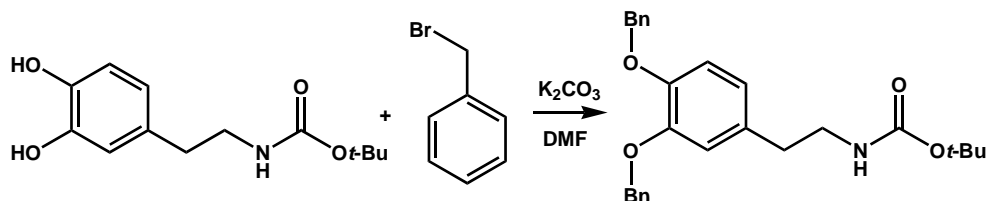
3.47 g Boc-protected dopamine was dissolved in 100.0 mL DMF. 12.6 g K_2CO_3 was added and the system was protected under N_2. 4.69 g (2 eq.) benzyl bromide was added drop wise. The mixture was stirred at room temperature for 24 h without light. The solid was removed by filtering through a short pad of celite and the filter-cake was washed with ether (3×100.0 mL). The combined filtrate and washing solution were washed with ice-water (3×50.0 mL) and brine (15.0 mL). The organic layer was dried over anhydrous Na_2SO_4 and concentrated to 150.0 mL. After setting at -5 °C for 5 h, white precipitate came out as product and was collected by vacuum filtration. (overall yield 90%). ^{1}H NMR (CDCl$_3$) δ: 1.45 (s, 9H); 2.70 (t, 2H); 3.31 (q, 2H); 4.49

(s, 1H); 5.15 (d, 4H); 6.71 (d, 1H); 6.80 (s, 1H); 6.88 (d, 1H); 7.32 (t, 2H); 7.37 (t, 4H); 7.45 (d, 4H).

2.5.4 Deprotection of Boc-group
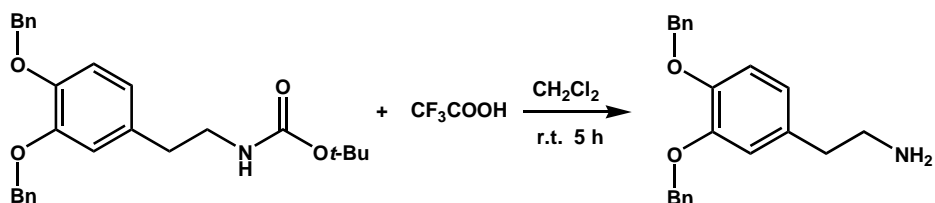
4.3 g Bn-Boc-dopamine was dissolved in 150.0 mL 5% TFA, CH$_2$Cl$_2$ solution and stirred at room temperature for 5 h. The solvent was removed under vacuum and clear oil was obtained as product. (100% yield). ^{1}H NMR (CDCl$_3$) δ: 2.79 (t, 2H); 3.08 (m, 2H); 5.11 (s, 4H); 6.68 (d, 1H); 6.75 (s, 1H); 6.90 (d, 1H); 7.32 (t, 2H); 7.35 (t, 4H); 7.42 (d, 4H). ^{13}C NMR (CDCl$_3$) δ: 32.90; 41.85; 71.50; 72.00; 115.60; 116.25; 122.30; 127.60; 127.85; 128.35; 128.45; 128.63; 128.85; 136.70; 136.85; 148.45; 149.00; 160.88; 161.20; 161.58; 161.90.

2.5.5 Amide Formation
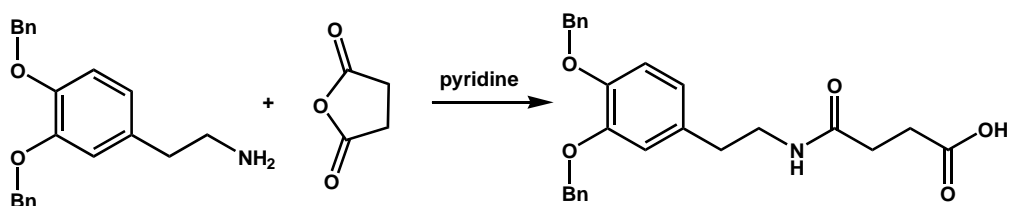
1.43 g Bn-dopamine and 0.43 g succinic anhydride (1/1 ratio) were dissolved in 6.0 mL pyridine. The solution was stirred at room temperature for 5 h. The solvent was removed by co-evaporation with toluene (toluene 5×5.0 ml). White solid was obtained and washed with CH$_2$Cl$_2$ for 3 times. After drying under vacuum, 1.4 g product was obtained. 75% yield. ^{1}H NMR (DMSO-d_6) δ: 2.29 (t, 2H); 2.42 (t, 2H); 2.60 (t, 2H); 3.21 (q, 2H); 5.09 (d, 4H); 6.71 (d, 1H); 6.94 (s, 1H); 6.96 (d, 1H); 7.32 (t, 2H); 7.38 (d, 4H); 7.45 (t, 4H); 7.90 (t, 1H); 12.08 (s, 1H). MS-ESI$^+$: m/z 434.2. Molecular weight calculated for 433.5.

2.5.6 Synthesis of Ligand A
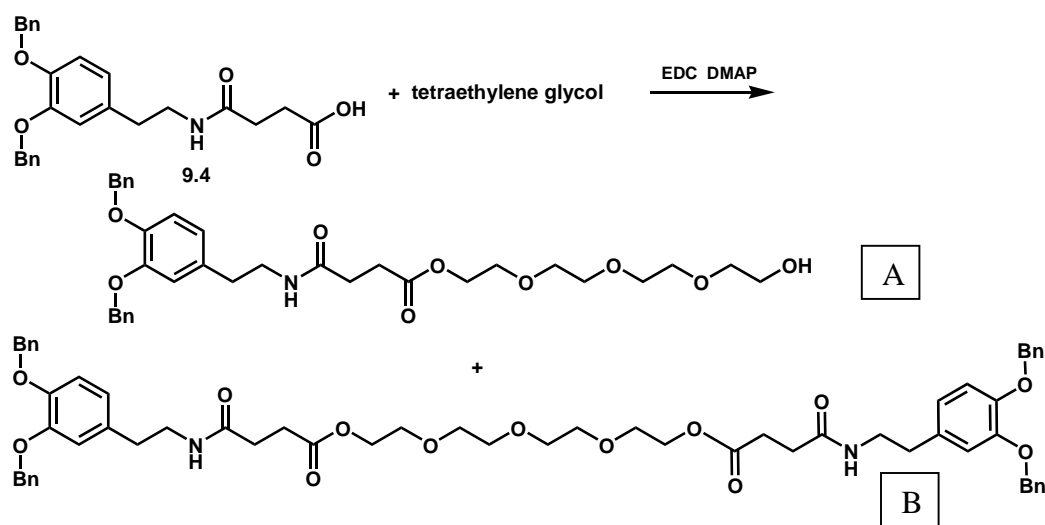
0.964 g dopamine-based carboxylic acid and 0.426 g EDC (1/1 ratio) were dissolved in 100.0 mL CH_2Cl_2 and stirred at room temperature for 10 min. 0.433 g tetraethylene glycol was added followed by 5.0 mg DMAP. After stirring for 12 h at room temperature, the organic phase was washed with 10% H_3PO_4 solution (3×10.0 mL), water (3×10.0 mL) and brine (10.0 mL). The organic phase was dried over anhydrous Mg_2SO_4. After removing the solvent under vacuum, the residue was loaded on column and eluted with 1/1 acetone/methylene chloride. 0.42 g ideal product (A) was obtained. (40% yield). 0.21 g side product (B) was isolated. ^1H NMR for A, (CDCl$_3$) δ: 2.39 (t, 2H); 2.57 (t, 1H); 2.70 (q, 4H); 3.44 (q, 2H); 3.60 (t, 2H); 3.65 (broad 12H); 4.24 (t, 2H); 5.15 (d, 4H); 5.74 (t, 1H); 6.71 (d, 1H); 6.81 (s, 1H); 6.89 (d, 1H); 7.31 (t, 2H); 7.37 (t, 4H); 7.46 (d, 4H). MS-ESI$^+$: m/z 610.4. Molecular weight calculated for 609.3. ^1H NMR for B, (CDCl$_3$) δ: 2.37 (t, 4H); 2.67 (m, 8H); 3.42 (q, 4H); 3.63 (s, 8H); 3.67 (t, 4H); 4.22 (t, 4H); 5.15 (d, 8H); 5.70 (t, 2H); 6.70 (d, 2H); 6.80 (s, 2H); 6.88 (d, 2H); 7.31 (t, 4H); 7.36 (t, 8H); 7.45 (d, 8H). MS-ESI$^+$: m/z 610.4. Molecular weight calculated for 609.3.

2.5.7 De-protection of Benzyl Groups to Produce Ligand
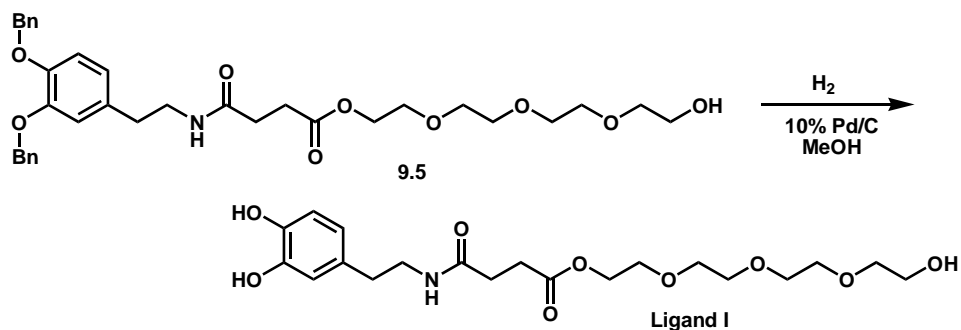
0.34 g Bn-dopamine-based tetraethylene glycol was dissolved in 50.0 mL methanol. 77.0 mg Pd/C was added under N_2. After evacuating three times, 1 atm. H_2 was applied and the mixture was stirred for 24 h at room temperature. The catalyst was removed by filtering through a short pad of celite. After removing solvent under vacuum, 0.23 g **ligand I** was obtained as product. (100% yield). ^{1}H NMR (DMSO-d_6) δ: 2.33 (t, 2H); 2.48 (q, 2H); 3.15 (broad multiplet, 4H); 3.41 (t, 2H); 3.49 (t, 2H); 3.51 (broad multiplet, 8H); 3.59 (t, 2H); 4.11 (t, 2H); 6.41 (d, 1H); 6.55 (s, 1H); 6.61 (d, 1H). MS-ESI$^+$: m/z 430.4. Molecular weight calculated for 429.4.

2.5.8 Synthesis of Glycine-tiped Ligand

94
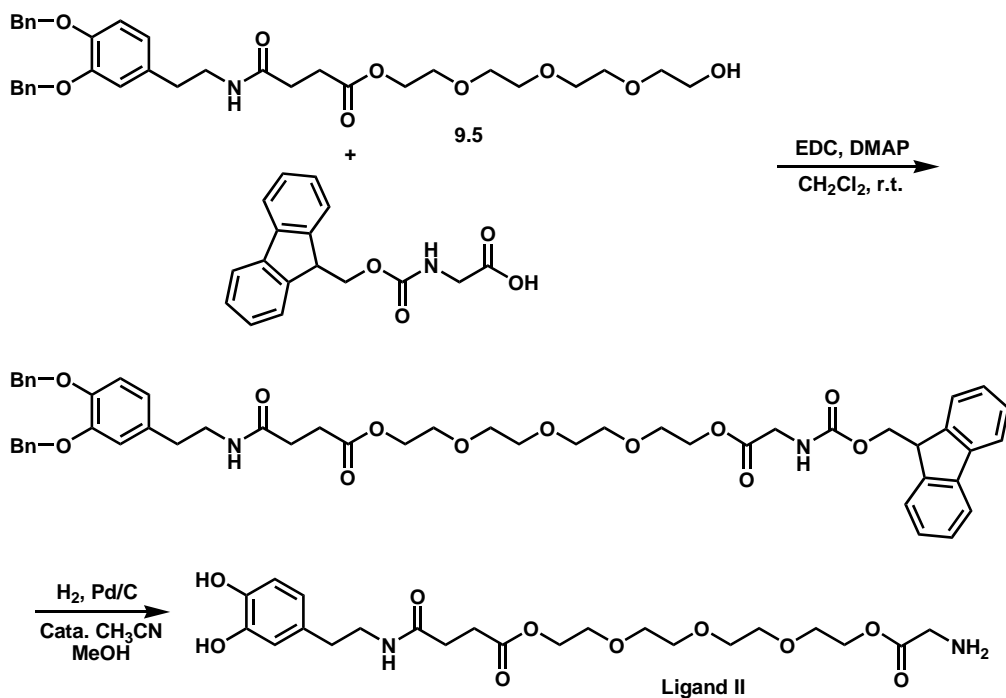
Bn-protected dopamine tetraethylene glycol was treated with 1 equv. of Fmoc-Glycine and 1.2 equiv. of EDC in the presence of catalytic amount of DMAP in methylene chloride. After stirring for 12 h at room temperature, the organic phase was washed with 10% H_3PO_4 solution (3×10.0 mL), water (3×10.0 mL) and brine (10.0 mL). The organic phase was dried over anhydrous Mg_2SO_4. After removing the solvent under vacuum, a white solid was obtained as pure product with 95% yield. The Bn and Fmoc groups were deprotected at the same time under the H_2-Pd/C condition in the presence of catalytic amount of CH_3CN. After removing the catalyst by filtration, solvent was removed under reduced pressure, clear oil together with some white solid formed. The white solid was removed by washing the mixture with hexane (3×5.0 mL), after concentration, **ligand II** was obtained as clear oil with 85% yield. ^{1}H NMR (DMSO-d_6) δ: 2.33 (t, 2H); 2.46 (q, 2H); 3.14 (q, 2H); 3.41 (t, 2H); 3.49 (t, 4H); 3.51 (broad multiplet, 8H); 3.59 (t, 2H); 4.10 (t, 2H); 4.57 (t, 2H); 6.43 (d, 1H); 6.55 (s, 1H); 6.61 (d, 1H); 7.90 (t, 1H); 8.62 (s, 1H); 8.73 (s, 1H). ^{13}C NMR (DMSO-d_6) δ: 28.95, 29.83, 34.73, 60.23, 63.32, 68.30, 69.79, 72.37, 115.48, 115.95, 119.21, 130.22, 143.53, 145.06, 170.44, 172.47.

2.5.9 Modification of Fe/Fe₃O₄ Nanoparticles with Dopamine-based Ligands I and II and Introducing of Porphyrin (TCPP)
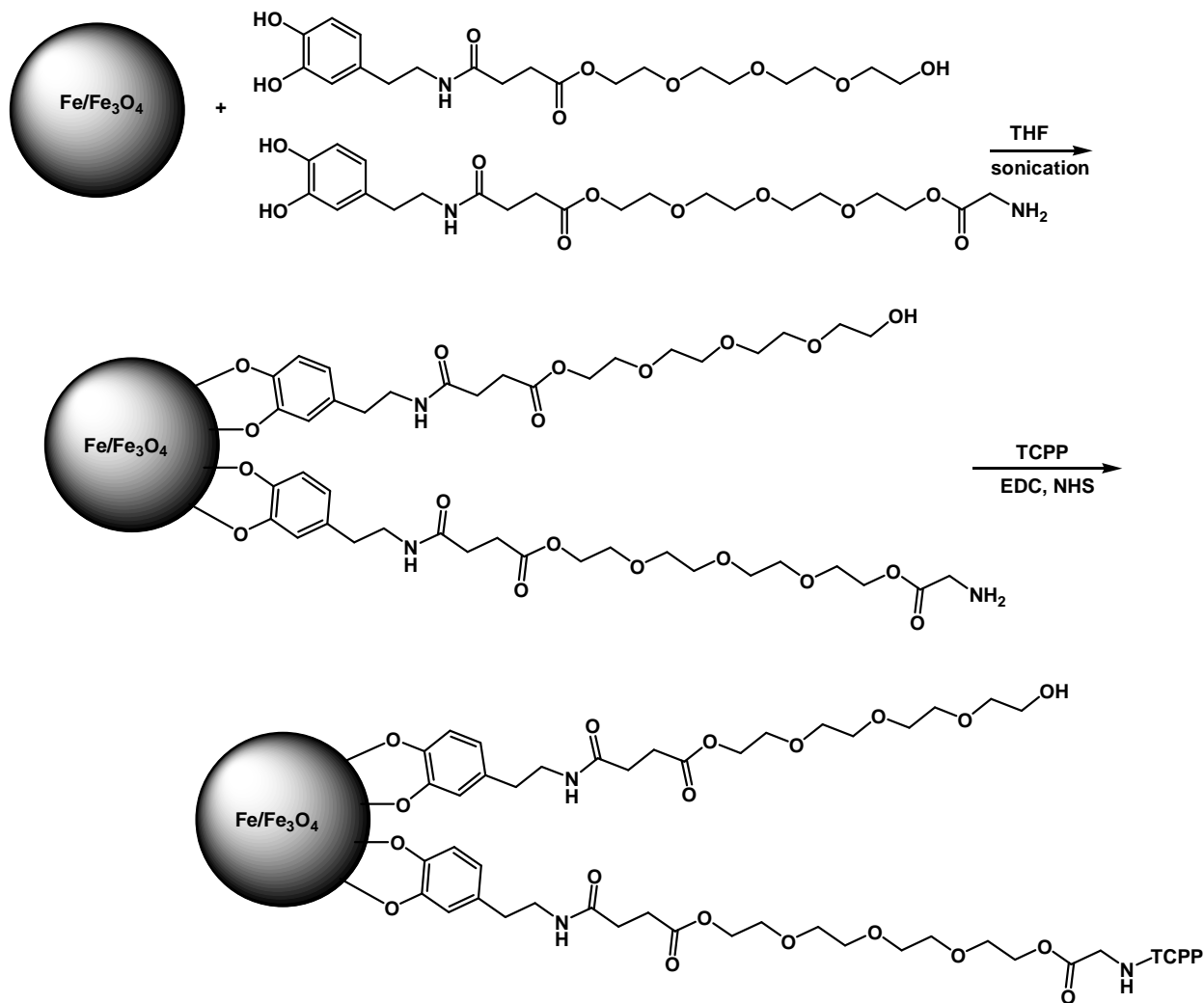
A typical example for preparing surface modified Fe/Fe₃O₄ nanoparticles featuring 5 TCPP per nanoparticle is described here. 50.0 mg dopamine-based **ligand I** and 3.0 mg dopamine-based **ligand II** (mole ratio 95/5) were dissolved in 10.0 mL THF, 20.0 mg Fe/Fe₃O₄ nanoparticles were added, after sonicating for 1h, the nanoparticles were collected by a magnet. The solid was washed with 3.0 mL portion of THF for 10 washing-magnetoprecipitation-re-dispersion cycles. The surface modified nanoparticles were dispersed in 10.0 mL of THF, 1.5 mg porphyrin (TCPP), 1.0 mg N-hydroxysuccinimide (NHS) and 2.0 mg EDC were added to the

suspension and sonicated for 1 h. The nanoparticles were collected by a strong magnet and further washed with 3.0 mL portion of THF. This was repeated for 10 washing-magnetoprecipitation-re-dispersion cycles. The solid was dried under vacuum. 17.6 mg nanoparticles were obtained.

2.5.10 Transmission Electron Microscopy

The sizes of nanoparticles were determined using TEM images. (Philips C-200 TEM instrument operating at 100 kV) 1-2 mg of Fe/Fe_3O_4 core shell nanoparticles were dissolved in anhydrous THF 5.0 mL and one drop of the resulting solution was spread over a copper grid (300 mesh size) forming a thin film of particles. The samples were kept under liquid nitrogen atmosphere during the experiments to avoid the damage from the electron beam.

2.5.11 Determination of the Iron Content in Magnetic Nanoparticles

Inductively coupled plasma atomic emission spectroscopy (ICP-AES). The amount of Fe^{2+} in the nanoparticles sample was estimated to be 23.03 ppm.
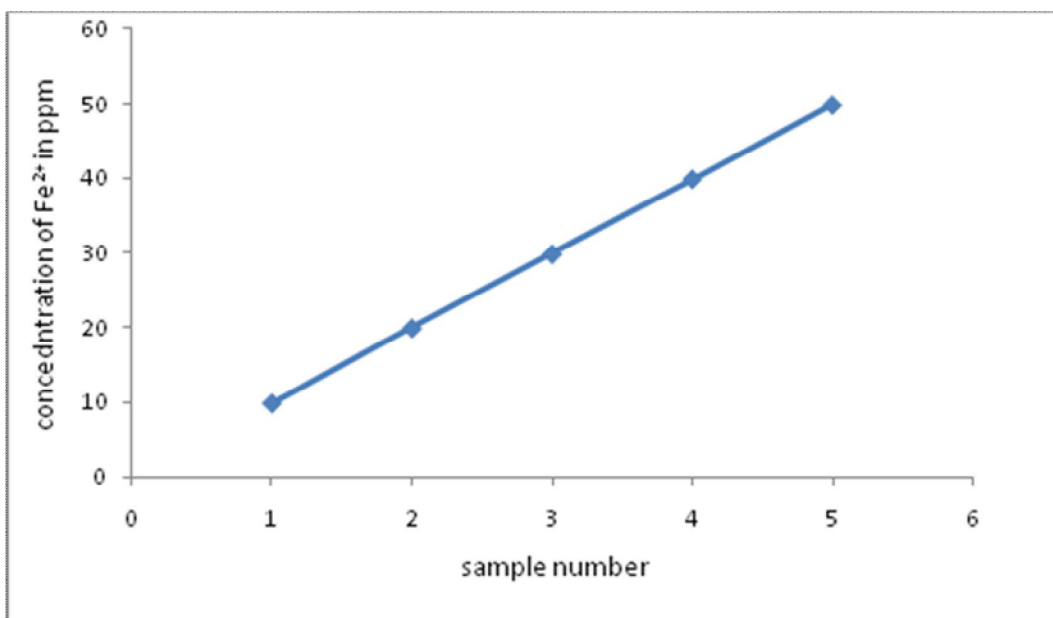
2.5.12 Ferrozine Based UV/Vis-Spectrophotometric Assay

A standard curve was prepared using 0, 0.1, 0.2, 0.5, 1, 2, 5 µg/mL ferrous ammonium sulfate samples. Water with all other reagents is used as blank. The optical density of the nanoparticles were measured and the actual concentration was calculated using the calibration curve.
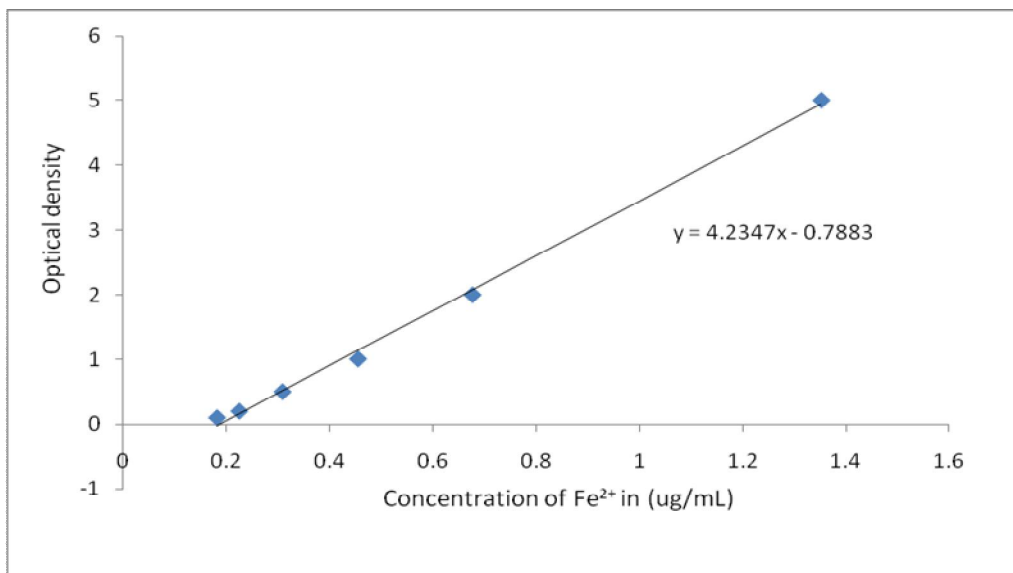
2.5.13 Prussian Blue Staining on B16-F10 Cells

The loading efficiency of MNPs into B16-F10 cells was assessed using Perl's Prussian Blue stain kit (Polysciences, Inc., Warrington, PA). After overnight incubation in B16-F10 cells medium containing 25 µg/mL iron in MNPs, cells were washed twice with DMEM and PBS and fixed with 4% glutaraldehyde for 10 min. Fixed B16-F10 cells were incubated in 4% potassium ferrocyanide and 4% HCl for 20 min. After 20 min incubation, cells were washed twice with 1x PBS and counterstained with nuclear fast red solution for 30 min. Images were captured using a Zeiss Axiovert 40 CFL microscope (New York) and a Jenoptik ProgRes C3 camera.

References

1. Mornet, S.; Vasseur, S.; Grasset, F.; Veverka, P.; Goglio, G.; Demourgues, A.; Portier, J.; Pollert,E.; Duguet, E., Magnetic Nanoparticle Design for Medical Applications, *progress in solid state Chemistry*, **2006**, *34*, 237-247

2. Rai, J.; Dragulescu-Andrasi , A.; Yao, H., Fluorescence Imaging *in vivo*: Recent Advances, *current opinion in Biotechnology*, **2007**, *18(1)*, 17-25

3. Osaka, T.; Matsunaga,T., Nakanishi, T.; Arakaki, A.; Niwa, D., Iida, H., Synthesis of Magnetic Nanoparticles and Their Application to Bioassays, *Analytical and Bioanalytical Chemistry*, **2006**, *384(3)*, 593-600

4. Ito, A.; Shinkai, M.; Honda, H.; Kobayashi, T., Medical Application of Functionalized Magnetic Nanoparticles, *Journal of Bioscience and Bioengineering*, **2005**, *100(1)*, 1-11

5. Pankhurst , Q. A.; Connolly, J.; Jones, S. K.; Dobson, J., Applications of Magnetic Nanoparticles in Biomedicine, *J. Phys. D: Appl. Phys.*, **2003**, *36*, 167-181

6. Gupta A.K.; Wells S, Surface-modified Superparamagnetic Nanoparticles for Drug Delivery: Preparation, Characterization, and Cytotoxicity Studies, *IEEE Trans Nanobioscience*, **2004**, *3(1)*, 66-73

7. Huber D.L., Synthesis, Properties, and Applications of Iron Nanoparticles, *Small*, **2005**, *1(5)*, 482-501

8. Schluep, T.; Hwang, J.; Hildebrandt, I. J., Czernin, J.; Chung Hang J. C.; Alabi, Christopher A.; Mack, B. C.; Davis, M. E., Pharmacokinetics and Tumor Dynamics of the Nanoparticle IT-101 from PET Imaging and Tumor Histological Measurements, *Proc Natl Acad Sci U S A*, **2009**, *106(27)*, 11394–11399

9. Allen, T. M.; Cullis, P. R., Drug Delivery Systems: Entering the Mainstream, *Science*, **2004**, *303*, 818 - 1822

10. Cho, K.; Wang, X.; Nie, S.; Chen, Z. G.; Shin, D. M., Therapeutic Nanoparticles for Drug Delivery in Cancer, *Clinical Cancer Research*, **2008**, *14*, 1310-1316

11. Yang, R.; Kolb, E. A.; Qin, J.; Chou, A.; Sowers, R.; Hoang, B.; Healey, J. H.; Huvos, A. G.; Meyers, P. A.; Gorlick, R., The Folate Receptor α is Frequently Overexpressed in Osteosarcoma Samples and Plays a Role in the Uptake of the Physiologic Substrate 5-Methyltetrahydrofolate, *Clinical Cancer Research*, **2007**, *13*, 2557-2567

12. Zhang, Y.; Kohler, N.; Zhang, M., Surface Modification of Superparamagnetic Magnetite Nanoparticles and Their Intracellular Uptake, *Biomaterials*, **2002**, *23(7)*, 1553-1561

13. Steinhauser I.; Spänkuch, B.; Strebhardt, K.; Langer, K., Trastuzumab-modified Nanoparticles: Optimisation of Preparation and Uptake in Cancer Cells, *Biomaterials*, **2006**, *27(28)*, 4975-4983

14. Brust, M.; Walker, M.; Bethell, D.; Schiffrin, D. J.; Whyman, R., Synthesis of Thiol-Derivatised Gold Nanoparticles in a Two-phase Liquid–liquid System, *J. Chem. Soc., Chem. Commun.*, **1994**, 801-802

15. Xu, C.; Xu, K.; Gu, H.; Zheng, R.; Liu, H.; Zhang, X.; Guo, Z.; Xu, B., Dopamine as A Robust Anchor to Immobilize Functional Molecules on the Iron Oxide Shell of Magnetic Nanoparticles, *J. Am. Chem. Soc.*, **2004**, *126 (32)*, 9938–9939

16. Shultz, M. D.; Reveles, J. U.; Khanna, S. N.; Carpenter, E. E., Reactive Nature of Dopamine as a Surface Functionalization Agent in Iron Oxide Nanoparticle, *J. Am. Chem. Soc.*, **2007**, *129 (9)*, 2482–2487

17. Cao, H.; He, J.; Deng, L.; Gao, X., Fabrication of Cyclodextrin-Functionalized Superparamagnetic Fe_3O_4/amino-silane Core–shell Nanoparticles via Layer-by-layer Method, *Applied surface science*, **2009**, *255(18)*, 7974-7980

18. Bonder, M.J.; Zhang, Kiick, Y. K.L.; Papaefthymiou, V.; Hadjipanayis, G.C., Controlling Synthesis of Fe Nanoparticles with Polyethylene glycol, *Journal of magnetism and magnetic materials*, **2007**, *311(2)*, 658-664

19. Shan, L.; Polyethylene glycol–coated and Folic Acid–conjugated Superparamagnetic Iron oxide Nanoparticles, Molecular Imaging and Contrast Agent Database, 1-5

20. Parshetti, G. K.; Doong, R., Dechlorination of Trichloroethylene by Ni/Fe Nanoparticles Immobilized in PEG/PVDF and PEG/nylon 66 Membranes, *Water research*, **2009**, *43(12)*, 3086-3094

21. Leamon, C. P.; Cooper, S. R.; Hardee, G. E., Folate-liposome-mediated Antisense Oligodeoxynucleotide Targeting to Cancer Cells: Evaluation *in vitro* and *in vivo*, *Bioconjugate Chem.*, **2003**, *14 (4)*, 738–747

22. Ndungu, J. M.; Lu, Y. J.; Zhu, S.; Yang, C.; Wang, X.; Chen, G.; Shin, D. M.; Snyder, J. P.; Shoji, M.; Sun, A., Targeted Delivery of Paclitaxel to Tumor Cells: Synthesis and *in vitro* Evaluation, *J. Med. Chem.*, **2010**, *53(8)*, 3127–3132

23. Hill, R. H., Effects of Polyhalogenated Aromatic Compounds on Porphyrin Metabolism, *Environmental health perspectives*, **1985**, *60*, 139-143,

24. Maziere, J.C.; Santus, R.; Morliere, P.; Reyftmann, J.P.; Candide, C.; Mora, L.; Salmon, S.; Maziere, C.; Gatt, S.; Dubertret, L., Cellular Uptake and Photosensitizing Properties of Anticancer Porphyrins in Cell Membranes and Low and High Density Lipoproteins, *Journal of Photochemistry and Photobiology B: Biology*, **1990**, *6(1)*, 61-68

25. Lukšienė, Ž., Photodynamic Therapy: Mechanism of Action and Ways to Improve the Efficiency of Treatment, *MEDICINA*, **2003**, *39(12)*, 1137-1150

26. Davis, M. E.; Davis, Chen, Z.; Shin, D. M., Nanoparticle Therapeutics: an Emerging Treatment Modality for Cancer, *Nature Reviews Drug Discovery*, **2008**, *7*, 771-782,

27. Hambley, T. W.; Hait, W.N., Is Anticancer Drug Development Heading in the Right Direction? *Cancer Res.*, **2009**, *69(4)*, 1259-1262

28. Chicheł, A.; Skowronek, J.; Kubaszewska, M.; Kanikowski, M., Hyperthermia – Description of a Method and a Review of Clinical Applications, *Reports of Practical Oncology & Radiotherapy*, **2007**, *12(5)*, 267-275

29. Zee, J. V., Heating the Patient: a Promising Approach?, *Ann Oncol*, **2002**, *3(8)*, 1173-1184

30. Hildebrandt, B.; Wust, P.; Ahlers, O.; Dieing, A.; Sreenivasa, G.; Kerner, T.; Felix, R. R., The Cellular and Molecular Basis of Hyperthermia, *Crit Rev Oncol Hematol.*, **2002**, *43(1)*, 33-56

31. Kong, G.; Braun, R. D.; Dewhirst, M. W., Hyperthermia Enables Tumor-specific Nanoparticle Delivery: Effect of Particle Size, *Cancer Res*, **2000**, *60*, 4440-4445

32. Koh, I.; Wang, X.; Varughese, B.; Isaacs, L.; Ehrman, S. H.; English, D.S., Magnetic Iron oxide Nanoparticles for Biorecognition: Evaluation of Surface Coverage and Activity, *J. Phys. Chem. B*, **2006**, *110(4)*, 1553–1558

33. Cantillon-Murphy, P.; Wald, L. L.; Zahn, M.; Adalsteinsson, E., Proposing Magnetic Nanoparticle Hyperthermia in Low-field MRI, *Concepts in Magnetic Resonance Part A*, **2010**, *36A(1)*, 36 – 47

34. Katschinski1, D. M.; Robins, H. I.; Schad, M,; Frede, S.; Fandrey, J., Role of Tumor Necrosis Factor α in Hyperthermia-induced Apoptosis of Human Leukemia Cells, *Cancer Res*, **1999**, *59*, 3404-3410

35. Myers, R.; Rogers, M. A.; Hume, S. P., Histochemical Evidence for Radiation Enhancement of Lysosomal Response Following Hyperthermia of Tail Cartilage in Baby Rat, *Radiation Research*, **1981**, *87(2)*, 329-340

36. Yoo, J.; Kim, H. C.; Lee, Y. J., Hyperthermia Enhances Tumor Necrosis Factor-related Apoptosis-inducing Ligand (TRAIL)-induced Apoptosis in Human Cancer Cells, *Int J Hyperthermia*, **2006**, *22(8)*, 713-728

37. Gonzales-Weimuller, M.; Zeisberger, M.; Krishnan, K.M., Size-dependant Heating Rates of Iron oxide Nanoparticles for Magnetic Fluid Hyperthermia, *Journal of Magnetism and Magnetic Materials*, **2009**, *321(13)*, 1947-1950

38. Qiang, Y.; Antony, J.; Sharma, A.; Nutting, J.; Sikes, D.; Meyer, D., Iron/iron oxide Core-shell Nanoclusters for Biomedical Applications, *Journal of Nanoparticle Research*, **2006**, *8(3)*, 489-496

39. Mehdaoui, B.; Meffre, A.; Lacroix, M.; Carrey, J.; Lachaize, S.; Gougeon, M.; Respaud, M.; Chaudret, B., Large Specific Absorption Rates in the Magnetic Hyperthermia Properties of Metallic Iron Nanocubes, *Journal of Magnetism and Magnetic Materials*, **2010**, *322(19)*, 49-52

40. Riemer, J.; Hoepken, H. H.; Czerwinska, H.; Robinson, S. R.; Dringen, R., Colorimetric Ferrozine-based Assay for the Quantitation of Iron in Cultured Cells, *Analytical Biochemistry*, **2004**, *331(2)*, 370-375

41. Zheng, W.; Shan, N.; Yu, L.; Wang, X., UV–visible, Fluorescence and EPR Properties of Porphyrins and Mmetalloporphyrins, *Dyes and Pigments*, **2008**, *77(1)*, 153-157

42. Berg, K.; Selbo, P.K.; Weyergang, A.; Dietze, A.; Prasmickaite, L.; Bonsted, A.; Engesaeter, B.O.; Angell-Petersen, E.; Warloe, T.; Frandsen, N.; Høgset, A., Porphyrin-Related Photosensitizers for Cancer Imaging and Therapeutic Applications, *J Microsc.*, **2005**, *218*, 133-147

43. Zhang, S.; Chen, X.; Gu, C.; Zhang, Y.; Xu, J.; Bian, Z.; Yang, D.; Gu, N., The Effect of Iron oxide Magnetic Nanoparticles on Smooth Muscle Cells, *Nanoscale Research Letters*, **2010**, *4(1)*, 70-77

Chapter 3 - Proteases Based *in vivo* and *in vitro* Assays for Detection of Cancer

3.1 Introduction

In vivo fluorescence imaging is used to generate images from cells to small animals and human tissues. Recent improvements in imaging devices and imaging agents have directed medical imaging into a new level.[1] This technique studies the biological processes in tissues using fluorescence microscopy. The changes in emission light of a fluorophore are depending on the changes in the cellular functions and cell physiological conditions like pH is recorded as an increasing fluorescence signal. Sometimes also the direct fluorescence occurring from a contrast agent like quantum dots or conjugated fluorophores accumulated in mammalian tissues are imaged.[1,2] *In vivo* molecular imaging techniques are used to extract information on, tissue metabolism, measure specific enzyme activities, which permit the diagnosis of various diseases including cardiovascular diagnosis and oncology.[2] The majority of the applications recently reported are mainly focused on diagnosis and imaging of tumors *in vivo*. There are probes that are activated by a specific enzyme that is over expressed by tumor tissue. Other probes are semiconductor nanocrystal or quantum dot based.[3,4]

Here in this chapter we discuss the Förster resonance energy transfer (FRET) based sensors developed for the early diagnosis of tumors in mice using *in vivo* imaging techniques and *in vitro* protease assays. For the *in vivo* studies the iron/ iron core shell nanoparticles were modified with a tumor specific protease sequence (e.g. for urokinase-type plasminogen activator (uPA) or the matrix metalloproteinase (MMP)), which is linked to a porphyrin unit. Upon reaching the tumor site, the peptide sequence is cleaved off thus releasing the porphyrin molecule. Its fluorescence signal is then detected using fluorescence spectroscopic methods.

During the *in vitro* studies the same platform is used to detect protease activity in a fluid sample comprising a biological fluid, such as urine or blood samples of a mammal. We have successfully developed a system for the detection of various tumor proteases in urine samples of mammals. This system has been further developed to obtain *in vivo* imaging of mice tumors.

3.1.1 *In vivo* Detection of Tumors Using Enzyme Activatable Fluorophores

These activatable targeting probes are normally based on the fluorescence phenomena know as Förster resonance energy transfer (FRET).

The development of the system involves positioning of two fluorophores in close proximity where their fluorescence will be quenched. The fluorophores are linked to a stable platform via an enzyme specific protease sequence. This initially holds the fluorophores in suitable distance to each other to achieve maximum quenching, but upon the enzyme activity on the protease substrate, the fluorophores are released restoring the fluorescence which can easily be detected. [5]

The quenching of fluorescence of two fluorophores could be due to self quenching of closely placed fluorescent molecules. Bremer and cowokers[5] reported the development of a self quenched fluorescence probes to detect matrix metalloproteinase (MMP) that are over-expressed in cancers. In the system the methoxy-polyethylene-glycol-derivatized poly-L-lysine copolymer was used as the platform for the peptide substrate which is specific for the MMP-2 protease. Near-infrared fluorophores with overlapping excitation and emission spectra spectrum were selected to obtain self quenching. Upon cleavage of the enzyme substrate the increase of the fluorescence was imaged using NIRF (near infrared fluorescence) microscopy.[5] There are similar studies reported on which make use of the same structural units, the platform, peptide substrate and the fluorophores, but uses two different fluorophores. In this scenario one molecule act as the fluorophore while the other functions as the quencher.[5]
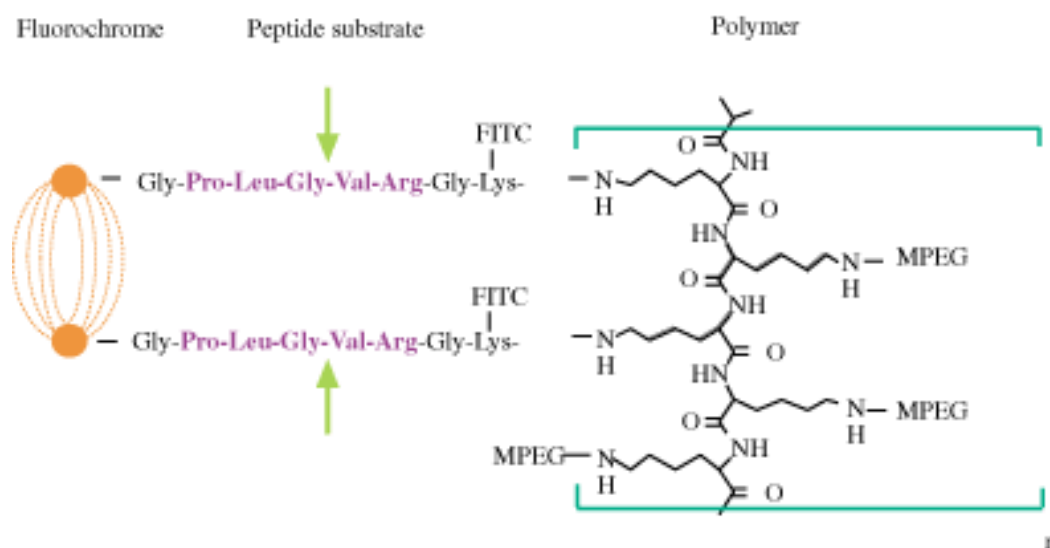
Figure 3.1: The self fluorescence quenching of the fluorophores linked by a MMP-2 specific peptide substrate[5]

Recently, there are significant advances emerging in this field. The use of inorganic nanomaterials like gold nanoparticles, iron oxide nanoparticles and quantum dots for fluorescence based imaging studies were reported.[4,6,7] These particles were studied as FRET based sensors due to their high extinction coefficients, and their ability to absorb energy in the visible range which is over lapping with organic fluorophores thus leading to fluorescence quenching. The interesting feature of this system is that the basic platform used to build the imaging system itself is acting as the quencher.[4]

Josephson and coworkers[6] have reported that the attachment of fluorescein organic dye to magnetic nanoparticles is associated with a noticeable fluorescence quenching effect. There are two distinct processes involved in the quenching. Nonradiative energy transfer between the dye and iron oxide is the most dominant process and the collisions between the dye and the nanoparticle also plays a significant role in the mechanism of fluorescence quenching. Upon activation of the probe with protease the fluorescence is enhanced.[8]
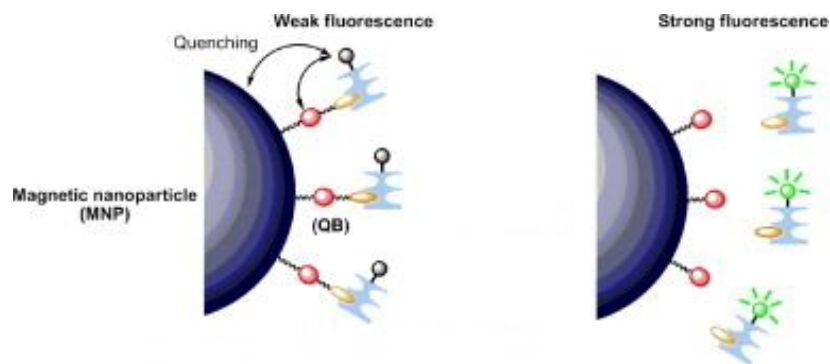
Figure 3.2: Fluorophore labeled magnetic nanoparticles activatable by a specific protease[8]
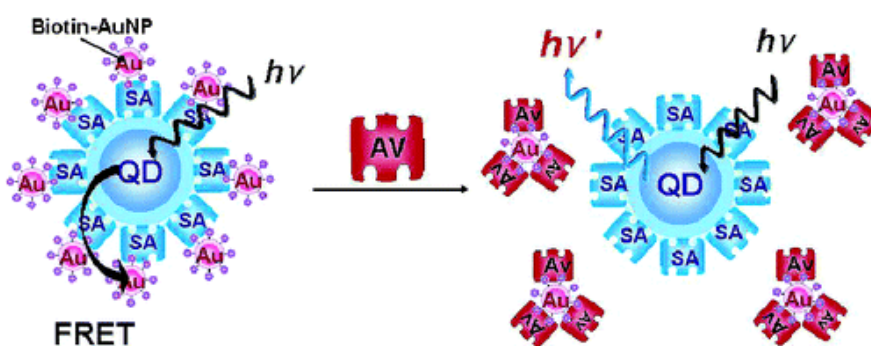
Figure 3.3: The fluorescence quenching of quantum dots (QD) by gold nanoparticles (Au)[4]

The above example further explains the suitability of using nanoparticles for the development of FRET based systems. The fluorescence from the quantum dots is quenched by the gold nanoparticles and their separation will increase the fluorescence intensity of the system.[4]

3.1.2 Förster Resonance Energy Transfer (FRET)

Förster resonance energy transfer is a popular tool to study molecular interactions in a cell, such as folding and unfolding of proteins and DNA, monitoring protease activities during enzyme catalysis, and observing stability of cellular macromolecules.[9] FRET can be defined as a distance dependent photophysical process which transfers excitation energy of a donor molecular fluorophore to a neighboring acceptor via long range dipole-dipole coupling.[10,11,12] This is a non irradiative process. The process is highly efficient of the donor and the acceptor are within a distance of 3-6 nm,

The minimal special distance is known as the Förster radius which can be defined as the distance between the donor and the acceptor at which the half of the excitation energy of the donor is transferred to the acceptor.[10] These phenomena can be illustrated using the Jablonski diagram.
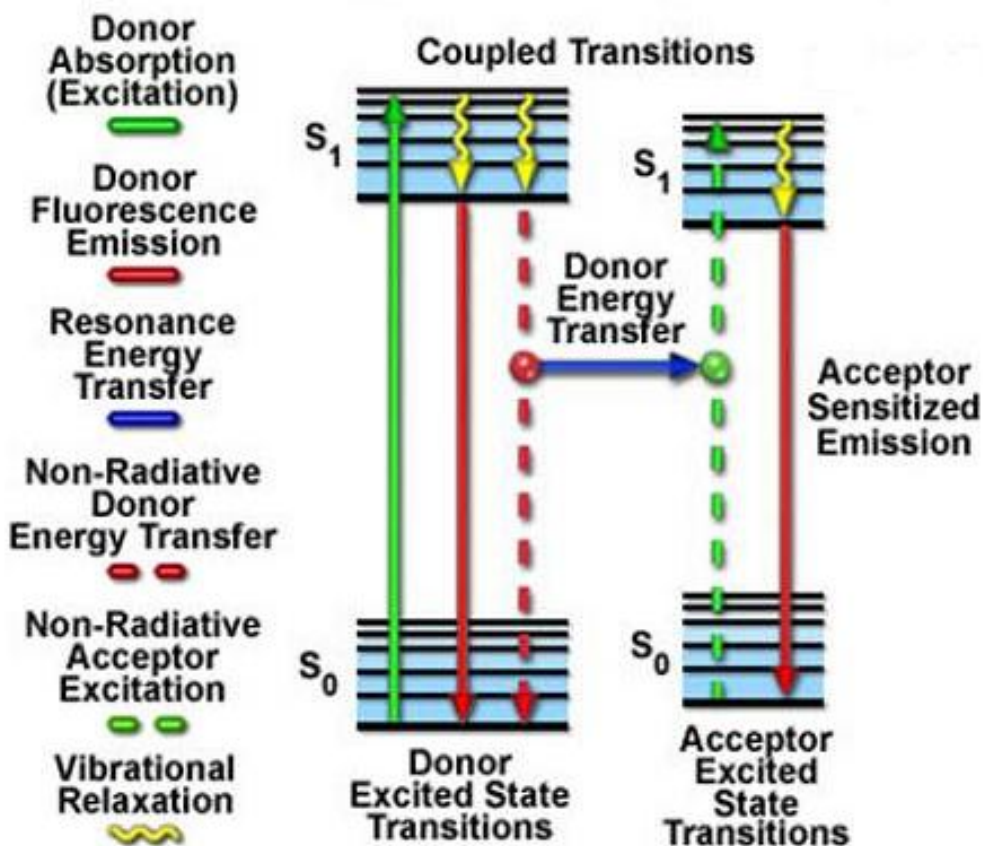
Figure 3.4: Jablonski diagram showing the distance-dependent interaction between the electronic excited states of the donor and the acceptor molecule during the Förster resonance energy transfer[11]

Tyas and coworkers[13] observe the enzymatic activity of caspase-3 which is an enzyme identified during the cell apoptosis process using this technique. They were able to link a fluorescent protein to the acceptor. Its yellow fluorescence was activated via a cleavage sequence specific to caspase-3.

The cleavage or the separation of the donor from the acceptor results in an increase in the fluorescence ratios of the two molecules reflecting a decrease in FRET process.[13]

3.1.3 Fluorophores

There are several criteria that need to be successfully met for a fluorophore to be used in *in vivo* imaging. This includes the excitation and emission wavelength, stability of the dye in physiological conditions, and pharmacokinetics.[1,13] It is important that the dye molecules absorb and emits in the near-infrared (NIR) range (650-1000 nm). In this wavelength range the tissue penetration is at a maximum and the tissue autofluorescence and the background signal is limited. It is noteworthy that many tissues and also molecules like hemoglobin can be excited at lower wavelengths leading to strong autofluorescence. The signal to noise ratio of a fluorophore should be at its maximum in order to achieve deep tissue penetration. It is important to select brighter fluorophores with higher quantum yields which can be excited with minimal amount of light[1]. The stability of the fluorophore under physiological conditions is another important fact to consider during *in vivo* imaging. It is important that the fluorophore has the ability to accumulate in the target tissues and be stable for a certain period of time until its function is fulfilled, but on the other hand they must be degraded and excreted from the body.[1,3,13]

Cyanines, rhodamine and fluorescein are the most commonly used VIS/NIR fluorophores. Recently quantum dots are used as brighter contrasting agents than organic dyes, but the applications are limited due to their toxicity and slow metabolic rate.[1,3] Indocyanine green and fluorescein are approved by the food and drug administration to be used in medical diagnosis and treatments of humans in several different disease conditions.[1]

3.1.4 Matrix Metalloproteinases and Serine Proteases

A number of proteases are associated with disease progression in cancer, and are known to be over-expressed by various cancer cell lines. Examples include Matrix Metalloproteinases (MMPs) e.g. MMP-7, Tissue Serine Proteases e.g. urokinase type plasminogen activator (uPA), and cathepsins. Many of these proteases are upregulated in the cancer cells and play a vital role in cell surface proteolysis during degradation of extracellular matrix (ECM), cell growth, tumor cell migration, apoptosis, and invasion.[14,15]

3.1.4.1 Serine Proteases

The presence of a serine amino acid in the active site of the enzyme is the characteristic feature of a serine protease.[16] There are several serine proteases that have well-documented roles in cancer growth, especially urokinase plasminogen activator (uPA) and plasmin. Tumor malignancy is closely related to the elevated expression levels of urokinase and several other components of the plasminogen activation system.[15] uPA is a very specific protease that binds to its receptor, a specific glycosylphosphophatidylinositol (GPI) anchored receptor, uPAR, and due to the catalytic activity, cleaves the inactive plasminogen (a zymogen) to the active plasmin. This is the first step in a well-known cascade that causes angiogenesis in tumors. There is a strong dependence of the tissue degradation and the activation of plasminogen, which promotes and stimuli tissue invasion and contributes to metastasis. There is an elevated level of uPA detected in rapid growing malignant tissues compared to normal tissues.[15] Plasmin is a somewhat non-specific protease that goes on to cleave many things including degrading the ECM, and releasing/activating growth factors and has the potential to activate certain MMPs. Although plasmin is somewhat non-specific and a consensus sequence is hard to determine, uPA does have a well-defined consensus sequence and directly degrade fibronectin and collagenase

IV substrates.[17] Urokinase can cleave the SGRSA consensus sequence 1363 times faster than the actual cleavage site in plasmogen thus identified as the primary optimized cleavage sequence for urokinase.[18] This peptide sequence can be used as a spacer between ethylene glycol chains of modifies nanoparticles and a fluorophore such as the porphyrin TCPP. Then the-linked porphyrin will be released in the presence of urokinase and will drastically change the observed luminescence spectrum. This simple urokinase-assay will permit the fast and much more accurate prognosis of the malignancy of numerous (invasive) cancer types.

3.1.4.2 Matrix Metalloproteinases

Matrix metalloproteinases are the classic cancer associated proteases. MMPs are a family of zinc containing endopeptidases that are named due to the role played by zinc for the catalytic activity of the enzyme. They are normally synthesized as inactive zymogens or proMMPs which will later be activated by serine proteases or other MMPs. MMPs are sub grouped based o their structure and active substrate. There are 21 different known MMPs that are grouped into families based on their specificity for extracellular matrix components: collagenases, gelatinases, stromelysins, matrilysin, metalloelastase, enamelysin, and membrane-type MMPs. As can be seen from the family names, MMPs degrade the proteins that make up the extracellular matrix (ECM) and the basement membrane (BM).[19,20] Interestingly, MMPs are usually produced by the cancerous cells themselves, but the major producer of the MMP's are the stromal cells surrounding the tumor.[20] This is because the cancerous cells give off a variety of cell signals that cause the surrounding stromal cells to highly upregulate their production of MMPs. MMPs are vital to cancer survival and progression for several reasons – they cleave cell surface bound growth factors from the stromal and epithelial cells and release them to interact with the cancer cells to stimulate growth, and they play a role in angiogenesis by opening the ECM to new vessel

110

development and by releasing pro-angiogenic factors and starting pro-angiogenic protease cascades. They play a major role in tumor metastasis and invasion by degrading the ECM and the BM allowing the cells to pass through and releasing ECM and BM fragments which stimulates cell movement.[19,20,21] MMPs are not perfectly specific, they usually cleave several related proteins, but consensus sequences (the sequence of amino acids that a protease targets) have been determined for several MMPs and are shown in Table 3.2, allowing peptides to be created that are selectively cleaved by the target MMP.

Table 3.1: The matrix metalloproteinase family – Categorization[19]

MMP designation	Structural class	Common name (s)
MMP-1	Simple hemopexin domain	Collagenase-1, interstitial collagenase, fibroblast collagenase, tissue collagenase
MMP-2	Gelatin-binding	Gelatinase A, 72-kDa gelatinase, 72-kDa type IV collagenase, neutrophil gelatinase
MMP-3	Simple hemopexin domain	Stromelysin-1, transin-1, proteoglycanase, procollagenase- activating protein
MMP-7	Minimal domain	Matrilysin, matrin, PUMP1, small uterine metalloproteinase
MMP-8	Simple hemopexin domain	Collagenase-2, neutrophil collagenase, PMN collagenase, granulocyte collagenase
MMP-9	Gelatin-binding	Gelatinase B, 92-kDa gelatinase, 92-kDa type IV collagenase
MMP-10	Simple hemopexin domain	Stromelysin-2, transin-2
MMP-11	Furin-activated and secreted	Stromelysin-3
MMP-12	Simple hemopexin domain	Metalloelastase, macrophage elastase, macrophage metalloelastase

MMP-13	Simple hemopexin domain	Collagenase-3
MMP-14	Transmembrane	MT1-MMP, MT-MMP1
MMP-15	Transmembrane	MT2-MMP, MT-MMP2
MMP-16	Transmembrane	MT3-MMP, MT-MMP3
MMP-17	GPI-linked	MT4-MMP, MT-MMP4
MMP-18	Simple hemopexin domain	Collagenase-4 (Xenopus; no human homologue known)
MMP-19	Simple hemopexin domain	RASI-1, MMP-18‡
MMP-20	Simple hemopexin domain	Enamelysin
MMP-21	Vitronectin-like insert	Homologue of Xenopus XMMP
MMP-22	Simple hemopexin domain	CMMP (chicken; no human homologue known)
MMP-23	Type II transmembrane	Cysteine array MMP (CA-MMP), femalysin, MIFR

Table 3.2: Consensus sequences of different matrix metalloproteinase[22]

Protease	Consensus sequence (Cleavage sequence)
MMP-1	VPMS-MRGG
MMP-2	IPVS-LRSG
MMP-3	RPFS-MIMG
MMP-7	VPLS-LTMG
MMP-9	VPLS-LYSG
MMP-11	HGPEGLRVGFYESDVMGRGHARLVHVEEPHT
MMP-13	GPQGLA-GQRGIV
MT1-MMP	IPES-LRAG
uPA	SGR-SA

Cathepsin B	SLLKSR-MVPNFN
Cathepsin D	SLLIFR-SWANFN
Cathepsin L	SGVVIA-TVIVIT

The proteases with known consensus sequences that are activated at the tumor site can be used for drug delivery and imaging purposes. This has been primarily done with pro-drug activation through cleavage by one of the proteases. The drug is attached to a selected protease sensitive sequence which will reduce its toxicity and it will only be released in the presence of the protease. In 2001, Trouet and coworkers[23] demonstrated that the prodrugs b-Ala-Leu-Ala-Leu-Dox (Dox=doxorubicin) can selectively be activated in the presence of proteases in the tumor microenvironment. By using this methodology selective activation of the pro drug was observed and there was 14 times more accumulation of doxorubicin in MCF-7/6 human breast carcinoma cells and MRC-5 fibroblasts compared to normal cells.[23]
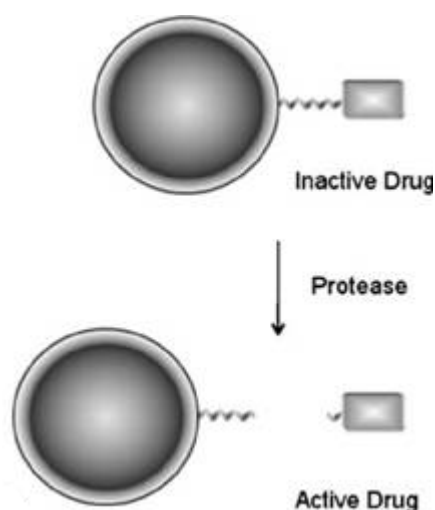
Figure 3.5: Protease activated drug release[23]

A selected protease specific sequence can be used as a spacer between two fluorophores, in this case it is iron nanoparticles and porphyrin. Since the fluorophores are in close proximity initially there will be energy transfer between them and there will be limited or no fluorescence.

The probe will be activated in the presence of the protease and the signal can be detected as an increase in the fluorescence. This method is used for *in vivo* imaging and detection of presence of certain proteases.[23]

McIntyre and coworkers in 2004 reported the development of protease-activated imaging agent for *in vivo* detection and imaging of tumor-associated MMP-7 activity. The MMP-7 substrate is fluorescein-Ahx-Arg-Pro-Leu-Ala-Leu-Trp-Arg-Ser-Ahx-Cys (Fl-M7). Fl-M7 is then reacted with polyamido amino (PAMAM) dendrimer, followed by tetramethylrhodamine (TMR), to generate the optical sensor, $(Fl-M7)_m$-PAMAM-$(TMR)_n$. Fl-M7. TMR has the ability to quench the fluorescence from fluorescein (Fl) in the intact conjugate and can be activated in the presence of the enzyme.[23]
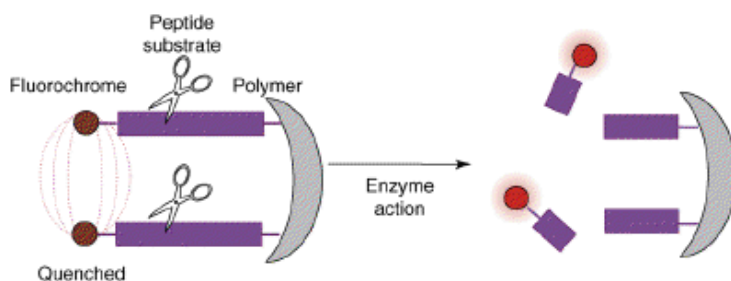
Figure 3.6: The action of enzyme activable fluorescence probes. The fluorophore is released in the presence of the specific protease[3]

The table summarizes the use of specific protease consensus to study the concepts of delivery of inactive pro drugs and in vivo imaging specially related to treatment of tumors.

Table 3.3: Sequences used for protease-activated drug delivery and imaging agents[23]

Protease	Sequence	Utility
MMP	Pro-Leu-Gly~Hof-Orn-Leu	Dox prodrug
MMP	Glu-Pro-Cit-Phe~Hof-Tyr-Leu	Dox prodrug
MMP	Gly-Pro-Leu-Gly~Val	Dox prodrug

MMP	Gly-Pro-Leu-Gly~Leu-Trp-Ala-Gln	Anthrax toxin PA prodrug
MMP-2	Pro-Gln-Gly~Ile-Ala-Gly-Gln	Melittin prodrug
MMP-2	Pro-Gln-Gly~Ile-Mel-Gly	Mel prodrug
MMP-2	Gly-Pro-Leu-Gly~Val-Arg-Gly-Lys	TNF prodrug
MMP-2	His-Pro-Val-Gly~Leu-Leu-Ala-Arg	TNF prodrug
MMP-2	Gly-Pro-Leu-Gly~Ile-Ala-Gly-Gln	Fusogenic liposomes
MMP-2	Gly-Pro-Leu-Gly~Val-Arg-Gly	Dox micelles
MMP-2	Pro-Leu-Gly~Leu-Trp-Ala	MLV envelope glycoprotein delivery
MMP-2	Gly-Gly-Pro-Leu-Gly~Leu-Trp-Ala-Gly-Gly	GALV envelope glycoprotein delivery
MMP-2	Gly-Pro-Leu-Gly~Val-Arg-Gly	Cy5.5 imaging agent
MMP-2	Pro-Leu-Gly~Val-Arg-Gly	QD imaging agent
MMP-2	Pro-Leu-Gly~Leu-Ala-Gly	Cy5, fluorescein imaging agents
MMP-2	Lys-Gly-Pro-Leu-Gly~Val-Arg-Gly	Nanoparticle imaging agent
MMP-9	Ala-Ala-Leu-Gly~Nva-Pro	FITC prodrug
MMP-9	Pro-Leu-Gly~Met-Thr-Ser	SeV prodrug
MMP-9	Triple-helical Gly-Pro-Gln-Gly~Ile-Ala-Gly-Gln-Arg	Liposomes
MMP-2, MMP-9	Pro-Leu-Gly~Leu	Auristan, Dox prodrugs
MMP-2, MMP-9	Gly-Pro-Leu-Gly~Ile-Ala-Gly-Gln	Dox prodrug
MMP-2, MMP-9	Pro-Val-Gly~Leu-Ile-Gly	MTX prodrug
MMP-2, MMP-9	Gly-Pro-Leu-Gly~Met-Leu-Ser-Gln	Anthrax toxin PA prodrug

Hof-homo Phe, Cit-citrulline, Mel-melphalan, PA-protective antigen, TNF-tumor necrosis factor, GALV-gibbon ape leukemia virus, FITC-fluorescein isothiocyanate, MTX-methotrexate

3.2 Design of the FRET-based Sensors

NanoScale Corporation's Fe/Fe_3O_4 core shell nanoparticles are a suitable candidate for the development of detection methods based upon surface plasmon resonance and Förster resonance energy transfer (FRET) between non-identical particles. The nanoparticles were modified with dopamine tetraethylene glycol ligand as described in chapter 2.
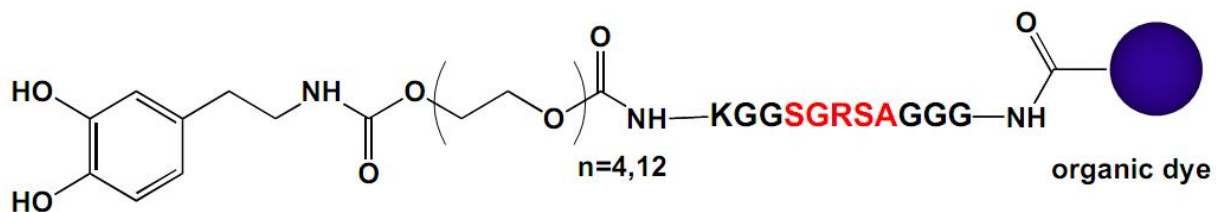
Figure 3.7: Synthesis of dopamine-oligoethylene glycol-oligopeptide- tetracarboxylphenyl porphyrin (organic dye)

During the synthesis, different target protease consensus sequences are linked to tetracarboxylphenyl porphyrin (TCPP). The last steps of the functionalization of the bimagnetic nanoparticles consist of the attachment of the second linker, the oligopeptide KGGSGRSAGGG to the stealth-nanoparticle, and then the attachment of TCPP (porphyrin B) to this peptide-linker. The unreacted end of the cleavage sequences are linked to the glycine tips of the stealth-coated Fe/Fe_3O_4 nanoparticles.
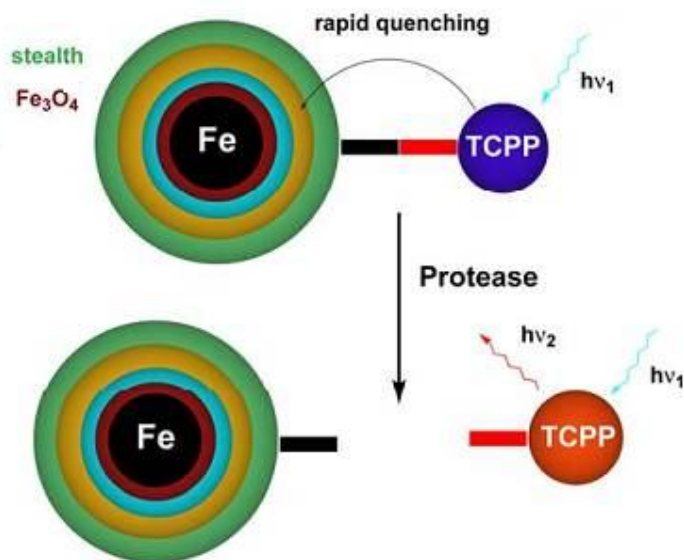
Figure 3.8: The cleavage of the peptide sequence by the specific protease releases the fluorophore

Before proceeding to study the enzyme cleavage activity of the proteases with these sensors, another series of modified nanoparticles were synthesized by linking porphyrin and zinc-doped porphyrin to the free tip of glycine of the stealth-coated Fe/Fe_3O_4 nanoparticles.
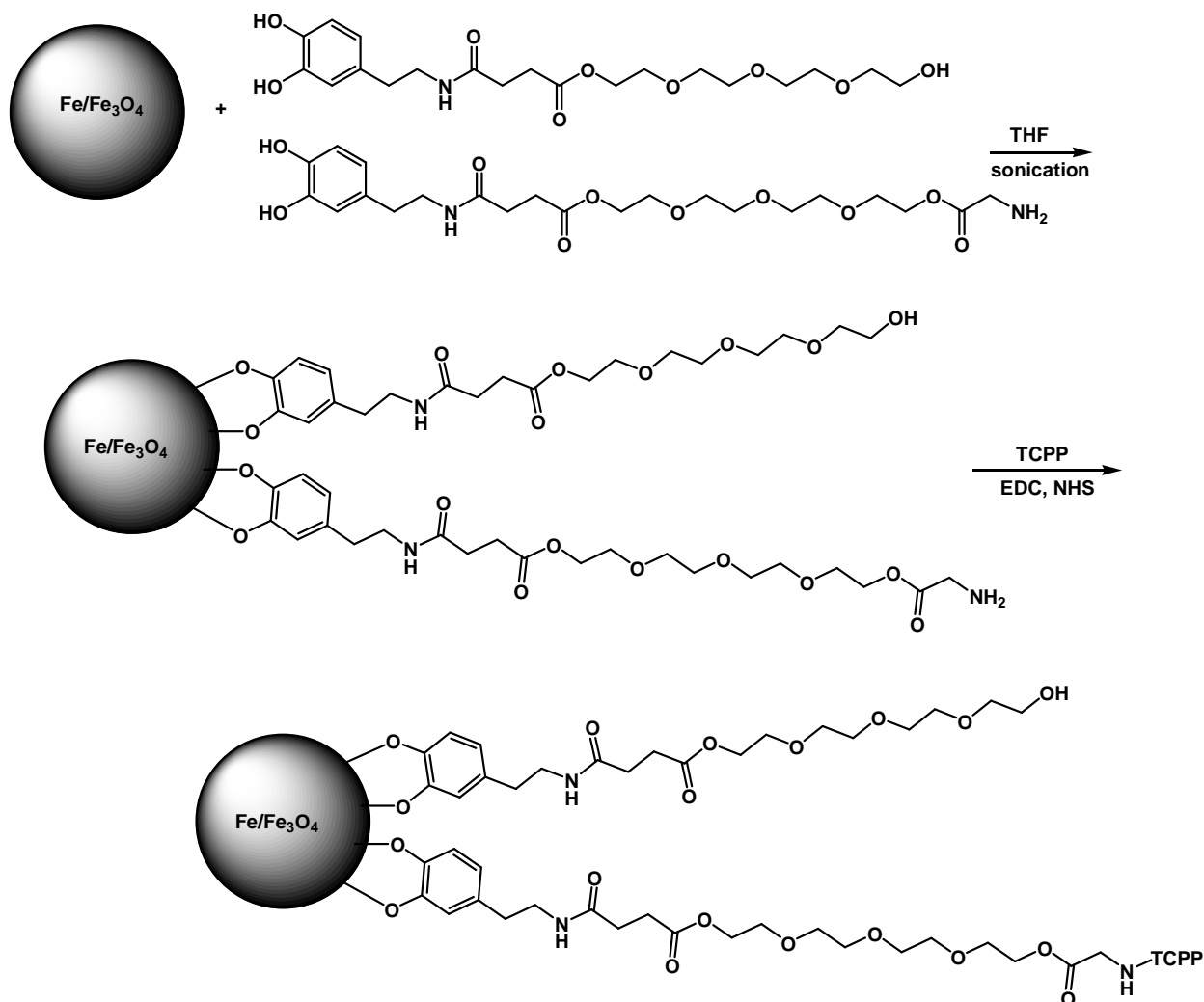
Figure 3.9: Synthesis of the zinc-doped porphyrin linked to stealth-coated Fe/Fe$_3$O$_4$ nanoparticles

The fluorescence of free sodium tetracarboxylate porphyrin (at pH=7.2 in PBS) and zinc-doped sodium tetracarboxylate porphyrin was studied, and results compared with those obtained for core/shell Fe/Fe$_3$O$_4$-nanoparticles featuring stealth ligands with chemically-attached metalated and unmetalated tetracarboxyphenyl porphyrin (TCPP). First, both the "free" sodium tetra-carboxylate porphyrin and the zinc-doped sodium tetracarboxylate porphyrin were tethered to Fe/Fe$_3$O$_4$-nanoparticles. As shown in Figure 3.10 for both tethered porphyrins, the emission intensity rises slightly less than linear with increasing concentration of the nanoplatforms. This

is a first indication of Förster energy transfer (FRET), as discussed below. The number of porphyrins that are tethered to one Fe/Fe$_3$O$_4$-nanoparticle (d=20 nm) in Figure 3.10 was estimated to be 4.8 (I) and 4.5 (II).
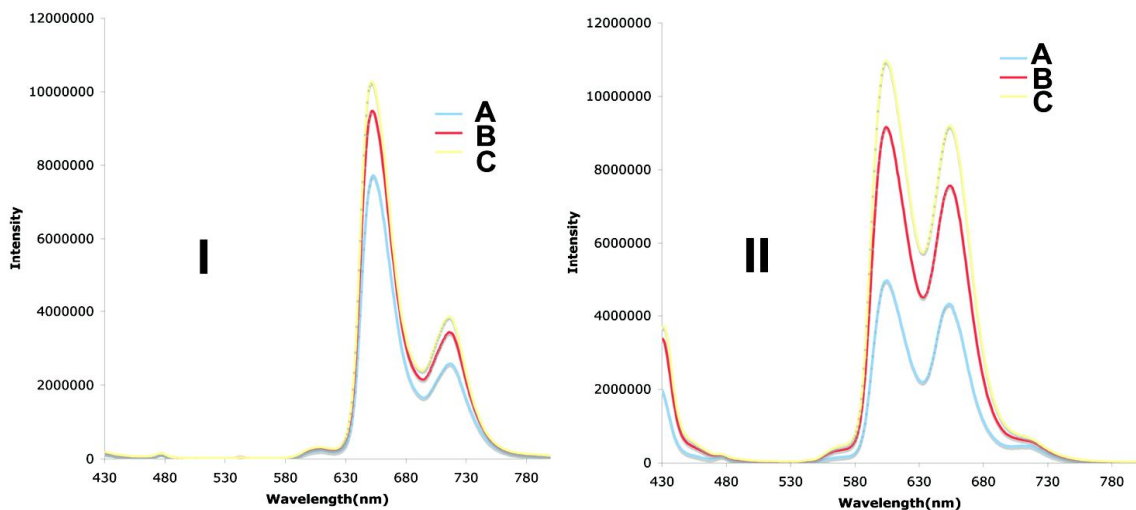
Figure 3.10: Relative fluorescence intensities of Fe/Fe$_3$O$_4$ – nanoplatform featuring "free" sodium tetracarboxylate porphyrin (I) and zinc-doped sodium tetracarboxylate porphyrin (II)

In Figure 3.11, the concentration dependence of zinc-doped sodium tetracarboxylate porphyrin and sodium tetracarboxylate porphyrin, in a relative molar ratio of 9 to 1, in PBS is shown. Whereas the first fluorescence band at λ=609 nm shows saturation, the second band at λ=657 nm shows a maximum of intensity at the concentration of c=8.0x10^{-6} mol nanoplatforms. As the concentration increases, Förster energy transfer (FRET) increases: the hopping of excited states from porphyrin to porphyrin increases the degree of internal (radiation-less) conversion. Consequently, the fluorescence quantum yield does not exceed a maximum of Φ=0.011 for the Fe/Fe$_3$O$_4$-bound porphyrins. It is noteworthy that the emissions from the zinc-doped sodium tetracarboxylate porphyrin (λ_1=607 nm, λ_2=657 nm) are higher in energy than those of the "free" sodium tetracarboxylate porphyrin (λ_1=654 nm, λ_2=718 nm). Therefore, FRET is directed

119

towards the "free" sodium tetracarboxylate porphyrin, which shows a slight relative emission enhancement (f<2.2 from the analysis of the spectra shown in Figure 3.11) when bound to Fe/Fe$_3$O$_4$-NPs.
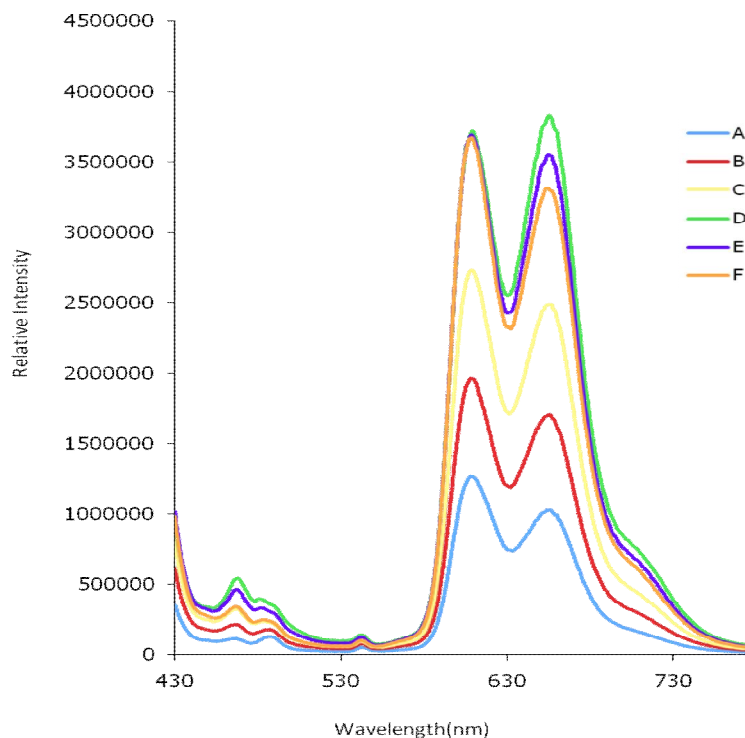
Figure 3.11: Relative fluorescence intensities of zinc-doped sodium tetracarboxylate porphyrin and sodium tetracarboxylate porphyrin in a relative molar ratio of 9 to 1

We have estimated that the number of porphyrins that are tethered to one Fe/Fe$_3$O$_4$-nanoparticle (d=20 nm) is approx.5. A: c=2.0x10^{-6} M nanoplatforms, B: c=4.0x10^{-6} M nanoplatforms, C: c=6.0x10^{-6} M nanoplatforms, D: c=8.0x10^{-6} M nanoplatforms, E: c=1.0x10^{-5} M nanoplatforms, F: c=1.2x10^{-5} M nanoplatforms

Untethered sodium tetracarboxylate porphyrin was added to the Fe/Fe$_3$O$_4$ – nanoplatform featuring zinc-doped sodium tetracarboxylate porphyrin and sodium tetracarboxylate porphyrin in a relative molar ratio of 9 to 1. Again, this experiment was performed in PBS. A distinct

decrease of the fluorescence band at λ_1=607 nm is discerned. The concentration dependence of the fluorescence occurring from the other two fluorescence bands at (λ_1=654 nm, λ_2=718 nm) is non-linear. The reason for the observed non-linear behavior can be found in the high fluorescence quantum yield of the non-metalated, untethered sodium tetracarboxylate porphyrin. We have estimated Φ=0.082, which is approximately eight times higher than in the tethered state, when the large porphyrin-concentration in the sphere around the Fe/Fe$_3$O$_4$-NP leads to increase FRET and, consequently, radiation-less deactivation of the excited states.
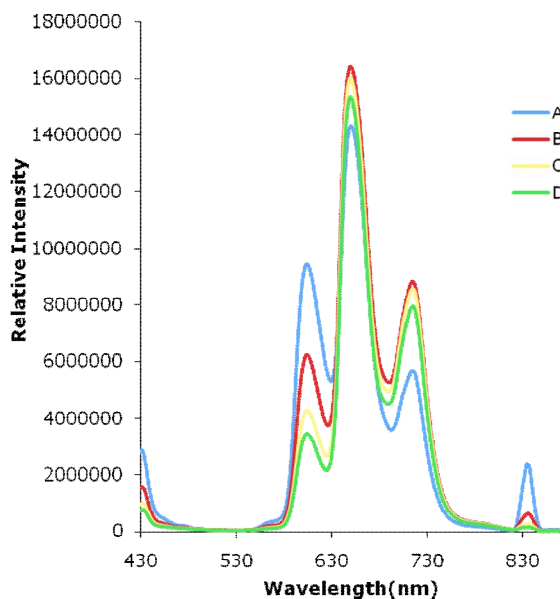
Figure 3.12: Relative fluorescence intensities of the Fe/Fe$_3$O$_4$ – nanoplatform (featuring tethered zinc-doped sodium tetracarboxylate porphyrin and sodium tetracarboxylate porphyrin in a relative molar ratio of 9 to 1. C$_{(nanoplatform)}$ = 2.0x10^{-6} mol) as unbound sodium tetracarboxylate porphyrin is added in PBS. A: c=2.8x10^{-6} M added porphyrin, B: c=5.6x10^{-7} M added porphyrin, C: c=8.4x10^{-7} M added porphyrin, D: c=1.2x10^{-7} M added porphyrin

The ratios of the integrals of the fluorescence bands shown at λ_1=607 nm, λ_2=654 nm and λ_3=718 nm are plotted versus the mol percent of added untethered sodium tetracarboxylate

porphyrin. The plots of $R=I(\lambda_2)/I(\lambda_1)$ and $R=I(\lambda_3)/I(\lambda_1)$ increase with increasing mol percent of added untethered porphyrin. They are quite linear in the concentration range from 0 to 7 mol percent of added untethered sodium tetracarboxylate porphyrin. Therefore, the concentration of porphyrin that is "freed" by the enzyme urokinase, which will be cleaving the urokinase-cleavage sequence (SRGSA) can be measured by recording fluorescence spectra of the nanoplatform at different time intervals and comparing the fluorescence intensities at the three wavelengths. It should be noted that all three wavelengths permit *in vivo* -measurements in mammalian tissue, especially when coupled with single-photon counting techniques.
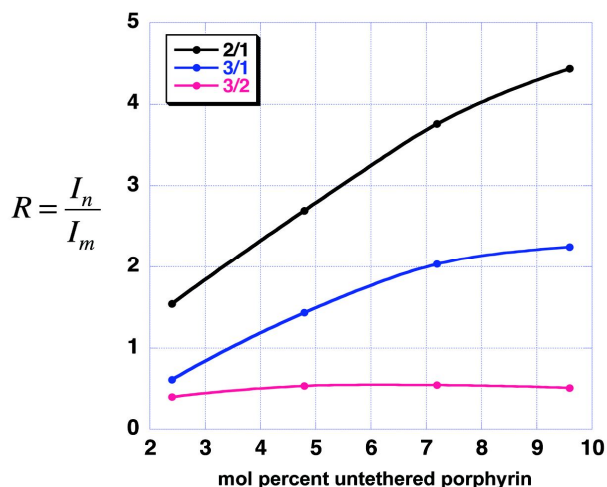
Figure 3.13: Ratios of the integrals of the fluorescence bands shown in Figure 3.12 at $\lambda_1=607$ nm, $\lambda_2=654$ nm and $\lambda_3=718$ nm, plotted versus the mol percent of added untethered sodium tetracarboxylate porphyrin

3.3 *In vivo* Urokinase Assay

In this Example, TCPP was tethered via a urokinase-specific cleavage sequence (KGGSGRSAGGG) to a dopamine-tetraethylene glycol ligand. This ligand was then bound to the Fe/Fe_3O_4-nanoparticles. The assembly is prepared using the same procedures described above, except that only one type of porphyrin used (non- metalated). An *in-vivo*

122

urokinase-assay was tested in Charles River female mice, which have been impregnated with B16-F10 mouse melanoma cells 10 days prior to these measurements. The mice were anesthetized and then a solution of a Fe/Fe_3O_4-nanoparticle-TCPP assembly was administered to the mice intravenously (IV) or via direct injection into the tumors (IT). The IV solution was 200 µg of the nanoparticle assembly in 200 µL PBS. The IT solution was 100 µg of the nanoparticle assembly in 200 µL PBS. To measure the activity of the assay, the mice were anesthetized again and placed under a fluorescence microscope employing a single-photo-counting detector. This instrument has been built in-house. The tumor regions at the hind legs of the mice were excited using laser light (Ti:sapphire-laser, $\lambda=870$ nm, P=6.5 mW) in the IR-region. The results of the single-photo-counting spectra, from the right and left limbs of the mice, recorded through a fluorescence microscope (resolution: 1 µm x 1 µm x 1 µm) is illustrated in Figure 3.14
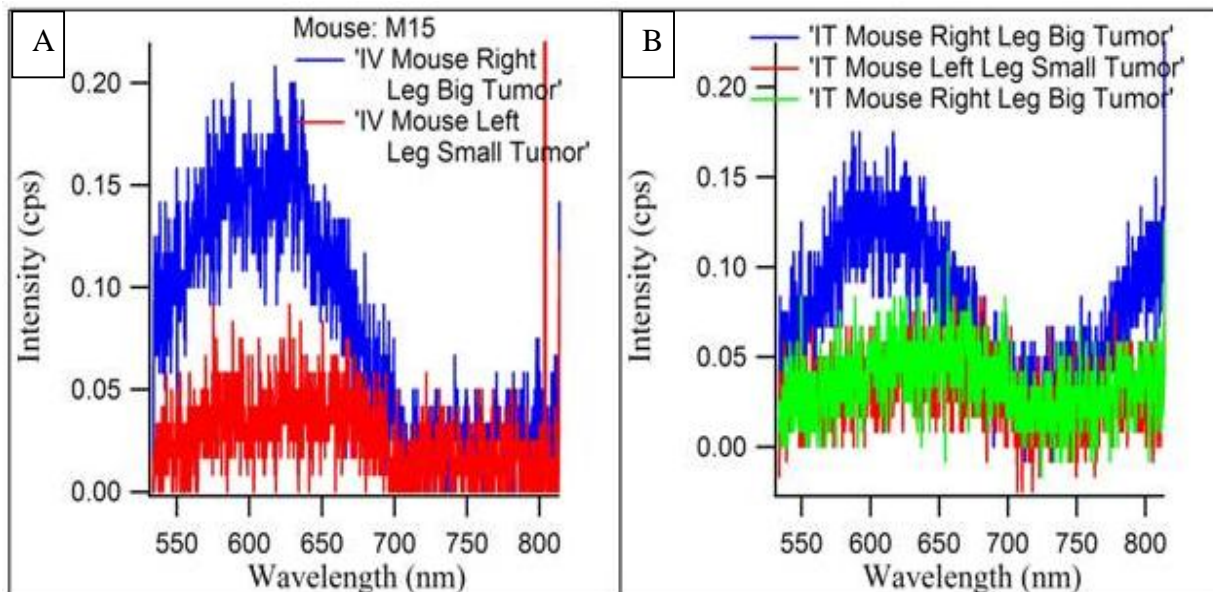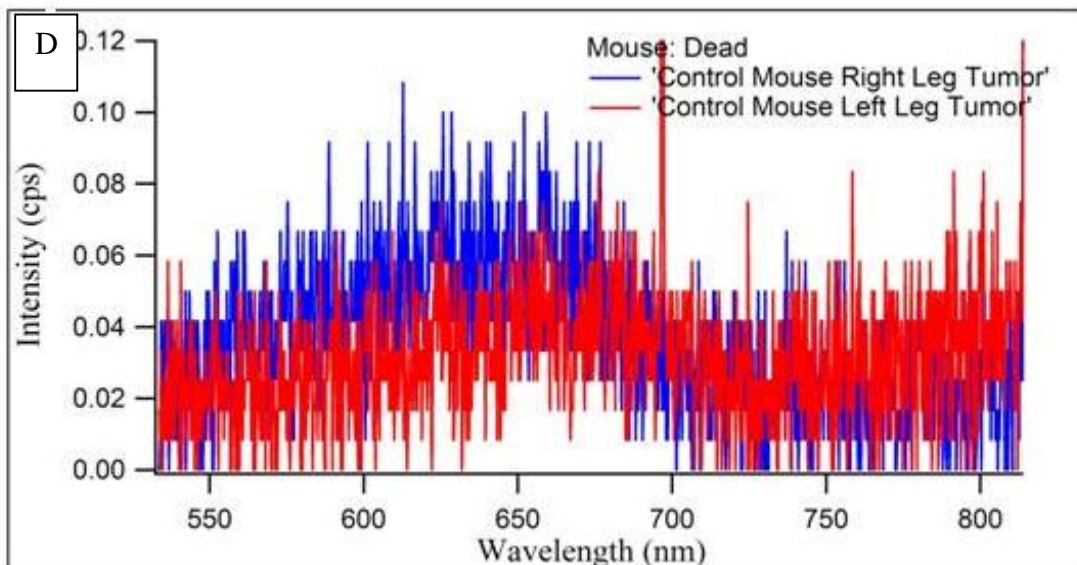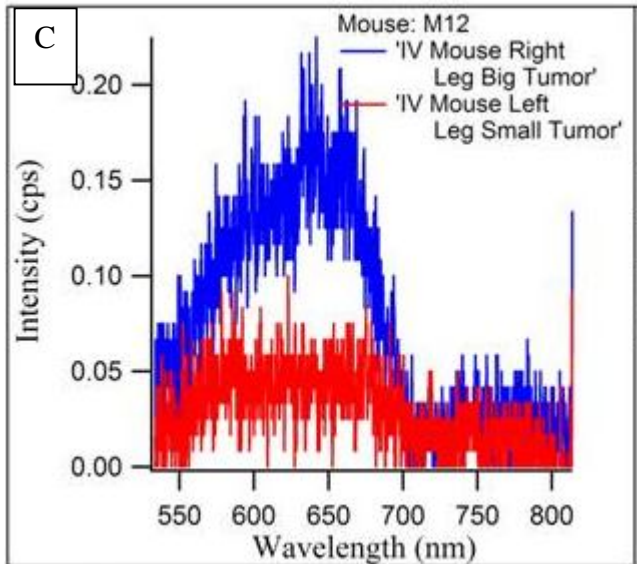
Figure 3.14: The single-photo-counting spectra, from the right and left limbs of the mice, recorded through the fluorescence microscope (red: left limb; blue: right limb)

Box A shows the results from mouse, which was IV-injected 12 h prior to measurement. Box B shows the results from mouse, which was IT-injected 30 min prior to measurement. Box C shows the results from mouse 3 (bearing tumors on both legs), which was IV-injected 12 h

prior to measurement. Box D shows the results from the control mouse, neither IT- nor IV-injected.

The porphyrin, TCPP, requires tri-photonic excitation at this excitation wavelength. It is remarkable that the signal strengths obtained in the right legs of the tumor-bearing mice correlates with the tumor size. The hypothesized explanation is that the uptake of the nanoparticle assembly by the tumors is so rapid, that the first tumor, which is encountered by the nanoparticles injected intravenously, incorporates almost everything. It was found that the IT-injection is less efficient than IV-injection, because the urokinase does not have the time to cleave the majority of the cleavage sequences and the porphyrin does not light up.

3.4 *In vitro* Urokinase Assay

Due to the small diameter of the nanoparticles, it was able to quench the luminescence occurring from TCPP. This type of sensor is based on the quenching of the excited states of chromophores (e.g. porphyrins) with organic (e.g. viologens) or inorganic quenchers (e.g. metal, alloy, and core/shell nanoparticles). Due to the proximity of the nanoparticle (~ 2 nm) to the porphyrin, the surface plasmon of the core/shell nanoparticle is able to quench the emission spectra from the chemically-attached porphyrin. Once released by urokinase cleavage, the luminescence increases significantly. This luminescence increase can be detected spectrally. When several chromophores featuring discernible emission spectra are used, the activity of various enzymes can be detected simultaneously.

3.4.1 Study the Enzyme Kinetics of Urokinase on a Urokinase-specific Cleavage Sequence (KGGSGRSAGGG)

A series of urokinase enzyme solutions were prepared ranging from 2.31×10^{-7}, 2.31×10^{-8}, 2.31×10^{-9}, 2.31×10^{-10}, 2.31×10^{-11} M in pH=7.2 PBS buffer. The concentration of the

nanoparticles modified with the dopamine tetraethylene stealth coating attached to porphyrin via the cleavage sequence, was dissolved in pH=7.2 buffer to obtain a final nanoparticle concentration of 0.2 mg/mL. The initial fluorescence was recorded for the solution (excitation at 420 nm). To this solution 50 µL of urokinase was added and the fluorescence change was observed every 2 min. The experiment was repeated for all 5 solutions keeping the concentration of the nanoparticles a constant.

The fluorescence spectra collected after the excitation at 420 nm shows an increase in the fluorescence intensity. The increase in the fluorescence intensity is related to the amount of porphyrin released from the particles. The urokinase cleaves the KGGSGRSAGGG peptide sequence from amide bond between argentine and serine releasing the porphyrin molecule.
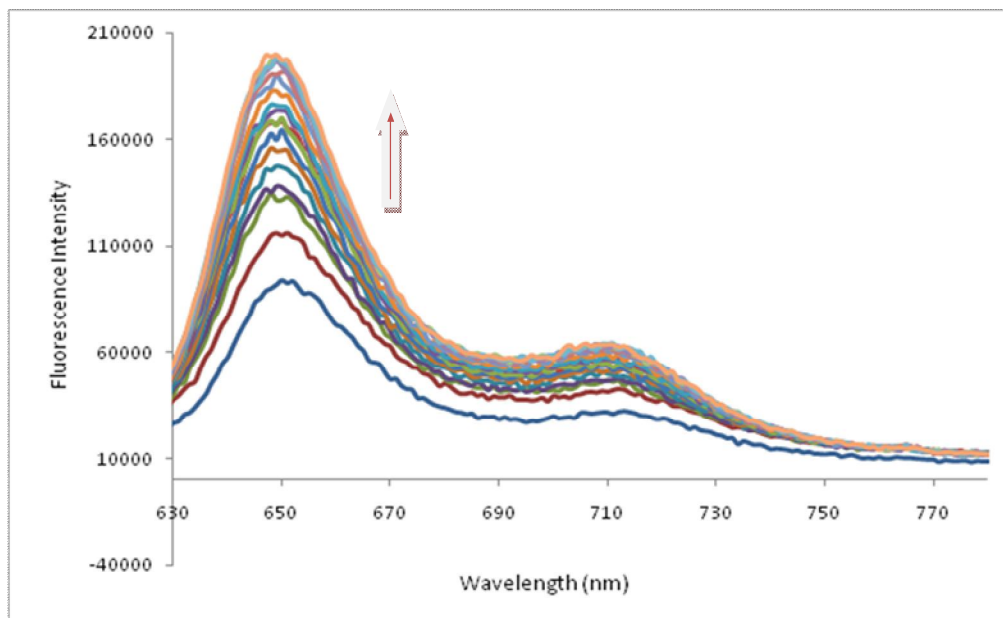

Figure 3.15: The fluorescence spectra obtained for the 0.2 mg/mL modified nanoparticle sample in 3 minute intervals, after addition of 50 µL of 2.31×10^{-7} M urokinase (Excitation at 420 nm)
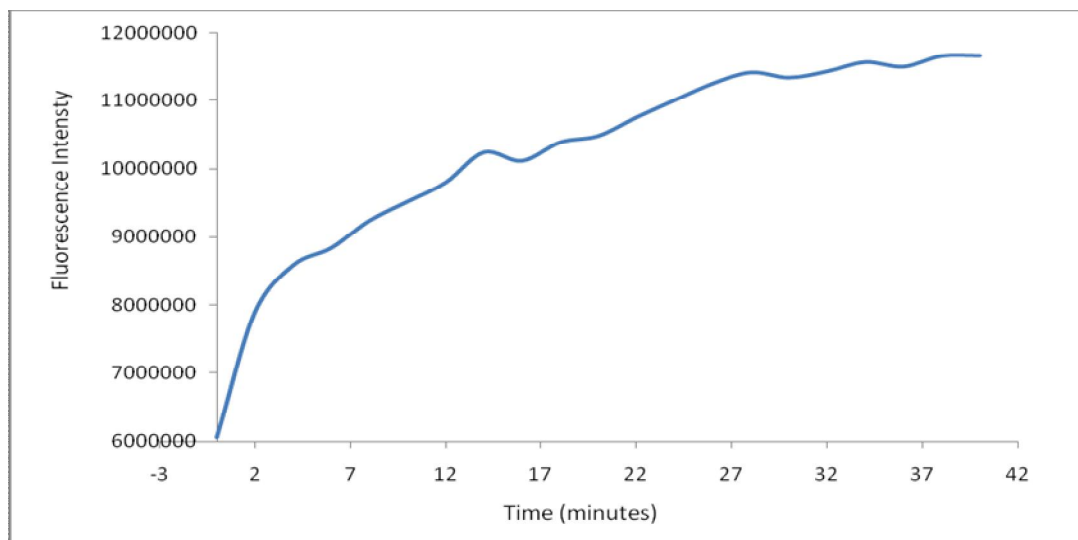
Figure 3.16: The graph is showing recording of the increase of the fluorescence intensity with time for graph 3.15. The readings were recorded until a plateau is reached

The plot of the time versus the substrate concentration, which in this case measured as an increase in the fluorescence, reaches a plateau after 22 min to the reaction. The initial rate of the reaction can be measured from the slope of the graph at the initial period of the reaction.

At very early stage of the reaction, the rate of product accumulation increases over time. For an extended period of time, the product concentration increases linearly with time. At later times, the substrate is depleted, so the curve starts to level off. Eventually the concentration of product reaches a plateau and doesn't change with time. As the reaction progresses product inhibition and slow denaturation of enzyme could also have an effect on the decrease level of reaction.[24]
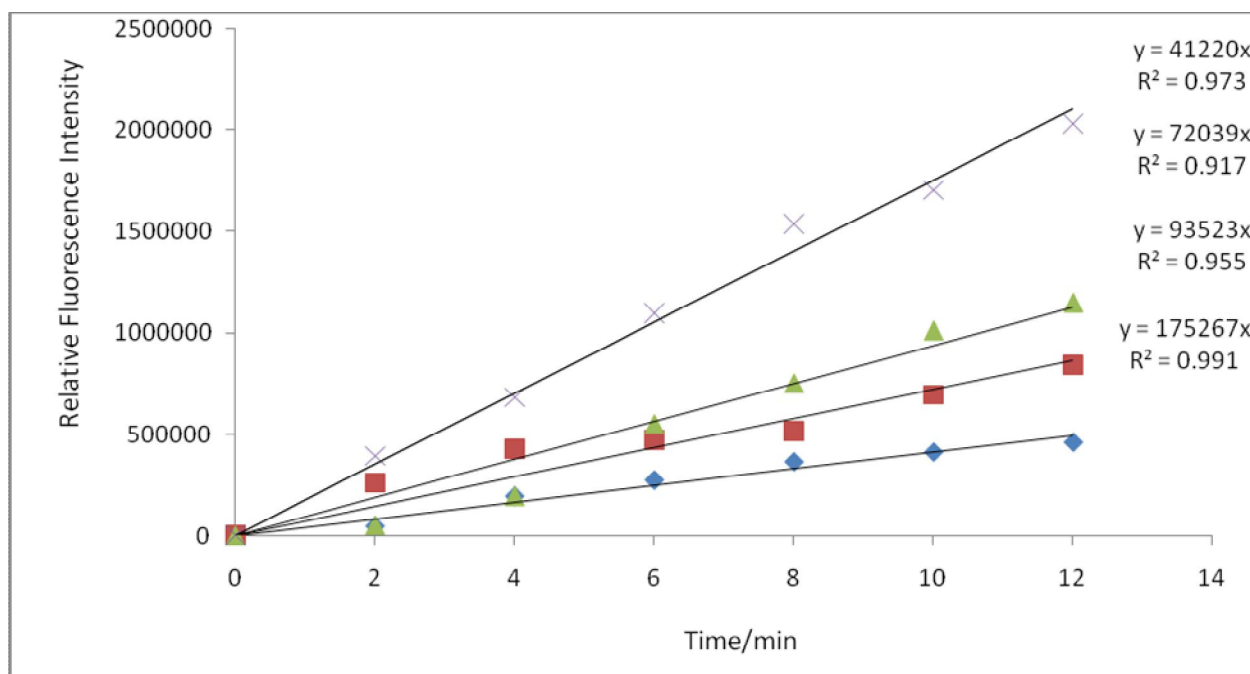
Figure 3.17: The effect of enzyme concentration on the velocity of the reaction (◆Concentration of urokinase 2.31×10^{-10} M, The velocity of the reaction was 41220 min^{-1}, ■ Concentration of urokinase 2.31×10^{-9} M, The velocity of the reaction was 72039 min^{-1}, ▲ Concentration of urokinase 2.31×10^{-8} M, The velocity of the reaction was 93523 min^{-1}, ✖ Concentration of urokinase 2.31×10^{-7} M, The velocity of the reaction was 175267 min^{-1})

The experiment is carried out at 25 ℃. The temperature is high enough to ensure a high reaction rate, and the enzyme denature is minimized at this temperature. We assume that there are sufficient substrate molecules available for the enzyme to bind and the enzyme is saturated by the substrate. The initial velocity of each reaction was obtained from the progress curve. The higher the enzyme concentration the greater is the reaction rate. At the lowest concentration of the urokinase (2.31×10^{-11} M) the reaction proceeded with a very low reaction rate.

3.4.2 The Study of the Rate of the Reaction with Different Substrate Concentrations

The same experiment was repeated using modified nanoparticle substrate concentrations of 0.05, 0.1, 0.15 mg/mL. The fluorescence were recorded every at 25 ºC in pH=7.2 PBS buffer for a time period of 40 min. The change in the fluorescence intensity as the reaction progresses was plotted with the reaction time.
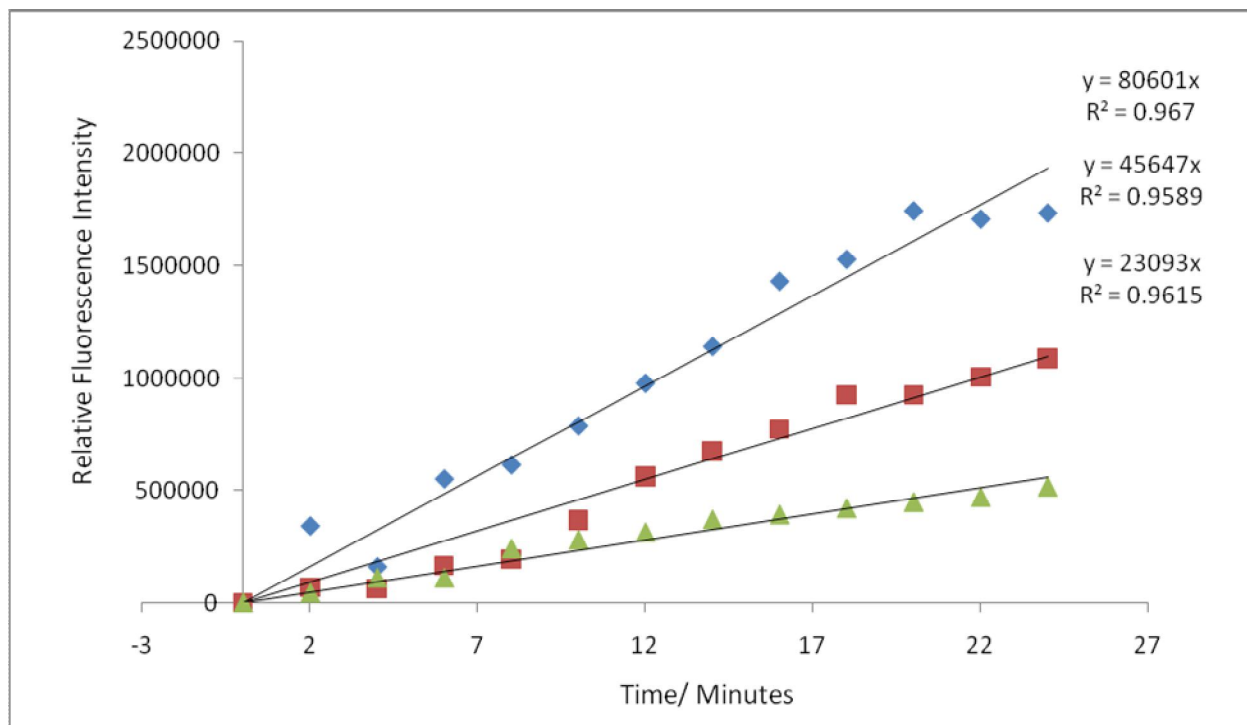
Figure 3.18: The effect of substrate concentration on the velocity of the reaction. The concentration of the enzyme was kept a constant at 2.31×10^{-7} M ($\blacklozenge$ Concentration of the substrate 0.15 mg/mL, $\blacksquare$ Concentration of the substrate 0.1 mg/mL, $\blacktriangle$ Concentration of the substrate 0.05 mg/mL)
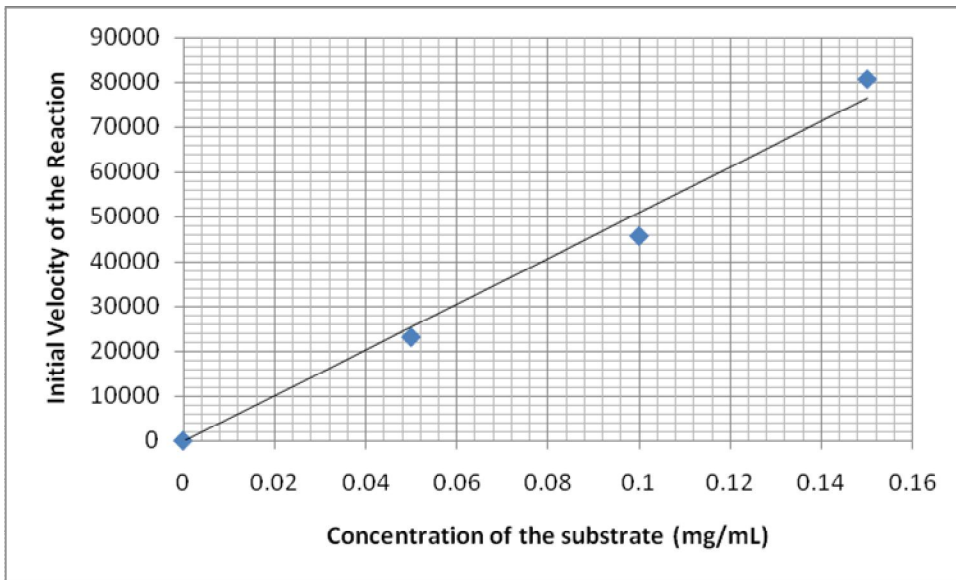
Figure 3.19: Linear relationship between the enzyme activity and substrate concentration

The rate of the production of porphyrin is proportional to the substrate concentration at least over the studied concentrations. At low values of substrate concentrations, the initial velocity, V_i, rises almost linearly with increasing [S]. But as [S] increases, the gains in V_i level off (forming a rectangular hyperbola). The maximum velocity of the reaction can be estimated using the graph.
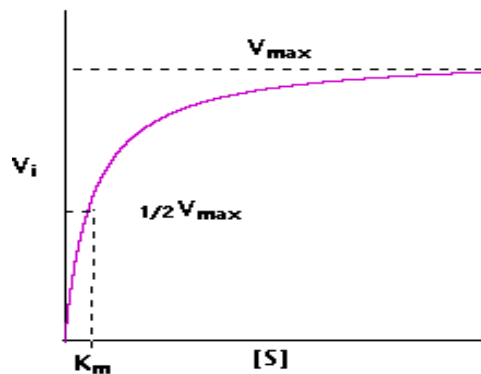
Figure 3.20: A typical saturation curve for an enzyme showing the relation between the concentration of substrate and rate[25]

The graph provides information on the K_m (Michaelis constant) which is the inverse measure of the affinity or strength of binding between the enzyme and its substrate.[24] We are in the process of further modifying our substrate for better enzyme kinetic studies. At this point we have limited our experiments to study the system functionality on various urokinase sources. Our observations strongly indicate that the urokinase substrate retains its activity after the chemical modifications and the proteolytic recognition and the hydrolysis of the substrate by urokinase is indeed a feasible process.

3.4.3 *In vitro* Study of Rat and Canine Urine Sample as a Screening Assay of Urokinase

3.4.3.1 Analysis of the Rat Urine Samples

The application of the above system was further extended to different sources of urokinase. At latter stages of cancer a high levels of urokinase is expressed in various types of cancer activity. Cancer patients have elevated levels of urokinase in the blood serum and that is correlated with the amount of urokinase excreted in the urine. Sidenius and coworkers[26] have reported presence of measurable amounts of urokinase in human urine samples collected from cancer patients. We investigated the activity of urokinase in urine samples of rats impregnated with MATB III type cancer cells. Further investigations were carried out with canine urine samples that were diagnosed with cancer, and were undergoing different stages and treatments.

The light-switch mechanism was tested using 3 samples of urine from rats impregnated with MATB III type cancer cells (rodent model for aggressive breast cancer), since urokinase can pass the mammalian kidneys and retains at least some activity in urine. The samples were collected 5 days (control), 14 days and 36 days after cancer impregnation, respectively, and immediately frozen at -80 ºC. Before testing, the urine samples were thawed and heated to 35 ºC. The following procedure was used to test each sample. The TCPP-nanoparticle nanoplatform

assembly was dissolved in pH=7.2 PBS buffer using sonication for 30 min. Next, 100 µL of

urine was added to a 0.1 mg/mL 2.0 mL, solution of the nanoplatform assembly in buffer. The

temperature was kept constant at 35 ℃. The fluorescence spectra were recorded every 2 min. As

can be seen from Figure 3.21, the luminescence from TCPP increased steadily over time for the

36 day urine. The control (5 day urine) did not demonstrate a significant increase in

luminescence. Figure 3.21 shows the plot of the relative intensities of the luminescence of TCPP

occurring at λ=656 nm using the measurement.

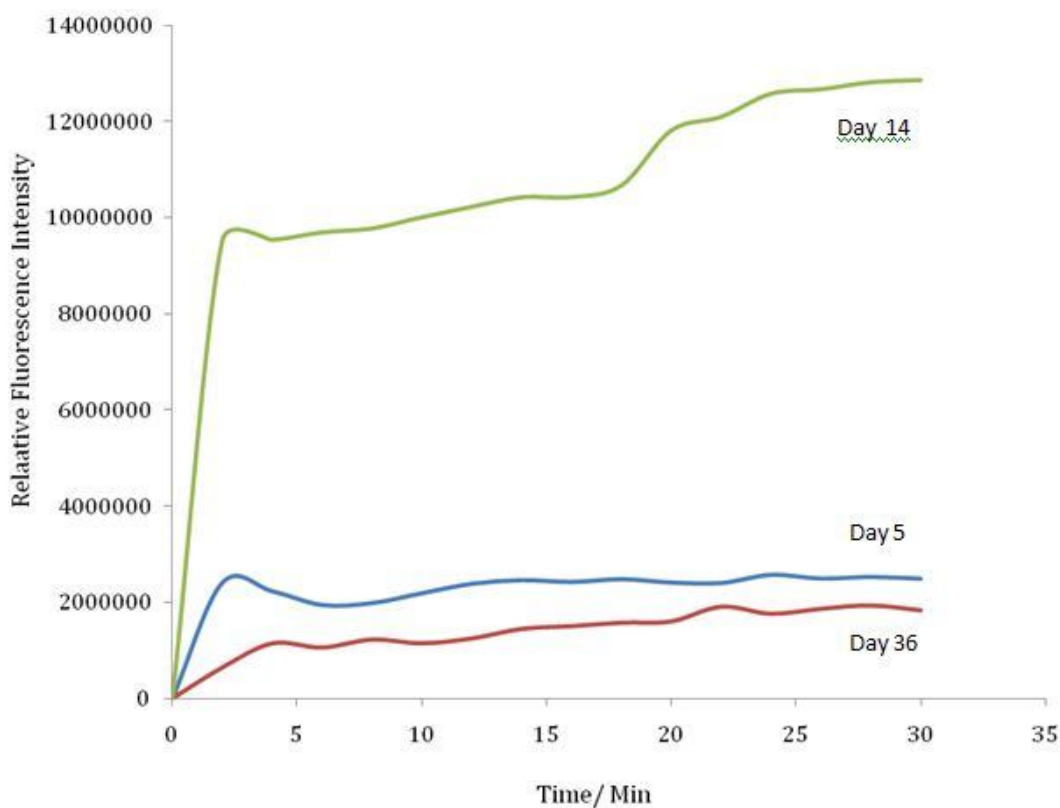Figure 3.21: The fluorescence spectra obtained for rat urine samples from Charles River female
mice, which were impregnated with MATB III cells at pH=7.2 PBS buffer at 35 ℃. (The
samples were obtained 5, 14, and 36 days after the impregnation)

According to the previous experiments, the enhancement in fluorescence signal is

proportional to the amount of urokinase present in the urine samples. Urokinase is an enzyme

overexpressed at latter stages of a cancer. According to the presented data, the day 36 rat urine samples showed a greater enhancement in fluorescence owing to the higher urokinase concentration.

3.4.3.2 Analysis of the Canine Urine Samples

The canine urine samples were analyzed following the same procedure. We received the urine samples from the Vetenary medicine laboratory at Kansas State University. The samples were identified with a code number. The urine samples were collected and stored at -80 °C prior to the experiment. The experiment was carried out at pH=7.2 buffer at 35 °C. The TCPP-nanoparticle, nanoplatform assembly was dissolved in the buffer using sonication for 30 min. The final concentration of nanoparticles in the solution was 0.1 mg/mL. 2.0 mL of the solution was taken to a fluorescence cuvette and initial reading was recorded. To this solution 25 µL of urine sample was added mixed and readings were recorded every 2 min. The samples were decoded as follows, sample 1 control, a normal healthy dog, sample 2 a dog diagnosed with anaplastic sarcoma; 2nd cancer; but was doing well with doxorubicin chemotherapy. The sample 3 was from a dog just diagnosed with renal lymphoma and was sick. The plot of time versus the enhancement of fluorescence indicates the amount of urokinase present in each sample.
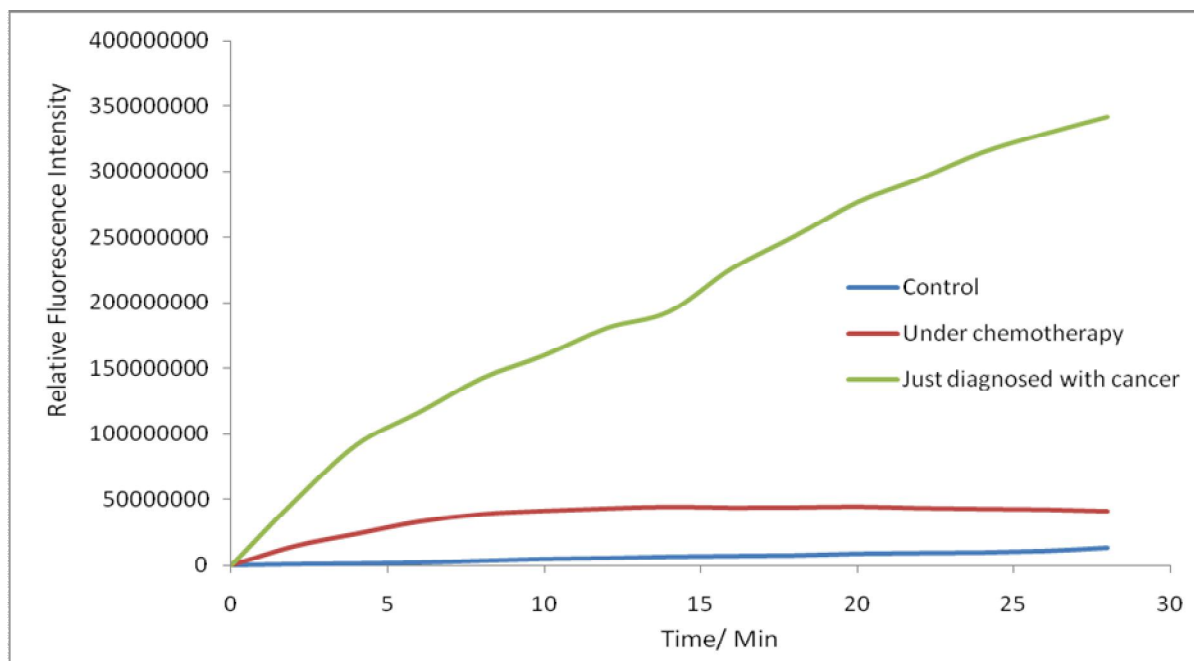
Figure 3.22: The plot of time versus the fluorescence enhancement of each run after addition of 25 μL of urine in pH=7.2 PBS buffer at 35 °C

The fluorescence signal generation of the samples after addition of dog urine was plotted against time. The data obtained indicates the feasibility of using this system for *in vitro* diagnosis of various cancers. The urine sample obtained from the dog just diagnosed with cancer showed a rapid increase in fluorescence and the measurements were collected every one minute, indicating a greater enzyme hydrolysis rate compared to other two samples. The urine sample from the dog undergoing chemotherapy, had a detectable enhancement in fluorescence than the control. Urine may contain fluorescent molecules that could excite in the 400-500 nm excitation wavelength range so it is important to analyze the urine sample by UV/Vis and fluorescence spectroscopy prior to the assays.

3.4.4 Time Resolved Spectroscopy

Time-resolved measurements clearly show that our light switch for cancer-related proteases is working. Free TCPP has a luminescence lifetime (monoexponential decay) of approx. 9 ns. In sharp contrast, Fe/Fe_3O_4-attached TCPP has a drastically shortened fluorescence lifetime due to the plasmon quenching effect of nanoparticle. When urokinase is added (after 10 min), part of the TCPP can escape the quenching influence of the NP.
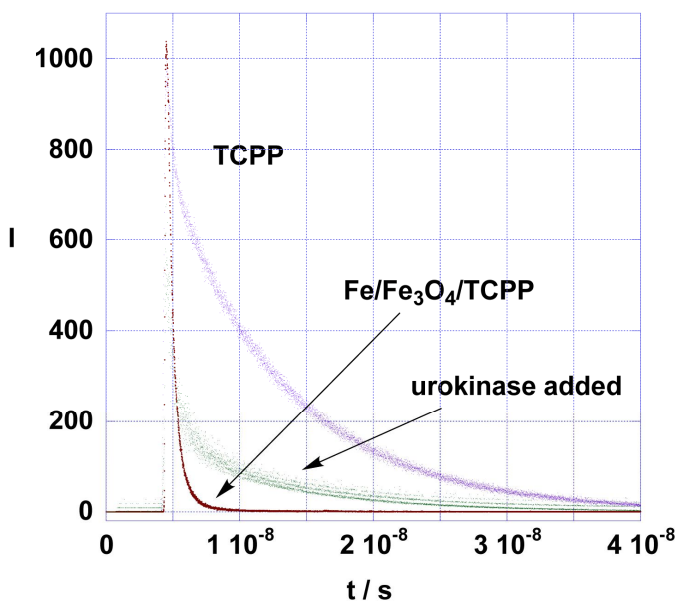
Figure 3.23: Fluorescence decay of free and Fe/Fe_3O_4-GAGSRGSAGAG-attached TCPP at 653 nm after excitation at 400 nm

Table 3.4: Fluorescence lifetimes (τ) and relative contributions (f) to the overall-decay for Fe/Fe_3O_4-GAGSRGSAGAG-TCPP (0.01 mg/mL) with and without 2.31 x 10^{-7} M urokinase in PBS

System	τ_1 (ns)	f_1	τ_2 (ns)	f_2
TCPP	9.02	100		
Fe/Fe_3O_4-	0.85	96	33.7	4

GAGSRGSAGAG-TCPP				
Fe/Fe_3O_4-GAGSRGSAGAG-TCPP, plus urokinase	1.39	78	30.0	22

3.5 Discussion

The assays utilize a nanoparticle linked by the oligopeptide-cleavage sequence to a porphyrin or other organic luminophore. In this method, the surface plasmon of the core/shell nanoparticle is able to quench the excited state emission spectra from the linked porphyrin. Once the protease cleaves the consensus sequence, the porphyrin is released and lights up, referred to herein as an "enzyme-triggered light switch." Advantageously, the appearance of an intense luminescence/fluorescence band allows for much more sensitive detection.

The detection of protease activity using the linked nanoplatforms may be done *in vivo* in a mammal. The assay can be administered intravenously by injection into the bloodstream. Alternatively, the assay dissolved in an aqueous buffer (e.g. phosphate buffered saline) can be administered by injection to a localized region, such as directly into or near the tumor site. Once the linked nanoplatform assay is in the vicinity of the cancerous tissue, excitation will be performed using an energy source of a light or a laser. The signal of porphyrin is preferably stronger in the cancerous tissues where the nanoplatforms aggregate than in the surrounding healthy tissue. In the presence of the protease, a typical change in the fluorescence will be observed. Thus, in the inventive method, this change in the optical properties of the tissues indicates the presence of a cancerous or precancerous cell in the mammal. The assay results can then be correlated with a prognosis for cancer progression, based upon the protease activity detected. Using either sensor method (*in vitro* or *in vivo*), the assay time of the present

invention is dependent upon the concentration of protease present in the sample or tissue. The cleavage speeds will increase by 3-5 times per order of magnitude of increase in protease concentration. In the presence of an aggressive tumor, assay time can be as fast as a fraction of a second. Thus, the faster the assay, the more aggressive the tumor, and the greater the likelihood of metastatic potential of the tumor. The use of protease-specific oligopeptides for the construction of a nanoparticle-based *in vivo* nanosensors for the determination of the metastatic potential of solid tumors permits the physician and surgeon to target the more advanced tumors first. When the assay is directly injected into the tumor region (or suspected tumor region), results can be determined about 30 min after injection. When the assay is administered intravenously, the results can be read within about 1 h after administration of the IV (to permit the assay to reach the target region), and up to 24 h after administration. In either case, once the assay is in the vicinity of the tumor, protease activity detected within 10 min can be correlated with a high probability that the tumor is aggressive. Preferably, if no activity is detected within the first 30 min, there is a very low probability that the tumor is aggressive. Likewise, for *in vitro* testing protease activity detected within 10 min can be correlated with a high probability that the tumor is aggressive, whereas no activity within the first 30 min after contacting the sample with the assay can be correlated with a very low probability that the tumor is aggressive.

The nanoplatforms may be used to detect protease activity in a fluid sample comprising of a biological fluid, such as urine or blood of a mammal. In one aspect, a urine sample is collected from the mammal and physically mixed with the nanoplatform assay. The changes in absorption and emission of the particles as the protease in the urine sample cleaves the oligopeptide linkers and will be observed over a time period of from about 1 second to about 30 min. These assay results (from urine or blood) can then be correlated with a prognosis

for cancer progression, based upon the specific protease activity detected, as discussed above with regard to the preferred proteases, uPA, MMP-1, MMP-2, and MMP-7, or based upon the speed of the assay.

3.6 Conclusions

The present invention provides multifunctional nanoplatforms for assessing the activity of a protease *in vivo* or *in vitro*, along with methods of detecting the presence of cancerous or precancerous tissues. The diagnostic nanoplatforms comprise nanoparticles linked via an oligopeptide linkage that comprises a consensus sequence specific for the target protease. Cleavage of the sequence by the target protease can be detected using various sensors, and the diagnostic results can be correlated with cancer prognosis. The majority of the experiments reported here were conducted with urokinase specific protease sequences. The observed kinetics permit an estimate of the amount of protease in the tissue. That is, the speed of cleavage is directly related to the concentration of urokinase, and thus, the speed of cleavage can be correlated with the aggressiveness of the tumor. We are in the process of designing and building of nanoplatforms specific to various enzymes for *in-vivo* and *in vitro* diagnosis of cancer.

3.7 Experimental

The fluorescence experiments were carried out in 4.0 mL quartz-cuvettes (Helma) using a spectrofluorometer (Fluoromax2) with dual monochromators and a diode array , and the UV reading were obtained from UV/Vis absorption spectrometer (HP 8453). Urokinase was purchased from Cell Sciences, Canton, MA. The urokinase-specific cleavage sequence (KGGSGRSAGGG) was purchased from Dr. John Tomich's laboratory at Department of Biochemistry, Kansas State University.

3.7.1 Synthesis of the Modified Iron/ iron Oxide Core Shell Nanoparticles

First, 6.0 mg of porphyrin (TCPP-COOH) was dissolved in 3.0 mL thionyl chloride. The solution was refluxed for 2 h at 85 ºC. The excess thionyl chloride was removed under vacuum. The solid was further dried under high vacuum for 6 h. After dissolving the solid in 5.0 mL dry DMF, 32.0 mg (4 equiv.) of cleavage sequence (KGGSGRSAGGG) was added, followed by 0.05 mL Et_3N and 2 mg DMAP. The solution was stirred at room temperature for 18 h. Stealth-coated nanoparticles were prepared by suspending 8.0 mg of Fe/Fe_3O_4 nanoparticles in 5.0 mL THF, followed by the addition of 20.0 mg of dopamine-based tetraethylene glycol ligand. The mixture was sonicated for 1h. The nanoparticles were then collected by a strong magnet, and the excess ligand was washed away by THF (5×3.0 mL). The dopamine tetraethylene glycol-modified (i.e., stealth coated) Fe/Fe_3O_4 nanoparticles were suspended in 5.0 mL THF, followed by the addition of 1.0 mL of the porphyrin tethered cleavage sequence in DMF solution and 6.0 mg of EDC were added. The mixture was sonicated at room temperature for 1 h. The nanoparticles were collected by a magnet again, and washed with THF (10×3.0 mL). 6.2 mg of porphyrin linked stealth-coated nanoparticles were obtained after drying under vacuum.

First, both the "free" sodium tetra-carboxylate porphyrin and the zinc-doped sodium tetracarboxylate porphyrin are tethered to Fe/Fe_3O_4-nanoparticles. To prepare the stealth-protected Fe/Fe_3O_4-nanoparticles, 35.0 mg of dopamine-tetraethylene glycol ligand were dissolved in 5.0 mL of THF. Next, 11.0 mg of Fe/Fe_3O_4-nanoparticles were added and sonicated at room temperature for 1 h. The solid was then collected with a magnet and solvent was decanted carefully. The solid was washed with THF (3×3.0 mL). After drying under vacuum for 2 h, 10.0 mg of stealth-protected nanoparticle product was obtained. To attach the porphyrins to the nanoparticles, the metalated porphyrin-oligopeptide solid was dissolved in 10.0 mL dry THF. Next, 5.0 mL of this solution was added to 10.0 mg of the dopamine tetraethyleneglycol

tethered Fe/Fe$_3$O$_4$-nanoparticles, followed by 10.0 mg 4-dimethylaminopyridine (DMAP) and 8.0 mg EDC. The resulting suspension was sonicated for 1 h at room temperature. The solid precipitate was collected by magnet and thoroughly washed with THF (8×2.0 mL). The sample was then dried under high vacuum for 5 h. 8.0 mg of product was obtained. The procedure was repeated to attach the non-metalated porphyrin to the nanoparticle.

3.7.2 Synthesis of Zn-doped Porphyrin

20.0 mg of TCPP and 20.0 mg of ZnCl$_2$.5H$_2$0 was dissolved in 5.0 mL of DMF. The mixture was heated to reflux for 1 h and then cooled to room temperature. To the cooled mixture 10.0 mL of water was added and the solid obtained was filtered under suction. The solid was then dried under vacuum and the final weight of the product was 15.0 mg. The compound was characterized using UV/Vis and fluorescence spectroscopy. The UV bands for TCPP are 417 nm, 512 nm, 589 nm, 645 nm. The Zn doped TCPP has characterized peaks at 425 nm, 553 nm and 593 nm. The fluorescence of TCPP is at 653 nm and 714 nm and Zn-doped TCPP showed fluorescence at 601 nm and 649 nm.
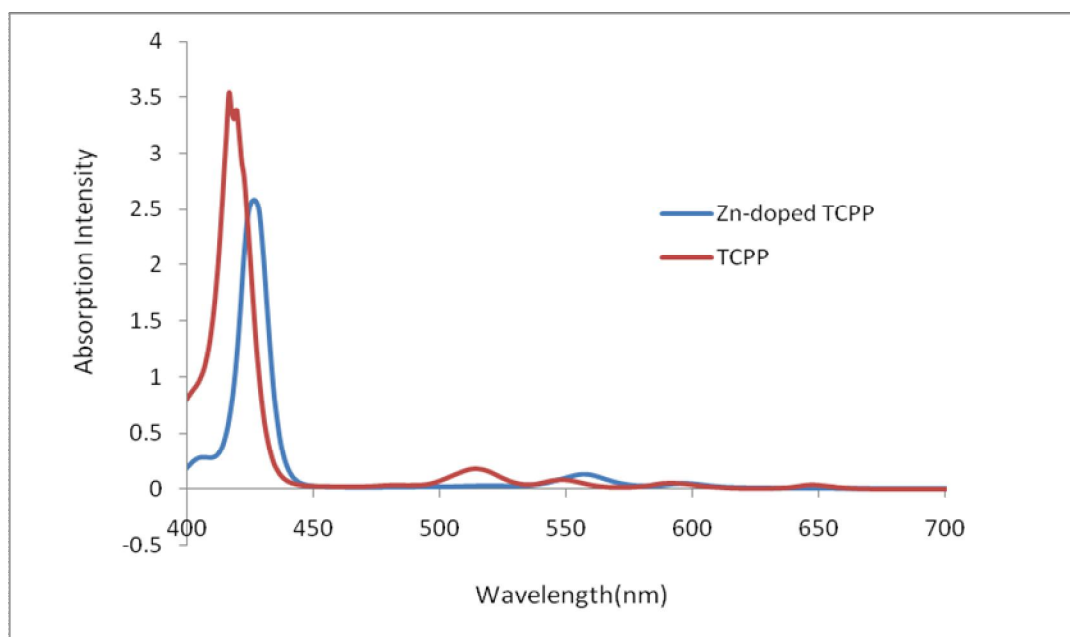
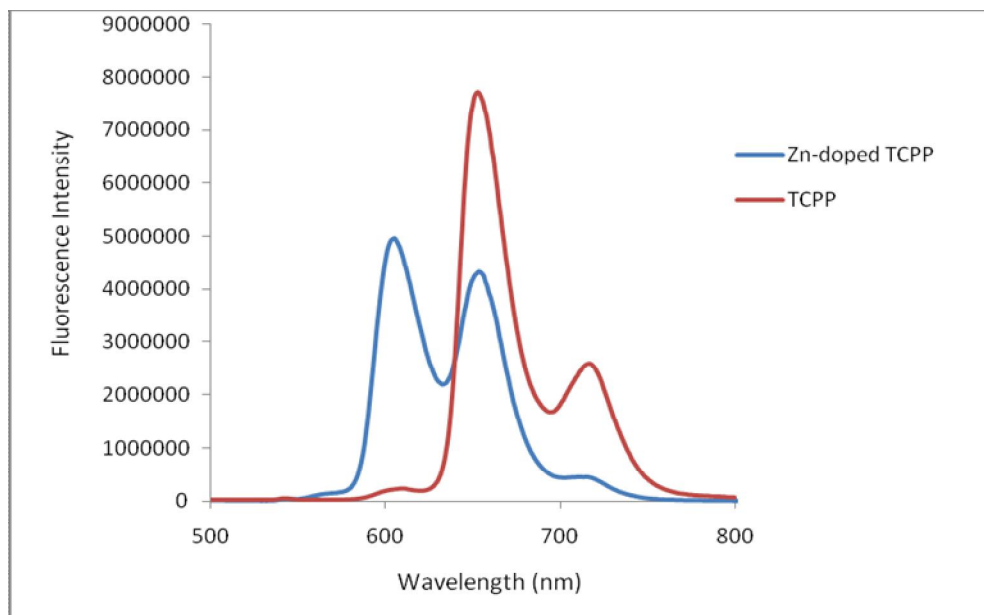Figure 3.24: UV/Vis spectrum of TCPP and Zn^{2+} doped TCPP

Figure 3.25: Fluorescence spectrum of TCPP and Zn^{2+} doped TCPP (Excitation at 417nm)

The concentration dependence of fluorescence from zinc doped sodium tetracarboxylate porphyrin, tethered to the Fe/Fe_3O_4-NPs and "free" (non-metalated) sodium tetracarboxylate porphyrin, tethered to the Fe/Fe_3O_4-NPs on the increasing concentration of nanoparticles was studied. The experiment was carried out in pH=7.2 PBS buffer. The concentration of porphyrin was 1.0×10^{-6} M. Both porphyrin modified nanoparticles were dissolved in 3.0 mL of PBS buffer after sonication for 30 min. The solutions were filtered and the initial fluorescence was recorded at an excitation wavelength of 420 nm. The experiment was repeated after adding 100.0 µL of 0.1 mg/ml nanoparticles in PBS buffer.

The effect of the nanoparticle concentration on zinc-doped sodium tetracarboxylate porphyrin and sodium tetracarboxylate porphyrin, in a relative molar ratio of 9 to 1 was monitored in pH=7.2 PBS buffer. The modified nanoparticles were dissolved in 2.0 mL PBS buffer and the final concentration was 0.1 mg/mL. The titration was carried out adding 100.0 µL

of nanoparticles solution and recording the fluorescence at 420 nm after each addition. The same experiment was conducted adding unbound sodium tetracarboxylate porphyrin in PBS.

3.7.3 *In vivo* Urokinase Assay

3.7.3.1 Study the Enzyme Kinetics of Urokinase on a Urokinase-specific Cleavage Sequence (KGGSGRSAGGG) (The concentration of Urokinase was the variable)

A series of urokinase enzyme solutions were prepared ranging from 2.31×10^{-7}, 2.31×10^{-8}, 2.31×10^{-9}, 2.31×10^{-10}, 2.31×10^{-11} M in pH=7.2 PBS buffer. The urokinase enzyme was purchased from Cell Sciences, Canton, MA. The dilution series was prepared and stored at $-20^{o}C$ for further use.

The nanoparticles modified with the dopamine tetraethylene stealth coating attached to porphyrin via the cleavage sequence, was dissolved in pH=7.2 buffer to obtain a final concentration of the nanoparticles was 0.2 mg/mL. The nanoparticles were dissolved completely in the buffer after sonication for 30 min at 25 ºC. The solution was filtered. The initial fluorescence was recorded for the solution (excitation at 417 nm). To this solution 50.0 µL of urokinase was added and the fluorescence change was observed every 2 min. The readings were collected until there was no significant change in the intensity of fluorescence observed. The experiment was repeated for all 5 solutions keeping the concentration of the nanoparticles a constant. The temperature was maintained at 25 ºC. The relationship between the concentration of urokinase against the change of the fluorescence was analyzed.
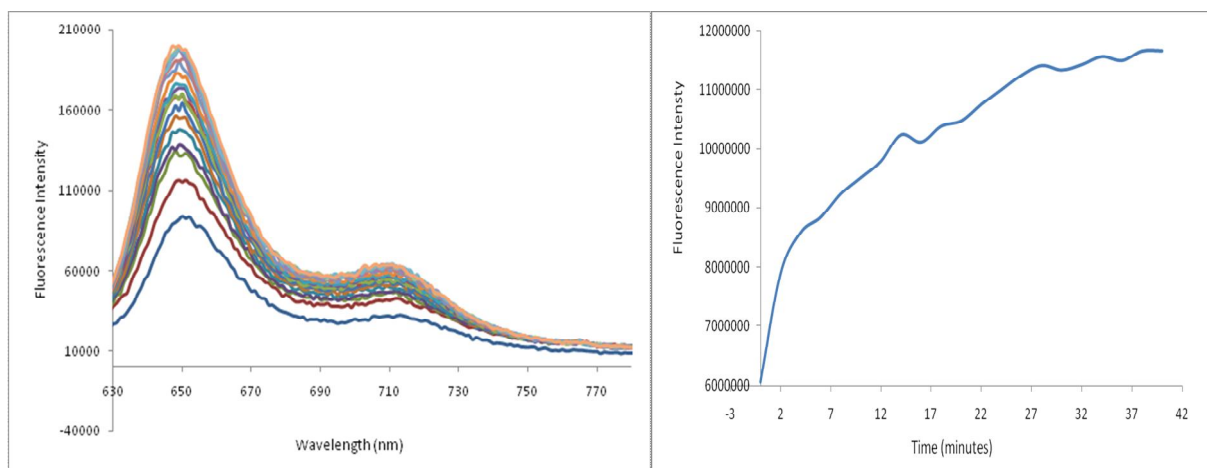
Dilution 1

Figure 3.26: The change in the fluorescence intensity of porphyrin with time. The concentration of urokinase was 2.31×10^{-7} M

Dilution 2
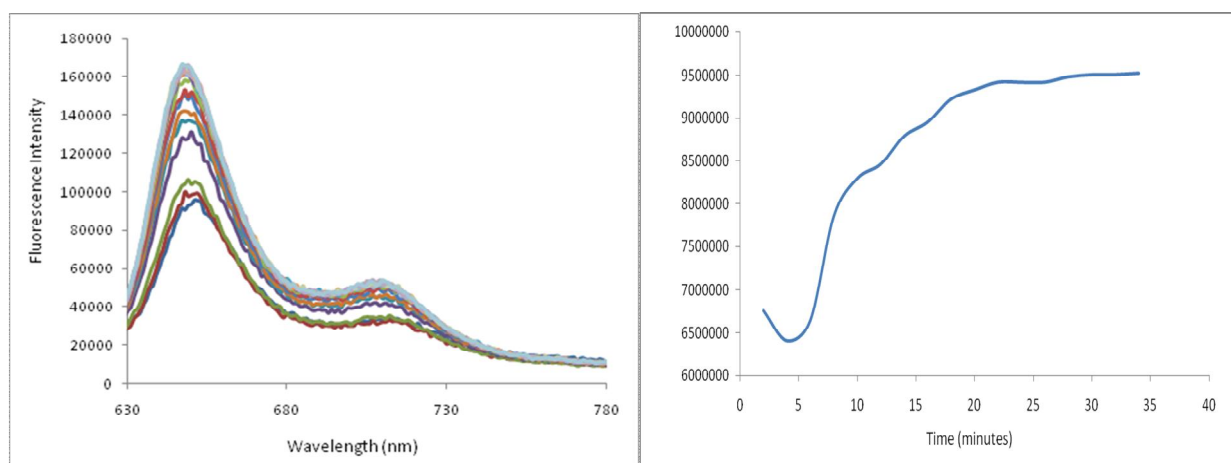

Figure 3.27: The change in the fluorescence intensity of porphyrin with time. The concentration of urokinase was 2.31×10^{-8} M
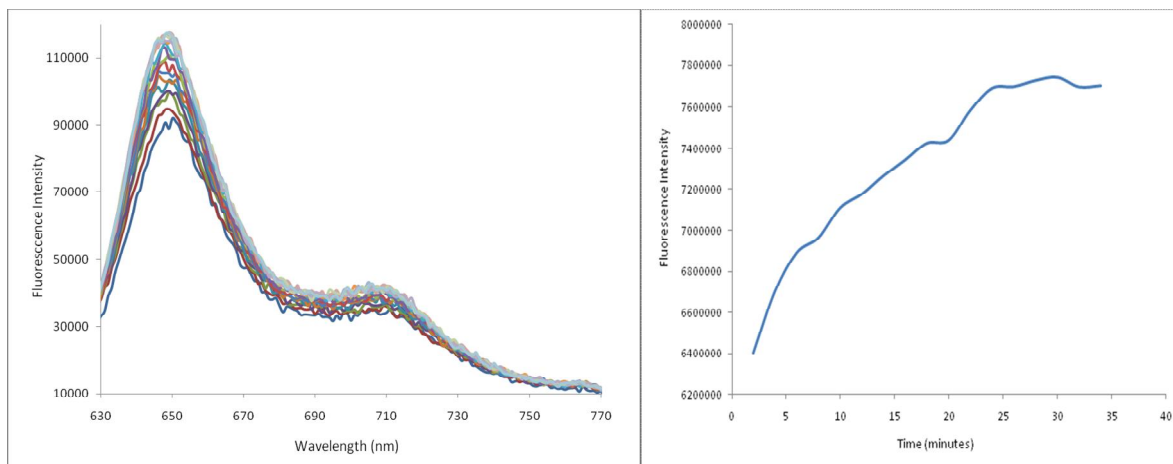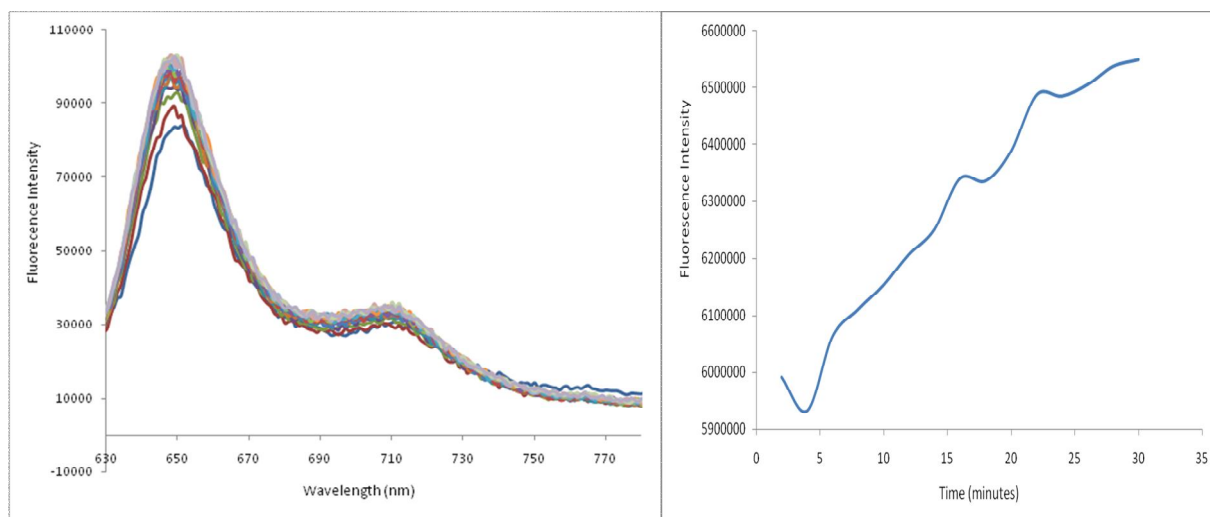
Dilution 3

Figure 3.28: The change in the fluorescence intensity of porphyrin with time. The concentration of urokinase was 2.31×10^{-9} M

Dilution 4

Figure 3.29: The change in the fluorescence intensity of porphyrin with time. The concentration of urokinase was 2.31×10^{-10} M
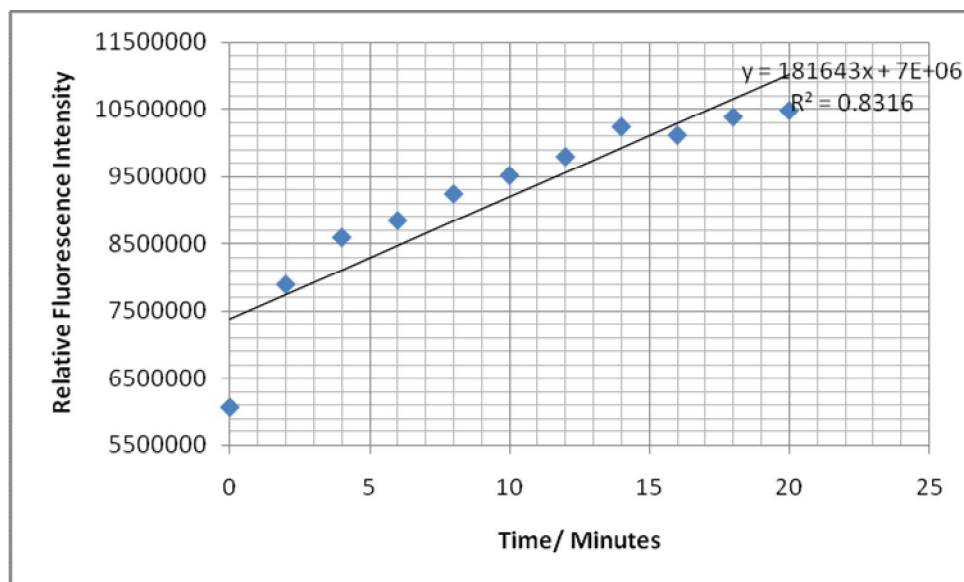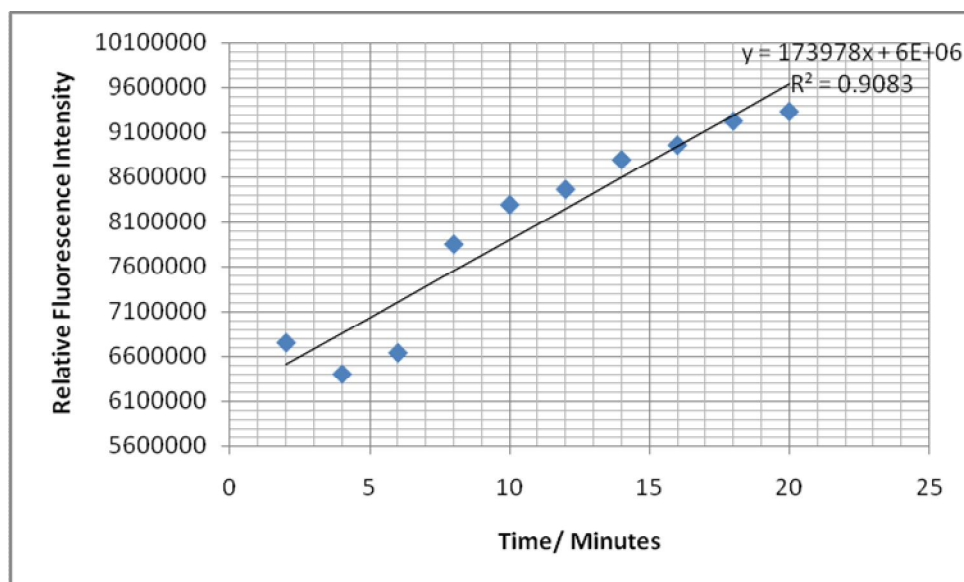
Figure 3.30: The plot of relative fluorescence intensity change of the system with time. From the plot the initial rate for the cleavage of the substrate from urokinase was calculated. The concentration of urokinase was 2.31×10^{-7} M
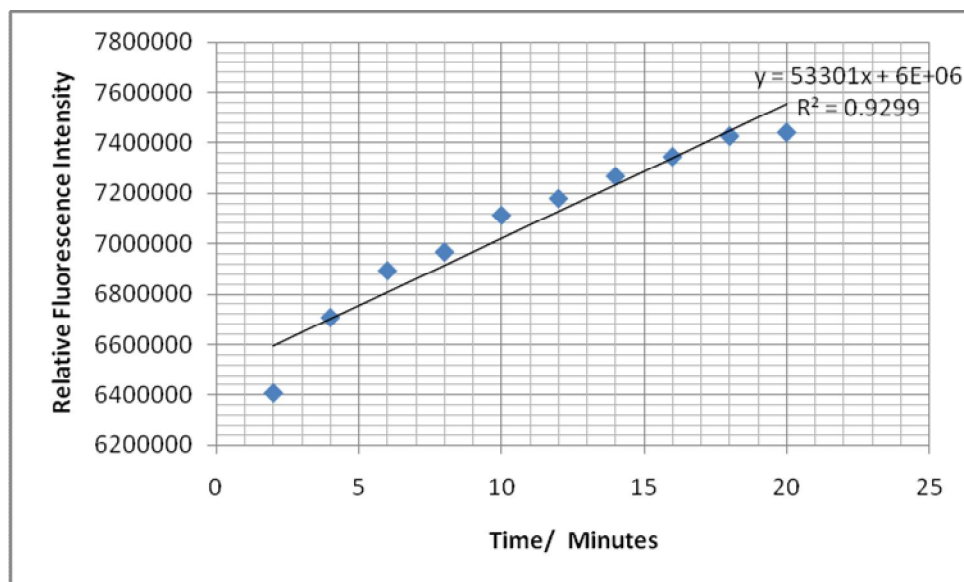

Figure 3.31: The plot of relative fluorescence intensity change of the system with time. From the plot the initial rate for the cleavage of the substrate from urokinase was calculated. The concentration of urokinase was 2.31×10^{-8} M

Figure 3.32: The plot of relative fluorescence intensity change of the system with time. From the plot the initial rate for the cleavage of the substrate from urokinase was calculated. The concentration of urokinase was 2.31×10^{-9} M
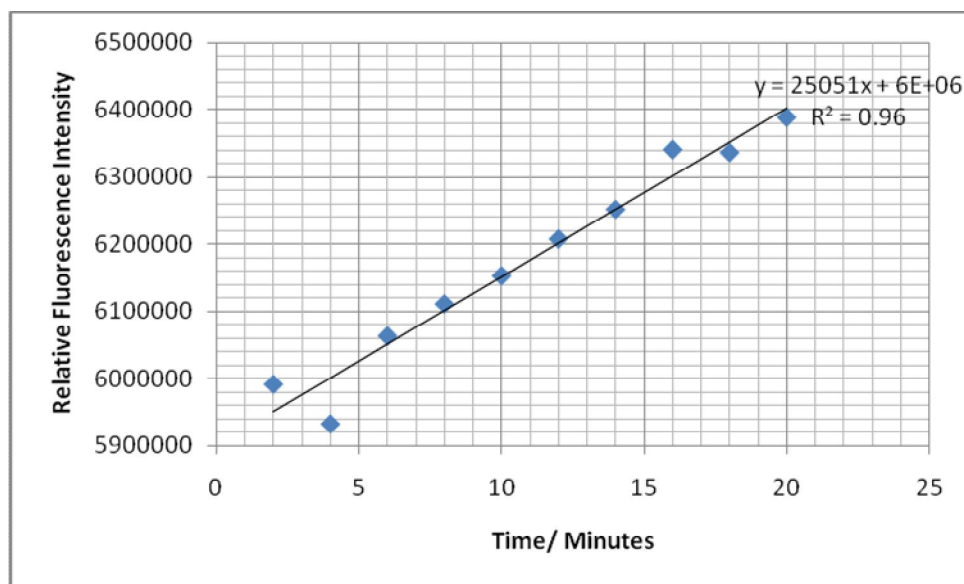

Figure 3.33: The plot of relative fluorescence intensity change of the system with time. From the plot the initial rate for the cleavage of the substrate from urokinase was calculated. The concentration of urokinase was 2.31×10^{-10} M

3.7.3.2 Study the Enzyme Kinetics of Urokinase on a Urokinase-specific Cleavage Sequence (KGGSGRSAGGG)(The concentration of the nanoparticles was the variable)

To study the effect of the substrate concentration on the reaction velocity of urokinase catalyzed peptide cleavage, a solution of 2.31×10^{-7} M urokinase was prepared in pH=7.2 PBS buffer. The cleavage sequence was purchased from Cell Sciences, Canton, MA. The dilution series was prepared and stores at -20 $^{\circ}$C for further use.

A series of nanoparticles solutions were prepared by dissolving the modified particles in pH=7.2 buffer to obtain a final concentration of 0.05, 0.1, 0.15 mg/mL. The nanoparticles were dissolved completely in the buffer after sonication for 30 min at 25 ºC. The solution was filtered. The initial fluorescence was recorded for the solution (excitation at 400 nm). To this solution 50.0 µL of urokinase was added and the fluorescence change was observed every 2 min. The readings were collected until the there was no significant change in the intensity of fluorescence observed. The experiment was repeated for different concentrations of nanoparticles with the same urokinase concentration. The temperature was maintained at 25 ºC. The effect of the substrate concentration on the rate of the enzyme catalyzed reaction was studied.
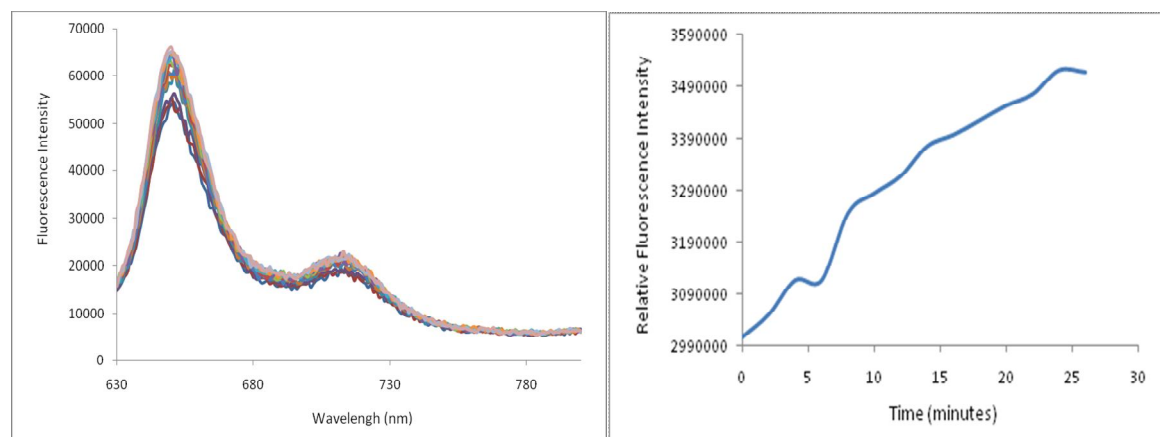

Figure 3.34: The change in the fluorescence intensity of porphyrin with time. The concentration of nanoparticles was 0.05 mg/mL
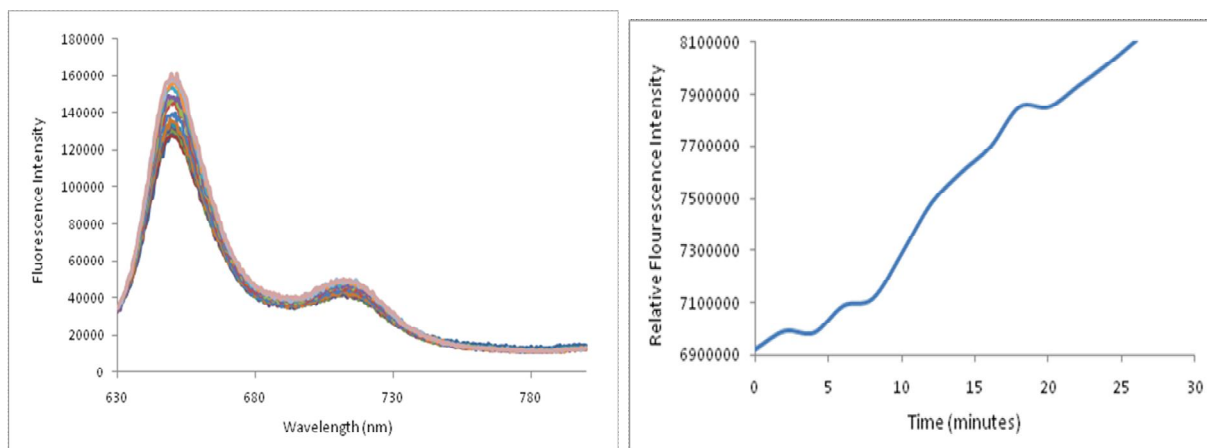
Figure 3.35: The change in the fluorescence intensity of porphyrin with time. The concentration of nanoparticles was 0.1 mg/mL
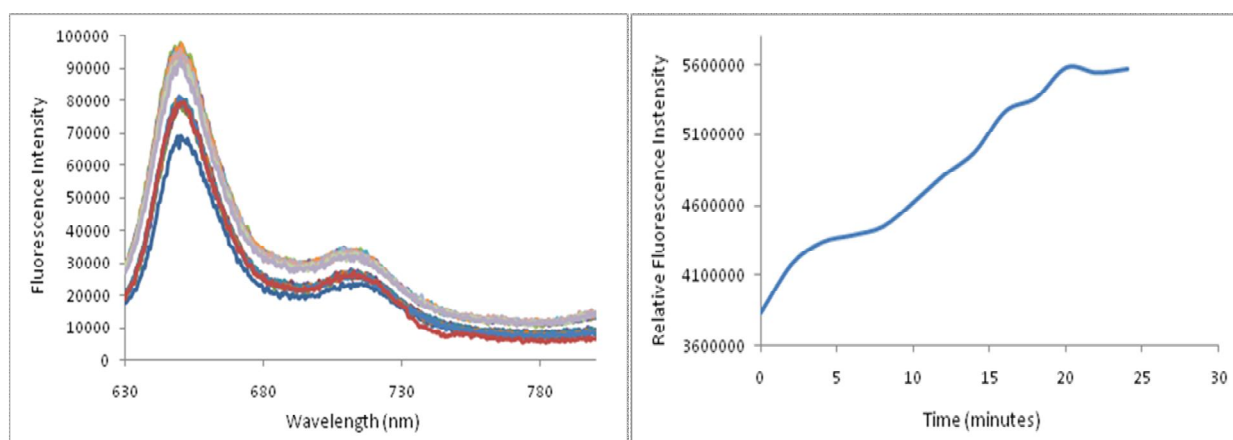

Figure 3.36: The change in the fluorescence intensity of porphyrin with time. The concentration of nanoparticles was 0.15 mg/mL

3.7.4 Measurements of the Emission Lifetimes of Free and Nanoparticle-attached TCPP in PBS

Time resolved emission results are obtained by time-correlated single photon counting. In the apparatus used in these studies, the sample is excited with approximately 15 nJ, 15 fs pulses from the second harmonic of a Ti:sapphire laser at a repetition rate of 80 MHz. The laser pulse is characterized using a home-built autocorrelator with a GaAsp photodiode as the non linear medium. The excitation wavelength is fixed at 400 nm with excitation spot sizes of about 1 mm.

Detection is accomplished with a Hamamatsu 6 μ MCP PMT and a time correlated single photon counting electronics. Wavelength selection is accomplished using interference filters. The instrument response function is determined by observing the laser scatter, and is about 60 ps FWHM. Polarized emission detection is accomplished using an emission polarizer in a perpendicular detection scheme relative to the excitation laser. During the experiment the samples were placed in a covered box to avoid the entering light.

References

1. Kobayashi,H.; Ogawa, M.; Alford, R.; Choyke, P. L.; Urano, Y., New Strategies for Fluorescent Probe Design in Medical Diagnostic Imaging, *Chem. Rev.*, **2010**, *110(5)*, 2620–2640

2. Andersson-Engels, S.; Klinteberg, C.; Svanberg, K.; Svanberg, S., *In vivo* Fluorescence Imaging for Tissue Diagnostics, *Phys. Med. Biol.*, **1997**, *42*, 815-824

3. Rao, J.; Dragulescu-Andrasi, A.; Yao, H., Fluorescence Imaging *in vivo*: Recent Advances, *Current Opinion in Biotechnology*, **2007**, *18(1)*, 17-25

4. Oh, E.; Hong, M.; Lee, D.; Nam, S.; Yoon, H. C.; Kim, H., Inhibition Assay of Biomolecules Based on Fluorescence Resonance Energy Transfer (FRET) Between Quantum Dots and Gold Nanoparticles, *J. Am. Chem. Soc.*, **2005**, *127(10)*, 3270–3271

5. Bremer, C.; Tung, C.; Weissleder, R., *In vivo* Molecular Target Assessment of Matrix Metalloproteinase Inhibition, *Nature Medicine*, **2001**, *7*, 743 - 748

6. Josephson, L.; Kircher, M. F.; Mahmood, U.; Tang, Y., Weissleder, R., Near-Infrared Fluorescent Nanoparticles as Combined MR/optical Imaging Probes, *Bioconjugate Chem.*, **2002**, *13(3)*, 554–560

7. Dubertret, B.; Calame, M,; Libchaber, A. J., Single-mismatch Detection Using Gold-Quenched Fluorescent Oligonucleotides, *Nature Biotechnology*, **2001**, *19*, 365 - 370

8. Hirata, N.; Tanabe, K.; Narita, A.; Tanaka, K.; Naka, K.; Chujo, Y.; Nishimoto, S., Preparation and Fluorescence Properties of Fluorophore-labeled Avidin–biotin System

Immobilized on Fe3O4 Nanoparticles Through Functional Indolequinone Linker, *Bioorganic & Medicinal Chemistry*, **2009**, *17(11)*, 3775-3781

9. Weiss, S., Measuring Conformational Dynamics of Biomolecules by Single Molecule Fluorescence Spectroscopy, *Nature Structural Biology*, **2000**, *7*, 724 - 729

10. Zhang, L.; Xu, Q.; Xing, D.; Gao, C.; Xiong, H., Real-time Detection of Caspase-3-like Proteases Activation *in vivo* Using Fluorescence Resonance Energy Transfer During Plant Programmed Cell Death Induced by Ultraviolet-C Overexposure, *Plant Physiology*, **2009**, *150*, 1773-1783

11. Saini, S.; Singh, H.; Bagch, B., Fluorescence Resonance Energy Transfer (FRET) in Chemistry and Biology: Non-Förster Distance Dependence of the FRET Rate, *Journal of Chemical Sciences*, **2006**, *118(1)*, 23-35

12. Sekar, R. B.; Periasamy, A., Fluorescence Resonance Energy Transfer (FRET) Microscopy Imaging of Live Cell Protein Localizations, *J Cell Biol.*, **2003**, *160(5)*, 629-633

13. Tyas, L.; Brophy, V.A.; Pope A.; Rivett, A.J.; Tavaré, J.M., Rapid Caspase-3 Activation During Apoptosis Revealed Using Fluorescence-resonance Energy Transfer, *European Molecular Biology Organization*, **2000**, *1(3)*, 266-70

14. Lee1, M., Matrix-Degrading type II Transmembrane Serine Protease Matriptase: Its Role in Cancer Development and Malignancy, *Journal of Cancer Molecules*, **2006**, *2(5)*, 183-190

15. Fischer,K.; Lutz, V.; Wilhelm, O,; Schmitt, M.; Graeff, H,; Heiss, P.; Nishiguchi, T,; Harbeck, N.; Kessler, H.; Luther, T.; Magdolen, V.; Reuning, U., Urokinase Induces Proliferation of Human Ovarian Cancer Cells: Characterization of Structural Elements Required for Growth Factor Function, *FEBS Letters*, **1998**, *438(1)*, 101-105

16. Hedstrom, L., Serine Protease Mechanism and Specificity, *Chem. Rev.*, **2002**, *102(12)*, 4501–4524

17. Duffy, M.J., Proteases as Prognostic Markers in Cancer, *Clin Cancer Res.*, **1996**, *2(4)*, 613-618

18. Liu, S.; Bugge, T. H.; Leppla, S. H., Targeting of Tumor Cells by Cell Surface Urokinase Plasminogen Activator-dependent Anthrax Toxin, *The Journal of Biological Chemistry*, **2001**, *276(21)*,17976-17984

19. Egeblad, M.; Werb,Z., New Functions for the Matrix Metalloproteinases in Cancer Progression, *Nat Rev Cancer*, **2002**, *2(3)*, 161-174

20. Rundhaug1, J. E., Matrix Metalloproteinases, Angiogenesis, and Cancer, *Clinical Cancer Research*, **2003**, *9*, 551-554

21. Itoh, T.; Tanioka, M.; Matsuda, H.; Nishimoto, H.; Yoshioka, T.; Suzuki, R.; Uehira, M., Experimental Metastasis is Suppressed in MMP-9-deficient Mice, *Clinical and Experimental Metastasis*, **1999**, *17(2)*, 177-181

22. Turk, B. E.; Huang, L. L.; Piro, E. T.; Cantley, L. C., Determination of Protease Cleavage Site Motifs Uusing Mixture-based Oriented Peptide Libraries, *Nature Biotechnology*, **2001**, *19*, 661-667.

23. Fields, G.B., Protease-Activated Delivery and Imaging Systems, *The Cancer Degradome Proteases and Cancer Biology*, **2008**, 827-851

24. Laurence, M.A., Biochemistry, Second edition, Neil Patterson Publishers, Englewood Cliffs, NJ 07632

25. http://users.rcn.com/jkimball.ma.ultranet/BiologyPages/E/EnzymeKinetics.html

26. Sier, C.F.; Sidenius, N.; Mariani, A.; Aletti, G.; Agape, V.; Ferrari, A.; Casetta, G.; Stephens R.W.; Brünner, N.; Blasi, F., Presence of Urokinase-type Plasminogen Activator Receptor in Urine of Cancer Patients and Its Possible Clinical Relevance, *Lab Invest.*, **1999**, *79(6)*, 717-22

Chapter 4 - Magnetic Resonance Imaging (MRI) with Modified Fe/Fe$_3$O$_4$ Core Shell Nanoparticles

4.1 Introduction

Magnetic Resonance Imaging (MRI) is a non-invasive diagnostic tool to obtain images of the inside of a body. It provides information about pathological alterations, such as tumors of living tissues (medical imaging). MR images are based on the variations of the spin-relaxation times of protons (^{1}H), which are excited using radio frequency (RF) pulse patterns in an external magnetic field.[1] The variation of the T_1 -relaxation (spin-lattice or longitudinal relaxation time) and T_2-relaxation (spin-spin or transverse relaxation time) times generate image contrasts between different tissues and pathologies depending upon how the MR image is collected.[2]

More specifically, when a patient is placed within the magnetic field (B_0) of the magnet of the MRI apparatus, the protons of the H_2O present in the body line up in the direction of the external magnetic field (B_0). In addition, the magnetic axis of each proton starts to rotate (precess) around the axis of this field. Some of these protons precess with their magnetic moments aiming in a direction closely parallel to the external magnetic field, while others precess with their magnetic moments aiming close to anti-parallel to the direction of magnetic field. This creates a net proton magnetic moment in the tissues of the patient, with the tissue magnetism (M) oriented exactly parallel to the external field (B_0). Short radio frequency pulses are transmitted into the patient at different angles changing the orientation of the proton magnetic moments, inducing an electric current in a receiver coil located outside of the patient's body. These signals are used to reconstruct the MR image. In general, tissues exhibiting a strong

152

magnetism will induce strong signals and appear bright in the image, while tissues exhibiting weak magnetism will induce weak signals and appear dark.[2]

To reconstruct an image, several MR signals are needed, and several pulses must be transmitted. Between the pulse transmissions, the protons undergo two different relaxation processes: T_1 and T_2 relaxation. The MRI operator determines whether the tissue contrast will be determined mainly by differences in T_1 (T_1-weighted image) or T_2 (T_2-weighted image) by modifying the pulse sequence and timing. Pulse sequences are performed by computer programs that control the hardware aspects of the MRI measurement process.
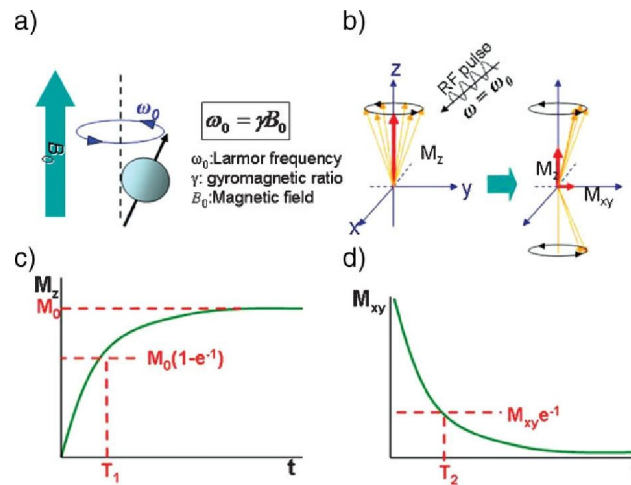
Figure 4.1: Principle of magnetic resonance imaging. a) Spins align parallel or antiparallel to the magnetic field axis and precess under Larmor frequency (v_0). b) After induction of RF pulse, direction of spins changes. Excited spins take relaxation process of c) T_1 relaxation and d) T_2 relaxation[2]

T_1 is defined as the time until the excited nuclei net magnetization has regained 63% of its original value. The T_1 relaxation time is a measure of the time that an excited nuclei requires to realign with the external magnetic field. T_2 relaxation is caused by energy exchange of the excited nuclei and nearby magnetic nuclei. T_2- weighted imaging relies on local dephasing (loss

of phase coherence) of spins oriented at an angle to the external field following the transmission of the RF pulse. T_2 is defined as the time when the transverse magnetization (M_{xy}) has lost 63% of its original value.[2] In other words T_2 refers to the time taken for M_{xy} to decay to 37% of its initial value.[3]

T_1 results in a decrease in the net magnetization (M_z) and the T_2 involves an induced magnetization on the perpendicular plane (M_{xy}). This is the basic principal behind T_1 and T_2 contrast agents.[2] The contrast agents shorten the T_1 and T_2 relaxation times by interacting with neighboring water molecules. Positive contrasting agents generate a brighter image by decreasing the T_1 relaxation time, while the shortening of T_2 lead to a darker image.[2,4] Paramagnetic and superparamagnetic MRI contrast agents can be used to change the signal intensity of the tissue being imaged by altering the T_1 and/or T_2 relaxation times of the ^1H nuclei in the tissue. Gadolinium based paramagnetic complexes are commonly used as positive contrast agents in MRI imaging.[5] Super paramagnetic iron oxide nanoparticles have attracted great attention as T_2 weighted imaging agents or negative contrasting agents. These nanoparticles range form 10-300 nm with water soluble, biocompatible shells. Feridex is a commercially available dextran coated iron oxide contrasting agent.[6] These agents exhibit strong T_1 relaxation properties, and due to susceptibility differences to their surrounding, also produce a strongly varying local magnetic field which enhances T_2 and T_2^* relaxations of the ^1H spins in the tissue. For iron nanoparticles to act as T_1 contrasting agents the core of the nanoparticles has to be around 5 nm and the particles must be well coated with biocompatible layers such as polyethylene glycol to prevent aggregation, which could lead to larger particle size and T_2 signal enhancement.[4] Small Particle Iron Oxide Nanoparticles (SPIONs) of less than 300 nm can remain intravascular for several hours and thus can serve as blood pool agents. However, they

can also be quickly taken up by the reticuloendothelial system and become distributed among healthy tissue and accumulate in the liver. They also tend to clump together into ineffective sizes due to the isoelectric charge on the surface at physiological pH. So the outer coating is an important factor to shift the isoelectric point and limit metabolic clearance.[6]

T_2^*, also known as the effective transverse relaxation time is a measure of the combination of transverse relaxation and magnetic field inhomogeneity resulting from tissue inherent factors and differences in the magnetic field. For example spin spin interactions between macromolecules in tissues can change the local magnetic field experienced by the protons and could result in a change of the actual magnetic field.[2]

The T_2^* can be calculated as follows,

$$\frac{1}{T_2^*} = \frac{1}{T_2} + \gamma B_s$$

γB_s = susceptibility effect
γ = gyromagnetic ratio
B_s = the strength of the locally varying field[2]

Relaxivity or the efficiency of a contrast agent is further defined as the relaxivity or the change in the relaxation rate per unit concentration of the contrast agent. The relaxivities r_1 and r_2 are measures of the ability of the agent to enhance or decrease, respectively, the longitudinal or transversal relaxations of the proton spins in the tissue.[4] The longitudinal and transverse relaxivities are calculated at different concentrations of the contrasting agents. The inverse of the T_1 and T_2 measurements are used in the calculation and a new parameter R_1 and R_2 is introduced.[7]

$$R_1 = \frac{1}{T_1}$$

$$R_2 = \frac{1}{T_2}$$

$$r_1 = \frac{T_{1,observed}^{-1} - T_{1,water}^{-1}}{c(Fe)} \qquad\qquad r_2 = \frac{T_{2,observed}^{-1} - T_{2,water}^{-1}}{c(Fe)}$$

The ratio of r_2/r_1(relaxivity ratio) is a useful factor in predicting the efficiency of the contrast agent and for a T_1 contrast agent the ratio should be small as possible.[4] The Gadolinium based positive contrast agents have relaxivity ratio of 1-2. For a negative contrast agent such as iron oxide nanoparticles the value should be at least 10.[7] The iron oxide nanoparticles are reported used as T_1 weighted imaging agents due to their smaller r_2/r_1 ratio. The T_1 values for these particles are greater than T_2 values.[7]

4.2 Results and Discussion

4.2.1 The NMR Study of T_1- and T_2-Relaxation Behavior of Fe/Fe$_3$O$_4$ Nanoparticles

The influence of various concentrations of the inventive Fe/Fe$_3$O$_4$ nanoparticle MRI contrast agents on the T_1 - and T_2-relaxation behavior of ^{1}H-spins in water were determined using a 400 MHz NMR (Varian, field strength 9.4 T). Nanoparticles stabilized with tetraethylene glycol ligands, and non-stealth coated nanoparticles were used. The stealth coated nanoparticles featured chemically attached porphyrins. Increasing concentrations (between 10 and 160 µg) of Fe/Fe$_3$O$_4$ nanoparticles were suspended (non-stealth) or dissolved (stealth coated) in 1.0 mL of H$_2$O/D$_2$O (90/10 v/v). The measurements were conducted at 300 K in standard NMR tubes, Standard T_1 and T_2 pulse sequences were used.

Pulse sequences

T_1 - Inversion recovery pulse sequence:[d1]-[180]-[t]-[90]-[acquisition], where the delay, t, was varied and for T_2 - Carr-Purcell Meiboom-Gill (CPMGT) or spin-echo pulse sequence:

[d1]-[90]-[spin-echo]-[acquisition], where the spin-echo period is a t-180-t block and the delay, t, was varied.
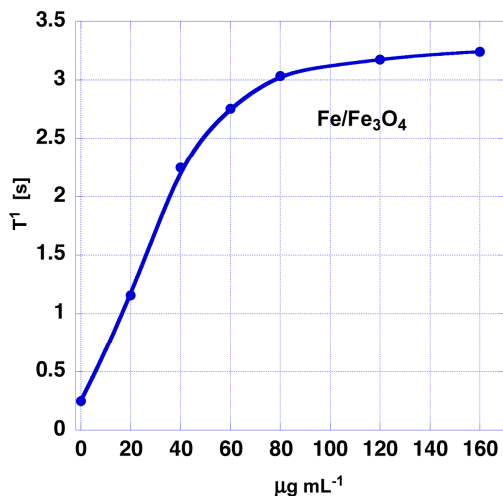
Figure 4.2: T_1-relaxation times of H_2O/D_2O (9/1) at 9.4 T, dependence on the concentration of Fe/Fe_3O_4-NPs
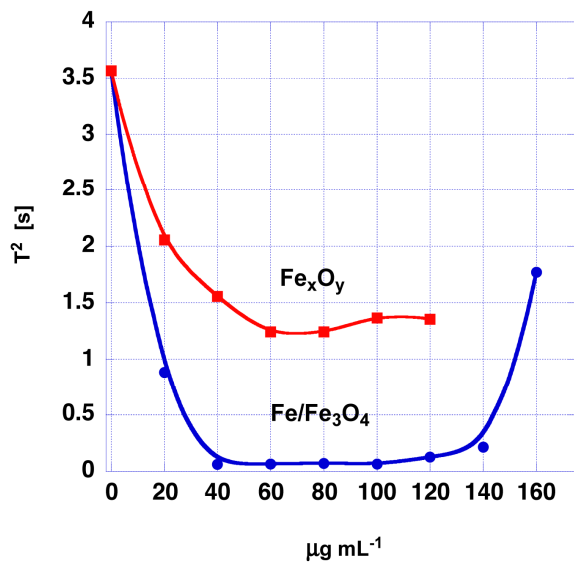
Figure 4.3: T_2-relaxation times of H_2O/D_2O (9/1) at 9.4 T, dependence on the concentration of NPs (Fe/Fe_3O_4, Fe_xO_y)

157

Table 4.1: Pulse sequence results

Amount of Fe (μg mL^{-1})	T_1 (A)	T_2 (B)	r_2/r_1
0	0.2475	3.565	
20	1.157	0.8845	-0.26765
40	2.245	0.06156	-4.4406
60	2.754	0.0652	-4.09456
80	3.033	0.0721	-3.66215
120	3.172	0.1253	-2.06712
160	3.239	1.77	-0.07623

The field strength used was higher than in clinical MRI's (0.5-3 T), however, the data obtained at higher fields are very comparable to the lifetimes in clinical MRI applications. The ratio of r_2/r_1 is dependent on the field strength and the concentration of the particles. We have obtained lower values for ratio of r_2/r_1 indicating suitability of the particles as T_1 imaging agents

The T_1-weighted MRI-images combined in Figure 4.4 have been recorded using the Hitachi 7000 permanent magnet MRI (B=0.38 T), which is available in the college of Veterinary Medicine at Kansas State University. It must be noted that the instrument used, possesses only a relatively small magnetic field. This is not high resolution MRI instrument. However, this experiment clearly indicates the suitability of our new materials as MRI contrast agents.

4.2.2 Study of Cells Loaded with Nanoparticles

Three million cells were taken into NMR tubes in 100.0 μL of PBS buffer. For the MRI studies one tube was filled with cells loaded with nanoparticles. The cells were mixed with 0.8% of agar and 1% of copper sulfate in distilled water and boiled by microwaving for 5-7 min and cooled it for 1 h. T_1 images of the vials were obtained.
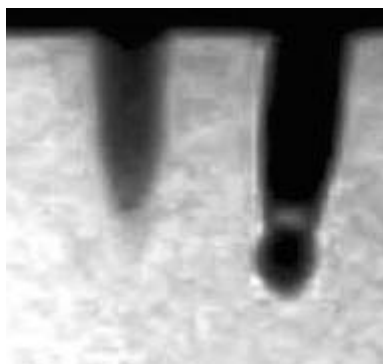
Figure 4.4: left tube contains cells loaded with magnetic Fe/Fe_3O_4 nanoparticles. Right tube is the control.

4.2.3 MRI Study of Mice Injected with Nanoparticles

Two eight-week-old CB57BL/6 female mice (euthanized prior to this experiment) were injected with 0.50 mL of water (A) or magnetic nanoparticles (B-D). Site (B) contained 500 mg of stealth-coated Fe/Fe_3O_4 nanoparticles. Site (C) contained 25 mg of mouse stem cells, isolated from bone marrow, that have been allowed to take up porphyrin-tethered stealth coated Fe/Fe_3O_4 nanoparticles. Site (D) contained 500 mg of commercially available iron oxide nanoparticles (Feridex®). MRI data was acquired using a Hitachi 7000 permanent magnet MRI. Standard T_1 and T_2 pulse sequences were used. As shown in the MR image in Figure 4.5, except for the injection of water, discernible T_1 contrasts were obtained for all injections.

10
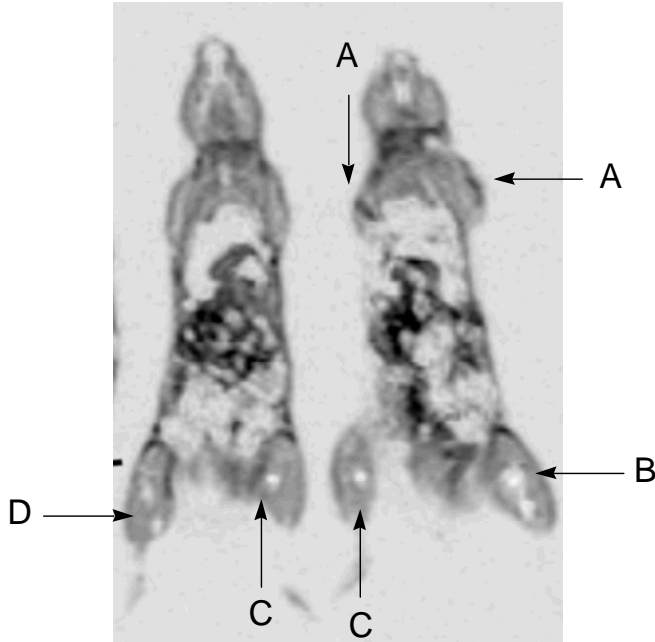
Figure 4.5: MRI (Hitachi 7000 permanent magnet MRI) of two CB57BL6 female mice.

The T_1 images shown in Figure 4.6 have been recorded in the Oklahoma Imaging Center, MRI FACILITY, Oklahoma Medical Research Facility (OMRF), 825 NE, 13th ST, Oklahoma City, Oklahoma, 73104. All images were recorded with C57/BL6 mice, which were impregnated with lung melanomas (melanomas growing on the surface of the lung tissue) 18 days prior to the measurements. The mice have been euthanized 6 h prior to these measurements. The measurements have been conducted on a Varian 500 MHz NMR-spectrometer featuring a wide-bore probe for rodent MRI measurements.
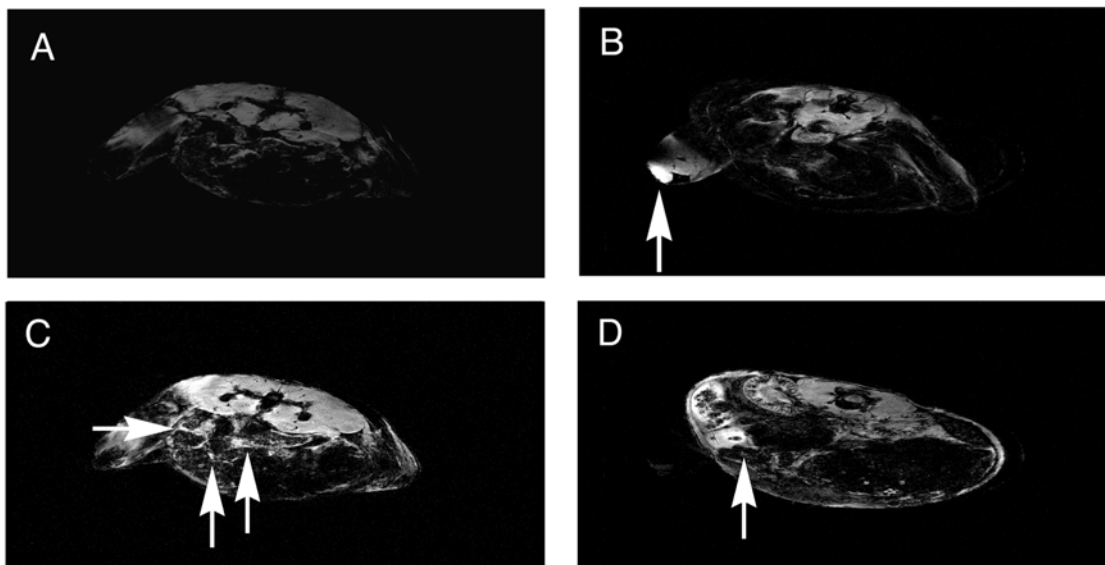
Figure 4.6: Control experiment: Healthy mouse that has been intravenously injected with 100 μg of stealth-coated, TCCP-labeled Fe/Fe$_3$O$_4$-nanoparticles 24 h before euthanasia (30 h prior to the MRI measurement); B: Intramuscular injection of TCCP-labeled Fe/Fe$_3$O$_4$/stealth nanoparticles (50 μg, 24 h before euthanasia (30 h prior to the MRI measurement); C: Accumulation of the nanoparticles in lung melanomas causes a sharp T$_1$-constrast (as labeled by the three arrows). The mouse has been intravenously injected with 100 μg of stealth-coated, TCCP-labeled Fe/Fe$_3$O$_4$-nanoparticles 24 h before euthanasia (30 h prior to the MRI measurement). D: Accumulation of the TCCP-labeled Fe/Fe$_3$O$_4$-nanoparticles in the liver (arrow) and kidney (above liver) of the same mouse than shown in C (different position).

4.3 Conclusion

The TCPP and tetraethylene glycol modified Fe/Fe$_3$O$_4$ core shell nanoparticles were tested as T$_1$ MRI contrasting agents. In the mice obtained images, the presence of the nanoparticles in the tissues is clearly visible as brighter areas, indicating the suitability of the particles as T$_1$ contrast agents. .

4.4 Experimental

NMR data acquisition

All measurements were carried out on a Varian Inova NMR instrument operating at 400 MHz for ^{1}H resonance using a direct detection probe at 25 ^{o}C. The VNMRJ software was used for data acquisition, processing and curve fitting.

The spin-spin relaxation times (T_2) were measured with the CPMG (Carr-Purcell-Meiboom-Gill) pulse sequence $90^o – [d2 – 180^o – 2*d2– 180^o – d2]_n$ where the total time for T_2 relaxation bt=(4n*d2) was varied from 0.02 to 8s over 12 equally spaced values. A number of 4 scans were collected for each bt with a 60s recycle delay between sequences.

The spin-lattice relaxation times (T_1) were measured using the inverse recovery pulse sequence: $180^o – d2 – 90^o$. The delay times, d2, were varied between 125 s to 131 s over 21 values equally spaced on a logarithmic scale. A number of 4 scans were collected for each d2 by applying a 80 s recycle delay between sequences.

In both cases, the NMR data obtained at various delay times were plotted showing the evolution from the negative to positive intensities. An exponential curve fitting was used to determine the values of T_1 and T_2.

References

1. http://onoimaging.blogspot.com/2008/07/basic-principles-of-magnetic-resonance.html

2. Pankhurst, Q. A.; Connolly, J.; Jones, S. K.; Dobson, J., Applications of Magnetic Nanoparticles in Biomedicine, *Journal of physics -London- D Applied Physics*, **2003**, *36(13)*, 167-181

3. Gluch, L., Magnetic Resonance in Surgical Oncology: I - On the Origin of the Spectrum, *ANZ Journal of Surgery*, **2005**, *75(6)*, 459–463

4. Tromsdorf, U. I.; Bruns, O. T.; Salmen, S. C.; Beisiegel, U.; Weller, H., A Highly Effective, Nontoxic T_1 MR Contrast Agent Based on Ultra Small PEGylated Iron oxide Nanoparticles, *Nano Lett.*, **2009**, *9(12)*, 4434–4440

5. Sosnovik, D.E.; Nahrendorf, M.; Weissleder, R., Magnetic Nanoparticles for MR Imaging: Agents, Techniques and Cardiovascular Applications, *Basic Res Cardiol.*, **2008**, *103(2)*, 122–130

6. Cho, S.J.; Jarrett, B.R.; Louie, A.Y.; Kauzlarich, S.M., Gold-coated Iron Nanoparticles: a Novel Magnetic Resonance Agent for T_1 and T_2 Weighted Imaging, *Nanotechnology*, **2006**, *17(3)*, 640-645

7. Meledandri, C. J.; Stolarczyk, J. K.; Ghosh, S.; Brougham, D. F., Nonaqueous Magnetic Nanoparticle Suspensions with Controlled Particle Size and Nuclear Magnetic Resonance Properties, *Langmuir*, **2008**, *24(24)*,14159–14165

Appendix A - NMR
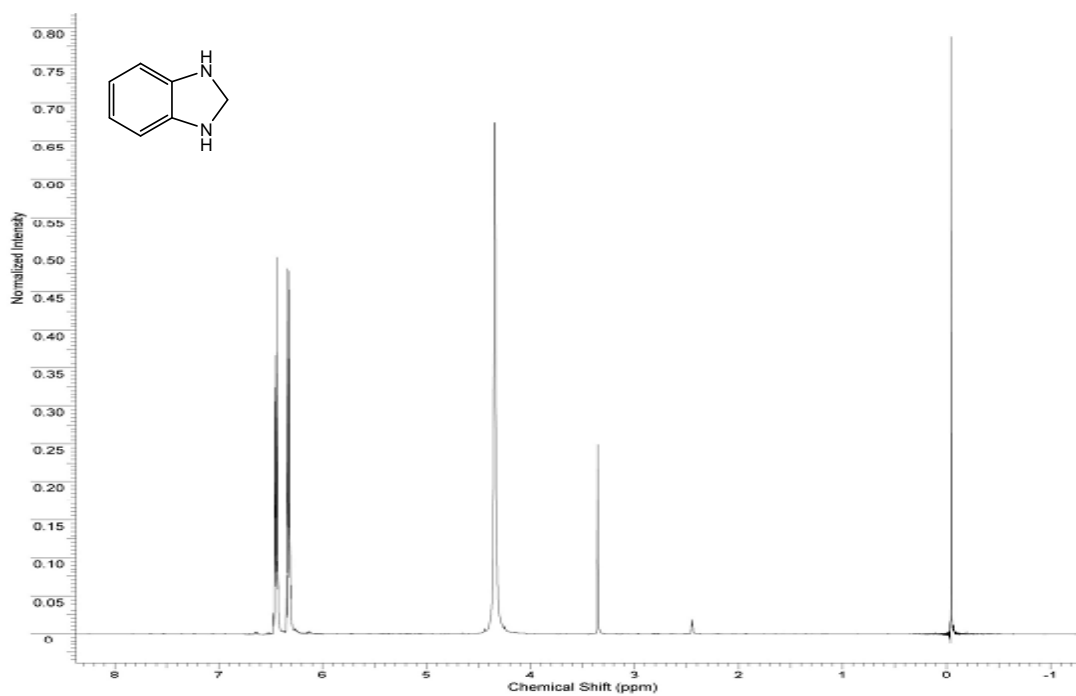
Figure A.1: ^{1}H NMR of 1.10.1
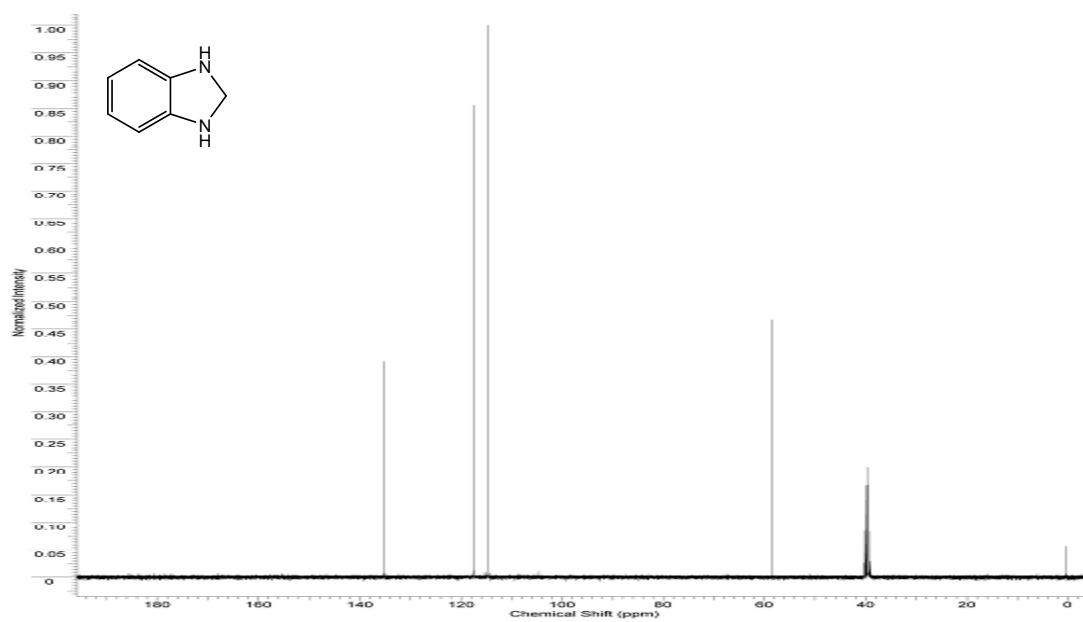
Figure A.2: ^{13}C NMR of 1.10.1
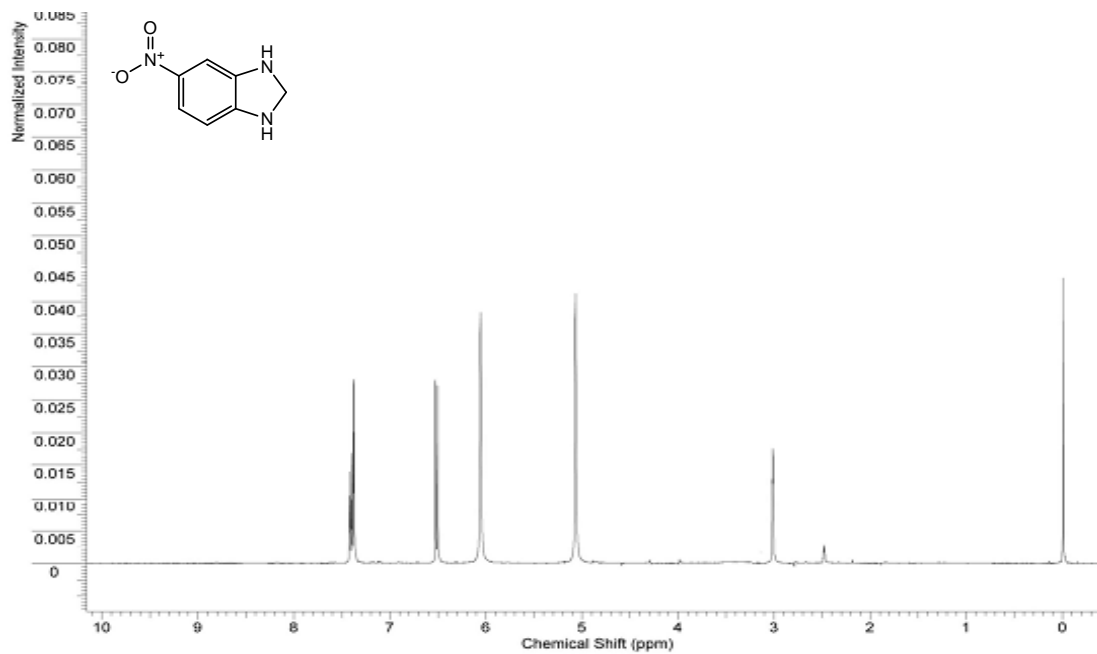
Figure A.3: ^{1}H NMR of 1.10.2
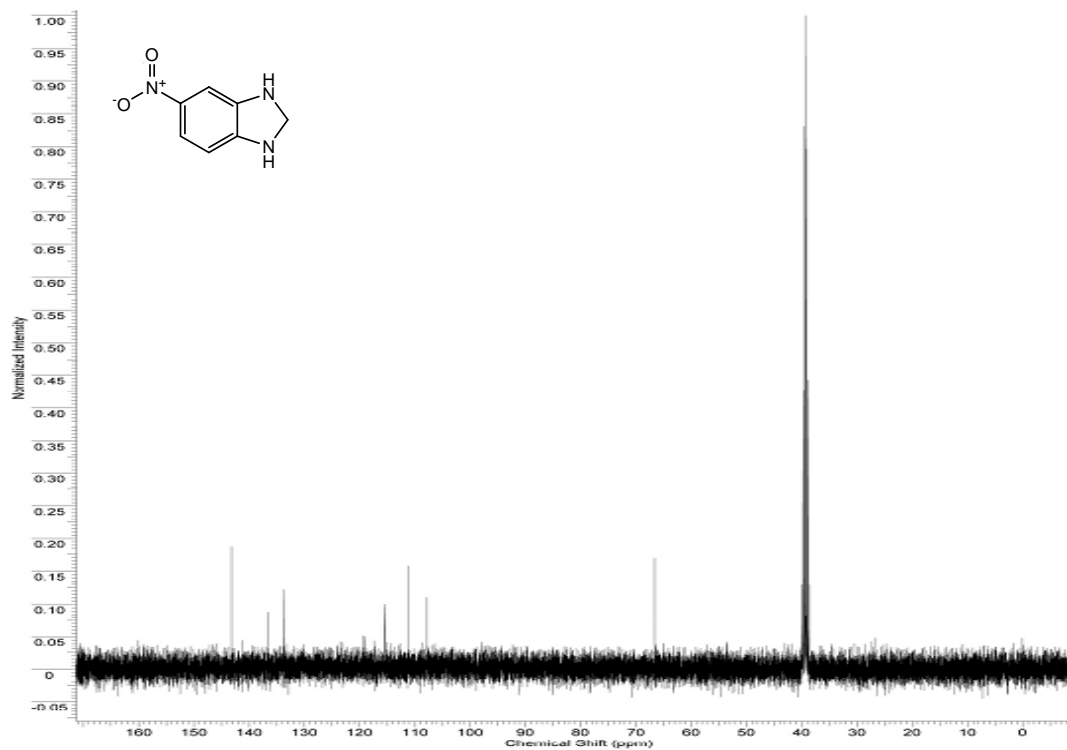
Figure A.4: ^{13}C NMR of 1.10.2
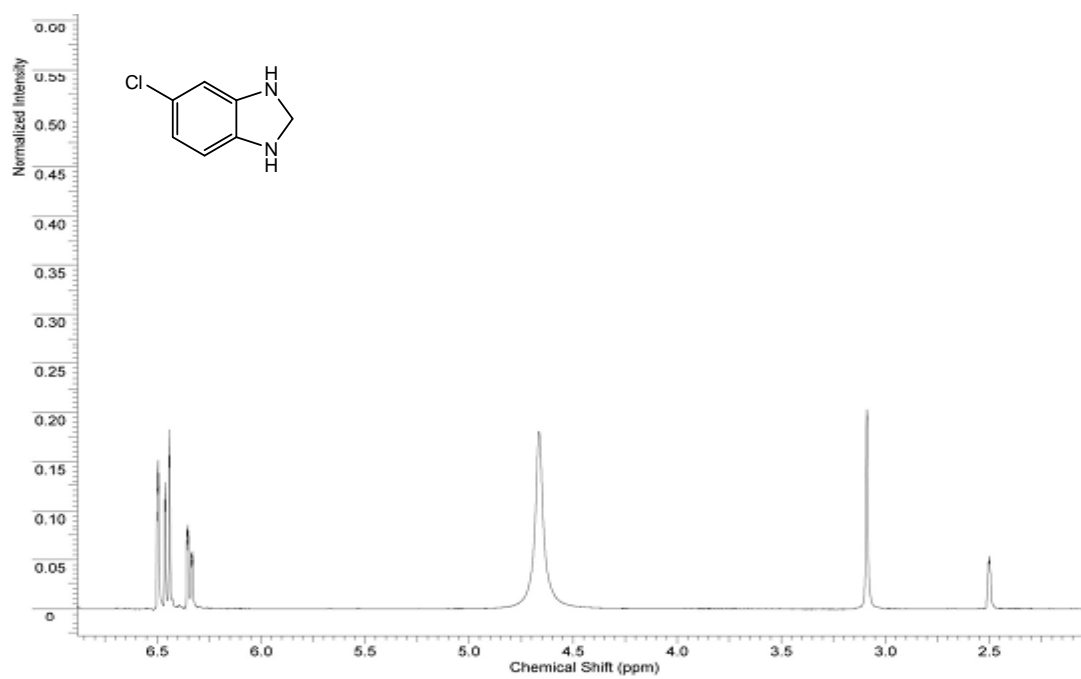
Figure A.5: ^{1}H NMR of 1.10.3
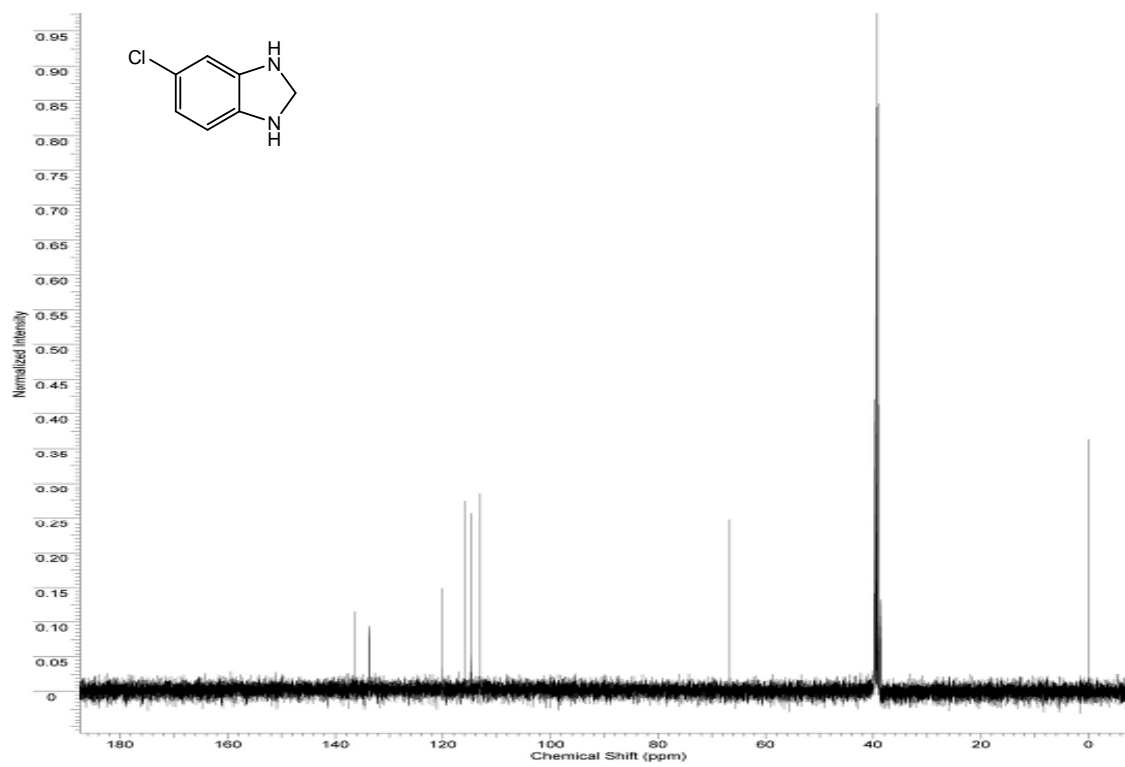
Figure A.6: ^{13}C NMR of 1.10.3
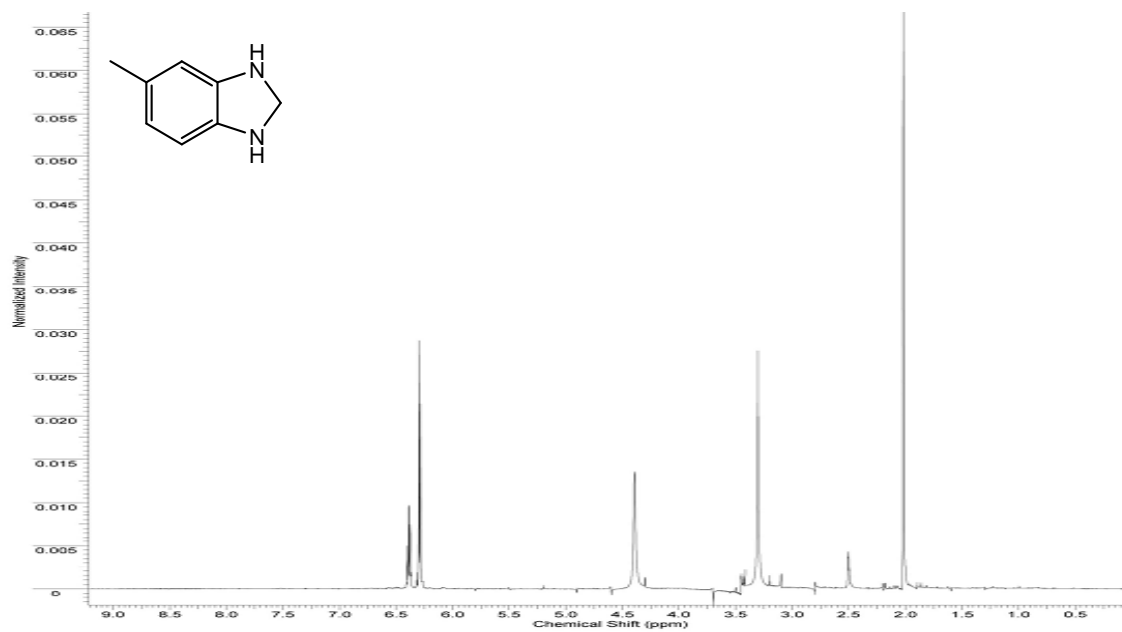
Figure A.7: ^{1}H NMR of 1.10.4
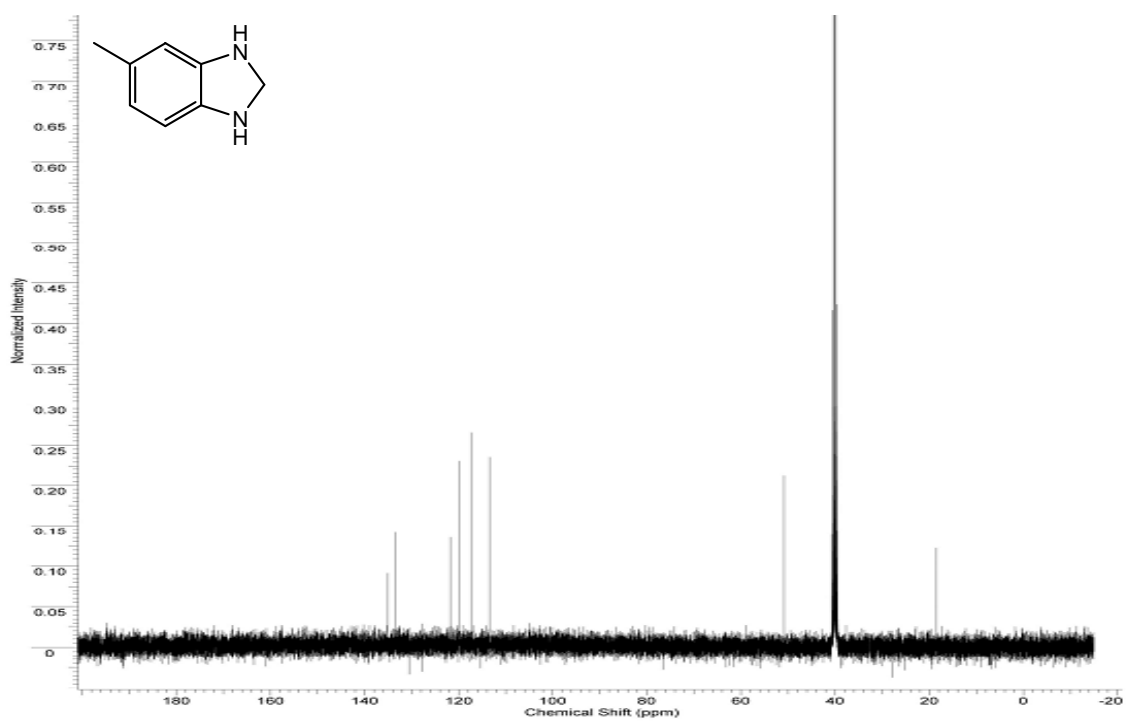
Figure A.8: ^{13}C NMR of 1.10.4

Figure A.9: ^{1}H NMR of 1.10.5

Figure A.10: ^{13}C NMR of 1.10.5
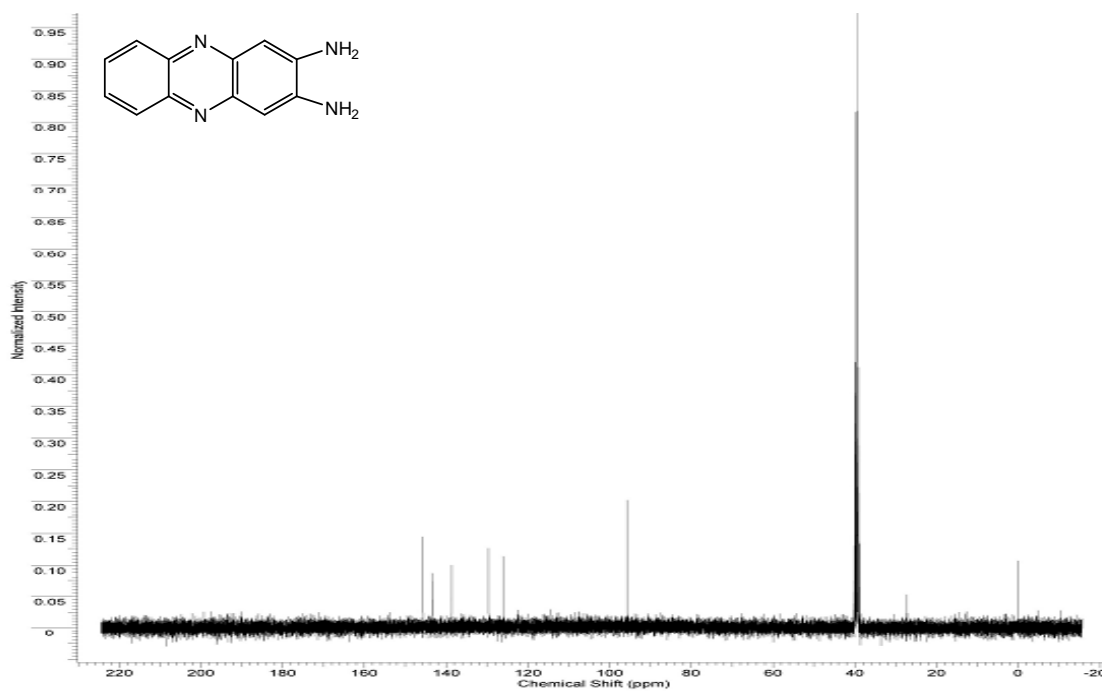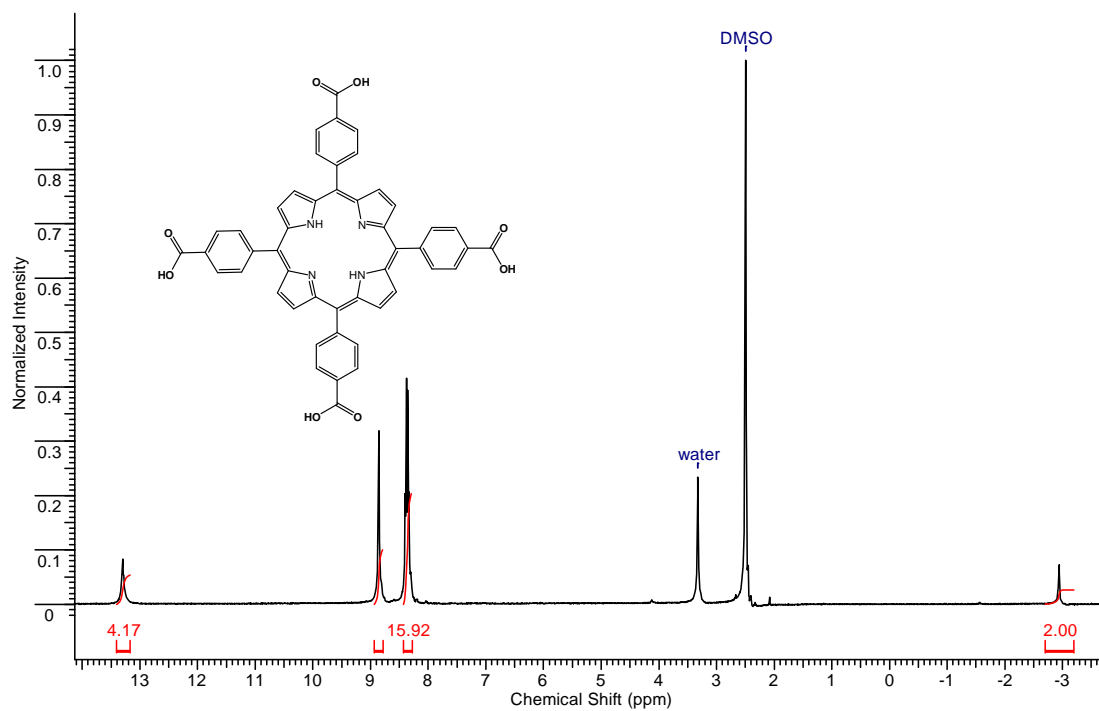
Figure A.11: ^{1}H-NMR of porphyrin TCPP
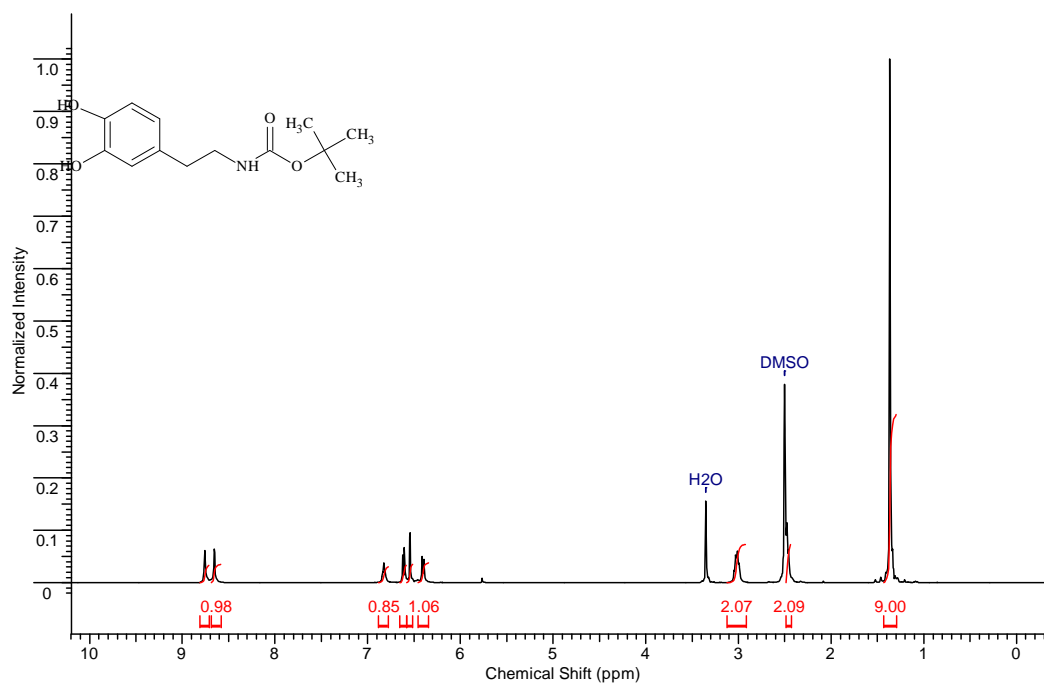
Figure A.12: ^{1}H -NMR of 2.5.2
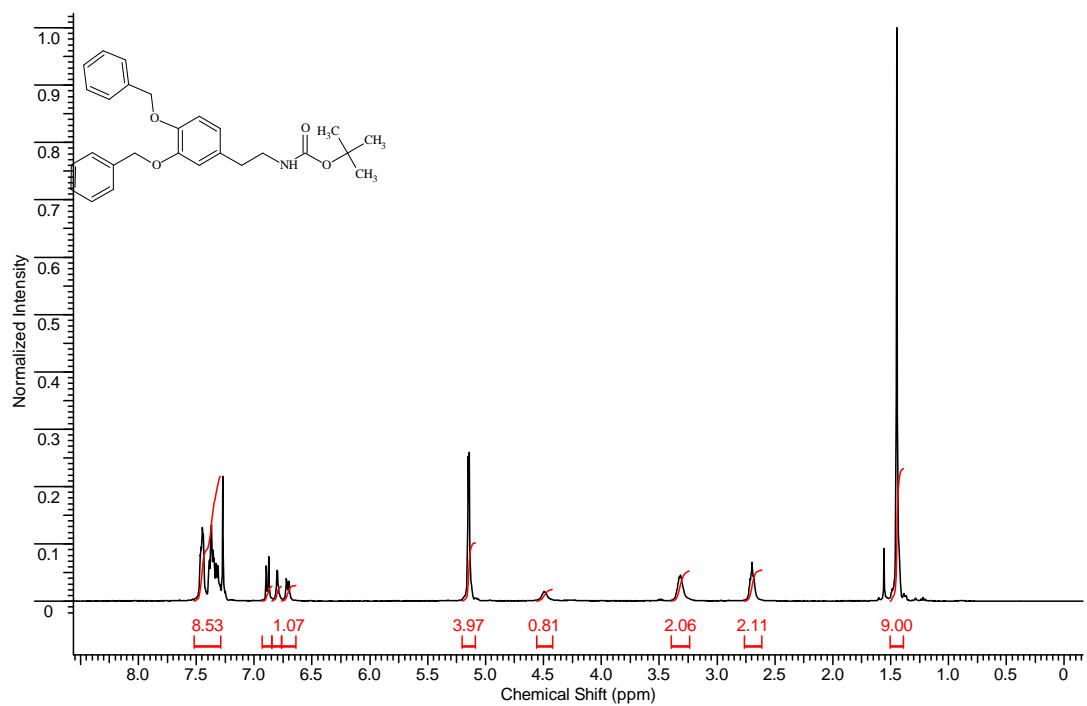
Figure A.13: ^{1}H NMR of 2.5.3
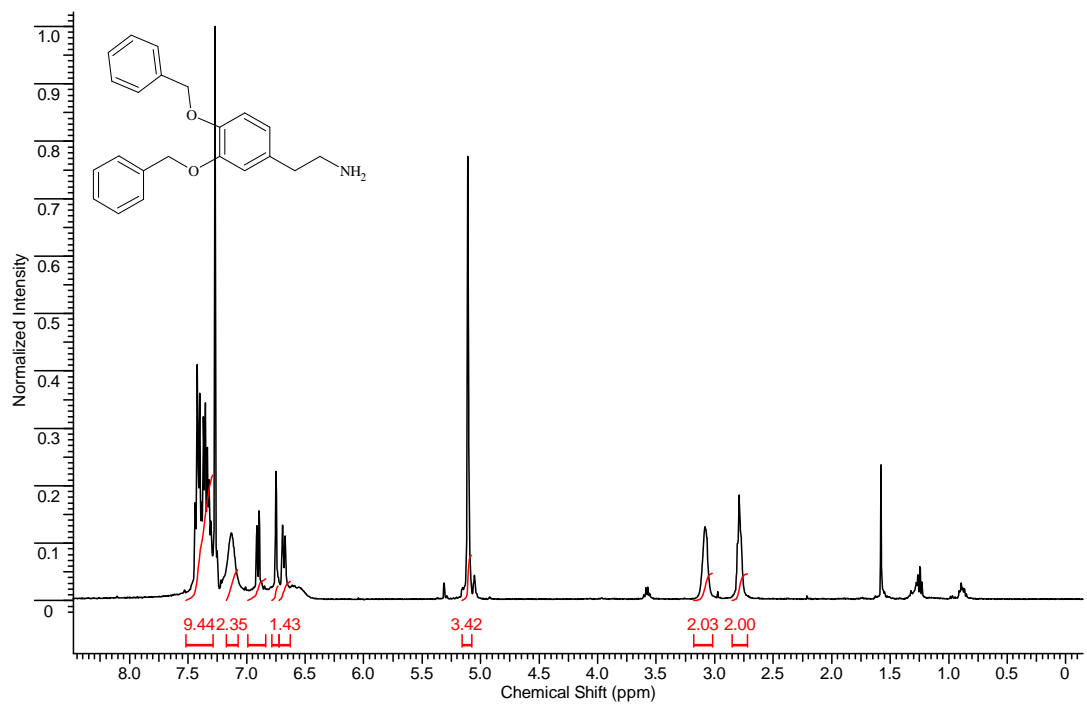
Figure A.14: ^{1}H NMR of 2.5.4
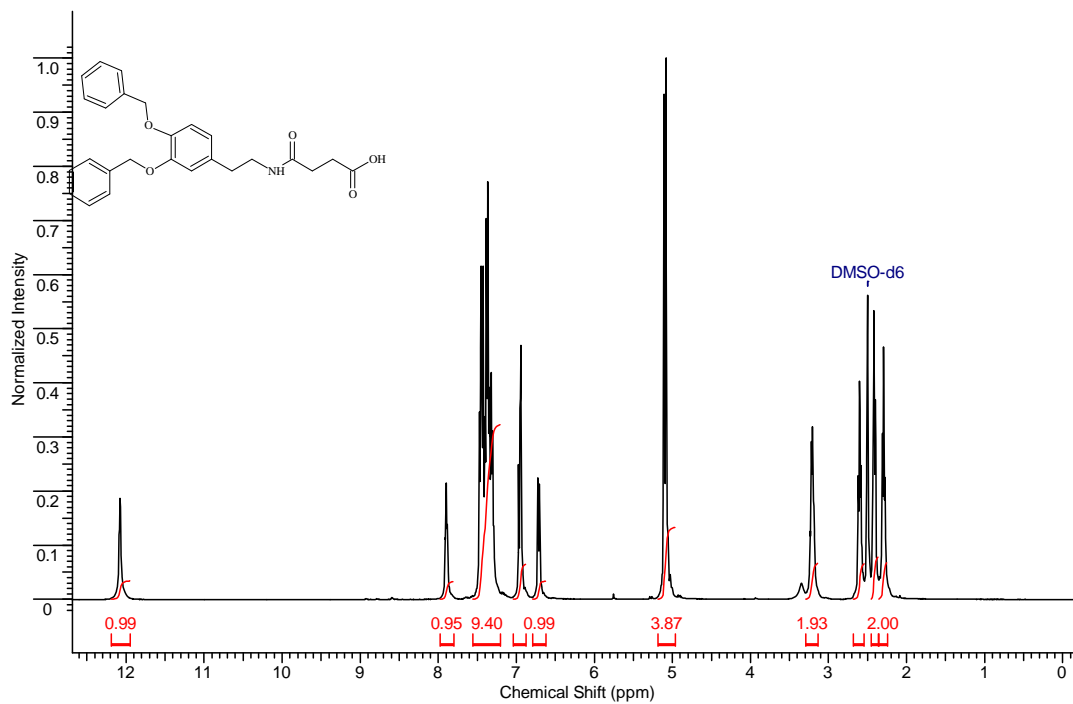
Figure A.15: ^{1}H NMR of 2.5.5
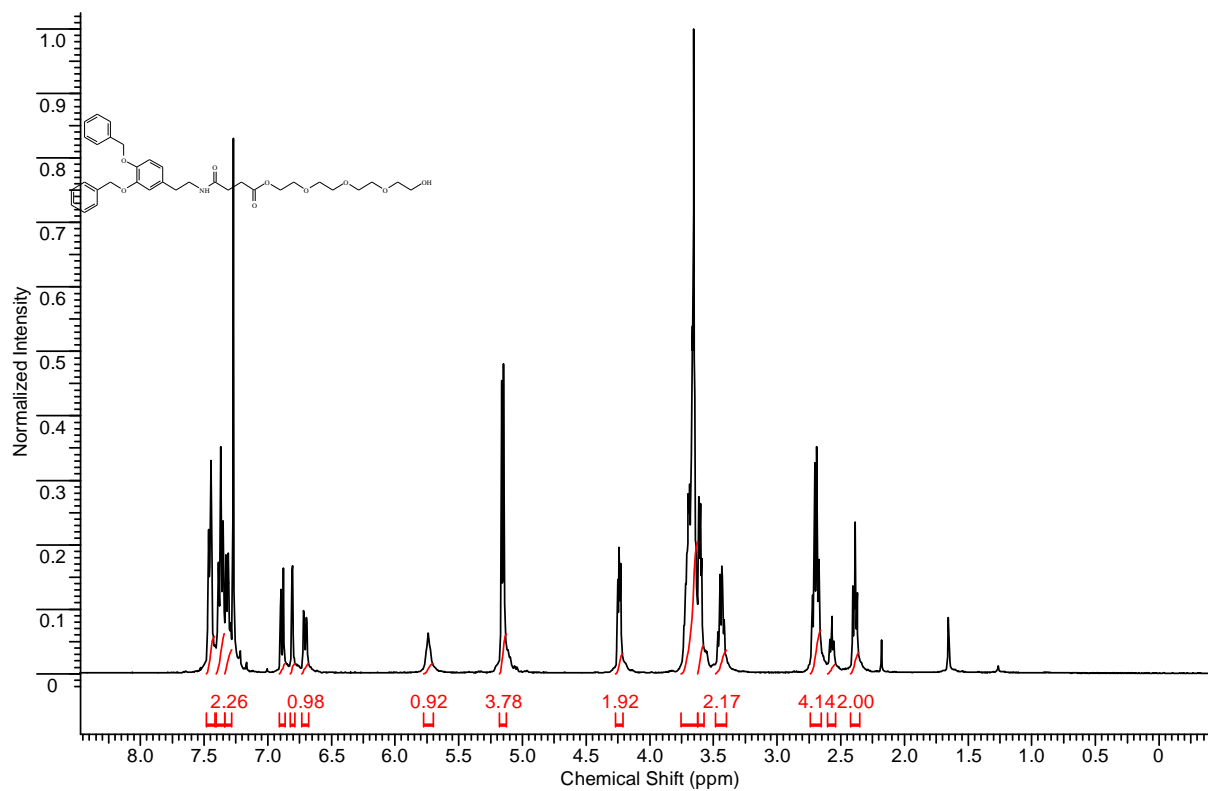
Figure A.16: ^{1}H NMR of 2.5.6 (A)
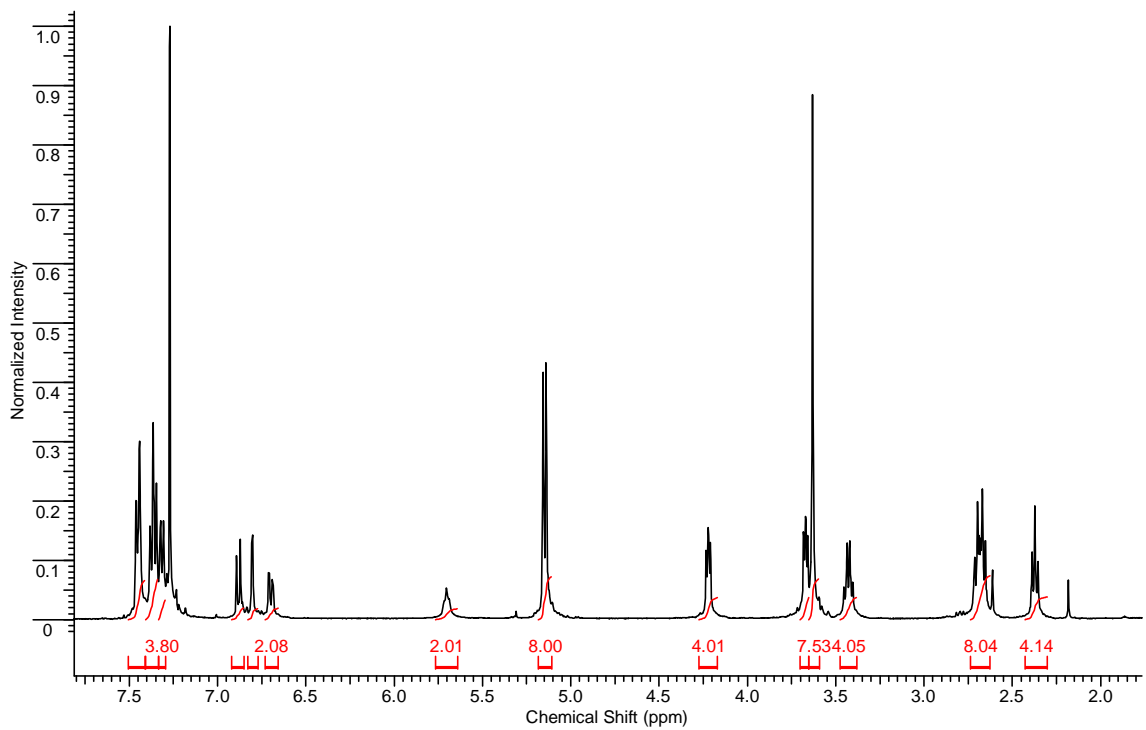
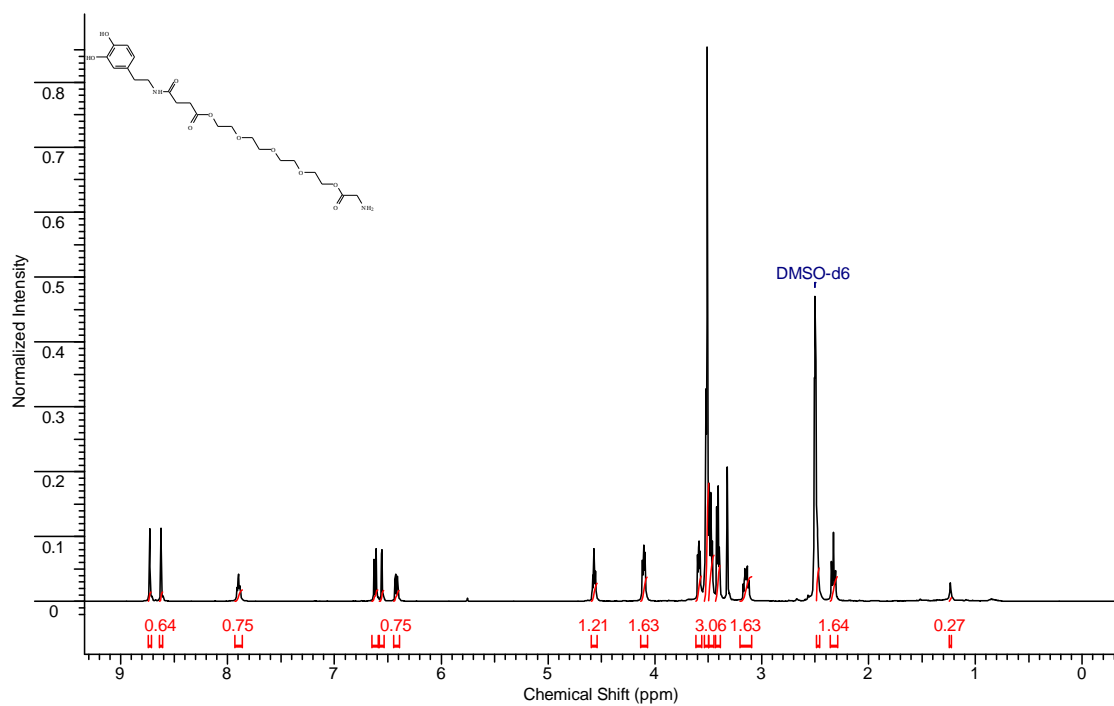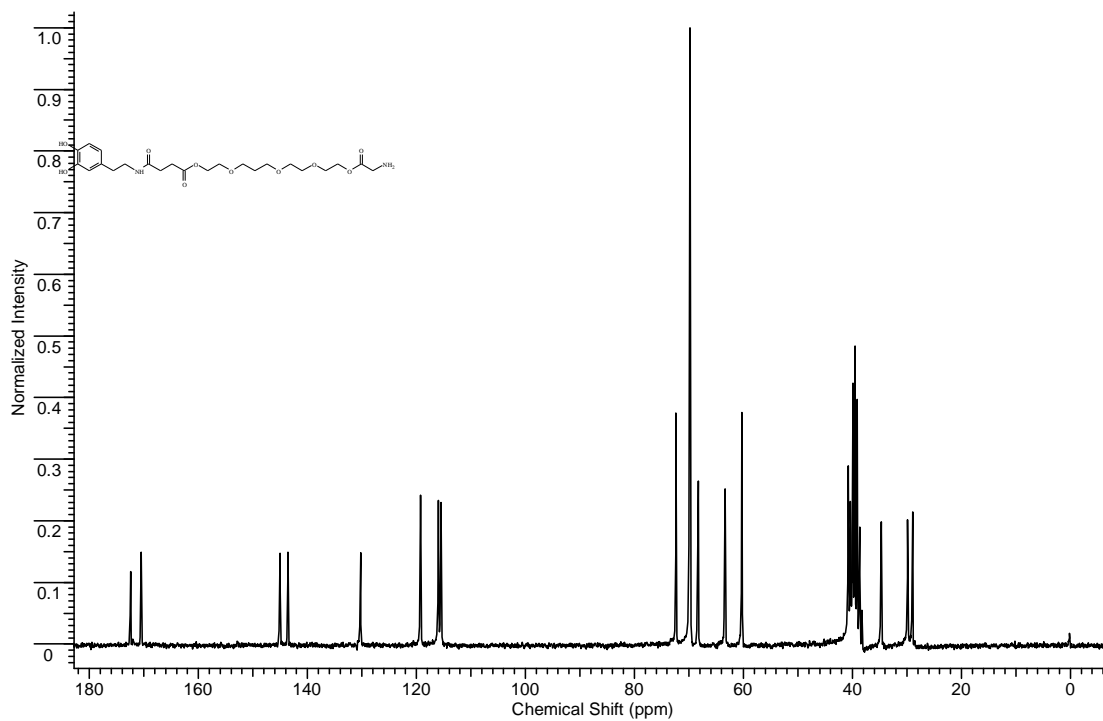Figure A.17: ^{1}H NMR of (B)
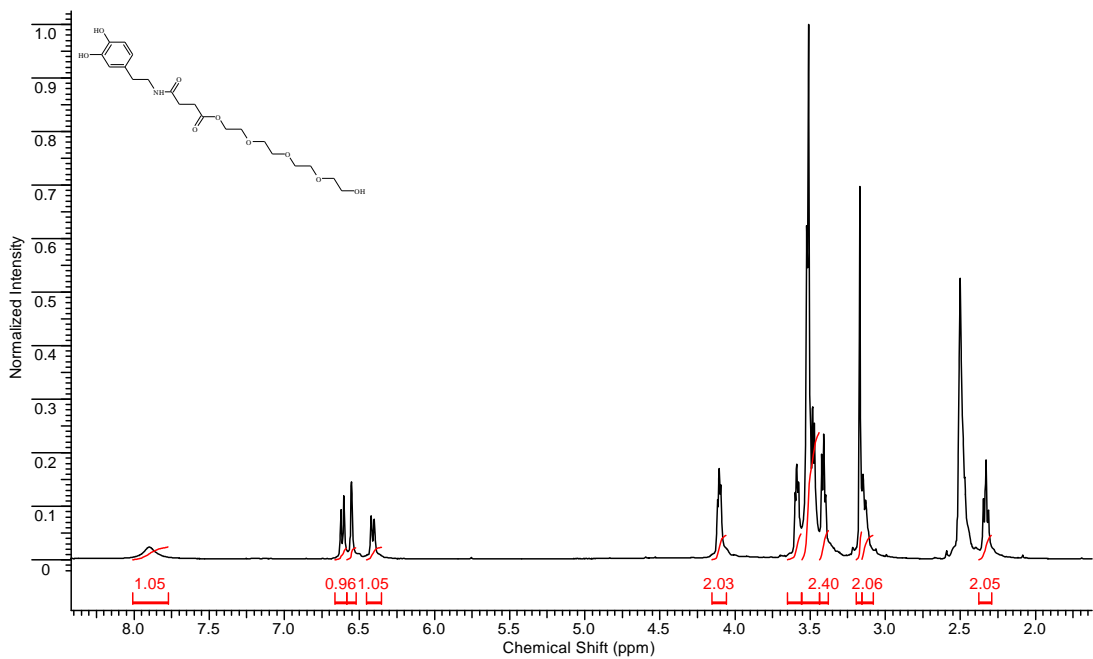
Figure A.18: ^{1}H NMR of ligand 2.5.7

172

Figure A.19: (a) ^{1}H NMR and (b) ^{13}C-NMR of ligand II

The NMR A: 11 to A 19 were obtained from the dissertation of Hongwang Wang.